

**Doctoral Dissertation (Shinshu University)**

**Hygroscopic nature  
of detonation nanodiamonds**

デトネーションナノダイヤモンドの吸湿性

**September 2019**

**Elda-Zoraida Piña-Salazar**



## アブストラクト

本論文は十一章で構成されている。第一章ではナノダイヤモンドとは何か、水蒸気吸着法、ナノダイヤモンドの吸湿性およびナノダイヤモンドの電気伝導性と水蒸気吸着との関係の研究の意義を述べる。第二章ではナノダイヤモンドの集合体の細孔構造を評価するのに用いる気体吸着の基礎に触れる。第三四六七と八章は印刷公表された論文の内容について述べる。第三章では走査電子顕微鏡、透過電子顕微鏡、電子エネルギーロス分光法、X線回折、X線光電子分光法、ならびに 77 K での窒素および 298K での水蒸気吸着法により行われたナノダイヤモンドの構造と性状について述べられている。これらの手法によるキャラクタリゼーションから、ナノダイヤモンドは  $sp^2$  混成のカーボンで覆われた  $sp^3$  混成カーボンのダイヤモンド粒子からなる細孔性集合体であることが示される。気体吸着と分子シミュレーションによる検討によって、ナノダイヤモンドの吸湿性の本質が明らかにされた。水に対して吸湿性を示すナノダイヤモンドのメソ細孔の壁には、親水性の官能基があるうえに、 $sp^2$  混成のグラフェン様膜とダイヤモンド粒子間のウルトラマイクロ細孔がある。これらの構造によってマクロな水を受け入れることができる極めて親水的なメソ細孔が存在して、著しい吸湿性を生じている。第四章は 423 K から 623 K で 2 h の加熱処理に伴う、ナノダイヤモンドの水蒸気吸着に対する選択的サイトの結果の記述にあてられる。端的に言えば、真空中の高温で処理すればするほど、水への選択吸着サイトが増えるという結果が得られた。第五章では 52 h という長時間の加熱処理に伴うナノダイヤモンドの細孔構造について述べる。短時間の加熱処理では見られない、より強くナノダイヤモンドに束縛されている吸着水の存在が示される。第六章ではナノダイヤモンドの吸湿性を他の吸湿性材料と比較する。水吸湿量で言えばナノダイヤモンドは粘土鉱物のモンモリロナイトと同程度であり、ZSM-5 および MS5A というゼオライトより大きい。第七章ではナノダイヤモンドに極めて強く束縛された水と電気伝導性との関係が述べられている。第八章および第九章では、SWCNH 上の水吸着に関する補足的な研究、およびナノダイヤモンドの吸湿性を理解する鍵となる SAXS によるナノダイヤモンド構造の決定を示す。第十章と第十一章では、現在の研究から得られた一般的な結論と科学的成果を示す。

## Abstract

The present thesis is organized into eleven chapters. The first chapter presents a general introduction of nanodiamonds, the state of art on the study of their water adsorption, hygroscopic behavior and influence of water adsorption on their electrical conductivity, and the justification of this research. The second chapter gives basic knowledge of gas adsorption as a means of evaluating the pore structure of nanodiamond aggregates. Chapters three, four, six, seven and eight are based on published papers. The third chapter presents the characterization of nanodiamond aggregates by scanning electron microscopy, transmission electron microscopy, electron energy loss spectroscopy, X-ray diffraction, X-ray photoelectron spectroscopy, adsorption of nitrogen at 77 K and water at 298 K. This characterization shows that nanodiamonds are porous aggregates of  $sp^3$ -hybridized carbon particles surrounded by  $sp^2$ -hybridized graphene-like carbon (partially oxidized graphene-like carbon). The adsorption and molecular simulation studies elucidated the origin of the hygroscopic nature of nanodiamonds; the hygroscopic nature of nanodiamonds stems from hydrophilic mesopore walls having surface functionalities and ultramicropores between the graphitic shell and nanodiamond particle. The fourth chapter shows the influence of thermal heating (423 K to 623 K) for 2 h on the selective sites for water adsorption in nanodiamond aggregates, showing that the higher the heating temperature in *vacuo*, the larger the amount of water-selective adsorption sites. The fifth chapter presents the influence of thermal heating for 52 h on the pore structure of nanodiamond aggregates. The prolonged heating (423 K for 52 h) induces an anomalous water adsorption behavior due to pre-removal of strongly bound water molecules from nanodiamonds. The sixth chapter compares the hygroscopic nature of nanodiamonds and other well-known materials. The water absorption capacity of nanodiamonds is comparable to that of the clay Montmorillonite and higher than those of the zeolites ZSM-5 and molecular sieve 5A. The seventh chapter shows the changes in the electrical conductivity of pre-adsorbed water nanodiamonds. The eighth chapter shows a supplementary study on water adsorption on SWCNH, which gives the key to understand the hygroscopic behavior of nanodiamonds. The ninth chapter is about the determination of the nanodiamond structure more accurately by SAXS, which is essential to understand the hygroscopic nature of nanodiamonds. The tenth and eleventh chapters show general conclusions and the scientific products from the present research.

## Acknowledgments

*I am very grateful to **Prof. Toshio Sakai** and **Prof. Katsumi Kaneko** for the opportunity of being a member of their research group at Shinshu University in Nagano; for their support, guidance and suggestions of improvement during the experimental and writing phases of this research. I thank **Prof. Eiji Ōsawa** for providing the target material to develop my doctoral research and valuable comments about its synthesis and properties.*

*I thank the **Grant-in-Aid-for Scientific Research** and the **OPERA project** for the economic support for my research. I am thankful for the support to join a variety of domestic and international conferences to present my research update and do networking.*

*I thank **Ms Manami Hoya** and **Ms Kumiko Miyajima** for helping with the administrative work related to my research and occasionally personal issues. I thank **my friends** and **colleagues** for personal, moral and professional support.*

*I am deeply grateful to **my family, parents, siblings, husband** and **daughter** for their moral support and encouragement. I thank **my husband Prof. Mr Aaron Morelos Gomez** for being my personal partner supporting with family issues, and my professional colleague having valuable scientific discussions on my doctoral research. I thank **my daughter Ariana Itzel Morelos Piña** for her patience, support and understanding the occasional family compromises to accomplish my professional goal of this PhD degree. I thank **my recently born baby Elissa Yatzil Morelos Piña** for accompanying me patiently from my womb the last year of my doctoral studies.*

***With a special dedication to my lovely family Aaron, Ariana & Elissa***

***Pursue your dreams through hard work and perseverance...***



## Preface

This thesis presents the research work performed during the period of the PhD program, organized in several chapters, as indicated below:

The first chapter is a general introduction to nanodiamonds. It gives a general idea of nanodiamonds and the state of art on the study of their interfacial properties of water adsorption and hygroscopic nature, as well as how these properties influence electrical conductivity. The justification, scope and aim of this research thesis, as well as a general research methodology, are explained at the end of the chapter.

The second chapter gives the reader basic knowledge of adsorption as a means of evaluating the pore structure of nanodiamond aggregates based on nitrogen, argon and water adsorption isotherms. It presents fundamentals, technical recommendations and a general methodology to assess the pore structure analysis.

The third chapter presents elementary nanodiamond aggregates characterization by scanning electron microscopy (SEM), transmission electron microscopy (TEM), electron energy loss spectroscopy (EELS), X-ray diffraction (XRD), X-ray photoelectron spectroscopy (XPS), nitrogen and water adsorption isotherms at 77 K and 298 K, respectively. Afterward, it deals with the identification of water adsorption sites in the nanodiamond aggregates, through adsorption experiments and simulations.

The fourth chapter is about the influence of thermal heating (423 K to 623 K); for a short time; in the selective sites for water adsorption in nanodiamond aggregates, which donate the hygroscopic nature of nanodiamonds.

The fifth chapter is an extension on the research of the influence of thermal heating for a longer time in the pore structure of nanodiamond aggregates, identified as sites for water adsorption. This has a great impact on the nanodiamonds ability to retain water.

The sixth chapter shows the extent of the hygroscopic nature of nanodiamonds compared to that of other well-known porous materials.

The seventh chapter discusses the impact of the hygroscopic nature of nanodiamonds and water affinity in their electrical conductivity.

The eighth chapter shows a supplementary study on water adsorption on single-wall carbon nanohorns (SWCNH), which gives the key to understand the hygroscopic behavior of nanodiamonds.

The ninth chapter is about the determination of the nanodiamond structure more accurately by SAXS, which is essential to understand the hygroscopic nature of nanodiamonds.

The tenth chapter gives a summary and conclusions of the present research. It summarizes the progress in the analysis of the hygroscopic nature of nanodiamonds and gives perspectives of the fundamental research presented in this thesis.

Finally, the eleventh chapter lists the scientific contributions resulted from the present doctoral research; indexed scientific publications and attendance to conferences.

## Table of contents

Abstract (Japanese version) .....	3
Abstract (English version) .....	4
Acknowledgments .....	5
Preface .....	7
Table of contents .....	9
1. General introduction .....	15
1.1 Allotropes of carbon .....	15
1.1.1 Nanodiamonds .....	17
1.1.1.1 Detonation nanodiamonds .....	18
1.1.1.2 Importance and uses of nanodiamonds .....	21
1.2 Interfacial properties .....	23
1.2.1 Hygroscopic nature of nanodiamonds .....	23
1.2.2 Wettability of some well-known porous materials.....	26
1.2.3 Influence of surface oxygen functionalities on water adsorption properties of carbon .....	27
1.2.4 Overview of previous studies about water adsorption on nanodiamonds .....	27
1.2.5 Influence of water in the electrical conductivity of carbon materials.....	31
1.3 Justification of the thesis research .....	33
1.4 Hypothesis and research questions .....	34
1.5 Purpose of the present study .....	35
1.6 General methodology .....	36
1.6.1 Study of hygroscopic nature of nanodiamonds .....	36
1.6.2 Physicochemical characterization .....	37
1.6.3 Relevance of water on the electrical conductivity of nanodiamonds	37
1.7 Applicability of the present research .....	38
1.8 References .....	39
2. Fundamentals of adsorption .....	49
2.1 General definitions and terminology .....	49
2.1.1 Physisorption process in micropores and mesopores .....	51
2.2 Methodology for physisorption measurements .....	53
2.2.1 Sample preparation .....	53

2.2.2	Choosing an adsorptive for the adsorption isotherm measurement	54
2.2.3	Measurement of the adsorption isotherm .....	55
2.2.4	Evaluation of the adsorption data .....	55
2.2.4.1	Classification of physisorption isotherms .....	56
2.2.4.2	Classification of hysteresis loops .....	59
2.2.5	Surface area evaluation .....	62
2.2.5.1	Brunauer-Emmet-Teller (BET) method .....	62
2.2.5.1.1	Applicability of BET surface area method .....	63
2.2.5.1.2	Application of BET to microporous materials .....	63
2.2.5.1.3	Methodology for application of BET method .....	64
2.2.5.1.4	BET equation and theory .....	64
2.2.5.2	Comparison to standard isotherms .....	65
2.2.5.2.1	Subtracting pore effect (SPE) method of the $\alpha_s$ -plots ...	66
2.2.6	Total pore volume evaluation .....	69
2.2.6.1	Micropore volume .....	70
2.2.7	Pore size distribution .....	70
2.3	Gas adsorption in non-rigid materials .....	73
2.4	Water adsorption .....	73
2.5	Adsorptives commonly used in physisorption .....	74
2.6	References .....	74
3.	Water adsorption property of hierarchically nanoporous detonation nanodiamonds .....	75
3.1	Introduction .....	76
3.2	Experimental section .....	78
3.2.1	Materials and methods .....	78
3.2.2	Characterization of nanodiamonds .....	78
3.3	Modeling and simulation section .....	79
3.3.1	Modeling of nanodiamond and simulation of water adsorption isotherm .....	79
3.4	Results and discussion .....	80
3.4.1	Water adsorption property and hygroscopic nature .....	88
3.5	Conclusions .....	91
3.6	Acknowledgments.....	92
3.7	References .....	92
4.	Water-selective adsorption sites on detonation nanodiamonds .....	99
4.1	Introduction .....	100
4.2	Experimental section .....	101
4.2.1	Samples and their thermal treatments .....	101

4.2.2	Characterization of nanodiamonds .....	101
4.2.2.1	Thermogravimetric analysis .....	101
4.2.2.2	Structural analysis .....	102
4.2.2.3	Water adsorption .....	103
4.3	Results and discussion .....	103
4.3.1	Morphology and surface chemistry of thermally treated nanodiamonds.....	103
4.3.2	Pore structure change of nanodiamond aggregates on heating .....	111
4.3.3	Relationship between water adsorption property and hydrophilic pore mouth structure .....	118
4.4	Conclusions .....	123
4.5	Acknowledgments.....	124
4.6	References .....	124
5.	Anomalous water adsorption behavior of prolonged heated nanodiamonds.....	131
5.1	Introduction .....	132
5.2	Experimental section .....	133
5.2.1	Sample preparation .....	133
5.2.2	Characterization of nanodiamonds .....	134
5.2.3	Porosity change of nanodiamonds on pre-adsorption of water .....	135
5.2.4	Water adsorption .....	135
5.3	Results and discussion .....	135
5.3.1	Structure and chemistry change of nanodiamond aggregates on heating .....	135
5.3.2	Effect of heating time on the pore structure of nanodiamond aggregates .....	138
5.4	Conclusions .....	147
5.5	Acknowledgments.....	148
5.6	References .....	148
6.	Unusual hygroscopic nature of nanodiamonds in comparison with well-known porous materials .....	151
6.1	Introduction .....	152
6.2	Experimental section .....	154
6.2.1	Materials .....	154
6.2.2	Characterization.....	155
6.2.3	Wettability for water and semi-quantitative evaluation of water absorption.....	156
6.3	Results and discussion .....	157
6.3.1	Scanning electron microscopic images of pelletized materials.....	157

6.3.2	Porosity of pelletized porous materials .....	157
6.3.3	Water absorption ability and wettability for water.....	167
6.4	Conclusions .....	180
6.5	Acknowledgments.....	181
6.6	References .....	181
7.	Electrical conductivity changes of water-adsorbed nanodiamonds with thermal treatment .....	187
7.1	Introduction .....	188
7.2	Experimental section .....	189
7.2.1	Electrical conductivity measurement .....	189
7.2.2	Characterization .....	189
7.3	Results and discussion .....	190
7.3.1	Effect of thermal outgassing on the morphology and surface chemistry of nanodiamonds .....	190
7.3.2	Effect of heating and compression on the porosity of nanodiamonds.....	192
7.3.3	Effect of compression on the electrical conductivity of nanodiamonds .....	195
7.3.4	Effect of water adsorption on the electrical conductivity of nanodiamonds .....	196
7.4	Conclusions .....	201
7.5	Acknowledgments .....	202
7.6	References .....	202
8.	Adsorption of water vapor on mesoporosity-controlled single-wall carbon nanohorn .....	207
8.1	Introduction .....	208
8.2	Experimental section .....	209
8.2.1	Opening of SWCNH .....	209
8.2.2	Characterization of SWCNH samples and water adsorption .....	210
8.3	Results and discussion .....	211
8.3.1	Nanoporosity and surface chemistry .....	211
8.3.2	Water adsorption .....	216
8.4	Conclusions .....	222
8.5	Acknowledgements .....	222
8.6	References .....	223
9.	Atomistic model-aided Small Angle X-ray Scattering method for evaluation of the individual particle size of aggregated detonation nanodiamonds .....	227
9.1	Introduction .....	228

9.2 Theory and modeling .....	230
9.2.1 Atomistic structural model of NDs .....	230
9.2.2 Polydispersity of DNs: Small-Angle X-ray Scattering .....	233
9.3 Results and discussion .....	236
9.4 Conclusions .....	244
9.5 Acknowledgments .....	245
9.6 References .....	245
10. General conclusions .....	251
11. Scientific products .....	255
11.1 Publications .....	255
11.2 Seminars and conferences .....	256



# Chapter 1

## 1. General introduction

### 1.1 Allotropes of carbon

Nature presents many different forms of carbon, many others have been produced synthetically by man through time. Carbon materials are classified in ordered and disordered depending upon the crystal structure. Ordered carbon is found commonly as graphite or diamond. Graphite is composed of several layers of hexagonal lattices, having the conducting character of a semimetal. Diamond possesses a crystal structure resembling two interpenetrated faces centered cubic lattices displaced  $\frac{1}{4}$  along the x, y and z directions, being the hardest material and exhibiting a wide band; electrical insulator. Fullerenes; formally discovered in 1985; may also be found in small quantities in nature. The most stable of this family is  $C_{60}$ ; having a structure that resembles a truncated icosahedron with twenty hexagons and twelve pentagons. Nanotubes are tubes formed by the rolling of a single hexagonal lattice in a determined direction. Amorphous carbon is free and reactive carbon that does not have any crystalline structure (contains microscopic amount of graphite-like carbon and/or diamond-like carbon). It might contain hydrogen terminations to stabilize dangling- $\pi$  bonds. Recently, nanodiamonds; nanoscale diamonds that conserve many diamond properties but at the nanoscale size; have emerged as a new type of carbon to be investigated. The frame structure of all these materials is represented in **Figure 1-1**.

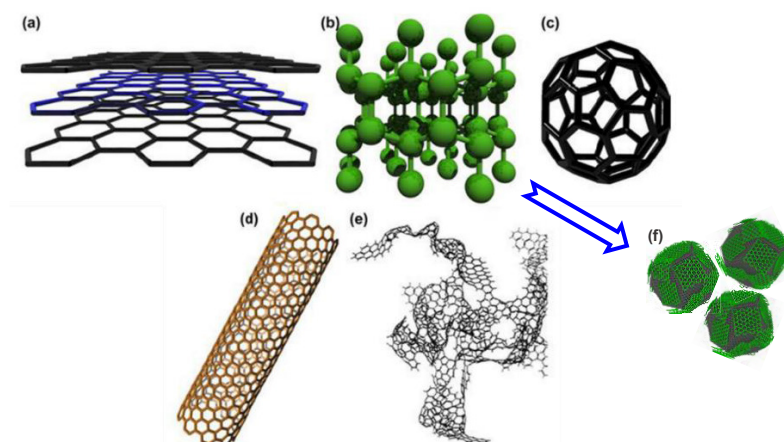


**Figure 1-1.** Carbon allotropes: (a) graphite, (b) diamond, (c) buckminsterfullerene, (d) carbon nanotube, (e) amorphous carbon and (f) nanodiamonds. (Image adapted from reference 1).

Porous carbons are nanoporous materials with a regular, porous structure, whose pores sizes are about 100 nm or less. **Figure 1-2** shows some of the representative porous materials. Although activated carbons are the classical example of porous carbons, other materials are also porous due to the intraparticle or interparticle pores, for example, zeolites, clays and nanodiamond particles in the form of aggregates. Porous carbon materials are of interest because of their capability to store molecules being used as filters, in catalysis, as sensors, etc.<sup>2,3</sup> Each porous material possess specific characteristics that give it unique properties. Properties at the interface of nanodiamonds; known as interfacial properties; are still in research to exploit their whole properties.

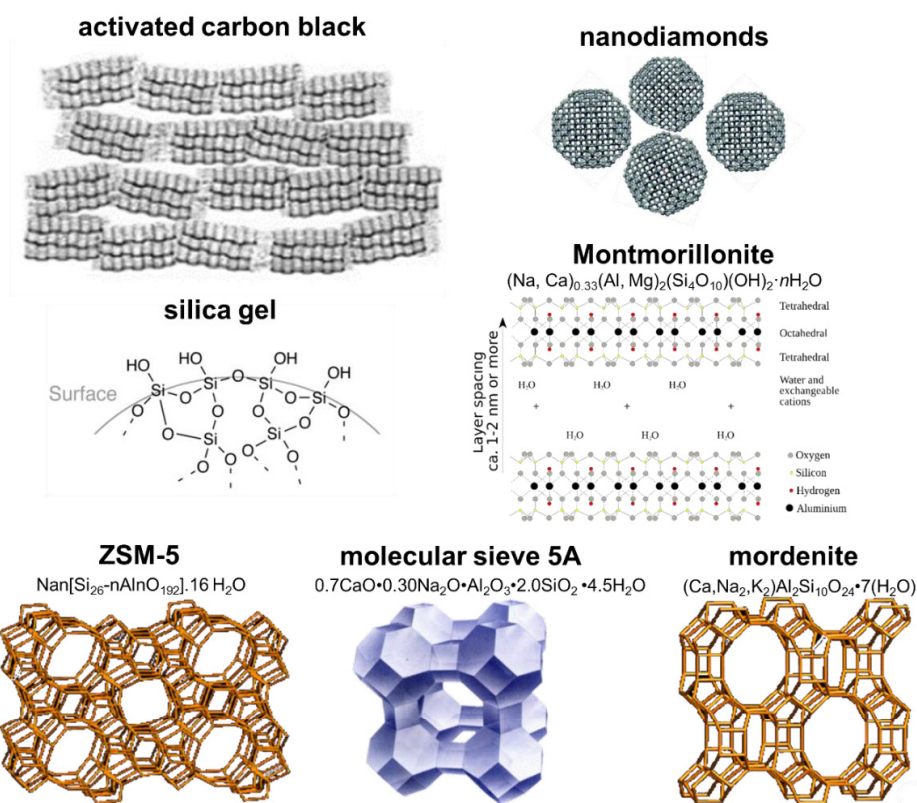


**Figure 1-2.** Representative porous materials: carbons such as activated carbon and nanodiamond, silica gel, clays as Montmorillonite, and zeolites such as ZSM-5, molecular sieve 5A and mordenite.

### 1.1.1 Nanodiamonds

Origin of nanodiamonds dates back to 1960s, when Soviet scientists obtained them as a product of detonation of carbon molecules of explosives in presence of an inert gas or water.<sup>4</sup> Nowadays, nanodiamonds are produced by several routes such as detonation, plasma-assisted chemical vapor deposition (CVD),<sup>5</sup> electron irradiation of carbon “onions”,<sup>6</sup> ion irradiation of graphite,<sup>7</sup> and high-energy ball milling at high-pressure and high-temperature (HPHT).<sup>8</sup> Detonation nanodiamonds are the most widely used, among them.

### 1.1.1.1 Detonation nanodiamonds

Detonation synthesis consists in the explosion of compounds with a negative oxygen balance; for example a mixture of 60 wt.% TNT ( $C_6H_2(NO_2)_3CH_3$ ) and 40 wt.% hexogen ( $C_3H_6N_6O_6$ ) inside a detonation chamber in an atmosphere of  $N_2$ ,  $CO_2$  and liquid or solid  $H_2O$ , as seen in **Figure 1-3a**. Afterward, diamond-containing soot is collected from the bottom and the walls of the chamber. Synthesis of nanodiamonds requires specific conditions of temperature and pressure, as seen in the phase diagram in **Figure 1-3b**. The most stable phase of carbon is graphite at low pressures, and diamond at high pressures, with both phases melting at temperatures above 4500 K (with the precise melting temperature for each phase depending on the pressure). The phase diagrams for nanoscale carbon are similar, but the liquid phase is found at lower temperatures. During detonation, the pressure and temperature rise instantaneously, reaching the Jouguet point (point A), which falls within the region of liquid carbon clusters of 1–2 nm in size for many explosives. As the temperature and pressure decrease along the isentrope (red line), carbon atoms condense into nanoclusters, which further coalesce into larger liquid droplets and crystallize. When the pressure drops below the diamond-graphite equilibrium line, the growth of diamond is replaced by the formation of graphite. **Figure 3c** shows the different phases of nanodiamond formation during synthesis; starting from the decomposition of explosives by the detonation wave and ending with the crystallization and agglomeration of nanodiamonds.<sup>9,10</sup>

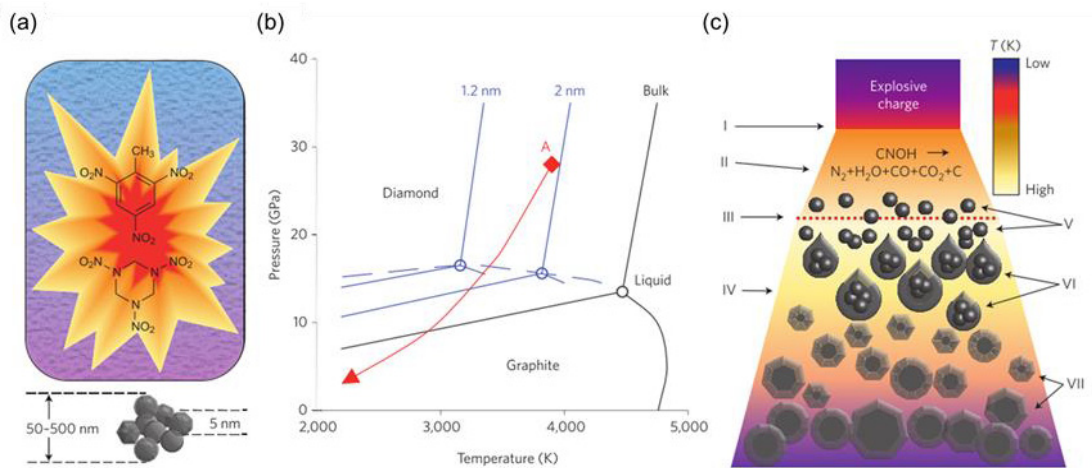


**Figure 1-3.** Detonation synthesis of nanodiamonds. (a) Mixture of TNT ( $C_6H_2(NO_2)_3CH_3$ ) and hexogen ( $C_3H_6N_6O_6$ ) in a detonation chamber with an atmosphere of  $N_2$ ,  $CO_2$  and liquid or solid  $H_2O$ . A nanodiamond aggregate is shown in the lower part. (b) Phase diagram of the diamond formation. (c) Scheme of the detonation wave propagation during the synthesis of nanodiamond in a detonation chamber. (I) the front of the shock wave caused by the explosion; (II) the zone of chemical reaction in which the explosive molecules decompose; (III) the Chapman–Jouguet plane (where P and T correspond to point A in Fig. 1b), indicating the conditions when reaction and energy release are essentially complete; (IV) the expanding detonation products; (V) the formation of carbon nanoclusters; (VI) the coagulation into liquid nanodroplets; and (VII) the crystallization, growth and agglomeration of nanodiamonds. (Image from reference 10).

Nanodiamonds produced by detonation consist of polyhedral particles of  $sp^3$ -hybridized carbon with a mean diameter around 4 nm.<sup>11,12</sup> These polyhedral particles tend to form aggregates of 50-500 nm in diameter, leaving inter-granular gaps that form a porous structure,<sup>13,14</sup> as seen in **Figure 1-4**. Nanodiamonds particles are wrapped with graphene-like films of  $sp^2$ -hybridized carbon atoms or amorphous carbon layers.<sup>15,16</sup>

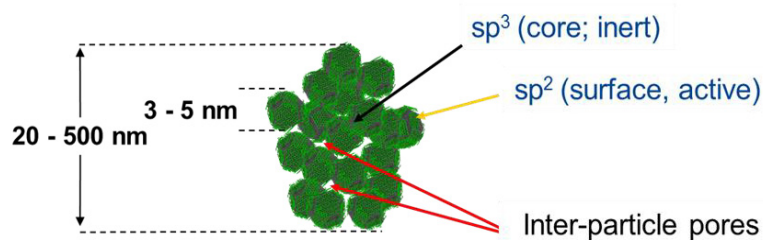


**Figure 1-4.** Representation of a nanodiamond aggregate showing  $sp^2$  and  $sp^3$  carbon, and pores.

Raman spectrum of nanodiamonds shows a signal at about  $1330\text{ cm}^{-1}$  corresponding to diamond bonds and the G band near  $1580\text{ cm}^{-1}$  due to the C-C stretching bonds in graphitic carbons,<sup>17</sup> as shown in **Figure 1-5**.

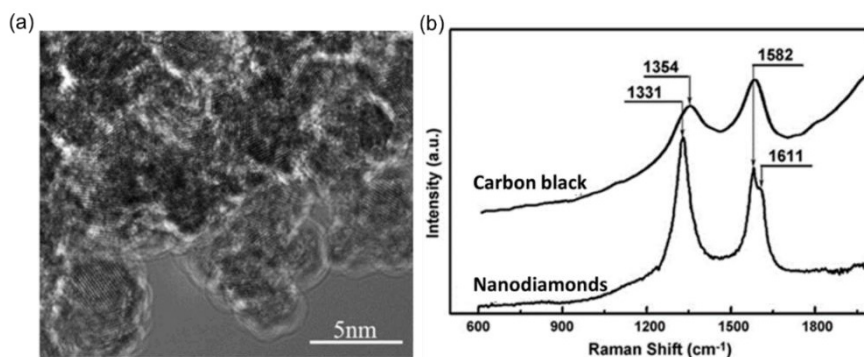


**Figure 1-5.** (a) TEM image of nanodiamond aggregates prepared by detonation method and (b) Raman spectra of carbon black and nanodiamonds formed by irradiation. (Image adapted from reference 17).

The elemental composition of nanodiamonds is examined by XPS analysis showing that the major component is carbon. In addition, 3% of oxygen and 1% of nitrogen are included. The presence of oxygen comes from the purification treatments and aggregate

disintegration by oxidation with acids and bead milling. Such oxygen is located on the surface as oxygen-containing functional groups, while nitrogen comes from the precursors used during the synthesis and locates mainly in the core.<sup>11,18</sup>

Properties of nanodiamonds depend on the method and conditions of synthesis. A general view of the properties of nanodiamonds is presented in **Figure 1-6**.

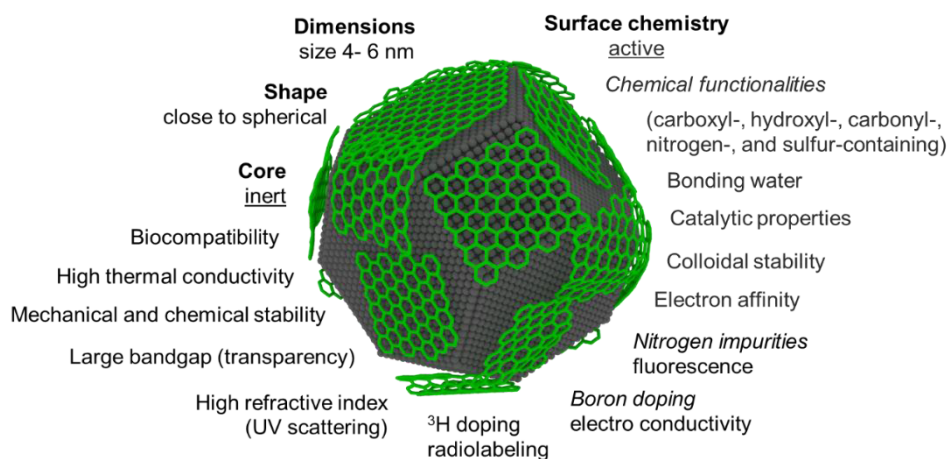


**Figure 1-6.** General characteristics of nanodiamonds and remarkable applications.

### 1.1.1.2 Importance and uses of nanodiamonds

Since their discovery and recently after the successful development of detonation nanodiamond particles of about 3-4 nm in diameter by Ōsawa *et al.* (2007),<sup>12</sup> worldwide studies have been carried out on them. **Figure 1-7** shows some of the applications of nanodiamonds nowadays. For example, use of functionalized nanodiamonds as chemotherapeutic drug carriers taking advantage of their greater biocompatibility compared to other nanocarbon materials, use in the fabrication of solar cells to increment their efficiencies, as bio labels due to their photo-luminescent properties, and as additives

to enhance mechanical or thermal properties.<sup>10,13,19–22</sup> It is worthy to say that the above mentioned and many other of the plausible applications of nanodiamonds depend on their properties and the result of their manipulation.

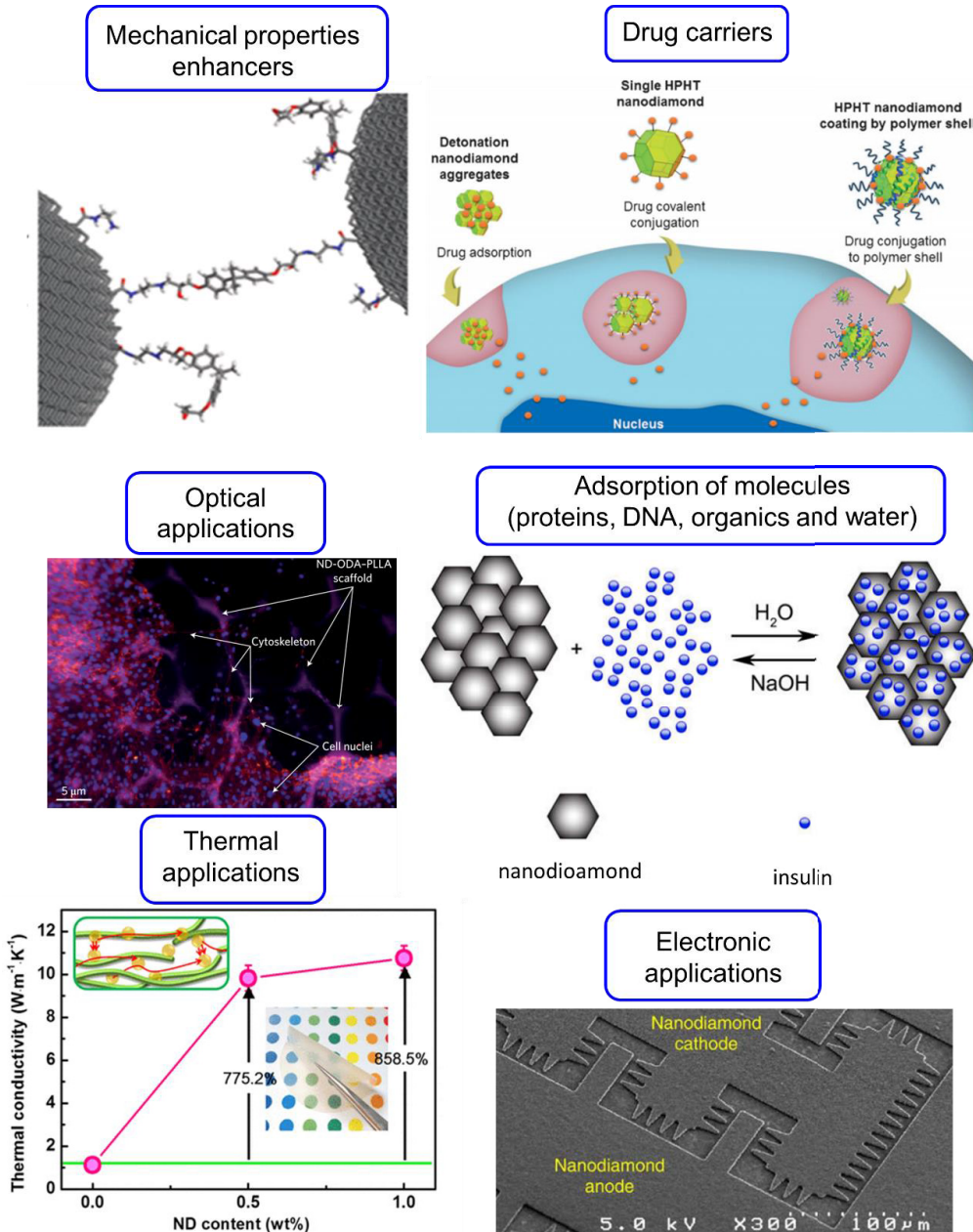


**Figure 1-7.** Several current uses of nanodiamonds. (Image adapted from references 10,23–27).

## 1.2 Interfacial properties

Interfacial properties of a material refer to their attributes, qualities, or characteristics that are related to or form a common boundary between two portions of matter or space. Hygroscopic property of nanodiamonds is addressed in the present research work.

### 1.2.1 Hygroscopic nature of nanodiamonds

Hygroscopic property refers to the ability of a material to absorb or release water as a function of humidity (ie. water activity). Specifically, in porous materials, this water should be retained in their structure, depending on their hydrophilic characteristics, texture and the arrangement of particles.<sup>28</sup>

Nowadays, water studies on nanodiamonds are of special interest because the vast majority of research involves water interaction, for their potential application on water recovery taking advantage of their physicochemical properties, as well as by their potential use as a model to explain water-material associations that exist in nature.<sup>20,29–32</sup> Some organisms have the ability to trap water and use it for their own benefit. Recent studies have shown that plants, such as the desert moss *Syntrichia caninervis* survives the dryness of its environment by collecting water from the moist air and transporting it through a hair-like structure in its leaves.<sup>33</sup> A similar process occurs in animals such as the *Stenocara* beetle, which lives in the desert and survives in the aridity by drinking water that collects from mist by using its wings and then rolling it out. In order to reach its goal, this beetle lifts up its back to the wind direction to capture water droplets suspended as mist due to the affinity of the hydrophilic sites on its back. Through time, more droplets adhere to the same sites and grow bigger until they reach a critical size, and

then roll out from the hydrophobic background where the hydrophilic humps are situated.<sup>34</sup> In a similar way, nanodiamonds could be used to explain the mechanism by which mist water is harvested from the air and transformed into droplets by some organisms. Besides, certain animals can survive arid conditions by taking advantage of a natural mechanism to retain water; such as camels in the desert.<sup>35</sup> Thus, in order to understand the mechanism of water collection in living organisms, research on materials with both hydrophilic and hydrophobic surfaces has been conducted. For example, vertically aligned multi-walled carbon nanotube forests (NTF) with one hydrophilic and one hydrophobic side, mimicked structures in *Stenocara* beetle to harvest water.<sup>36</sup>

First, it is necessary to carry out fundamental research on the physical and chemical properties involved in the interactions of nanodiamonds with water and the role of structural parameters in order to understand their behavior in the presence of water. Porosity of materials, known as well as structural parameters of materials, are widely described by means of nitrogen adsorption.<sup>37,38</sup> Lately, the use of argon; a spherical and nonpolar molecule; is being implemented because interactions between argon atoms can be more easily described than those involving diatomic nitrogen molecules with quadrupole, resulting in more sensitive measurements through the description of smaller porous dimensions due to its small molecular size.<sup>39,40</sup> Water affinity of a material can be indicated indirectly by means of water adsorption, but mainly by measurements of water contact angle.<sup>41</sup> Adsorption of water refers to the adhesion of water molecules to the surface of the adsorbent material. So far, few attempts to analyze deeply water adsorption on nanodiamonds are described. For example, adsorption of water on nanodiamond particles with a modified surface by the introduction of chlorinated species, carboxylate

and amine groups showed that their ability to adsorb water, and to aggregate, depends on the energy and chemical state of their surface and the intra and inter-particle porous structure. As supportive evidence, adsorption of benzene vapor (of different polarity than water) was conducted in that study.<sup>42</sup> Aside, detonation nanodiamonds have been reported to adsorb water from 0.03 g g<sup>-1</sup> to about 0.24 g g<sup>-1</sup> depending on their post-purification treatments.<sup>43</sup> Carbon nanohorns adsorb water on micropores and small mesopores of less than 5 nm in diameter.<sup>45-47</sup> FTIR observation of the adsorption of water on non-modified nanodiamonds and modified by different oxidative treatment under gasses and high temperature shows that water can be easily adsorbed forming hydrogen bonding on the sites of acid or base Lewis of oxidized nanodiamonds.<sup>44</sup> To this date, limited understanding of the physicochemical properties involved in the adsorption mechanism that governs the adsorption of water still exists. The ability of water molecules to be adsorbed in narrower spaces than nitrogen molecules could be used as a way to characterize the small porosity of a material.

One of the ways to elucidate the water sorption onto materials is defining the water surface tension of the material, which is an indicator of wettability. Water contact angle; the angle of the liquid on a solid surface; well defines the hydrophilic (or hydrophobic) character. In that regard, the air-water contact angles of polished diamond faces were reported to be 75.9° (for the diamond face 111) and 71.0° (for the diamond face 110).<sup>48</sup> The contact angle for as-grown un-doped nanocrystalline diamond films in air at room temperature was 73 ± 3°.<sup>49</sup> The contact angle of chemical vapor produced nanodiamonds was reported lower than that of graphite. It should be noted that these nanodiamonds have sensitive surface chemistry (oxidized 32° and reduced 93°).<sup>50</sup>

### 1.2.2 Wettability of some well-known porous materials

Former observations showed that nanodiamond pellets could absorb water at a faster rate than graphite ones. A droplet of water on a graphite pellet required at least 200 seconds to disappear, while for a nanodiamond pellet required only a few seconds (to be absorbed by the nanodiamond structure). However, a fair comparison should compare quantitatively the wettability of nanodiamond pellets to that of other representative well-known porous materials, in order to give a better insight on the wettability efficiency. The most studied materials for water absorption are microporous materials, as inorganic zeolites or silica gels, as well as activated carbon. Silica gels ( $\text{SiO}_2 \cdot x\text{H}_2\text{O}$ ) are widely studied due to their high affinity towards water vapor, large water sorption at low humidity, low price and easy regeneration. Previous research reported that silica aerogel,  $\text{CaCl}_2/\text{SiO}_2$  aerogel, alumina aerogel, and  $\text{CaCl}_2/\text{SiO}_2$  xerogel exhibited high water sorption capacity; 1.35, 1.27, 1.25 and 1.17  $\text{g g}^{-1}$ , respectively. Meanwhile, zeolites showed high water sorption due to their electrostatic charged framework and the abundance of extra-framework cations. For example, zeolites of 12-rings size, like ZSM-20, Mg-X, Mg-Y, LiNa-X, Li-Y showed high water sorption capacity (0.46, 0.45, 0.42, 0.38 and 0.36  $\text{g g}^{-1}$ ), and 0.34  $\text{g g}^{-1}$  for Na-Y, Ca-Y and Na-X.<sup>28</sup> Adsorption of water on activated carbon fibers (ACF) was reported as dependent on the pore size; the larger the pore, the greater the adsorption.<sup>51,52</sup> So then, ACF-20 showed an adsorption amount of water of about 0.7  $\text{g g}^{-1}$ .<sup>53</sup> Similarly, inorganic clays are described as highly hydratable substances that swell in the presence of water. Montmorillonite; an alumino-silicate clay containing silica tetrahedral external layers; is highly hydratable; 0.4  $\text{g g}^{-1}$  of water were adsorbed by Na-montmorillonite.<sup>54-56</sup>

### **1.2.3 Influence of surface oxygen functionalities on water adsorption of carbon**

Oxidation treatments introduce oxygen-containing functionalities to materials, which influence water adsorption behavior. Then, it could cause the same effect for the absorption of water. On one hand, chemical oxidation by hydrogen peroxide ( $\text{H}_2\text{O}_2$ ) and nitric acid ( $\text{HNO}_3$ ) have gained attention. For example, surface oxygen groups were successfully donated to activated carbon (AC) treated under those oxidative agents<sup>57</sup> and carbon nanotubes (CNT) were selectively oxidized by  $\text{H}_2\text{O}_2$ .<sup>58,59</sup> An acid treatment of Single-Walled Carbon Nanotubes (SWCNTs) using  $\text{HNO}_3/\text{H}_2\text{SO}_4$  derived in the introduction of oxygen functionalities to SWCNTs.<sup>60</sup> On the other hand, gas oxidation process is an alternative treatment to modify the surface chemistry of nanodiamonds without using aggressive chemicals. In this sense, air used as an oxidant of nanodiamonds has been widely reported. The used gas modifies the nanodiamond surface depending on the temperature applied, due to the removal of different materials from the diamond surface. For example, temperatures in the range of 673 to 703 K under air atmosphere oxidize  $\text{sp}^2$ -bonded carbon, ergo, selective removal of  $\text{sp}^2$ -hybridized carbon, preserving the complete  $\text{sp}^3$ -hybridized carbon structure (or with minimal loss of diamond).<sup>61,62</sup> The purification process of nanodiamonds by using acids partially oxidize their outer graphene-like layer, even when they are no further oxidized.<sup>61</sup> It is worthy to mention that the oxidation state of carbons influences other properties such as water adsorptivity in activated carbons.<sup>63</sup>

### **1.2.4 Overview of previous studies about water adsorption on nanodiamonds**

Nanodiamonds tend to be hydrated when they are exposed to humid air.<sup>31,43,44,64</sup> Complementary, thermal programmed desorption analysis shows the evolution of water

from nanodiamonds when heating.<sup>44</sup>

Commercial detonation nanodiamonds reveal the presence of mesopores by using the standard Barrett, Joyner, Halenda (BJH) method. The primary nanodiamond particles form a porous network with voids smaller and larger than the particles itself, readily available for water,<sup>13</sup> as seen in **Figure 1-8** of the nitrogen adsorption isotherms and the corresponding pore size distributions. There, the authors addressed the porosity of the nanodiamond aggregates by using the BJH method. This method determines the pore size distribution of a mesoporous solid based on the Kelvin equation. Nowadays, it is outdated due to the heterogeneity of the carbon sample; instead, the IUPAC recommends using the Density Functional Theory (DFT) method and the comparison method  $\alpha_s$ -plot to obtain more accuracy on the hierarchical pore structure and pore size distribution.

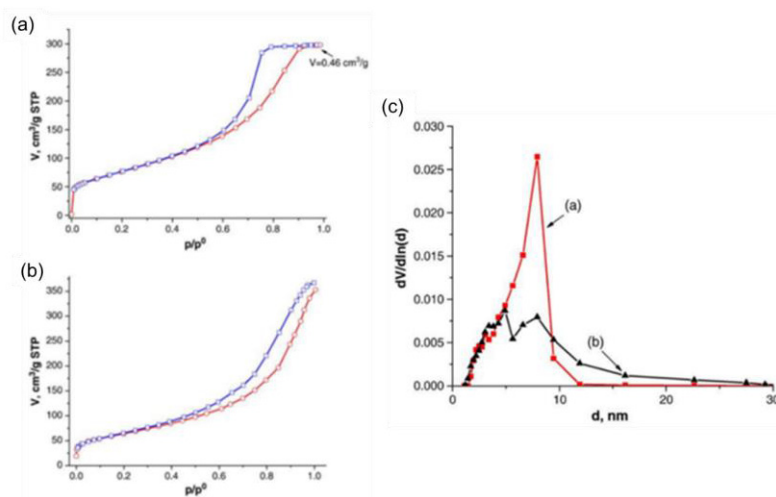


**Figure 1-8.** Nitrogen adsorption (red)-desorption (blue) isotherms at 77 K of (a) dry powder and (b) commercial diamond nanoparticles (agglutinates). (c) BJH analysis of the desorption isotherms of (a) dry powder and (b) commercial diamond nanoparticles (agglutinates). (Image adapted from reference 13).

Denisov *et al.* (2013)<sup>65</sup> showed water adsorption isotherms of nanodiamonds (only the adsorption branch) and suggested a model of the primary adsorption centers (PAC), as seen in **Figure 1-9a** and **Figure 1-9b**, respectively. The authors stated that water adsorption begins starting from the interaction of water molecules with these PACs. Oxygen-containing surface functional groups on the material, on which water molecules primarily adsorb, can appear as PACs. Water molecules adsorbed on PACs themselves then begin to act as secondary adsorption centers. During adsorption of water molecules on a carbon adsorbent surface, clusters from associated water molecules are formed around individual PACs, as shown in **Figure 1-9b** (upper), clusters merge with the formation of a continuous aqueous film when the distance between them is less than 3 nm, as seen in **Figure 1-9b** (down). Here, the authors suggested that the sites of strong water vapor adsorption on nanodiamonds are surface functional groups, following a similar mechanism like in the activated carbon case. Nevertheless, the pore structure of nanodiamond aggregates was not considered in the proposed mechanism of water adsorption for oxygen-containing nanodiamonds.

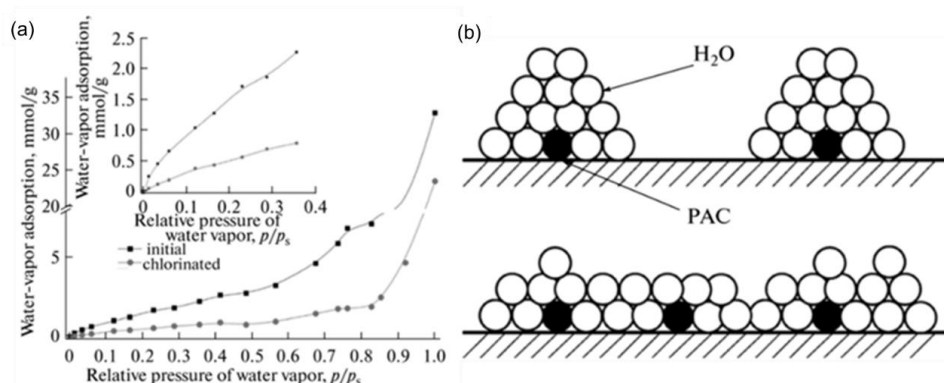


**Figure 1-9.** (a) Isotherms of water-vapor adsorption at 293 K on initial and chlorinated nanodiamonds. (b) Scheme of filling of carbon adsorbent surface by water. (Image from reference 65).

Petit *et al.* (2017)<sup>66</sup> experimented with dry nanodiamonds exposed to liquid water, dry air and finally to humid air (**Figure 1-10a**). FTIR analysis evidenced that exposure to air of nanodiamonds previously wetted with liquid water, could not remove completely the water hydration layer deposited on nanodiamonds, especially for the case of hydrogenated nanodiamonds, as shown by the differences between the solid and dashed green lines, in the FTIR of **Figure 1-10b**. In hydrogenated nanodiamonds, a long-range disruption of the water hydrogen bond network is associated with hydrogenated surface groups, which could be the consequence of electron accumulation at the hydrogenated diamond–water interface.

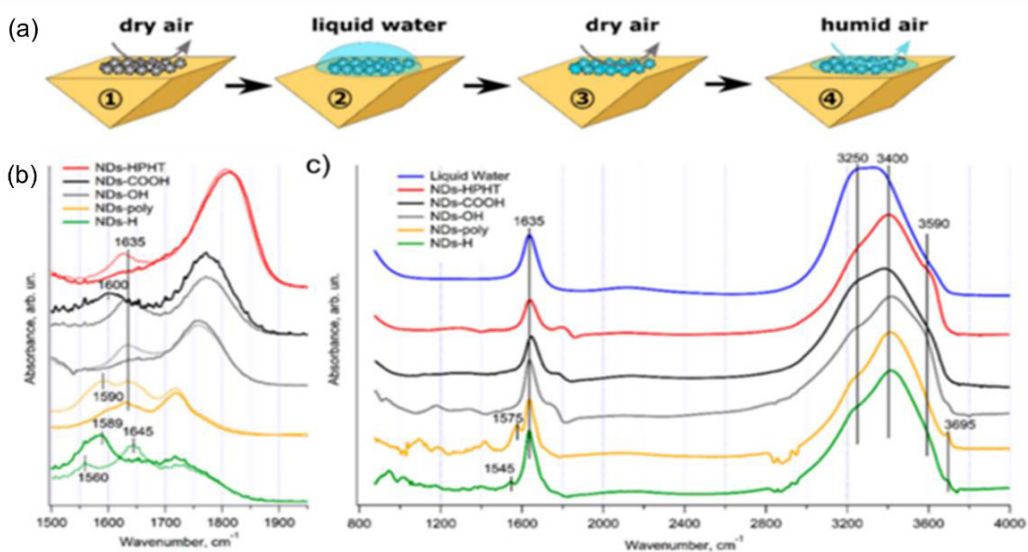


**Figure 1-10.** (a) Sequence of FTIR measurements of nanodiamonds (NDs) in the ATR cell. Step 1: NDs are dried overnight and measured under dry air flow. Step 2: NDs are exposed to liquid water. Step 3: NDs are exposed to dry air for a few minutes. Step 4: NDs are exposed to humid air. (b) Comparison of normalized FTIR spectra in the OH bending vibration region between NDs at step 1 (solid) and step 3 (dashed). (c) FTIR difference normalized spectra between steps 4 and 3. (Image from reference 66).

In summary, studies on the interactions of nanodiamonds with the solvent water indicates that hydrogenated or oxidized nanodiamonds show different interaction with water; highlighting the surface functionalities and/or the electron accumulation effect as responsible of the water affinity in oxidized and/or hydrogenated nanodiamonds.<sup>67</sup> Studies have shown that nanodiamonds have the ability to adsorb water, as mentioned above. Then, fundamental research about porosity and adsorption properties of nanodiamond aggregates, as well as the hygroscopic nature must be conducted to draw an inclusive mechanism of the hygroscopic nature of nanodiamonds, in order to exploit the properties dependent of water adsorption. Therefore, our present research introduces the pore structure analysis to the explanation of the water affinity of nanodiamonds.

### **1.2.5 Influence of water in the electrical conductivity of carbon materials**

Diamond; a monocrystal of carbon; has the physical properties of a wide bandgap semiconductor.<sup>68</sup> Diamonds at nanoscale should share this property. Semiconductors can be applicable to power device technology, electronic circuits, control of electrical current, to mention some. For example, a nanodiamond field-emitter array diode and device electrodes were developed for high power applications.<sup>27</sup> Electrical properties of nanodiamonds have been studied. Typical values of electrical conductivity of detonation nanodiamonds are in the range of  $10^{-7} \Omega^{-1} \text{ cm}^{-1}$  to  $10^{-12} \Omega^{-1} \text{ cm}^{-1}$ <sup>69</sup> Electrical conductivity is influenced by the presence of defects, impurities or dopants: oxygen, nitrogen, boron, phosphorus and adsorption of H<sub>2</sub>O, O<sub>2</sub> or CO<sub>2</sub>. In addition, the electronic properties of hydrogenated diamond and other carbon materials are sensitive to adsorption of water from the surrounding environment.<sup>70,71</sup> Single-wall carbon nanotubes annealed in *vacuo* may change the dominant charge carrier from electrons to holes when exposed to air at

room temperature.<sup>72</sup> Recently, it was suggested that nanodiamonds are a novel candidate for the development of a quartz crystal microbalance humidity sensor using them to produce sensing films.<sup>73</sup> Besides, electrical conductivity measurements are an indirect way of evaluating the presence of water in the nanodiamond assembly.

### **1.3 Justification of the thesis research**

A projection from the United Nations Environment Program indicates that severe water shortages will affect 4 billion people by 2050 increasing the need for water research. Fundamental research on water adsorption on carbons is vital because carbon has a vast family of different structures and properties that influence water affinity. It has been more than 50 years since the discovery of detonation nanodiamonds (the 1960s). Even though, their fundamental understanding requires improvement to exploit more applications. The pre-treatment of materials through an extensive adsorption study is necessary since the existing water in materials could cover their pores potentially used for adsorption of target substances.

The planet has been managing water for 3.8 billion years in natural ways, like those present in some plants and organisms that survive in dry areas. Nanodiamond aggregates have the potential for harvesting and retention of water. Therefore, useful nanodiamond-based devices to produce drinking water in dry areas or places with a low supply of potable water could be designed in the future. Moreover, a deeper understanding of the hygroscopic property of nanodiamonds could help to explain natural mechanisms of water capture by insects, plants and animals.

Furthermore, water contained in nanodiamonds must influence other properties such as electrical conductivity where they could be used in the area of sensors.

## **1.4 Hypothesis and research questions**

The hygroscopic nature of nanodiamonds is ascribed to the mesostructure of their aggregates and/or the special core-shell structure of each nanodiamond particle (hierarchical structure or their wrapping graphitic layer).

Does the hygroscopic ability of nanodiamonds depend on the hierarchical porosity?

This hypothesis will be addressed by an extensive porosity analysis based on adsorption isotherms of various adsorptives. Complementary analysis using X-ray diffraction (XRD), X-ray Photoelectron Spectroscopy (XPS), Electron Energy Loss Spectroscopy (EELS) and Fourier-transform infrared spectroscopy (FTIR) will elucidate the association among these characteristic structures with the hygroscopic property of nanodiamonds.

The pore structure of materials contributes to the potential to retain fluids such as water, and later water can influence other properties, as it was described before. Is it possible that contained or adsorbed water by nanodiamonds influence other properties such as electrical conductivity of nanodiamonds?

## **1.5 Purpose of the present study**

This research proposal aims to elucidate the origin of the hygroscopic nature of hydrophobic nanodiamonds and the effect of this property in the electrical conductivity of nanodiamonds.

In order to address the general objective, the next specific question must be answered.  
Why hydrophobic nanodiamonds exhibit pronounced hydrophilic nature?

## **1.6 General methodology**

First, deeply understanding the pore structure of nanodiamonds is necessary. Nanodiamond hard-hydrogel of average particle diameter of 4 nm, obtained from Nano-Carbon Research Institute, Ltd., Japan, will be used during the experiments. Therefore, a study on the porosity of nanodiamonds, by analyzing adsorption isotherms of distinct adsorptive gasses (nitrogen and argon) using a volumetric method will be performed. Such study will help to elucidate the role of intra and inter-particle voids in nanodiamonds particles in the adsorption of different molecules, and together with TEM observations will reveal the structure and dimensions of nanodiamond aggregates in the experimental sample. Likewise, the description of the structure of nanodiamond aggregates will be addressed theoretically, since it is decisive in their pore structure.

### **1.6.1 Study of hygroscopic nature of nanodiamonds**

Firstly, the hygroscopic nature of nanodiamonds must be examined by a careful water absorption experiment. Then, this property will be studied experimenting on nanodiamonds pellets of known density produced by stacking together finely grounded nanodiamonds powder by applying hydraulic pressure. Specifically, liquid water will be added as droplets on those structures. Then, changes in the dimensions of the droplet on the pellet through time from time zero to its disappearance, as well as the amount of liquid water absorbed by the pelletized materials will be examined. Dimensions of the droplets will be obtained by analysis of the water contact angle.

Secondly, a careful comparison of the hygroscopic nature of nanodiamonds and that of several representative well-known porous materials with different hydrophilicity

characteristics will be conducted. Graphite, silica gel, zeolites such as mordenite and ZSM-5, molecular sieve 5A, and the clay Montmorillonite, will be tested for this purpose. The comparison will be based on information about water contact angle, pore structure obtained by nitrogen adsorption at 77 K and argon at 87 K, and morphologic characterization of the materials by means of SEM microscopy.

### **1.6.2 Physicochemical characterization**

Thirdly, the hygroscopic nature of nanodiamonds may be ascribed to the mesostructure of their aggregates or the special core-shell structure of primary particles of nanodiamonds (or a secondary arrangement or their wrapping structure). Nitrogen and water adsorption, XRD, XPS and EELS by TEM studies on nanodiamonds will be mainly used to elucidate the possible association among these structural factors with the hygroscopic property. Besides, the study of water adsorption behavior on carbon nanohorns of different nanoporosities will contribute to the understanding of the water adsorption mechanism on nanodiamonds including the pore structure.

### **1.6.3 Relevance of water on the electrical conductivity of nanodiamonds**

Finally, the influence of water in nanodiamonds on other properties will be examined, as a means of indirect evaluation of water content in nanodiamonds. The changes in electrical conductivity will be evaluated with the variations of relative humidity generated by a sprinkler in a closed chamber.

## **1.7 Applicability of the present research**

This doctoral research studies the interfacial property of the hygroscopic ability of nanodiamonds considering the pore structure. The development of nanodiamonds with properties of absorption of water would allow their application on the retention of water like occurs in nature; some insects in nature, desert animals, and human nose function, etc. The hygroscopic property of nanodiamonds can be applied as an alternative for providing water to places of low accessibility of potable water. The mechanism of the hygroscopic nature of nanodiamonds can be exploited to design a new type of porous carbons exhibiting hydrophobic to hydrophilic property transformation.

## 1.8 References

- (1) Morelos-Gomez, A. **2010**, Controlling Chemical and Physical Properties of Ordered Carbon Nanosystems, IPICYT, San Luis Potosi, Mexico.
- (2) Yang, C.-M.; Kaneko, K. Adsorption Properties of Nitrogen-Alloyed Activated Carbon Fiber. *Carbon* **2001**, *39* (7), 1075–1082.
- (3) Joo, S. H.; Choi, S. J.; Oh, I.; Kwak, J.; Liu, Z.; Terasaki, O.; Ryoo, R. Ordered Nanoporous Arrays of Carbon Supporting High Dispersions of Platinum Nanoparticles. *Nature* **2001**, *412* (6843), 169–172.
- (4) Danilenko, V. V. On the History of the Discovery of Nanodiamond Synthesis. *Phys. Solid State* **2004**, *46* (4), 595–599.
- (5) Frenklach, M.; Howard, W.; Huang, D.; Yuan, J.; Spear, K. E.; Koba, R. Induced Nucleation of Diamond Powder. *Appl. Phys. Lett.* **1991**, *59* (5), 546–548.
- (6) Banhart, F.; Ajayan, P. M. Carbon Onions as Nanoscopic Pressure Cells for Diamond Formation. *Nature* **1996**, *382* (6590), 433–435.
- (7) Daulton, T. L.; Kirk, M. A.; Lewis, R. S.; Rehn, L. E. Production of Nanodiamonds by High-Energy Ion Irradiation of Graphite at Room Temperature. *Nucl. Instruments Methods Phys. Res. Sect. B Beam Interact. with Mater. Atoms* **2001**, *175*, 12–20.
- (8) Boudou, J.-P.; Curmi, P. A.; Jelezko, F.; Wrachtrup, J.; Aubert, P.; Sennour, M.; Balasubramanian, G.; Reuter, R.; Thorel, A.; Gaffet, E. High Yield Fabrication of Fluorescent Nanodiamonds. *Nanotechnology* **2009**, *20* (23), 235602.
- (9) Greiner, N. R.; Phillips, D. S.; Johnson, J. D.; Volk, F. Diamonds in Detonation Soot. *Nature* **1988**, *333* (6172), 440–442.
- (10) Mochalin, V. N.; Shenderova, O.; Ho, D.; Gogotsi, Y. The Properties and

- Applications of Nanodiamonds. *Nat. Nanotechnol.* **2012**, *7* (1), 11–23.
- (11) Krüger, A.; Kataoka, F.; Ozawa, M.; Fujino, T.; Suzuki, Y.; Aleksenskii, A. E.; Vul', A. Y.; Osawa, E. Unusually Tight Aggregation in Detonation Nanodiamond: Identification and Disintegration. *Carbon* **2005**, *43* (8), 1722–1730.
- (12) Ozawa, M.; Inaguma, M.; Takahashi, M.; Kataoka, F.; Krüger, A.; Ōsawa, E. Preparation and Behavior of Brownish, Clear Nanodiamond Colloids. *Adv. Mater.* **2007**, *19* (9), 1201–1206.
- (13) Korobov, M. V.; Batuk, M. M.; Avramenko, N. V.; Ivanova, N. I.; Rozhkova, N. N.; Osawa, E. Aggregate Structure of “Single-Nano Buckydiamond” in Gel and Dried Powder by Differential Scanning Calorimetry and Nitrogen Adsorption. *Diam. Relat. Mater.* **2010**, *19* (5), 665–671.
- (14) Kondo, T.; Kobayashi, M.; Saito, T.; Kadota, Y.; Kameshima, T.; Aikawa, T.; Kawai, T.; Yuasa, M. Micrometer-Sized Mesoporous Diamond Spherical Particles. *Diam. Relat. Mater.* **2014**, *43*, 72–79.
- (15) Raty, J.-Y.; Galli, G.; Bostedt, C.; Van Buuren, T. W.; Terminello, L. J. Quantum Confinement and Fullerenelike Surface Reconstructions in Nanodiamonds. *Phys. Rev. Lett.* **2003**, *90* (3), 037401.
- (16) Petit, T.; Arnault, J. C.; Girard, H. A.; Sennour, M.; Bergonzo, P. Early Stages of Surface Graphitization on Nanodiamond Probed by X-Ray Photoelectron Spectroscopy. *Phys. Rev. B - Condens. Matter Mater. Phys.* **2011**, *84* (23), 233407.
- (17) Hu, S.; Tian, F.; Bai, P.; Cao, S.; Sun, J.; Yang, J. Synthesis and Luminescence of Nanodiamonds from Carbon Black. *Mater. Sci. Eng. B Solid-State Mater. Adv. Technol.* **2009**, *157* (1–3), 11–14.
- (18) Post, G.; Dolmatov, V. Y.; Marchukov, V. A.; Sushchev, V. G.; Veretennikova, M.

- V.; Sal'ko, A. E. Industrial Synthesis of Ultradisperse Detonation Diamonds and Some Fields of Their Use. *Russ. J. Appl. Chem.* **2002**, *75* (5), 755–760.
- (19) Krueger, A. New Carbon Materials: Biological Applications of Functionalized Nanodiamond Materials. *Chem. - A Eur. J.* **2008**, *14* (5), 1382–1390.
- (20) Shenderova, O. A.; McGuire, G. E. Science and Engineering of Nanodiamond Particle Surfaces for Biological Applications (Review). *Biointerphases* **2015**, *10* (3), 030802.
- (21) Osawa, E.; Ho, D. Nanodiamond and Its Application to Drug Delivery. *J. Med. Allied Sci.* **2012**, *2* (2), 31–40.
- (22) Lee, D. K.; Kim, S. V.; Limansubroto, A. N.; Yen, A.; Soundia, A.; Wang, C. Y.; Shi, W.; Hong, C.; Tetradis, S.; Kim, Y.; Park, N. H.; Kang, M. K.; Ho, D. Nanodiamond-Gutta Percha Composite Biomaterials for Root Canal Therapy. *ACS Nano* **2015**, *9* (11), 11490–11501.
- (23) Mochalin, V. N.; Neitzel, I.; Etzold, B. J. M.; Peterson, A.; Palmese, G.; Gogotsi, Y. Covalent Incorporation of Aminated Nanodiamond into an Epoxy Polymer Network. *ACS Nano* **2011**, *5* (9), 7494–7502.
- (24) Wu, Y.; Jelezko, F.; Plenio, M. B.; Weil, T. Diamond Quantum Devices in Biology. *Angew. Chemie - Int. Ed.* **2016**, *55* (23), 6586–6598.
- (25) Shimkunas, R. A.; Robinson, E.; Lam, R.; Lu, S.; Xu, X.; Zhang, X. Q.; Huang, H.; Osawa, E.; Ho, D. Nanodiamond-Insulin Complexes as PH-Dependent Protein Delivery Vehicles. *Biomaterials* **2009**, *30* (29), 5720–5728.
- (26) Song, N.; Cui, S.; Hou, X.; Ding, P.; Shi, L. Significant Enhancement of Thermal Conductivity in Nanofibrillated Cellulose Films with Low Mass Fraction of Nanodiamond. *ACS Appl. Mater. Interfaces* **2017**, *9* (46), 40766–40773.

- (27) Subramanian, K.; Kang, W. P.; Davidson, J. L.; Howell, M. Nanodiamond Lateral Field Emitter Devices on Thick Insulator Substrates for Reliable High Power Applications. *Diam. Relat. Mater.* **2008**, *17* (4–5), 786–789.
- (28) Ng, E. P.; Mintova, S. Nanoporous Materials with Enhanced Hydrophilicity and High Water Sorption Capacity. *Microporous Mesoporous Mater.* **2008**, *114*, 1–26.
- (29) Krueger, A. Diamond Nanoparticles: Jewels for Chemistry and Physics. *Adv. Mater.* **2008**, *20* (12), 2445–2449.
- (30) Dolenko, T. A.; Burikov, S. A.; Rosenholm, J. M.; Shenderova, O. A.; Vlasov, I. I. Diamond-Water Coupling Effects in Raman and Photoluminescence Spectra of Nanodiamond Colloidal Suspensions. *J. Phys. Chem. C* **2012**, *116* (45), 24314–24319.
- (31) Petit, T.; Yuzawa, H.; Nagasaka, M.; Yamanoi, R.; Ōsawa, E.; Kosugi, N.; Aziz, E. F. Probing Interfacial Water on Nanodiamonds in Colloidal Dispersion. *J. Phys. Chem. Lett.* **2015**, *6* (15), 2909–2912.
- (32) Stehlik, S.; Glatzel, T.; Pichot, V.; Pawlak, R.; Meyer, E.; Spitzer, D.; Rezek, B. Water Interaction with Hydrogenated and Oxidized Detonation Nanodiamonds - Microscopic and Spectroscopic Analyses. *Diam. Relat. Mater.* **2016**, *63*, 97–102.
- (33) Pan, Z.; Pitt, W. G.; Zhang, Y.; Wu, N.; Tao, Y.; Truscott, T. T. The Upside-down Water Collection System of *Syntrichia Caninervis*. *Nat. Plants* **2016**, *76*, 1–5.
- (34) Parker, A. R.; Lawrence, C. R. Water Capture by a Desert Beetle. *Nature* **2001**, *414* (6859), 33–34.
- (35) Schmidt-Nielsen, K.; Schroter, R. C.; Shkolnik, A. Desaturation of Exhaled Air in Camels. *Proc. R. Soc. B Biol. Sci.* **1981**, *211* (1184), 305–319.
- (36) Ozden, S.; Ge, L.; Narayanan, T. N.; Hart, A. H. C.; Yang, H.; Sridhar, S.; Vajtai,

- R.; Ajayan, P. M. Anisotropically Functionalized Carbon Nanotube Array Based Hygroscopic Scaffolds. *ACS Appl. Mater. Interfaces* **2014**, *6* (13), 10608–10613.
- (37) Katsumi, K. Determination of Pore Size and Pore Size Distribution. 1. Adsorbents and Catalysts. *J. Memb. Sci.* **1994**, *96* (1–2), 59–89.
- (38) Zeiger, M.; Jäckel, N.; Aslan, M.; Weingarh, D.; Presser, V. Understanding Structure and Porosity of Nanodiamond-Derived Carbon Onions. *Carbon* **2015**, *84*, 584–598.
- (39) Pikunic, J.; Llewellyn, P.; Pellenq, R.; Gubbins, K. E. Argon and Nitrogen Adsorption in Disordered Nanoporous Carbons: Simulation and Experiment. *Langmuir* **2005**, *21* (10), 4431–4440.
- (40) Thommes, M.; Kaneko, K.; Neimark, A. V.; Olivier, J. P.; Rodriguez-Reinoso, F.; Rouquerol, J.; Sing, K. S. W. Physisorption of Gases, with Special Reference to the Evaluation of Surface Area and Pore Size Distribution (IUPAC Technical Report). *Pure Appl. Chem.* **2015**, *87* (9–10), 1051–1069.
- (41) Alghunaim, A.; Kirdponpattara, S.; Newby, B. M. Z. Techniques for Determining Contact Angle and Wettability of Powders. *Powder Technol.* **2016**, *287*, 201–215.
- (42) Lapina, V.; Akhremkova, G.; Gubarevich, T.; Schreiber, Y. Adsorption and Structural Characteristics of the Surface of Modified Nanodiamond Powders. *Russ. J. Phys. Chem. A, Focus Chem.* **2010**, *84* (2), 267–271.
- (43) Korobov, M. V.; Avramenko, N. V.; Bogachev, A. G.; Rozhkova, N. N.; Ōsawa, E. Nanophase of Water in Nano-Diamond Gel. *J. Phys. Chem. C* **2007**, *111* (20), 7330–7334.
- (44) Ji, S.; Jiang, T.; Xu, K.; Li, S. FTIR Study of the Adsorption of Water on Ultradispersed Diamond Powder Surface. *Appl. Surf. Sci.* **1998**, *133* (4), 231–238.

- (45) Hanzawa, Y.; Kaneko, K. Lack of a Predominant Adsorption of Water Vapor on Carbon Mesopores. *Langmuir* **1997**, *13* (22), 5802–5804.
- (46) Bekyarova, E.; Hanzawa, Y.; Kaneko, K.; Silvestre-Albero, J.; Sepulveda-Escribano, A.; Rodriguez-Reinoso, F.; Kasuya, D.; Yudasaka, M.; Iijima, S. Cluster-Mediated Filling of Water Vapor in Intratube and Interstitial Nanospaces of Single-Wall Carbon Nanohorns. *Chem. Phys. Lett.* **2002**, *366* (5), 463–468.
- (47) Pina-Salazar, E. Z.; Kaneko, K. Adsorption of Water Vapor on Mesoporosity-Controlled Single Wall Carbon Nanohorn. *Colloids Interface Sci. Commun.* **2015**, *5*, 8–11.
- (48) Hansen, J. O.; Copperthwaite, R. G.; Derry, T. E.; Pratt, J. M. A Tensiometric Study of Diamond (111) and (110) Faces. *J. Colloid Interface Sci.* **1989**, *130* (2), 347–358.
- (49) Ostrovskaya, L.; Perevertailo, V.; Ralchenko, V.; Saveliev, A.; Zhuravlev, V. Wettability of Nanocrystalline Diamond Films. *Diam. Relat. Mater.* **2007**, *16* (12), 2109–2113.
- (50) Ostrovskaya, L.; Perevertailo, V.; Ralchenko, V.; Dementjev, A.; Loginova, O. Wettability and Surface Energy of Oxidized and Hydrogen Plasma-Treated Diamond Films. *Diam. Relat. Mater.* **2002**, *11* (3), 845–850.
- (51) Miyawaki, J.; Kanda, T.; Kaneko, K. Hysteresis-Associated Pressure-Shift-Induced Water Adsorption in Carbon Micropores. *Langmuir* **2001**, *17* (3), 664–669.
- (52) Diallo, S. O. Pore-Size Dependence and Characteristics of Water Diffusion in Slitlike Micropores. *Phys. Rev. E - Stat. Nonlinear, Soft Matter Phys.* **2015**, *92* (1), 1–10.

- (53) Suzuki, M. Activated Carbon Fiber: Fundamentals and Applications. *Carbon* **1994**, 32 (4), 577–586.
- (54) Fu, M. H. Changes in the Properties of a Montmorillonite-Water System during the Adsorption and Desorption of Water: Hysteresis. *Clays Clay Miner.* **1990**, 38 (5), 485–492.
- (55) Uddin, F. Clays, Nanoclays, and Montmorillonite Minerals. *Metall. Mater. Trans. A Phys. Metall. Mater. Sci.* **2008**, 39 (12), 2804–2814.
- (56) Hatch, C. D.; Greenaway, A. L.; Christie, M. J.; Baltrusaitis, J. Water Adsorption Constrained Frenkel-Halsey-Hill Adsorption Activation Theory: Montmorillonite and Illite. *Atmos. Environ.* **2014**, 87, 26–33.
- (57) Moreno-Castilla, C.; Ferro-Garcia, M. A.; Joly, J. P.; Bautista-Toledo, I.; Carrasco-Marín, F.; Rivera-Utrilla, J. Activated Carbon Surface Modifications by Nitric Acid, Hydrogen Peroxide, and Ammonium Peroxydisulfate Treatments. *Langmuir* **1995**, 11 (11), 4386–4392.
- (58) Kraft, A.; Stadelmann, M.; Blaschke, M. Anodic Oxidation with Doped Diamond Electrodes: A New Advanced Oxidation Process. *J. Hazard. Mater.* **2003**, 103 (3), 247–261.
- (59) Morelos-Gómez, A.; Fujishige, M.; Magdalena Vega-Díaz, S.; Ito, I.; Fukuyo, T.; Cruz-Silva, R.; Tristán-López, F.; Fujisawa, K.; Fujimori, T.; Futamura, R.; Kaneko, K.; Takeuchi, K.; Hayashi, T.; Kim, Y. A.; Terrones, M.; Endo, M.; Dresselhaus, M. S. High Electrical Conductivity of Double-Walled Carbon Nanotube Fibers by Hydrogen Peroxide Treatments. *J. Mater. Chem. A* **2016**, 4 (1), 74–82.
- (60) Kuznetsova, A.; Popova, I.; Yates, J. T.; Bronikowski, M. J.; Huffman, C. B.; Liu,

- J.; Smalley, R. E.; Hwu, H. H. Oxygen-Containing Functional Groups on Single-Wall Carbon Nanotubes: NEXAFS and Vibrational Spectroscopic Studies. *J. Am. Chem. Soc.* **2001**, *123*, 10699–10704.
- (61) Osswald, S.; Yushin, G.; Mochalin, V.; Kucheyev, S. O.; Gogotsi, Y. Control of Sp<sup>2</sup>/Sp<sup>3</sup> Carbon Ratio and Surface Chemistry of Nanodiamond Powders by Selective Oxidation in Air. *J. Am. Chem. Soc.* **2006**, *128* (35), 11635–11642.
- (62) Shenderova, O.; Petrov, I.; Walsh, J.; Grichko, V.; Grishko, V.; Tyler, T.; Cunningham, G. Modification of Detonation Nanodiamonds by Heat Treatment in Air. *Diam. Relat. Mater.* **2006**, *15*, 1799–1803.
- (63) Salame, I. I.; Bandosz, T. J. Surface Chemistry of Activated Carbons: Combining the Results of Temperature-Programmed Desorption, Boehm, and Potentiometric Titrations. *J. Colloid Interface Sci.* **2001**, *240* (1), 252–258.
- (64) Batsanov, S. S.; Gavrilkin, S. M.; Batsanov, A. S.; Poyarkov, K. B.; Kulakova, I. I.; Johnson, D. W.; Mendis, B. G. Giant Dielectric Permittivity of Detonation-Produced Nanodiamond Is Caused by Water. *J. Mater. Chem.* **2012**, *22* (22), 11166–11172.
- (65) Denisov, S. A.; Sokolina, G. A.; Bogatyreva, G. P.; Grankina, T. Y.; Krasil'nikova, O. K.; Plotnikova, E. V.; Spitsyn, B. V. Adsorption and Electrical Properties of Nanodiamond Powders in the Presence of Water Vapor. *Prot. Met. Phys. Chem. Surfaces* **2013**, *49* (3), 286–291.
- (66) Petit, T.; Puskar, L.; Dolenko, T.; Choudhury, S.; Ritter, E.; Burikov, S.; Laptinskiy, K.; Brzustowski, Q.; Schade, U.; Yuzawa, H.; Nagasaka, M.; Kosugi, N.; Kurzyp, M.; Venerosy, A.; Girard, H.; Arnault, J. C.; Osawa, E.; Nunn, N.; Shenderova, O.; Aziz, E. F. Unusual Water Hydrogen Bond Network around Hydrogenated

- Nanodiamonds. *J. Phys. Chem. C* **2017**, *121* (9), 5185–5194.
- (67) Petit, T. Interactions with Solvent. In *Nanodiamonds*; Arnault, J.-C., Ed.; Elsevier: Amsterdam, 2017; pp 301–321.
- (68) Wort, C. J. H.; Balmer, R. S. Diamond as an Electronic Material. *Mater. Today* **2008**, *11* (1–2), 22–28.
- (69) Shenderova, O.; McGuire, G. Nanocrystalline Diamond. In *Nanomaterials Handbook*; Gogotsi, Y., Ed.; Taylor & Francis Group, 2007.
- (70) Collins, P. G.; Bradley, K.; Ishigami, M.; Zettl, A. Extreme Oxygen Sensitivity of Electronic Properties Extreme Oxygen Sensitivity of Electronic Properties of Carbon Nanotubes. *Science* (80-. ). **2000**, *287* (2000), 1801–1805.
- (71) Chakrapani, V.; Angus, J. C.; Anderson, A. B.; Wolter, S. D.; Stoner, B. R.; Sumanasekera, G. U. Charge Transfer Equilibria Between Diamond and an Aqueous Oxygen Electrochemical Redox Couple. *Science* (80-. ). **2007**, *318* (5855), 1424–1430.
- (72) Bradley, K.; Jhi, S. H.; Collins, P. G.; Hone, J.; Cohen, M. L.; Louie, S. G.; Zettl, A. Is the Intrinsic Thermoelectric Power of Carbon Nanotubes Positive. *Phys. Rev. Lett.* **2000**, *85* (20), 4361–4364.
- (73) Yao, Y.; Chen, X.; Ma, W.; Ling, W. Quartz Crystal Microbalance Humidity Sensors Based on Nanodiamond Sensing Films. *IEEE Trans. Nanotechnol.* **2014**, *13* (2), 386–393.



## Chapter 2

### 2. Fundamentals of adsorption

The sorption capacity of a material depends on several factors; total volume, internal surface area, pressure and temperature. The existence and development of nanoporous materials of uniform pore structures have requested high-resolution experimental protocols for the adsorption of various subcritical fluids (nitrogen at  $T = 77$  K, argon at  $T = 87$  K, carbon dioxide at  $T = 273$  K) and novel procedures for more accurate data analysis of porosity. Following accurately the gas physisorption methodology and understanding the advantages and limitations of using physisorption techniques for the study of pore structures and surface areas become essential. Hence, this section includes a brief summary of the fundamentals of adsorption.

#### 2.1 General definitions and terminology

*Adsorption.* Enrichment of molecules, atoms or ions near an interface. Adsorption takes place in the vicinity of the solid surface and outside of the solid structure in gas/solid systems. The material in the adsorbed state is known as the adsorbate, while the adsorptive is the same component in the fluid phase.

Types of adsorption

- Physisorption: Physical adsorption. Occurs whenever an adsorbable gas (the adsorptive) is in contact with the surface of a solid (the adsorbent) due to particular geometric and electronic properties of the adsorbent and adsorptive. The

intermolecular forces involved are attractive dispersion forces, short-range repulsive forces, specific molecular interactions (e.g., polarisation, field-dipole, field gradient- quadrupole).

- Chemisorption: Chemical adsorption. Occurs due to intermolecular forces that lead to the formation of chemical bonds.

*Adsorption space.* Space occupied by the adsorbate.

*Absorption.* Occurs when the molecules of the adsorptive penetrate the surface layer and enter the structure of the bulk solid. The terms sorption, sorbent, sorbate and sorptive must be used when it is impossible to distinguish between adsorption and absorption.

*Desorption.* The converse process of adsorption, in which the amount adsorbed progressively decreases as the relative pressure  $P/P_0$  decreases.

*Adsorption hysteresis.* Adsorption and desorption curves do not coincide.

*Adsorption isotherm.* Relation, at a constant temperature, between the amount adsorbed,  $n_a$  and the equilibrium pressure of the gas. At an adsorption temperature below the critical point, one usually adopts the relative pressure  $P/P_0$ , where  $P$  is the equilibrium pressure and  $P_0$  the saturation vapor pressure at the adsorption temperature. At an adsorption temperature above the critical one, where there is no condensation and no  $P_0$  exists, one must necessarily use the equilibrium pressure  $P$ .

### *Subdivision of the surface of porous materials*

#### *External surface.*

- In the general case, it refers to the surface of the bulk sample outside the pores.
- In the presence of microporosity, it refers to the non-microporous surface.

#### *Internal surface.*

- In the general case, it is the surface of all pore walls.
- In the presence of microporosity, it refers to the microporous surface.

Accessibility of pores depends on the size and shape of the probe molecules. Therefore, the calculated internal area and pore volume may depend on the dimensions of the adsorptive molecules (packing and molecular sieve effects).

### *Classification of pores according to the IUPAC recommendation, 1985*

- Macropores: pores with widths exceeding about 50 nm.
- Mesopores: pores of widths between 2 nm and 50 nm.
- Micropores: pores with widths not exceeding about 2 nm.

*Nanopores.* Micropores, mesopores and macropores with an upper limit  $\leq 100$  nm.

#### **2.1.1 Physisorption process in micropores and mesopores**

*Micropore filling.* Primary physisorption process of the occupation of the accessible volume (adsorption space) present in micropores by the adsorbate. Micropore filling includes narrow micropores (also called ultramicropores) of approximate width  $< 0.7$  nm

and wide micropores (also called supermicropores) of width  $> 0.7$  nm but  $< 2$  nm.

*Physisorption in mesopores.* First, monolayer adsorption takes place when all the adsorbed molecules are in contact with the surface layer of the adsorbent. Then, multilayer adsorption occurs by the arrangement of more than one layer of molecules in the adsorption space. In mesopores, multilayer adsorption is followed by pore condensation.

*Capillary (or pore) condensation.* The phenomenon whereby a gas condenses to a liquid-like phase in a pore at a pressure  $P$  less than the saturation pressure  $P_0$  of the bulk liquid. It reflects a vapor-liquid phase transition in a finite-volume system.

*Monolayer capacity ( $n_m^a$ ).* Amount of adsorbate sufficient to cover the surface with a complete monolayer of molecules. In some cases, this may be a close-packed array but in others, the adsorbate may adopt a different structure.

*Surface coverage ( $\theta$ ).* For both monolayer and multilayer adsorption is defined as the ratio of the amount of adsorbed substance to the monolayer capacity. The surface area ( $A_s$ ) of the adsorbent is calculated from the monolayer capacity, provided that the area ( $\sigma_m$ ) effectively occupied by an adsorbed molecule in the complete monolayer is known.

$$A_s = n_m^a L \sigma_m$$

where

L: Avogadro constant

The specific surface area ( $a_s$ ) refers to the unit mass of adsorbent (m).

$$a_s = \frac{A_s}{m}$$

## 2.2 Methodology for physisorption measurements

Types of apparatus used for the determination of physisorption isotherms

- Manometric methods: measurement of the amount of gas removed from the gas phase.
- Gravimetric methods: direct measurement of the uptake of gas of the change in mass of the adsorbent.

In practice, static or dynamic techniques may be used in either case.

Adsorption of gases such as nitrogen and argon (at their boiling temperatures) within the relative pressure range  $10^{-7} \leq P/P_0 \leq 1$  with sufficiently high accuracy requires special equipment such as a highly efficient turbomolecular *vacuum* pumping system for the complete evacuation of the sample cell and the manifold (at very low pressures).

### 2.2.1 Sample preparation

Outgassing; exposure of the surface to a high *vacuo* (for microporous materials, pressures  $< 1$  Pa are desirable) usually at an elevated temperature; must be carried out prior to the determination of an adsorption isotherm for the removal of all the physisorbed

species from the surface of the adsorbent while avoiding irreversible changes of the surface or the solid structure.

Control the outgassing conditions (heating program, change in pressure over the adsorbent and residual pressure) within the limits; which depends on the nature of the adsorbent, is important for reproducible results.

Further application of temperature-programmed desorption in association with evolved gas analysis (by using mass spectrometry) gives additional information on the effect of outgassing in the sample.

### **2.2.2 Choosing an adsorptive for the adsorption isotherm measurement**

Nitrogen: at 77 K (boiling temperature) this adsorptive has a  $\sigma_m = 0.162 \text{ nm}^2$  (assuming a closed packed monolayer).

Advantage: liquid nitrogen is easily available. Many adsorbents exhibit a well-defined point B in the adsorption isotherm.

Disadvantage: nitrogen has a quadrupole moment; therefore, its orientation on the adsorbent depends on the surface chemistry of the adsorbent. Then  $\sigma_m$  varies about 20%.

Argon: at 87 K or at 77 K.

Advantage: it does not have a quadrupole moment and it is less reactive than the

nitrogen molecule when used at 87 K (using liquid argon or a cryocooler as temperature controller).

Disadvantage: The structure of the argon monolayer highly depends on the surface chemistry of the adsorbent at 77 K. In this sense, argon at 87 K (liquid argon temperature) must be chosen, assuming a  $\sigma_m = 0.142 \text{ nm}^2$ .

Surface areas as low as  $0.5 - 1.0 \text{ m}^2$  can be determined using nitrogen or argon.

### **2.2.3 Measurement of the adsorption isotherm**

After choosing the adsorbent, run the adsorption isotherm.

### **2.2.4 Evaluation of the adsorption data**

Checking on the isotherm quality. In general, in adsorption analysis of  $\text{N}_2$  (77 K) and Ar (87 K), it is important to verify the non-existence of instrumentation issues, incorrect analysis parameters or an inadequate amount of sample through the next suspicious scenarios:

- Desorption branch crossing the adsorption branch.
- Non-monotonic behavior (adsorbed amount does not increase when increasing the relative pressure or vice versa).
- Extended adsorption hysteresis below  $P/P_0 = 0.38$  as an indication of insufficient equilibration parameters, or never closed hysteresis as indicative of leaks or experimental artifacts.

*Exceptions:* materials of flexible structure can present low-pressure adsorption hysteresis. Therefore, do not follow the typical IUPAC classification.

- Swelling charcoals present prolonged low-pressure hysteresis.
- Flexible MOFs present low-pressure hysteresis loops associated with gate opening or breathing transitions.
- Low-pressure analysis especially for microporous materials. The isotherms of such materials should be plotted on a logarithmic scale where the micropore filling occurs.

*Note: It is recommended to run a reference material (BAM, NIST) when occurs an issue that compromises the isotherm data.*

#### **2.2.4.1 Classification of physisorption isotherms**

Once obtained adsorption isotherm quality data, it is recommended to classify the isotherm and hysteresis (if present) following the IUPAC recommendation. **Figure 2-1** presents representative plots of the types of physisorption isotherms.

- ✓ Type I isotherms. Reversible isotherm characteristic of microporous solids having relatively small external surfaces (e.g., some activated carbons, molecular sieve zeolites and certain porous oxides). This isotherm is concave to the  $P/P_0$  axis and the amount adsorbed approaches a limiting value, depending on the accessible micropore volume. The steep uptake at very low  $P/P_0$  is due to enhanced adsorbent-adsorptive interactions in narrow micropores (of molecular dimensions). There exist two kinds of Type I isotherms (when measuring nitrogen at 77 K or argon at 87 K).

- Type I(a) isotherms. Isotherm of microporous materials of mainly narrow micropores of a width  $< \sim 1$  nm.
- Type I(b) isotherms. Isotherm of wider micropores and possibly narrow mesopores of a width  $< \sim 2.5$  nm.

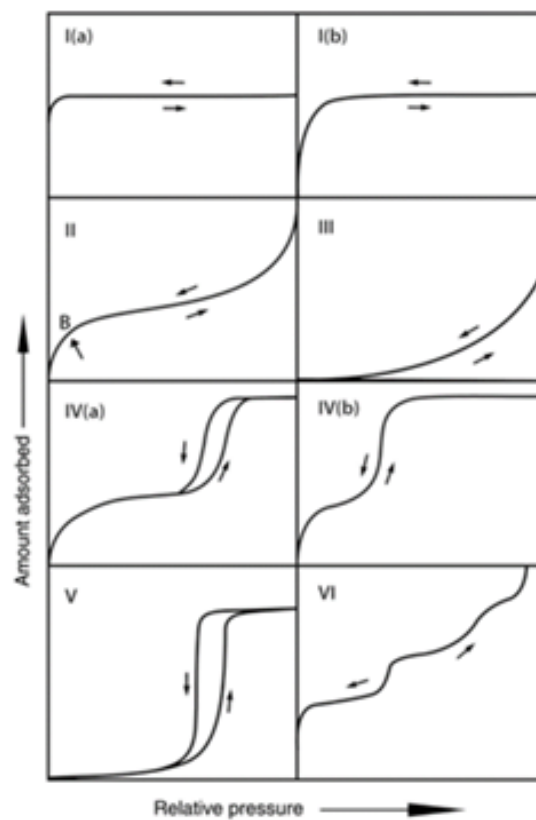


**Figure 2-1.** Classification of physisorption isotherms.

- ✓ Type II isotherms. Reversible isotherm characteristic of physisorption of most gases on nonporous or macroporous adsorbents, by unrestricted monolayer-multilayer adsorption up to high  $P/P_0$ . There are two cases:

- If the knee is sharp, the beginning of the middle almost linear section (B) usually corresponds to the completion of monolayer coverage.
  - A more gradual curvature (less distinctive point B) indicates overlapping of monolayer coverage and the onset of multilayer adsorption.
- ✓ Type III isotherms. There is no identifiable monolayer formation by the absence of point B, as a result of adsorbent-adsorbate relatively weak interactions that produce clusters of adsorbed molecules around the most favorable sites on the surface of a nonporous or macroporous solid. In contrast to a Type II isotherm, the amount adsorbed remains finite at the saturation pressure ( $P/P_0 = 1$ ).
- ✓ Type IV isotherms. Characteristic of mesoporous adsorbents (many oxide gels, industrial adsorbents and mesoporous molecular sieves), due to adsorbent-adsorptive interactions and interactions between the molecules in the condensed state. The initial monolayer-multilayer adsorption on the mesopore walls, which takes the same path as the corresponding part of a Type II isotherm, is followed by pore condensation. A typical feature of Type IV isotherms is a final saturation plateau, of variable length (sometimes reduced to a mere inflection point).
- Type IVa isotherm. Isotherm with hysteresis by capillary condensation because the pore width exceeds a certain critical width, which is dependent on the adsorption system and temperature. For example, hysteresis occurs for pores  $> \sim 4$  nm for nitrogen and argon adsorption in cylindrical pores at 77 K and 87 K, respectively.

- Type IVb isotherms. Completely reversible isotherms of adsorbents with mesopores of small width than those in Type IVa. Also given by conical and cylindrical mesopores that are closed at the tapered end.
  
- ✓ Type V isotherm. Similar to that of Type III. Relatively weak adsorbent–adsorbate interactions. At higher  $P/P_0$ , molecular clustering is followed by pore filling. For instance, Type V isotherms are observed for water adsorption on hydrophobic microporous and mesoporous adsorbents.
  
- ✓ Type VI isotherm. Reversible stepwise isotherm representative of layer-by-layer adsorption on a uniform nonporous surface. The step-height represents the capacity for each adsorbed layer, while the sharpness of the step depends on the system and the temperature. For example, isotherms of argon or krypton at low temperature on graphitized carbon blacks.

#### **2.2.4.2 Classification of hysteresis loops**

Reproducible and permanent hysteresis loops in the multilayer range of physisorption isotherms are generally associated with capillary condensation due to adsorption metastability and/or network effects. For example, in an open-ended pore, like cylindrical pore geometry, delayed condensation results of metastability of the adsorbed multilayer. Adsorption branch of the hysteresis loop is not in thermodynamic equilibrium, but desorption branch is.

In more complex pore structures, the desorption path is often dependent on network effects and various forms of pore-blocking because wide pores have access to the external surface only through narrow necks (ink-bottle pore shape). The wide pores are filled and remain filled during desorption until the narrow necks empty at lower vapor pressures.

In a pore network, the desorption vapor pressures are dependent on the size and spatial distribution of the necks. The network may empty at a relative pressure corresponding to a characteristic percolation threshold, in the presence of very small neck diameters. Then, useful information concerning the neck size can be obtained from the desorption branch of the isotherm. The mechanism of desorption from the larger pores involves cavitation (spontaneous nucleation and growth of gas bubbles in the metastable condensed fluid) when the neck diameter is lower than the critical size (5–6 nm for nitrogen at 77 K). Therefore, no quantitative information on neck size can be obtained. For example, some micro-mesoporous silicas, mesoporous zeolites, clays, and also some activated carbons.

**Figure 2-2** shows the representative hysteresis loops in physisorption isotherms.

- ✓ Type H1 hysteresis loop. It exists in materials with a narrow range of uniform mesopores. For example, templated silicas (e.g., MCM-41, MCM-48, SBA-15), some controlled pore glasses and ordered, mesoporous carbons, where the network effects are minimal and the steep, narrow loop is a clear sign of delayed condensation on the adsorption branch. However, Type H1 hysteresis has also been found in networks of ink-bottle pores where the width of the neck size distribution is similar to the width of the pore/cavity size distribution. For example, in 3DOm carbons.

- ✓ Type H2 hysteresis loop. It exists in materials with more complex pore structures in which network effects are important. There are two kinds of Type H2.

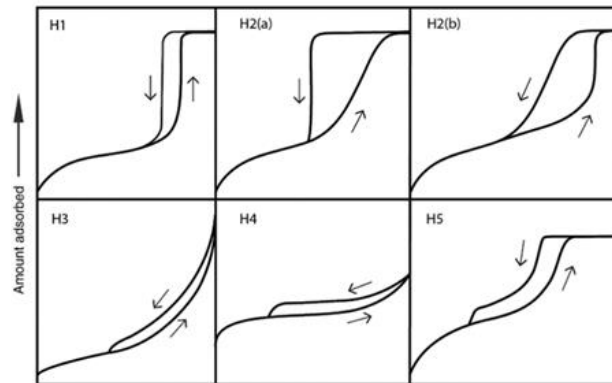


**Figure 2-2.** Classification of hysteresis loops.

- Type H2(a) hysteresis loop. Very steep desorption branch due to pore-blocking/percolation in a narrow range of pore necks or to cavitation-induced evaporation. For example, in silica gels, some porous glasses (like vycor) and some ordered mesoporous materials (like SBA-16 and KIT-5 silicas).
- Type H2(b) hysteresis loop. Associated with pore blocking, but the size distribution of neck widths is much larger. For example, in mesocellular silica foams and some mesoporous ordered silicas after hydrothermal treatment.
- ✓ Type H3 hysteresis loop. Adsorption branch resembles a Type II isotherm, and the lower limit of the desorption branch is normally located at the cavitation-induced  $P/P_0$ . For example, in non-rigid aggregates of plate-like particles (certain clays) but

also if the pore network consists of macropores, which are not completely filled with pore condensate.

- ✓ Type H4 hysteresis. Unusual loop of a high-pronounced uptake at  $P/P_0$  associated with the filling of micropores. For example, aggregated crystals of zeolites, some mesoporous zeolites, and micro-mesoporous carbons.
  
- ✓ Type H5 hysteresis loop. Associated with certain pore structures containing both open and partially blocked mesopores. For example, in plugged hexagonal templated silica.

A common feature of H3, H4 and H5 loops is the sharp step-down of the desorption branch, generally located in a narrow range of  $P/P_0$  for the particular adsorptive and temperature. For example, at  $P/P_0 \sim 0.4 - 0.5$  for nitrogen at 77 K.

### **2.2.5 Surface area evaluation**

Reported values of the surface area should include the next:

- Range of application of BET equation.
- Adsorptive used and the operating temperature.
- Assumed cross-sectional area.

#### **2.2.5.1 Brunauer-Emmet-Teller (BET) method**

The Brunauer-Emmet-Teller (BET) method is the most widely used method for the determination of the surface area of porous materials, despite its theoretical limitations.

### **2.2.5.1.1 Applicability of BET surface area method**

Type I isotherms. BET surface area is only an apparent surface area when applying an appropriating linear range using the Rouquerol method.

Type II isotherms. True probe accessible surface area (the effective area available for the adsorption of specific adsorptive). The classical  $P/P_0$  range of the application of this method is 0.05 – 0.3.

Type III isotherms. Not applicable.

Type IV(a) isotherms. True probe accessible surface area (the effective area available for the adsorption of specific adsorptive). The classical  $P/P_0$  range of the application of this method is 0.05 – 0.3.

Type IV(b) isotherms. Not straightforward application of the method. An applicable range should be found considering that the pore condensation may begin in the classical range of application of the BET equation. The linear BET range is shifted to lower  $P/P_0$ .

Type V isotherms. Not applicable.

### **2.2.5.1.2 Application of BET to microporous materials**

BET can be applicable to Type II and Type IV isotherms, as mentioned before. However, for microporous materials (Type I, and combinations with Type II and Type IV)

the separation of mono-multilayer adsorption and micropore filling should be done carefully following the next criteria to avoid subjectivity in the calculation of BET monolayer capacity.

- a. C value should be positive (a negative value of C indicates that one is outside the appropriate BET range).
- b. BET equation should be restricted to a range where  $n(1-P/P_0)$  continuously increases with  $P/P_0$ .
- c. The  $P/P_0$  value corresponding to the monolayer capacity  $n_m$  should be within the selected BET range.

#### **2.2.5.1.3 Methodology for application of BET method**

1. Transform the physisorption isotherm ( $P/P_0$  vs adsorbed amount) into the BET plot.
2. Derive the BET monolayer capacity  $n_m$  from the BET plot, and use it to calculate the BET specific surface area  $a_{s(\text{BET})}$  by using an appropriate value of the molecular cross-sectional area  $\sigma_m$  occupied by the adsorbate molecule in the complete monolayer and using the adsorbent mass  $m$ .

$$a_{s(\text{BET})} = n_m L \sigma_m / m$$

#### **2.2.5.1.4 BET equation and theory**

The linear form of the BET equation is shown next:

$$\frac{\frac{P}{P_0}}{n(1 - \frac{P}{P_0})} = \frac{1}{n_m C} + \frac{C - 1}{n_m C} \left(\frac{P}{P_0}\right)$$

where

$n$ : specific amount adsorbed at the relative pressure  $P/P_0$

$n_m$ : monolayer capacity

$C$ : value exponentially related to the energy of monolayer adsorption. It gives an indication of the shape of the isotherm in the BET range

$\frac{P}{P_0}$ : relative pressure

For example,

When  $C > 150$ , filling of narrow micropores or high-energy surface sites exist.

When  $C = 80$ , the knee of the isotherm is sharp and the point B is well defined. B indicates the monolayer completion and the beginning of multilayer adsorption.

When  $C < 50$ , point B is not well defined as a single one due to the overlapping of the monolayer and multilayer adsorption. Therefore,  $n_m$  is questionable.

When  $C < 2$ , the isotherm corresponds to Type III or Type V and the BET method is not applicable.

### 2.2.5.2 Comparison to standard isotherms

Comparison to standard isotherms refers to the comparison of the experimentally measured isotherm to a reference isotherm with the aim of evaluating the micropore volume and the “external” surface area (surface area of pores  $> 2$  nm). The  $t$ -plot and  $\alpha_s$ -plot (micro- and mesoporosity) methods are comparison methods, being the last one the

most adaptable due to its applicability even when the BET method is not applicable. Here, the measured adsorbed amount of the experimental isotherm is plotted as a function of the expected adsorbed amount from a reference or standard isotherm. The reference isotherm is that of the adsorption on a non-porous material of similar chemical composition than the experimental material.

#### **2.2.5.2.1 Subtracting pore effect (SPE) method of the $\alpha_s$ -plots**

Nitrogen molecules are adsorbed on micropores by micropore filling. Physical adsorption is enhanced by overlapped surface fields in pore whose width is  $< 2$  nm. The overlapping of pore wall potentials results in stronger binding of the adsorbate, or enhanced adsorption. The routine application of the BET analysis overestimates the surface area because of the enhanced adsorption.

The  $\alpha_s$ -plots derives from the comparison of the experimental isotherm to a standard (reference) isotherm. It has the great advantage of not involving the surface area evaluated by the Brunauer-Emmet-Teller method ( $S_{\text{BET}}$ ) from the reference. However, it depends on the selection of an adequate material as reference. A standard isotherm describes the adsorption on a non-porous material of similar chemical composition to the compared material; for example, the type II isotherm with an evident B-point of nitrogen adsorbed on non-porous carbon black indicating that  $\text{N}_2$  molecules are adsorbed on the carbon surface by the multilayer adsorption mechanism. The enhancement of adsorption by the micropore field is observed below  $\alpha_s$  values of 0.5. The idea of the SPE method is to subtract the enhancement of adsorption in micropores, and any diffusion problem at the narrow entrance of micropores to determine the monolayer capacity of the micropores.

Its name derives from the subtraction of the enhancements from both micropore filling and capillary condensation.

The  $\alpha_s$ -plots for porous carbons are shown in **Figure 2-3**. The  $\alpha_s$ -plot for microporous carbon of high BET surface area has two upward swings from linearity below the downward bend, named filling and condensation swings (**Figure 2-3a**). The linearity ensures adsorption without the enhancement by the micropore field if the line between the two swings passes through the origin. Therefore, the dotted line that follows the linearity represents the multilayer adsorption without enhancement in those regions. The slope of the linear plot in the  $\alpha_s$  region 0.3 – 0.7 gives the  $\alpha_s$  surface area.

Filling swing (f-swing): Located in the lower  $\alpha_s$  region ( $\alpha_s < 0.3$ ; corresponding to a  $P/P_0$  of 0.001). It originates from the enhanced adsorption by the micropore field. This upward swing is more marked if the pore is smaller.

Condensation or cooperative swing (c-swing): Located in a higher  $\alpha_s$  region ( $\alpha_s \approx 0.7$ ; corresponding to a  $P/P_0$  of 0.13) before the saturated filling. It originates by a quasi-capillary condensation in pores whose width is  $< 2$  nm (or 0.17 nm in the case of the  $N_2$ -carbon system).

Capillary condensation swing (ccs-swing): Located in a higher  $\alpha_s$  region in mesoporous carbons ( $\alpha_s > 1.3 - 1.5$ ; corresponding to a starting  $P/P_0 \geq 0.4$ ; depending on the adsorbate-adsorbent pair). It originates by capillary condensation in pores whose width is  $> 4$  nm in the case of nitrogen or argon adsorption at 77 and 87 K, respectively.

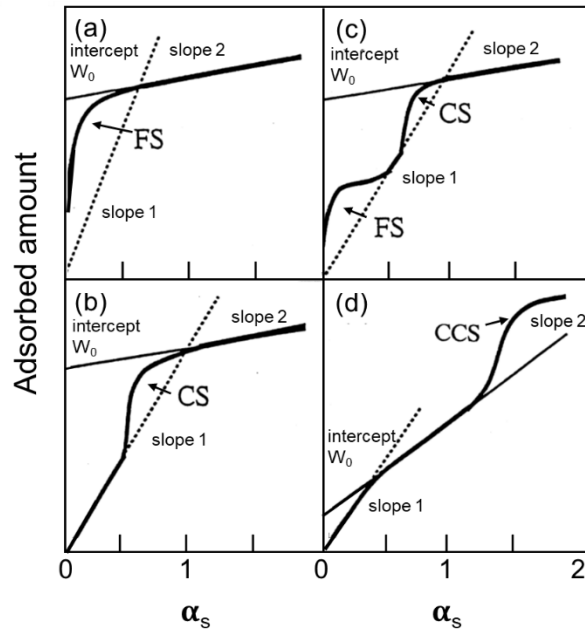


**Figure 2-3.** Representative types of  $\alpha_s$ -plots for porous carbons. (a) FS (f-swing) type: typical of low-burn off carbon, (b) CS (c-swing) type: typical of super-high surface area carbon, (c) FS/CS (f/c-swing) type: typical of ordinary microporous carbon, and (d) CCS (cc-swing) type: typical of mesoporous carbon. For the construction of the  $\alpha_s$ -plot of samples, it is necessary a reference isotherm data and its  $\alpha_s$ -plot. First, draw the plot of adsorbed amount ( $w$ ) vs  $\alpha_s$  of the reference material, and find the best fitting curve. Second, obtain  $\alpha_s$  of the sample isotherm related to each  $P/P_0$  by searching  $P/P_0$  of the sample in the reference fitting curve equation. Third, draw a new plot of sample adsorbed amount ( $w$ ) vs  $\alpha_s$ . (Adapted from references 5 and 6).

In a comparison  $\alpha_s$ -plot (**Figure 2-3**), the slopes give the total surface area and external surface area, while the extrapolated y-intercept is associated to the micropore volume, for adsorbed amount of nitrogen expressed in  $\text{mg g}^{-1}$ :

$$SA_{\text{tot}} = (\text{slope of reference material})(\text{slope 1}) = \frac{\text{m}^2}{\text{g}}$$

$$SA_{\text{ext}} = (\text{slope of reference material})(\text{slope 2}) = \frac{\text{m}^2}{\text{g}}$$

$$SA_{\text{micro}} = SA_{\text{tot}} - SA_{\text{ext}} = \frac{\text{m}^2}{\text{g}}$$

$$V_{\text{micro}} = \frac{(0.808)(W_0)}{1000} = \frac{\text{mL}}{\text{g}}$$

where

$V_{\text{micro}}$ : micropore volume. (Here, 0.808 is the nitrogen liquid density in  $\text{g mL}^{-1}$  at 77 K)

$SA_{\text{ext}}$ : external surface area

$SA_{\text{tot}}$ : total surface area

$SA_{\text{micro}}$ : micropore (or internal) surface area

$W_0$ : intercept of slope 2 to the "y" axis

It is important to note that this method is applicable to any system where the  $\alpha_s$  plot includes separable swings. However, it must not be applicable straightforward to materials with narrow mesopores; classified according to the IUPAC as Type IV(b) and Type IV(a) isotherms with hysteresis  $P/P_0 \leq 0.5$ ; pore width  $< 0.7$  nm (bilayer thickness of  $\text{N}_2$ ), as  $\text{N}_2$  cannot cover each wall as monolayer.

### 2.2.6 Total pore volume evaluation

The measurement of the total pore volume indicates the next:

- ✓ Complete filling of the accessible pore volume with an adsorbate.
- ✓ No significant further adsorption can occur prior to bulk condensation.

Case 1: A nearly horizontal isotherm over the upper range of  $P/P_0$  indicates that there is no significant macroporosity in the sample structure. The total pore volume is given by a point on the plateau near  $P/P_0 = 1.0$  ( $P/P_0 = 0.95$  or  $0.99$ ), assuming the fluid in the pores is at bulk liquid density (Gurvich rule)<sup>1</sup>.

For example, when using  $N_2$  as adsorbate, convert micropore volume in mL (STP)  $g^{-1}$  to  $cm^3 g^{-1}$

$$((N_2 \text{ molecular weight}) / (\text{molar volume} \times N_2 \text{ liquid density at 77 K}))$$

$$((28.0134 \text{ g mol}^{-1} / (22400 \text{ mL mol}^{-1} \times 0.808 \text{ g cm}^{-3})) = 0.00155$$

Case 2: A not nearly horizontal isotherm near  $P/P_0 = 1$ , but rather continuously increasing on the adsorbed amount may indicate the presence of macroporosity. The total pore volume is not calculable but could be estimated by extrapolating the nearly horizontal part of the isotherm close to  $P/P_0 = 1$ .

### 2.2.6.1 Micropore volume

The limiting uptake in Type I isotherms (since they have a horizontal plateau) indicates the micropore capacity  $n_p$  (of specific gas at a specific temperature), which can be converted into liquid micropore volume applying the Gurvich rule.

### 2.2.7 Pore size distribution

The classical methods for pore size analysis; Barrett, Joyner, and Halenda (BJH), Horvath and Kawazoe (HK), Saito and Foley (SF); are not applicable under all nanopore sizes (underestimate significantly porosity  $< 10$  nm by 20–30%).

The micropore analysis can be done by applying various semi-empirical methods such as HK method for slit pores, SF method for cylindrical pores and Cheng and Yang method for spherical pores. However, these methods tend to underestimate the pore size.

The mesopore analysis was based for many years in the application of the Kelvin equation. For cylindrical pores, the modified Kelvin equation is:

$$\ln \frac{P}{P_0} = \frac{2\gamma V_m}{RT(r_p - t_c)}$$

where

$\gamma$ : surface tension of the bulk fluid

$V_m$ : molar liquid volume

$r_p$ : pore radius

$t_c$ : thickness of the adsorbed multilayer film (form prior to pore condensation)

The limitations of the Kelvin equation can be avoided by applying methods based on molecular simulations or DFT (Density Functional Theory) methods.

DFT methods, as recommended by the IUPAC and the ISO 15909-3, allow obtaining reliable pore size distributions over the complete range of micro-mesopores. These are based on molecular simulations. Nowadays, commercial software is available (adsorption instrument manufacturers), with kernels (collection of isotherms representing adsorption in pores of different sizes (width) of a given pore shape at a given temperature) for particular adsorbate-adsorbent pairs. The calculation of the pore size distribution function

$f(W)$  is based on the solution of the General Adsorption Isotherm (GAI); that correlates the experimental to the theoretical adsorption isotherm; by using algorithms. The GAI is shown next:

$$N \frac{P}{P_0} = \int_{W_{\min}}^{W_{\max}} N \frac{P}{P_0} W f(W) dW$$

where

$$N \frac{P}{P_0} = \text{experimental isotherm}$$

$$N \frac{P}{P_0} W = \text{theoretical isotherm}$$

The types of Density Functional Theory (DFT) methods are:

- Non-Local Density Functional Theory (NLDFE). Solid surface is treated as molecularly smooth. However, surface roughness and defects can affect the shape of adsorption isotherms on real surfaces.

- Quenched solid density functional theory (QSDFT). The solid surface includes heterogeneity on the distribution of solid atoms improving the reliability of the pore size analysis. This is the preferred approach for heterogeneous carbons.

Reports of pore size distribution obtained by DFT methods must include the adsorptive/adsorbent pair, assumed pore geometry, and adsorption/desorption branch used for the analysis.

## **2.3 Gas adsorption in non-rigid materials**

Physisorption isotherms are usually reversible in the micropore filling or monolayer range. However, some aspects need to be considered for the study of certain microporous systems (clays, coal, and activated carbon) where a low-pressure hysteresis may appear. Low-pressure hysteresis may indicate a flexible material. However, it could also be the result of a low-quality isotherm or the presence of impurities in the adsorbate or adsorbent.

Low-pressure hysteresis is often associated with flexibility in the structure of materials (expansion and contraction of adsorbents) or with the slow diffusion of molecules through narrow pore entrances. The irreversible entry of the adsorbate molecules into pores of molecular dimensions can produce inelastic adsorbent distortion.

Small elastic deformation of the adsorbent commonly occurs in systems such as charcoal, activated carbon, porous glass, zeolites and silica gel (0.1 – 1%), which usually not affect significantly the sorption isotherm. Elastic deformation in some polymers, aerogels and other highly porous materials might be more problematic.

## **2.4 Water adsorption**

Water adsorption on carbonaceous materials is requested with the aim of understanding the water molecules interactions in the presence of functional groups in a material and for application in industrial processes. Generally, water adsorption isotherms are performed at 298 K. The small size of water molecules is the key for pore structure evaluation for being able to penetrate pores where argon and nitrogen are not accessible.

## 2.5 Adsorptives commonly used in physisorption

The adsorptives commonly used in physisorption are summarized in **Table 2-1**.

**Table 2-1.** Adsorptives commonly used in physisorption.

Name	Molecular weight g mol <sup>-1</sup>	Kinetic diameter nm	Cross-sectional area nm <sup>2</sup>
Water (H <sub>2</sub> O)	18	0.265	0.106 (at 298 K)
Carbon dioxide (CO <sub>2</sub> )	44	0.330	0.112 (at 273 K)
Argon (Ar)	40	0.340	0.142 (at 87 K)
Nitrogen (N <sub>2</sub> )	28	0.364	0.162 (at 77 K)

## 2.6 References

- (1) Sing, K. S. W.; Everett, D. H.; Haul, R. A. W.; Moscou, L.; Pierotti, R. A.; Rouquerol, J.; Siemieniewska, T. *Pure Appl. Chem.* **57**, **1985**.
- (2) Rouquerol, J.; Rouquerol, F.; Sing, K. S. W.; Llewellyn, P.; Maurin, G. *Adsorption by Powders and Porous Solids: Principles, Methodology and Applications*, Ac. Press. **2014**.
- (3) Thommes, M.; Kaneko, K.; Neimark, A. V.; Olivier, J. P.; Rodriguez-Reinoso, F.; Rouquerol, J.; Sing, K. S. Physisorption of gases, with special reference to the evaluation of surface area and pore size distribution. *Pure and Applied Chemistry*, **2015**, *87*, 1051-1069.
- (4) Sotomayor, F. J.; Cychosz, K. A.; Thommes, M. *Characterization of Micro/Mesoporous Materials by Physisorption: Concepts and Case Studies. Acc. Mater. Surf. Res.* **2018**.
- (5) Kaneko, K.; C. Ishii; M. Ruike Origin of superhigh surface area and microcrystalline graphitic structures of activated carbons. *Carbon* **1992**, *30*, 1075-1088.
- (6) Kaneko, K.; Ishii, C.; Kanoh, H.; Hanzawa, Y.; Setoyama, N.; Suzuki, T. Characterization of porous carbons with high resolution  $\alpha_s$ -analysis and low temperature magnetic susceptibility. *Adv. Colloid Interface Sci.* **1998**, *76*, 295-320.

## Chapter 3

### 3. Water adsorption property of hierarchically nanoporous detonation nanodiamonds<sup>1</sup>

**Abstract.** The detonation nanodiamonds are polyhedral particles of sp<sup>3</sup>-hybridized carbon. They are found as their aggregates having interparticle voids, showing a marked hygroscopicity. As the relationship between pore structure and water adsorption of aggregated nanodiamonds is not well understood yet, the nitrogen adsorption isotherm at 77 K and water vapor adsorption isotherm at 298 K of the well-characterized aggregated nanodiamonds prepared by the detonation method were measured. High-resolution transmission electron microscopy and X-ray diffraction showed that the nanodiamonds were crystalline and their average crystallite size was  $4.5 \pm 0.7$  nm. The presence of graphitic layers on the primary nanodiamond particles was confirmed by the electron energy loss spectroscopic examination. The pore size distribution analysis showed that nanodiamonds had slight ultramicropores with predominant mesopores of 4.5 nm in the average size. The water vapor adsorption isotherm of IUPAC Type V indicates the hydrophobicity of the nanodiamond aggregates. The hygroscopic nature of the nanodiamonds should be associated with the surface functionalities of the graphitic shell and the ultramicropores on the mesopore walls.

---

<sup>1</sup> Adapted from Pina-Salazar, E. Z. *et al.* (2017). Water adsorption property of hierarchically nanoporous detonation nanodiamonds. *Langmuir*, 33(42), 11180-11188.

Copyright © 2017, with permission from American Chemical Society.

### 3.1 Introduction

Diamond nanoparticle (nanodiamond)s were first discovered in the 1960s as a product of detonation processes.<sup>1,2</sup> Nanodiamonds are also found in nature as part of protoplanetary disks of certain types of stars.<sup>3,4</sup> Nowadays, nanodiamonds are produced by several routes such as plasma-assisted chemical vapor deposition (CVD),<sup>5</sup> autoclave synthesis from supercritical fluids,<sup>6</sup> electron irradiation of carbon ‘onions’,<sup>7</sup> ion irradiation of graphite,<sup>8</sup> chlorination of carbides,<sup>9</sup> ultrasound cavitation,<sup>10</sup> laser ablation<sup>11</sup> and high-energy ball milling of high-pressure and high-temperature (HPHT) diamond crystals.<sup>12</sup> The most popular nanodiamonds are the ones prepared by the detonation method.<sup>1</sup> This is because the multi-step oxidation-purification procedure has been actively studied for the detonation soots consisting of diamond particles (up to 75% wt.), other carbon allotropes, graphitic carbon, metal impurities, and oxides;<sup>13-15</sup> Ōsawa *et al.* succeeded to obtain highly pure detonation nanodiamonds.<sup>13</sup>

Nanodiamonds can be generally described as polyhedral particles of  $sp^3$ -hybridized carbon atoms, which can be obtained as colloidal individual particles as small as 4-5 nm in diameter, although their characteristics and properties depend on the production method, precursors, and conditions applied.<sup>1,13,2</sup> Nanodiamonds have chemically active surfaces, while the core remains inert. Such particles present a unique surface structure composed of mixed structures of  $sp^3$ diamond-like and  $sp^2$ -graphitic carbon atoms.<sup>14-16</sup> The graphitic or amorphous carbon layers of  $sp^2$  character wrap individual particles of nanodiamonds.<sup>17</sup> Nanodiamonds particles tend to aggregate each other at the nanometer scale of 50-500 nm due to their high surface energy.<sup>18,19</sup> The aggregates have intergranular gaps, which accounts mainly for mesoporosity.<sup>20-22</sup> Moreover, exceptional

properties of nanodiamonds are reported as mechanical and optical properties, fluorescence, high thermal conductivity and electrical resistivity, chemical stability, resistance to harsh environments and biocompatibility. In addition, water adsorption on the surfaces of diamonds and detonation nanodiamonds induces negative electron affinity<sup>23</sup> and giant electric permittivity,<sup>24</sup> respectively.

Wettability well defines the hydrophilic (or hydrophobic) character of a material. The water wettability is described by contact angle for liquid water. The air-water contact angles of polished diamond faces of the single crystal are  $75.9^\circ$  (for the diamond face [111]) and  $71.0^\circ$  (for the diamond face [110]).<sup>25</sup> Then, the surfaces of the diamond are not hydrophilic, but rather hydrophobic. Although the wettability of nanodiamonds has not been fully explored, the water contact angle of the nanodiamond film was  $73 \pm 3^\circ$  in the air at room temperature.<sup>26</sup> Besides, low water affinity of nanodiamond powders is reported.<sup>27</sup> The contact angles of nanodiamonds synthesized by chemical vapor deposition are  $32^\circ$  after oxidation and  $93^\circ$  after reduction.<sup>28</sup> Nanodiamond surfaces without oxidation treatment are also hydrophobic. However, no reports were found on the contact angle of detonation nanodiamonds due to difficult measurements through the hygroscopic nature.<sup>29</sup> Accordingly, water adsorption studies were carried out to evaluate the affinity of the detonation nanodiamonds for water,<sup>24,30,31</sup> giving no clear understanding yet. This study reports a new insight on the affinity of detonation nanodiamonds for water from the relationship between water adsorptivity and nanoporosity.

## 3.2 Experimental section

### 3.2.1 Materials and methods

Hard hydrogels of nanodiamonds obtained from Nano-Carbon Research Institute, Ltd., Japan (density of  $2.2 \times 10^{19}$  particles  $\text{g}^{-1}$ ) were used after grinding and sieving by using a  $0.7 \mu\text{m}$  sieve without further purification.

### 3.2.2 Characterization of nanodiamonds

The morphology of nanodiamonds was examined on powdered nanodiamonds by means of field-emission scanning electron microscopy (FE-SEM; JEOL, JSM-7000F). A high-resolution transmission electron microscope (HR-TEM) was used to observe the nanodiamond crystals. This measurement was carried out on fine powder samples placed on a Cu grid by using a 2100F microscope (JEOL, Japan) operated at 200 kV. Electron energy loss spectroscopy (EELS) was carried out with a scanning transmission electron microscope (STEM) ARM200CF to describe the electronic structure of carbon present in the nanodiamond particles. X-ray diffraction pattern (XRD) of nanodiamonds was measured at room temperature using the X-ray diffractometer (SmartLab X-Ray, Rigaku Co.) with a  $\text{CuK}\alpha$  (40 kV and 30 mA) source. The profiles of temperature-programmed desorption coupled with a mass spectrometer (TPD-MASS) of the as-received nanodiamonds were measured in the temperature range of 373 to 1273 K under He flow of  $300 \text{ mL min}^{-1}$  with a heating rate of  $10 \text{ K min}^{-1}$  using the TG-DTA-Photoionization mass spectrometer (Rigaku Co.) on samples that were degassed at 393 K for 2 h in *vacuo* prior to the measurement. The pore structure of the nanodiamond powder sample was determined volumetrically by nitrogen adsorption isotherm at 77 K using an apparatus Autosorb iQ; Quantachrome after preheating at 423 K and  $10^{-4}$  Pa for 2 h. Quenched

solid density functional theory (QS-DFT) analysis was applied to determine the pore size distribution from the nitrogen adsorption isotherm.<sup>32</sup> Water vapor adsorption isotherm of nanodiamonds was measured at 298 K using a volumetric equipment Quantachrome-Hydrosorb after pretreating at 423 K and 2 mPa for 2 h.

### **3.3 Modeling and simulation section**

#### **3.3.1 Modeling of nanodiamond and simulation of water adsorption isotherm**

The 4 nm nanodiamond was generated using a novel heuristic three-step approach. In the first step, a 4 nm carbon sphere was generated by cutting a perfect diamond supercell using spherical coordinates. The cubic diamond supercell was built by replication of the unit cell<sup>33</sup> in Mercury Visualization Package from the Cambridge Structural Database System.<sup>34</sup> In the second step, the energy of carbon atoms inside a sphere was optimized using Monte Carlo (MC) quench simulations in NVT ensemble. A three-body environmental-dependent interatomic potential (EDIP)<sup>35</sup> was used for computing carbon-carbon interactions. As previously, the temperature decreases linearly from 3000 K down to 30 K, with a step of 10 K. For each temperature, 1000 MC displacement steps were performed using the Metropolis algorithm.<sup>36</sup> The displacement of carbon atoms was adjusted every 1000 MC steps to maintain the acceptance ratio of 0.4. In the final step, the energy of a quenched 4 nm nanodiamond was minimized in the general utility lattice program (GULP)<sup>37</sup> implemented with EDIP potential. We used a constant volume optimization with conjugate gradients. The Grand Canonical Molecular Dynamics (GCMD) method proposed by Eslami and Müller-Plathe was applied to simulate a water isotherm.<sup>38</sup> The GCMD algorithm by Eslami and Muller-Plathe is almost fully deterministic. The only stochastic term is the choice of the initial velocity of the scaling

factor. The GCMD simulations of water adsorption were done with the self-made code; a TIP4P/2005 model was used for the description of water particles.<sup>39</sup> Simulations were done with the use of typical parameters and procedures. Time step was set to 2 fs and the temperature to 298.2 K. The structure of nanodiamond was kept rigid (no movement of structure atoms was considered). A RATTLE method was used to keep all bonds in the water molecules constrained.<sup>40</sup> Total time of each simulation varied from few up to more than 80 ns until no substantial change in the number of molecules was observed. Final adjusted parameters, describing the behavior of the structure are listed in **Table 3-1**. The modeling of nanodiamond and simulation procedures will be published in another journal.

**Table 3-1.** Parameters of interaction of nanodiamond structure atoms used in simulations.

Nanodiamond	Number	$\sigma_{C-O}$ m	$\epsilon_{C-O}$ kJ mol <sup>-1</sup>
Carbon atoms	5808	$3.19 \times 10^{-10}$	0.5
Hydrophilic sites	40	$3.19 \times 10^{-10}$	13

### 3.4 Results and Discussion

Detonation nanodiamonds used in this study are well depicted by the TEM images shown in **Figure 3-1**; analysis of such images gives information on the particle size of nanodiamonds, as well as on the aggregation structure of crystalline particles.

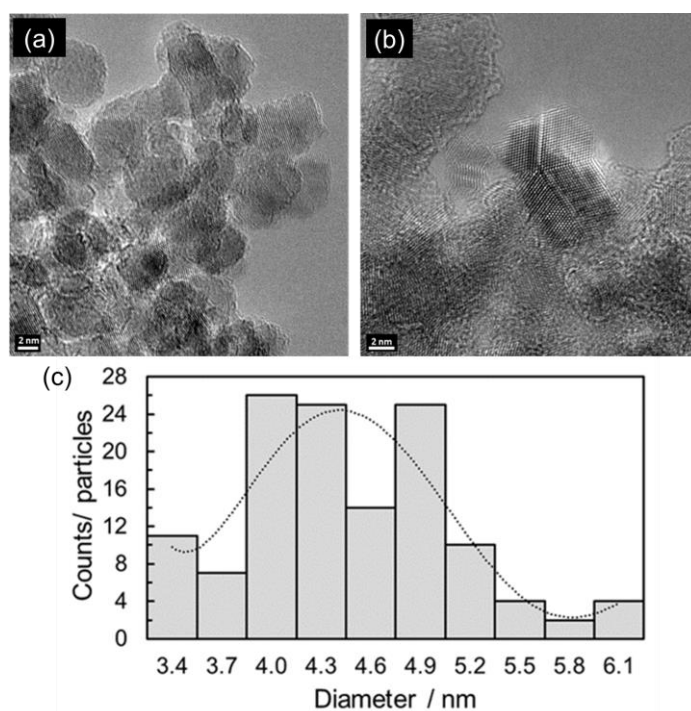


**Figure 3-1.** HR-TEM images of (a) aggregates of nanodiamond crystals and (b) nanodiamond twin crystal. The diamond crystal cores are wrapped with a non-diamond carbon shell. (c) Particle size distribution of nanodiamonds obtained from the measurement of 100 primary nanodiamond crystals in TEM images.

The TEM images in **Figure 3-1a** evidence aggregation of nanodiamond particles of an average particle diameter of  $4.5 \pm 0.7$  nm; as shown by the particle size distribution of nanodiamonds obtained from the measurement of 100 primary nanodiamond crystals in TEM images (**Figure 3-1c**). Primary nanodiamond crystals are interconnected to each other, providing intergranular gaps of a small mesopore and micropore dimensions. These nanodiamond crystals are highly crystalline and even twins of an explicit facet structure are often observed, as shown in **Figure 3-1b**. Additionally, the STEM mapping images in **Figure 3-2a** and **Figure 3-2b** shows that there are many structures surrounding the particles of nanodiamonds as a shell-like structure, as seen in **Figure 3-2c**.

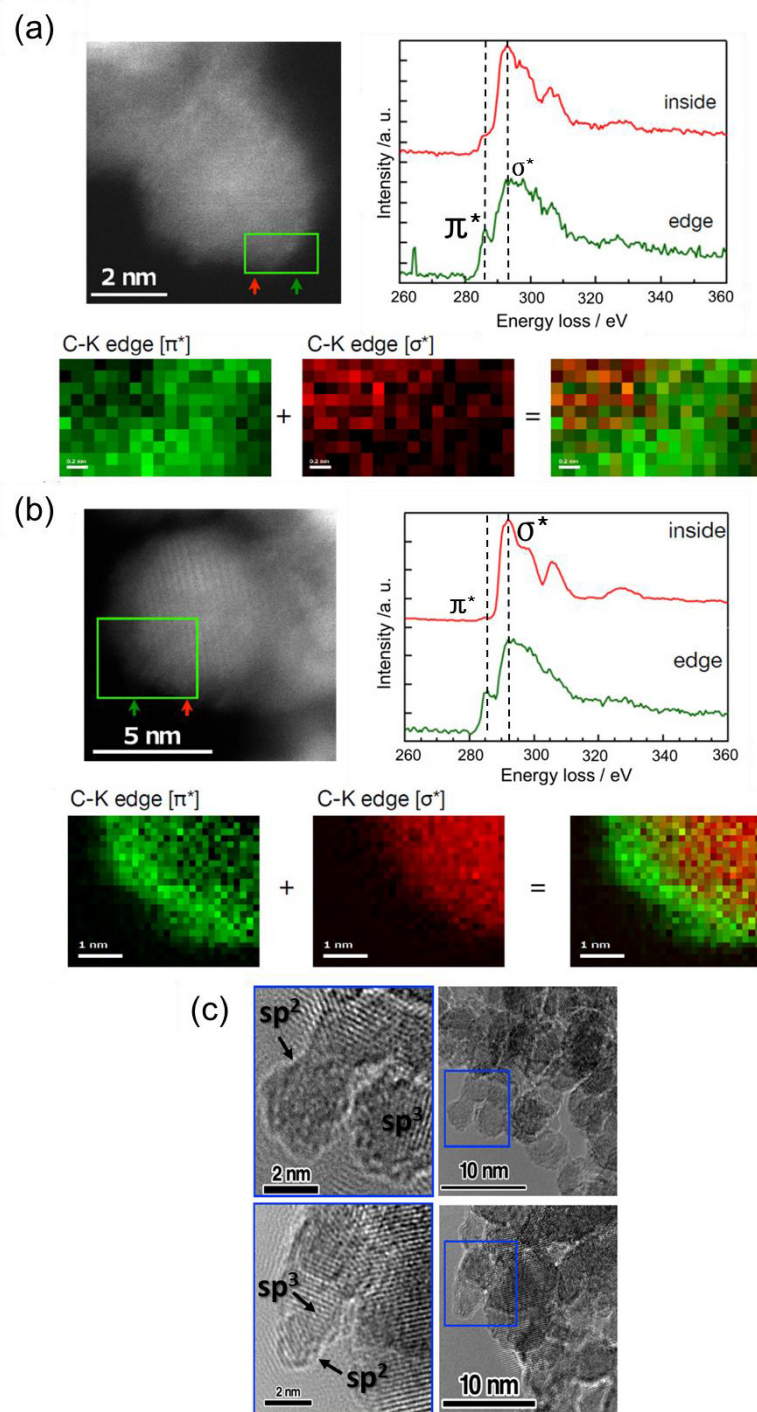


**Figure 3-2.** STEM-EELS mapping images of nanodiamonds at (a) 2 and (b) 5 nm distance to the edge. (c) TEM images of nanodiamonds from which STEM-EELS mapping images were obtained. Here,  $sp^3$  and  $sp^2$  (carbon) indicate diamond crystal cores and shells of non-diamond carbon clearly appreciated on the TEM images, respectively.

The first peak in the plots of **Figure 3-2a** and **Figure 3-2b**; at lower energy loss; is due to absorption by  $\pi^*$  states. The second peak; at higher energy loss; is due to absorption by the  $\sigma^*$  states. The spectrum labeled as inside in **Figure 3-2b** shows the characteristic signature of nanocrystalline diamond. The signal is composed of three main peaks, which indicate the first, second and third K-shell ionization loss peak of crystalline diamond in order of lower to higher energy loss, respectively. The EELS spectrum of the shell structure containing region indicates clearly the presence of graphitic  $sp^2$  carbon through the peak at 284 eV due to the  $\pi^*$  states. The peak derived from  $sp^2$  orbital is confirmed on the surface layer, while the  $sp^3$  signal becomes stronger as moving to the core of the nanodiamond (mapping images at 2 and 5 nm, respectively). These EELS findings agree with previous observations of nanodiamonds surrounded by graphitic shells, typically found for non-treated detonation nanodiamond samples.<sup>41,42</sup>

The crystal structure of nanodiamonds was analyzed by XRD. Nanodiamonds sample exhibits several facets of the crystallites [111], [220] and [311] (at 43.8° 75.4° and 91.5°, respectively), where the [111] facet is the most prominent, as shown in the profile in **Figure 3-3**. This agrees with the reported in the literature.<sup>43</sup> The inset in **Figure 3-3** gives a closer look of the outstanding diamond diffraction peak in the sample [111]; the shoulder at lower scattering angle indicates the presence of nanopores. Deconvolution of the non-symmetrical peak at 43.8° reveals the co-presence of graphitic carbons with a peak at 41.4°. The observed diffraction peak at 43.8° is deconvoluted into diamond [111] and graphitic [100] reflection peaks. The crystallites sizes for [111] and [220] of nanodiamonds are obtained from the half widths of the corresponding peaks after the instrumental broadening correction,<sup>44</sup> being 4.4 nm for [111], 4.3 nm for [220] and 3.5

nm for [311]. Those values are slightly smaller than published values ([111] = 5 nm, [220] = 4.3 nm and [311] = 4.6 nm).<sup>45</sup> The crystallite sizes are close to the average particle size from HR-TEM, indicating that nanodiamonds are highly crystalline.

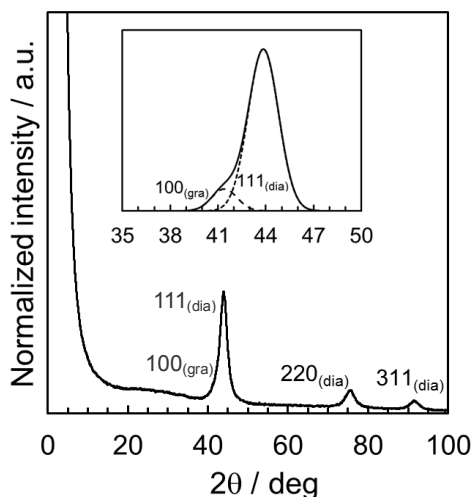


**Figure 3-3.** X-ray diffraction pattern of powdered nanodiamonds. Inset: Deconvoluted diffraction pattern of the [111] reflection. Solid and dotted lines indicate the experimental and deconvoluted peaks, respectively.

Thermogravimetric analysis under He gas flow in **Figure 3-4a** shows the decomposition of nanodiamonds; about 3% of a weight loss is observed up to 523 K, which stems from the evolution of CO<sub>2</sub> and CO, as seen in **Figure 3-4b** that shows the temperature-programmed desorption analysis. The evolved gases of  $m/z = 28$  and  $m/z = 44$  are assigned to CO and CO<sub>2</sub>, respectively, which are derived from oxygen containing-carbon groups or amorphous carbon situated on the graphitic surface. The evolution of the CO<sub>2</sub> gas must indicate the presence of such functionalities on the nanodiamond shell, since carboxyl, carboxyl anhydrous and lactone groups decompose as CO<sub>2</sub>.<sup>46</sup> Evolution of water vapor is observed mainly up to 523 K. Such desorbed water should come from

water strongly adsorbed in the narrow pore spaces in the nanodiamond aggregates even after degassing at 393 K prior to the measurement.

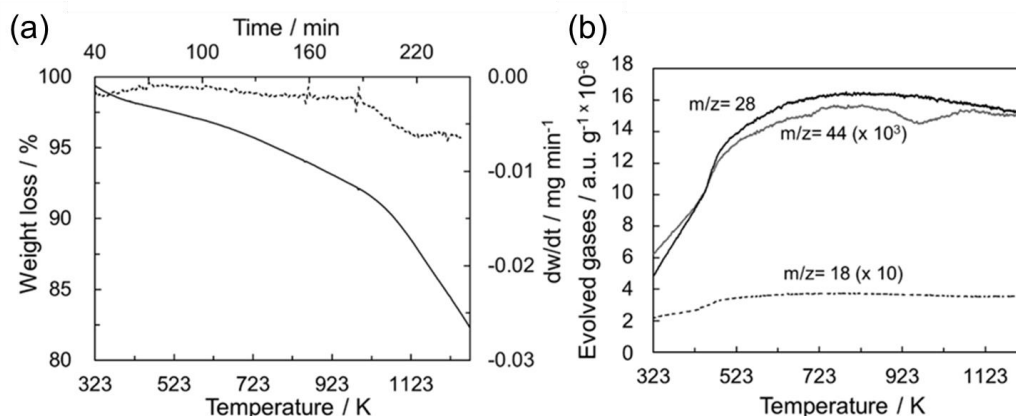


**Figure 3-4.** (a) TG analysis of nanodiamonds under He; weight loss (—) and derivative of TG curve (---), (b) Evolved gases on the course of TG measurement of nanodiamonds; CO — ( $m/z = 28$ ),  $\text{CO}_2$  — ( $m/z = 44$ ) and  $\text{H}_2\text{O}$  --- ( $m/z = 18$ ). In (b) the signal of evolved gases (a. u.  $\text{g}^{-1}$ ) water ( $m/z = 18$ ) and of  $\text{CO}_2$  ( $m/z = 44$ ) are divided by 10 and 1000, respectively to fit in the same scale as CO. Therefore, CO is higher than water, and water is higher than  $\text{CO}_2$  in all the range of temperature.

The aggregated structure of nanodiamonds is clearly confirmed by means of SEM observations, as shown in **Figure 3-5**. The SEM image shows the aggregates of units of about 20 nm agreeing with the TEM image in **Figure 3-1**.

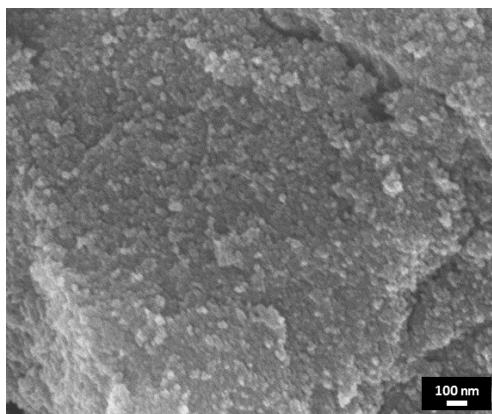


**Figure 3-5.** SEM image of nanodiamonds.

Nitrogen adsorption isotherm at 77 K gives average information on the aggregated structure of nanodiamonds. **Figure 3-6a** shows the nitrogen adsorption isotherm of powdered nanodiamonds and the pore size distribution derived from the adsorption isotherm. The nitrogen adsorption isotherm of nanodiamonds, is close to IUPAC Type IV, being indicative of mesoporous materials. A pronounced adsorption hysteresis from  $P/P_0 = 0.5$  to 0.8 supports the presence of predominant mesopores.<sup>47,48</sup> The nitrogen adsorption isotherm in terms of the logarithm of relative pressure shows the presence of micropores in addition to mesopores, as seen in **Figure 3-6b**. The BET surface area is  $247 \text{ m}^2 \text{ g}^{-1}$ . The pore size distribution is obtained using the QS-DFT method assuming a slit-pore model,<sup>49,50</sup> as shown in **Figure 3-6c**. The nanodiamonds have considerably uniform mesopores of 4.4 nm and a low amount of micropores whose width is in the range of 1 nm to 2 nm. The pore structural parameters are listed in **Table 3-2**.

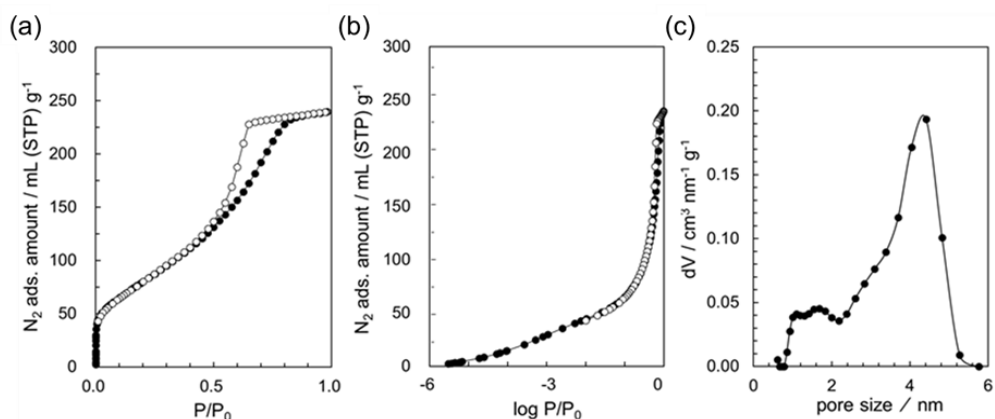


**Figure 3-6.** Nitrogen adsorption isotherms of powdered nanodiamonds at 77 K in (a) linear scale and (b) logarithmic scale, (c) QS-DFT derived pore size distribution. Solid and open symbols in figures (a) and (b) denote adsorption and desorption branches, respectively.

**Table 3-2.** Pore structural parameters of powdered nanodiamonds.

Total pore volume at $P/P_0 = 0.97$	$S_{\text{BET}}$	Micropore volume <sub>DFT</sub> ( $< 2$ nm)	Mesopore volume <sub>DFT</sub> (2-6 nm)
$\text{cm}^3 \text{g}^{-1}$	$\text{m}^2 \text{g}^{-1}$	$\text{cm}^3 \text{g}^{-1}$	$\text{cm}^3 \text{g}^{-1}$
0.37	247	0.047	0.310

The average mesopore size well agrees with the average crystal size, suggesting that the observed mesopores originate from a colloidal aggregation structure of uniform diamond crystals. As the primary nanodiamond crystal is wrapped with an ultra-thin graphitic layer, as mentioned above (see also **Figure 3-2c**), the micropores stem from interstices in nanocrystal contacts and incomplete wrapping with graphitic layers. Phenomenologically, it is well known that a hierarchical structure of micropores and small mesopores induce an unusual sorption property for water.<sup>51–53</sup>

### 3.4.1 Water adsorption property and hygroscopic nature

**Figure 3-7** shows the water vapor adsorption isotherm of nanodiamonds, which is characteristic IUPAC Type V, suggesting hydrophobicity.<sup>48</sup> The whole feature of water adsorption isotherm indicates that nanodiamonds exhibit a weak hydrophobicity, as shown in **Figure 3-7a**. Nevertheless, the slight adsorption of vapor water in the low-pressure range shown in **Figure 3-7b** suggests the presence of hydrophilic sites on nanodiamonds likely corresponding to the surface functional groups on the graphitic shells, which is shown by the TPD results.<sup>52</sup>

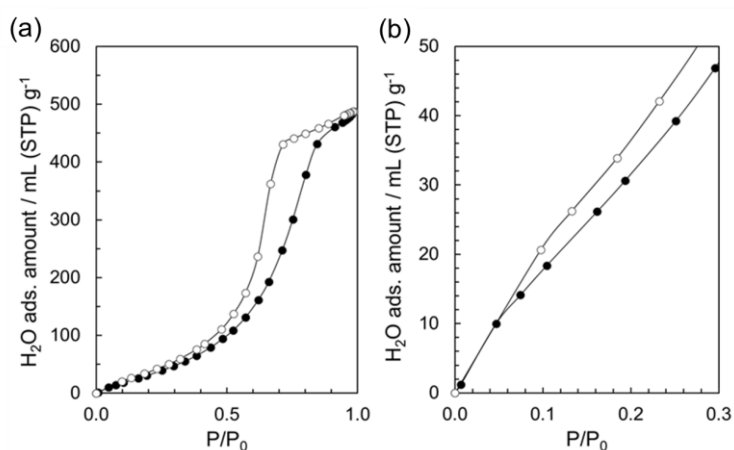


**Figure 3-7.** (a) Water vapor adsorption isotherm of powdered nanodiamonds at 298 K. (b) Closer look of the water adsorption isotherm in the low relative pressure range. Solid and open symbols indicate adsorption and desorption branches, respectively.

Nanodiamond aggregates are hierarchically porous materials, as shown above. Micropores from the outer graphitic shell and the surface functional groups donate local hydrophilicity to the mesopore walls of the nanodiamond-aggregated structures. As the mesopore volume is about seven times larger than micropore volume, adsorbed water should be close to liquid-like water. Correspondingly, the density of adsorbed water from

the adsorbed amount and pore volume is around  $1 \text{ g cm}^{-3}$ . Consequently, these mesopores of large pore volume can accept liquid water, exhibiting a marked hygroscopicity, as shown in **Figure 3-8**, which presents a photo describing the water droplet on pelletized graphite and nanodiamonds upon dropping a water droplet 20 sec after. We cannot see the water droplet on the nanodiamonds, while the water droplet is stable on the graphite. The nanodiamonds with intensive hygroscopicity absorb very quickly the entire water droplet.

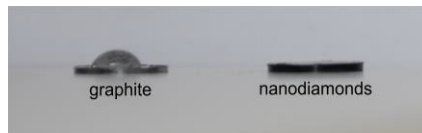


**Figure 3-8.** Water droplet on pelletized graphite and nanodiamonds on dropping a water droplet 20 sec after.

We created the structure model of the nanodiamond crystal and simulated the water adsorption isotherm using the nanodiamond model. **Figure 3-9** shows the GCMD simulated water vapor adsorption. **Figure 3-9a** presents the time course of the adsorption of water molecules on the model nanodiamond at  $P/P_0 = 1$ . The time-change of adsorption provides the equilibrium adsorption amount for each pressure and then we can determine the adsorption isotherm. **Figure 3-9b** shows a comparison of the experimental and simulated adsorption isotherms; the simulated adsorption isotherm coincides well with experimental desorption branch where the desorption branch describes the equilibrium adsorption.<sup>54</sup> Thus, the nanodiamond model expresses well the characteristic structure of the nanodiamonds in particular for water adsorption; the initial uptake and the kink at  $P/P_0 = 0.7$  are well described. We can obtain the molecular level understanding of water adsorption on nanodiamonds. The snapshots of the adsorption of water

molecules at the four  $P/P_0$  denoted by arrows in **Figure 3-9b** are shown in **Figure 3-10**.

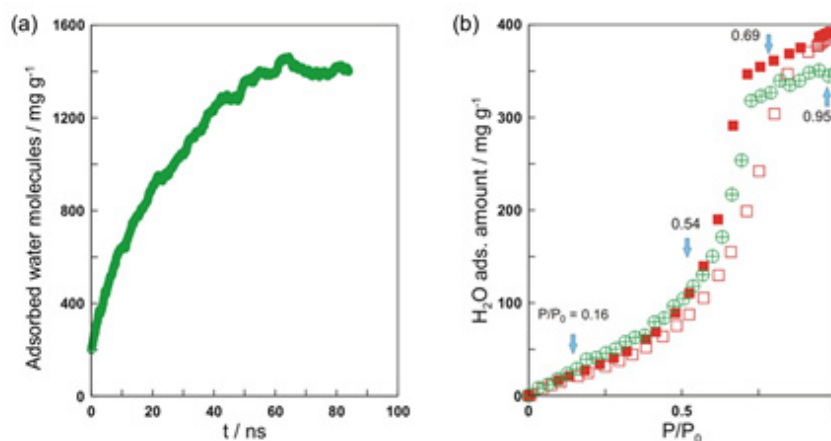


**Figure 3-9.** (a) Change in the number of adsorbed water molecules at saturated vapor pressure ( $P_0$ ) in GCMC simulation. (b) Experimental water adsorption (open squares) - desorption (closed squares) isotherms ( $T=298$  K). Green circles show the GCMC simulated of the adsorption isotherm (snapshots corresponding to blue arrows are shown in **Figure 10**).

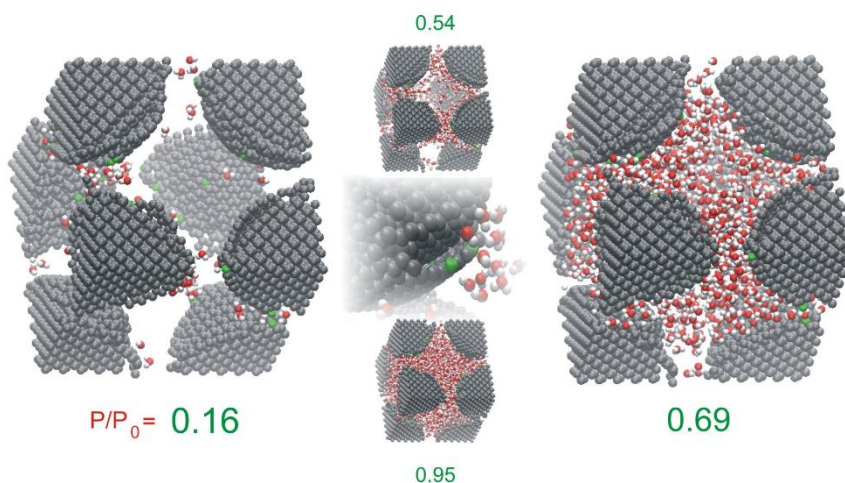


**Figure 3-10.** Snapshots from the simulation box for selected relative pressures pointed by arrows in **Figure 3-9**. The inset in the middle shows a typical water cluster formed at a hydrophilic site (C atoms marked in green) and  $P/P_0 = 0.16$ .

Water molecules are adsorbed only on hydrophilic sites on the graphitic shell at  $P/P_0$  of 0.16, and then water clusters grow to form a continuous water layer with an elevation of  $P/P_0$  and finally induce condensation in the mesopore. The nanodiamond with graphitic shell and their aggregated model can describe the experimental water vapor adsorption, as shown above. The modeling-aided approach should deepen the understanding of the hygroscopic nature of nanodiamonds in the future.

The interaction of water with nanodiamonds is shown in **Figure 3-11**. Nanodiamonds are a hygroscopic material at bulk scale; absorb quickly and efficiently liquid water in their inter-particle pores, even when they show a feature of hydrophobicity at microscale depicted in the water adsorption isotherm.

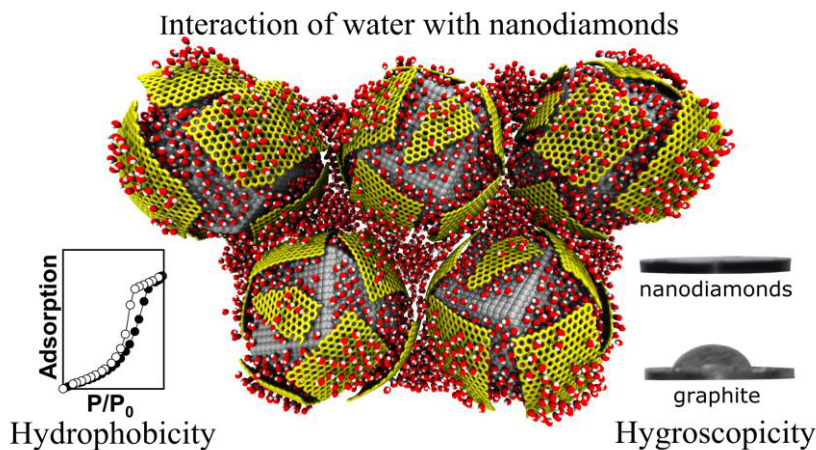


**Figure 3-11.** Graphic model of water interaction with nanodiamonds.

### 3.5 Conclusions

The detonation nanodiamonds are aggregates of crystalline particles of 4.5 nm in the average size, which have graphitic outer layers of surface functionalities. The

nanodiamond colloidal aggregates have small mesopores exhibiting hydrophobic behavior for water vapor adsorption. However, the surface functionalities on the graphitic outer layers on the nanodiamond and ultramicropores in interstices of the aggregates can work as hydrophilic sites. Those should accept liquid-like water in the mesopores, inducing the observed hygroscopic nature. Experimental and modeling studies support the above mechanism on the hygroscopicity of the detonation nanodiamonds. However, we need to evaluate quantitatively the hygroscopicity in order to clarify exactly the remarkable hygroscopicity in future studies.

### 3.6 Acknowledgments

The work was partially supported by Grant-in-Aid- for Scientific Research (B) (17H03039) and the Center of Innovation Program, “Global Aqua Innovation Center for Improving Living Standard and Water Sustainability” of the Japan Science and Technology Agency, JST.

### 3.7 References

- (1) Danilenko, V. V. On the History of the Discovery of Nanodiamond Synthesis. *Phys. Solid State* **2004**, *46* (4), 595–599.
- (2) Greiner, N. R.; Phillips, D. S.; Johnson, J. D.; Volk, F. Diamonds in Detonation Soot. *Nature* **1988**, *333* (6172), 440–442.
- (3) Guillois, O.; Ledoux, G.; Reynaud, C. Diamond Infrared Emission Bands in Circumstellar Media. *Astrophys. J.* **1999**, *521* (2), L133–L136.
- (4) Goto, M.; Henning, T.; Kouchi, A.; Takami, H.; Hayano, Y.; Usuda, T.; Takato, N.; Terada, H.; Oya, S.; Jäger, C.; Andersen, A. C. Spatially Resolved 3 Mm

- Spectroscopy of Elias 1: Origin of Diamonds in Protoplanetary Disks. *Astrophys. J.* **2009**, *693* (1), 610–616.
- (5) Frenklach, M.; Howard, W.; Huang, D.; Yuan, J.; Spear, K. E.; Koba, R. Induced Nucleation of Diamond Powder. *Appl. Phys. Lett.* **1991**, *59* (5), 546–548.
  - (6) Gogotsi, Y. G.; Nickel, K. G.; Bahloul-Hourlier, D.; Merle-Mejean, T.; Khomenko, G. E.; Skjerlie, K. P. Structure of Carbon Produced by Hydrothermal Treatment of  $\beta$ -SiC Powder. *J. Mater. Chem.* **1996**, *6* (4), 595–604.
  - (7) Banhart, F.; Ajayan, P. M. Carbon Onions as Nanoscopic Pressure Cells for Diamond Formation. *Nature* **1996**, *382* (6590), 433–435.
  - (8) Daulton, T. L.; Kirk, M. A.; Lewis, R. S.; Rehn, L. E. Production of Nanodiamonds by High-Energy Ion Irradiation of Graphite at Room Temperature. *Nucl. Instruments Methods Phys. Res. Sect. B Beam Interact. with Mater. Atoms* **2001**, *175*, 12–20.
  - (9) Welz, S.; Gogotsi, Y.; McNallan, M. J. Nucleation, Growth, and Graphitization of Diamond Nanocrystals during Chlorination of Carbides. *J. Appl. Phys.* **2003**, *93* (7), 4207–4214.
  - (10) Galimov, É. M.; Kudin, A. M.; Skorobogatskii, V. N.; Plotnichenko, V. G.; Bondarev, O. L.; Zarubin, B. G.; Strazdovskii, V. V.; Aronin, A. S.; Fisenko, A. V.; Bykov, I. V.; Barinov, A. Y. Experimental Corroboration of the Synthesis of Diamond in the Cavitation Process. *Dokl. Phys.* **2004**, *49* (3), 150–153.
  - (11) Yang, G.-W.; Wang, J.-B.; Liu, Q.-X. Preparation of Nano-Crystalline Diamonds Using Pulsed Laser Induced Reactive Quenching. *J. Phys. Condens. Matter* **1998**, *10* (35), 7923–7927.
  - (12) Boudou, J.-P.; Curmi, P. A.; Jelezko, F.; Wrachtrup, J.; Aubert, P.; Sennour, M.;

- Balasubramanian, G.; Reuter, R.; Thorel, A.; Gaffet, E. High Yield Fabrication of Fluorescent Nanodiamonds. *Nanotechnology* **2009**, *20* (23), 235602.
- (13) Ozawa, M.; Inaguma, M.; Takahashi, M.; Kataoka, F.; Krüger, A.; Osawa, E. Preparation and Behavior of Brownish, Clear Nanodiamond Colloids. *Adv. Mater.* **2007**, *19* (9), 1201–1206.
- (14) Petit, T.; Arnault, J. C.; Girard, H. A.; Sennour, M.; Bergonzo, P. Early Stages of Surface Graphitization on Nanodiamond Probed by X-Ray Photoelectron Spectroscopy. *Phys. Rev. B - Condens. Matter Mater. Phys.* **2011**, *84* (23), 233407.
- (15) Krueger, A.; Lang, D. Functionality Is Key: Recent Progress in the Surface Modification of Nanodiamond. *Adv. Funct. Mater.* **2012**, *22* (5), 890–906.
- (16) Carlisle, J. A.; Auciello, O. Ultrananocrystalline Diamond. *Interface-Electrochemical Soc.* **2003**, *12* (1), 28–32.
- (17) Raty, J.-Y.; Galli, G.; Bostedt, C.; Van Buuren, T. W.; Terminello, L. J. Quantum Confinement and Fullerene-like Surface Reconstructions in Nanodiamonds. *Phys. Rev. Lett.* **2003**, *90* (3), 37401.
- (18) Baidakova, M.; Vul', A. New Prospects and Frontiers of Nanodiamond Clusters. *J. Phys. D. Appl. Phys.* **2007**, *40* (20), 6300–6311.
- (19) Krüger, A.; Kataoka, F.; Ozawa, M.; Fujino, T.; Suzuki, Y.; Aleksenskii, A. E.; Vul', A. Y.; Osawa, E. Unusually Tight Aggregation in Detonation Nanodiamond: Identification and Disintegration. *Carbon* **2005**, *43* (8), 1722–1730.
- (20) Korobov, M. V.; Batuk, M. M.; Avramenko, N. V.; Ivanova, N. I.; Rozhkova, N. N.; Osawa, E. Aggregate Structure Of “single-Nano Buckydiamond” in Gel and Dried Powder by Differential Scanning Calorimetry and Nitrogen Adsorption. *Diam. Relat. Mater.* **2010**, *19* (5), 665–671.

- (21) Kondo, T.; Kobayashi, M.; Saito, T.; Kadota, Y.; Kameshima, T.; Aikawa, T.; Kawai, T.; Yuasa, M. Micrometer-Sized Mesoporous Diamond Spherical Particles. *Diam. Relat. Mater.* **2014**, *43*, 72–79.
- (22) Korobov, M. V.; Batuk, M. M.; Avramenko, N. V.; Ivanova, N. I.; Rozhkova, N. N.; Osawa, E. Do Primary Particles of Detonation Nanodiamond Form a Secondary Structure? *Fullerenes Nanotub. Carbon Nanostructures* **2011**, *19* (1–2), 58–62.
- (23) Gao, X.; Liu, L.; Qi, D.; Chen, S.; Wee, A. T. S.; Yu, X.; Moser, H. O. Water-Induced Negative Electron Affinity on Diamond (100). *J. Phys. Chem. C* **2008**, *100* (7), 2487–2491.
- (24) Batsanov, S. S.; Gavrilkin, S. M.; Batsanov, A. S.; Poyarkov, K. B.; Kulakova, I. I.; Johnson, D. W.; Mendis, B. G. Giant Dielectric Permittivity of Detonation-Produced Nanodiamond Is Caused by Water. *J. Mater. Chem.* **2012**, *22* (22), 11166–11172.
- (25) Hansen, J. O.; Copperthwaite, R. G.; Derry, T. E.; Pratt, J. M. A Tensiometric Study of Diamond (111) and (110) Faces. *J. Colloid Interface Sci.* **1989**, *130* (2), 347–358.
- (26) Ostrovskaya, L.; Perevertailo, V.; Ralchenko, V.; Saveliev, A.; Zhuravlev, V. Wettability of Nanocrystalline Diamond Films. *Diam. Relat. Mater.* **2007**, *16* (12), 2109–2113.
- (27) Denisov, S. A.; Sokolina, G. A.; Bogatyreva, G. P.; Grankina, T. Y.; Krasil'nikova, O. K.; Plotnikova, E. V.; Spitsyn, B. V. Adsorption and Electrical Properties of Nanodiamond Powders in the Presence of Water Vapor. *Prot. Met. Phys. Chem. Surfaces* **2013**, *49* (3), 286–291.
- (28) Ostrovskaya, L.; Perevertailo, V.; Ralchenko, V.; Dementjev, A.; Loginova, O.

- Wettability and Surface Energy of Oxidized and Hydrogen Plasma-Treated Diamond Films. *Diam. Relat. Mater.* **2002**, *11* (3), 845–850.
- (29) Alghunaim, A.; Kirdponpattara, S.; Newby, B. M. Z. Techniques for Determining Contact Angle and Wettability of Powders. *Powder Technol.* **2016**, *287*, 201–215.
- (30) Kulakova, I. I. Surface Chemistry of Nanodiamonds. *Phys. Solid State* **2004**, *46* (4), 636–643.
- (31) Ji, S.; Jiang, T.; Xu, K.; Li, S. FTIR Study of the Adsorption of Water on Ultradispersed Diamond Powder Surface. *Appl. Surf. Sci.* **1998**, *133* (4), 231–238.
- (32) Ravikovitch, P. I.; Neimark, A. V. Density Functional Theory Model of Adsorption Deformation. *Langmuir* **2006**, *22* (26), 10864–10868.
- (33) Pauling, L. The Structure and Properties of Graphite and Boron Nitride. *Proc. Natl. Acad. Sci.* **1966**, *56* (6), 1646–1652.
- (34) The Cambridge Structural Database System. <https://www.ccdc.cam.ac.uk/solutions/csd-system/components/mercury/>.
- (35) Marks, N. A. Generalizing the Environment-Dependent Interaction Potential for Carbon. *Phys. Rev. B* **2000**, *63* (3), 35401.
- (36) Kowalczyk, P.; Terzyk, A. P.; Gauden, P. a; Furmaniak, S.; Kaneko, K. Toward in Silico Modeling of Palladium-Hydrogen-Carbon Nanohorn Nanocomposites. *Phys. Chem. Chem. Phys.* **2014**, *16* (23), 11763–11769.
- (37) Gale, J. D. GULP: A Computer Program for the Symmetry-Adapted Simulation of Solids. *J. Chem. Soc. Faraday Trans.* **1997**, *93* (4), 629–637.
- (38) Eslami, H.; Müller - Plathe, F. Molecular Dynamics Simulation in the Grand Canonical Ensemble. *J. Comput. Chem.* **2007**, *28* (10), 1763–1773.
- (39) Abascal, J. L.; Vega, C. A General Purpose Model for the Condensed Phases of

- Water: TIP4P/2005. *J. Chem. Phys.* **2005**, *123* (23), 234505.
- (40) Andersen, H. C. Rattle: A “velocity” version of the Shake Algorithm for Molecular Dynamics Calculations. *J. Comput. Phys.* **1983**, *52* (1), 24–34.
- (41) Mochalin, V. N.; Shenderova, O.; Ho, D.; Gogotsi, Y. The Properties and Applications of Nanodiamonds. *Nat. Nanotechnol.* **2012**, *7* (1), 11–23.
- (42) Butenko, Y. V.; Krishnamurthy, S.; Chakraborty, A. K.; Kuznetsov, V. L.; Dhanak, V. R.; Hunt, M. R. C.; Šiller, L. Photoemission Study of Onionlike Carbons Produced by Annealing Nanodiamonds. *Phys. Rev. B - Condens. Matter Mater. Phys.* **2005**, *71* (7), 75420.
- (43) Shenderova, O. A.; Vlasov, I. I.; Turner, S.; Van Tendeloo, G.; Orlinskii, S. B.; Shiryaev, A. A.; Khomich, A. A.; Sulyanov, S. N.; Jelezko, F.; Wrachtrup, J. Nitrogen Control in Nanodiamond Produced by Detonation Shock-Wave-Assisted Synthesis. *J. Phys. Chem. C* **2011**, *115* (29), 14014–14024.
- (44) Waseda, Y.; Matsubara, E.; Shinoda, K. *X-Ray Diffraction Crystallography. Introduction, Examples and Solved Problems*; Springer Science & Business Media, 2011.
- (45) Ozerin, A. N.; Kurkin, T. S.; Ozerina, L. A.; Dolmatov, V. Y. X-Ray Diffraction Study of the Structure of Detonation Nanodiamonds. *Crystallogr. Reports* **2008**, *53* (1), 60–67.
- (46) Szymański, G. S.; Karpiński, Z.; Biniak, S.; Świątkowski, A. The Effect of the Gradual Thermal Decomposition of Surface Oxygen Species on the Chemical and Catalytic Properties of Oxidized Activated Carbon. *Carbon* **2002**, *40* (14), 2627–2639.
- (47) Katsumi, K. Determination of Pore Size and Pore Size Distribution. 1. Adsorbents

- and Catalysts. *J. Memb. Sci.* **1994**, *96* (1–2), 59–89.
- (48) Thommes, M.; Kaneko, K.; Neimark, A. V.; Olivier, J. P.; Rodriguez-Reinoso, F.; Rouquerol, J.; Sing, K. S. W. Physisorption of Gases, with Special Reference to the Evaluation of Surface Area and Pore Size Distribution (IUPAC Technical Report). *Pure Appl. Chem.* **2015**, *87* (9–10), 1051–1069.
- (49) Neimark, A. V.; Lin, Y.; Ravikovitch, P. I.; Thommes, M. Quenched Solid Density Functional Theory and Pore Size Analysis of Micro-Mesoporous Carbons. *Carbon* **2009**, *47* (7), 1617–1628.
- (50) Zeiger, M.; Jäckel, N.; Aslan, M.; Weingarth, D.; Presser, V. Understanding Structure and Porosity of Nanodiamond-Derived Carbon Onions. *Carbon* **2015**, *84*, 584–598.
- (51) Pina-Salazar, E. Z.; Kaneko, K. Adsorption of Water Vapor on Mesoporosity-Controlled Single Wall Carbon Nanohorn. *Colloids Interface Sci. Commun.* **2015**, *5*, 8–11.
- (52) Bekyarova, E.; Hanzawa, Y.; Kaneko, K.; Silvestre-Albero, J.; Sepulveda-Escribano, A.; Rodriguez-Reinoso, F.; Kasuya, D.; Yudasaka, M.; Iijima, S. Cluster-Mediated Filling of Water Vapor in Intratube and Interstitial Nanospaces of Single-Wall Carbon Nanohorns. *Chem. Phys. Lett.* **2002**, *366* (5), 463–468.
- (53) Hanzawa, Y.; Kaneko, K. Lack of a Predominant Adsorption of Water Vapor on Carbon Mesopores. *Langmuir* **1997**, *13* (22), 5802–5804.
- (54) Nakamura, M.; Ohba, T.; Branton, P.; Kanoh, H.; Kaneko, K. Equilibration-Time and Pore-Width Dependent Hysteresis of Water Adsorption Isotherm on Hydrophobic Microporous Carbons. *Carbon* **2010**, *48* (1), 305–308.

## Chapter 4

### 4. Water-selective adsorption sites on detonation nanodiamonds<sup>1</sup>

**Abstract.** Nanodiamond particles form aggregates having porosity in the range of micropores to mesopores with an average pore diameter of 4.5 nm. The measured porosity depends on the removal of pre-occupied water and gases from the nanodiamond aggregates, which is sensitive to thermal treatments. We heated hydrogel nanodiamonds at 423–623 K in *vacuo* in order to understand the relationship between water adsorptivity and pore structure evaluated from nitrogen and argon adsorption isotherms at 77 K and 87 K, respectively. Temperature-programmed evolved gas analysis showed the evolution of water and CO<sub>2</sub> on heating nanodiamonds in *vacuo* up to 700 K. The surface functional groups of nanodiamonds were not affected by the thermal treatments, as shown by FTIR and XPS analyses. However, the water adsorptivity was enhanced by heating at 623 K due to the removal of the pore blocking effect originated from water molecules selectively adsorbed. Water molecules adsorbed on these selective sites should cause the intensive hygroscopic property of nanodiamonds.

---

<sup>1</sup> Adapted from Piña-Salazar, E. Z. *et al.* (2018). Water-selective adsorption sites on detonation nanodiamonds. *Carbon*, 139, 853-860. Copyright © 2018, with permission from Elsevier.

## 4.1 Introduction

Detonation nanodiamonds are found as aggregates of polyhedral particles of  $sp^3$ -hybridized carbon covered by  $sp^2$ -hybridized carbon. The aggregation of nanodiamond particles comes from the facet-facet electrostatic attractions between multi-pole polyhedral primary particles.<sup>1-4</sup> The detonation nanodiamonds are produced as small as 3–5 nm in the form of hydrogels.<sup>5</sup> Hydrogel nanodiamonds contain water within their structure, inducing unique hydrophilic properties.<sup>6</sup> Water is adsorbed in the pores of the aggregated nanodiamonds. Those pores consist mainly of mesopores and micropores.<sup>7</sup> Dried hydrogel nanodiamonds tend to be hydrated in the humid air.<sup>6,8,9</sup> They can also absorb quickly and efficiently liquid water in their inter-particle pore structure.<sup>7</sup> The porosity of the aggregates should be influenced by the pre-occupied water and adsorbed gases. Thermal treatment is essential to determine the accurate porosity of nanodiamond aggregates. Our preceding study showed that nanodiamond aggregates have predominant mesopores of 4.5 nm in an average size and a few micropores after degassing at 423 K for 2 h, yielding a surface area of  $300 \text{ m}^2 \text{ g}^{-1}$ ,<sup>7</sup> being larger than that of nanodiamonds without degassing. It was also suggested that the graphene-like structure covering nanodiamonds is associated with the remarkable wettability to liquid water. The presence of water strongly bound in the detonation nanodiamonds was proposed by Jiang and Xu.<sup>10</sup> The pore structure of nanoporous graphene is sensitive to thermal heating.<sup>11</sup> Fundamental understanding of interfacial properties and structure of hydrogel nanodiamonds heated at different temperatures is indispensable to develop their applications in various fields such as nanomedicine, water filtration technologies and others. As the nanodiamonds have ultramicropores together with mesopores, comparative pore analysis using nitrogen adsorption at 77 K and argon adsorption at 87 K must be applied to the thermally treated

hydrogel nanodiamonds.<sup>12,13</sup> This chapter reports the relationship between water adsorptivity and pore structure from nitrogen and argon of hydrogel nanodiamonds thermally treated at different temperatures.

## **4.2 Experimental section**

### **4.2.1 Samples and their thermal treatments**

Nanodiamonds in the form of a hard hydrogel (Nano-Carbon Research Institute, Ltd., Japan) with a density of  $2.2 \times 10^{19}$  particles  $\text{g}^{-1}$  were ground and sieved (0.7  $\mu\text{m}$  in mesh size), followed by an outgassing treatment at 393 K and 0.1 Pa for 2 h. These obtained nanodiamonds were heated at 423, 523 and 623 K for 2 h at 0.001 and 0.1 Pa prior to the porosity and water adsorption measurements, respectively.

### **4.2.2 Characterization of nanodiamonds**

#### **4.2.2.1 Thermogravimetric analysis**

Thermogravimetric profiles of nanodiamonds isothermally heated at 423 and 623 K for 2 h and from room temperature to 1300 K under inert conditions ( $\text{N}_2$  300  $\text{mL min}^{-1}$ ) were measured with a heating rate of 5.0  $\text{K min}^{-1}$  by means of a thermogravimetric analyzer (STA7200, HITACHI). TG-mass analysis of nanodiamonds before thermal treatments was obtained under an oxidative atmosphere ( $\text{He-O}_2$  80:20%; 100  $\text{mL min}^{-1}$ ) and under an inert atmosphere ( $\text{He}$  300  $\text{mL min}^{-1}$ ) with a heating rate of 5.0  $\text{K min}^{-1}$  in a TG-DTA-Photoionization mass spectrometer (TG-DTA-PIMS 410/s, Rigaku Co.). A total gas flow between 100 and 300  $\text{mL min}^{-1}$  must be used for results nearly independent from the gas flow. For each case, the gas mixture is introduced to the system a few minutes before the beginning of the heating. Diluted oxygen gas must be used to avoid violent

oxidation when running an analysis under oxidative atmosphere. Therefore, a ratio 80:20 He-O<sub>2</sub> mixture was used, corresponding roughly to the air composition. Nanodiamonds were outgassed ex-situ at 393 K and 0.1 Pa for 2 h prior to the measurements.

#### 4.2.2.2 Structural analysis

The morphology of nanodiamonds was observed by using a field-emission scanning electron microscope (FE-SEM; JEOL, JSM-7000F, Japan) and a high-resolution transmission electron microscope (HR-TEM, JEOL, 2100F Japan) operated at 200 kV. Adsorption isotherms of nitrogen at 77 K and argon at 87 K were measured after heating nanodiamonds samples in *vacuo* of 1 mPa at 423, 523 and 623 K for 2 h using a volumetric apparatus (Quantachrome-Autosorb IQ2). The nanoporosities and the pore size distributions of the nanodiamonds were determined by BET and the subtracting pore effect (SPE) method of the  $\alpha_s$ -plot,<sup>14</sup> and by using the Quenched Solid Density Functional Theory (QS-DFT) assuming a slit shape pore,<sup>15,16</sup> respectively. Nonporous carbon black was used as the reference material for the SPE method. XPS analysis was conducted in order to study the surface chemistry of nanodiamonds by using a JPS-9200, JEOL spectrometer equipped with a polychromatic Mg K $\alpha$  X-ray beam X-ray source. Spectra were taken for as-received nanodiamonds and nanodiamonds treated at 423 and 623 K in *vacuo* of 0.1 Pa for 2 h. The calibration was carried out by use of the C1s peak at 285  $\pm$  0.2 eV associated with nanodiamond carbon. The C1s peak was deconvoluted into four peaks with assignments of the literature corresponding to sp<sup>2</sup>-hybridized carbon at 284.1 eV, sp<sup>3</sup>-hybridized carbon at 285.2 eV, C-H bonds and C-N at 286.3 eV and C-O bonds at 287.7 eV.<sup>17,18</sup> FTIR analysis of nanodiamonds was conducted under the relative humidity of 20% using a Nicolet 6700 FT-IR (Thermo scientific) equipment in the ATR-

FTIR measurement mode in order to evaluate the surface chemistry of nanodiamonds prior to the thermal treatments. Nanodiamond sample was outgassed ex-situ at 423 K and 0.1 Pa for 2 h prior to the measurement.

#### **4.2.2.3 Water adsorption**

Water vapor adsorption isotherms were measured at 298 K on the nanodiamond samples heated at 423, 523 and 623 K for 2 h under 0.1 Pa with a volumetric equipment (Quantachrome-Vstar).

### **4.3 Results and discussion**

#### **4.3.1 Morphology and surface chemistry of thermally treated nanodiamonds**

SEM micrographs in **Figure 4-1** exhibit the morphology of nanodiamonds before and after heating. There is no clear change in the assembly structure of nanodiamonds after heating. It clearly shows aggregated nanodiamond particles of non-uniform shape and the average size of about 20 nm. The crystal size of nanodiamonds is in the order of 4 nm, as shown in the TEM image of **Figure 4-1e**, **Figure 4-1f** and **Figure 4-1g**, which is similar to the statistical particle diameter obtained from TEM and XRD analysis reported in the preceding chapter.<sup>7</sup> There should be mesopores and micropores in the interparticle and inter-crystal structures. The purity of nanodiamonds used in this study is higher than 97% according to the oxidative TG-curve showing non-combustible residues (**Figure 4-2a**). Nanodiamonds burn at 823 K in air, leading to a sharp weight loss. The weight loss is associated with the evolution of CO, CO<sub>2</sub>, and H<sub>2</sub>O, as shown in **Figure 4-2b**.<sup>19-21</sup> **Figure 4-3** shows the temperature-programmed evolved gas analyses of nanodiamond samples over the temperature range of room temperature to 1300 K under a flow of He. The

evolution curves of water ( $m/z = 18$ ), CO ( $m/z = 28$ ) and CO<sub>2</sub> ( $m/z = 44$ ) become steeper around 420 K exhibiting a plateau about 700 K. These evolved gases originate from desorption of strongly adsorbed water and decomposition of surface functional groups.<sup>22–25</sup> The evolution of water is clearly larger than that of CO<sub>2</sub> below 623 K, as seen in **Figure 3-4b** of the previous chapter.

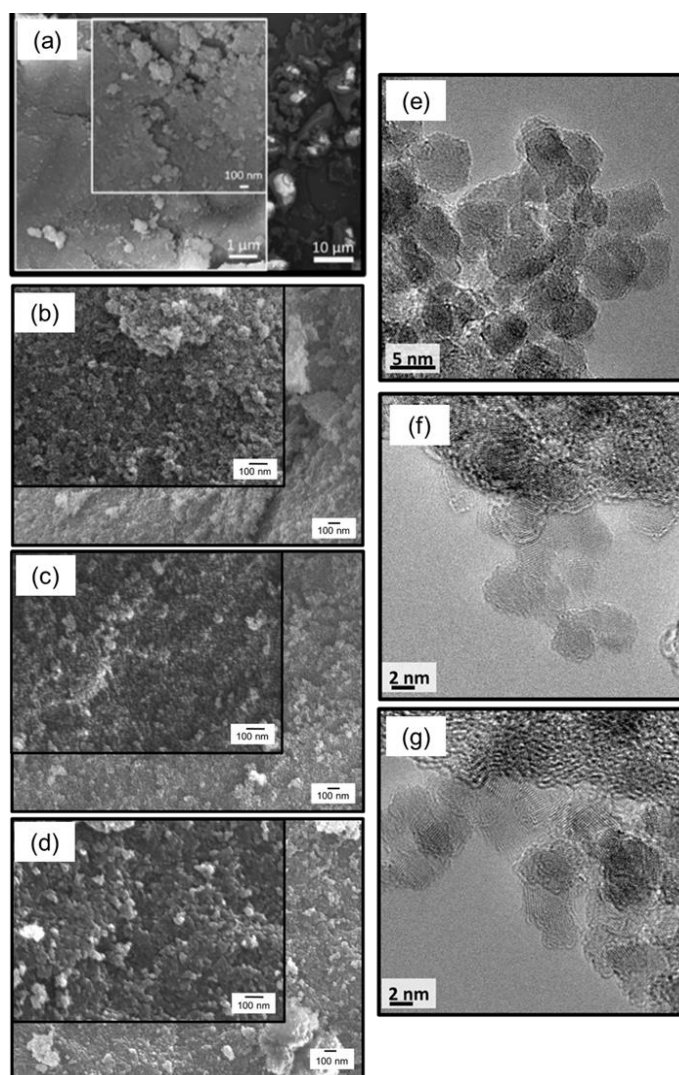


**Figure 4-1.** SEM images of detonation nanodiamonds (a) non-heated and heated at (b) 423 K and (c) 523 K and (d) 623 K for 2 h in *vacuo*. Representative HR-TEM images of detonation nanodiamonds prior to heating are shown in (e), (f) and (g).

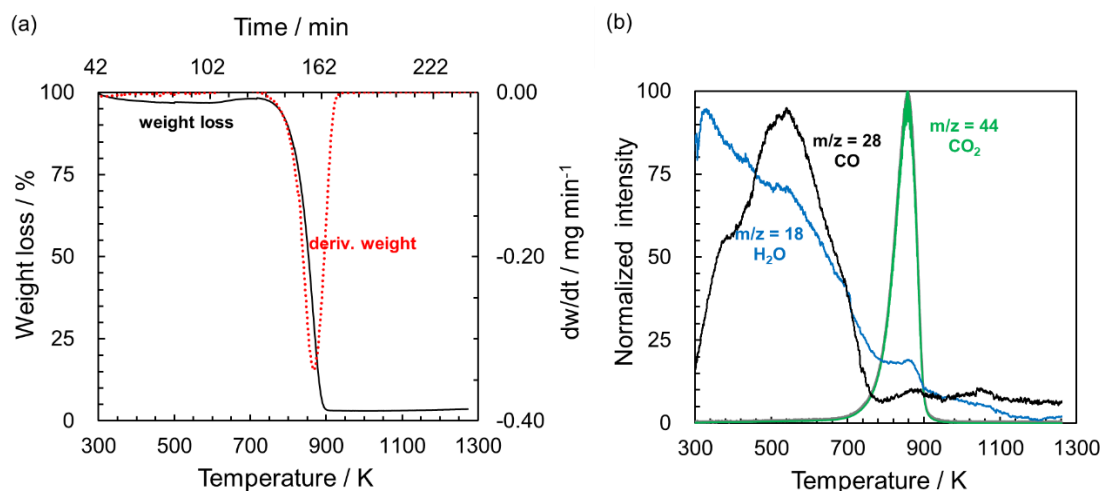


**Figure 4-2.** (a) Thermogravimetric profiles and (b) temperature-programmed evolved gas analyses of detonation nanodiamonds in He-O<sub>2</sub> (80:20). In (a): weight loss (-) and derivative of weight loss (···), in (b) evolved gases in the course of TG measurement: CO (black line, m/z = 28), CO<sub>2</sub> (green line, m/z = 44) and H<sub>2</sub>O (blue line, m/z = 18).

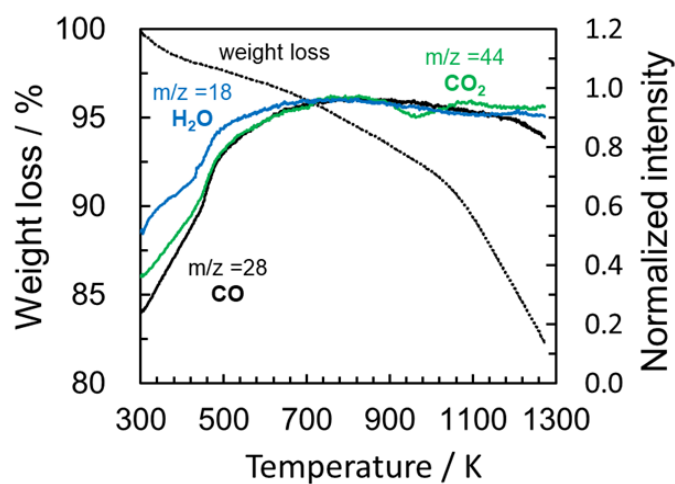


**Figure 4-3.** Temperature-programmed evolved gas analyses of detonation nanodiamonds under He flow of 300 mL min<sup>-1</sup>. Weight loss (···) and evolved gases: CO (black line, m/z = 28), CO<sub>2</sub> (green line, m/z = 44) and H<sub>2</sub>O (blue line, m/z = 18).

We studied porosity and water adsorptivity of nanodiamonds after removal of strongly adsorbed water since we need to understand the role of strongly adsorbed water in the effective pores and water adsorptivity of nanodiamonds. Accordingly, we heated nanodiamonds at 523 and 623 K in *vacuo* for 2 h to remove strongly adsorbed water as much as possible (**Figure 4-4**). Although water may remain in the samples at the applied temperature, in this chapter, we have addressed the relative water adsorptivity with the porosity change. Still, we cannot discuss absolutely the relationship between the porosity and water adsorption amount. Since the intensity of the water mass profile ( $m/z = 18$ ) was higher even after 450 K than those of CO ( $m/z = 28$ ) and CO<sub>2</sub> ( $m/z = 44$ ), we assume that the signal of water comes from strongly adsorbed water on the hydrophilic sites of nanodiamonds. The thermal treatment for 2 h at 423 K leads to a weight loss of 14 mg g<sup>-1</sup> while heating at 623 K gives rise to the weight loss of 27 mg g<sup>-1</sup>. The weight loss after heating at 623 K for 2 h is twice that by treating at 423 K for 2 h (1.6 and 0.5%, respectively). Here, we assume that the weight loss from the sample comes from desorption of water from the nanodiamond sample. The extent of desorption of water is associated with the porosity change, as discussed here. Moreover, when preheating at 423 K or lower temperature, only water loosely adsorbed is removed, as seen for a massive weight loss in the derivative of weight loss. The derivative of weight loss of nanodiamonds heated at 623 K shows several peaks. These are probably due to the removal of water from different pore sizes and the low degree of reduction of oxygen-containing functional groups such as lactone or carboxylic groups.<sup>24</sup> The weight loss observed after both heating treatments is related to desorption of water or functionalities, and the unblocking of pores.

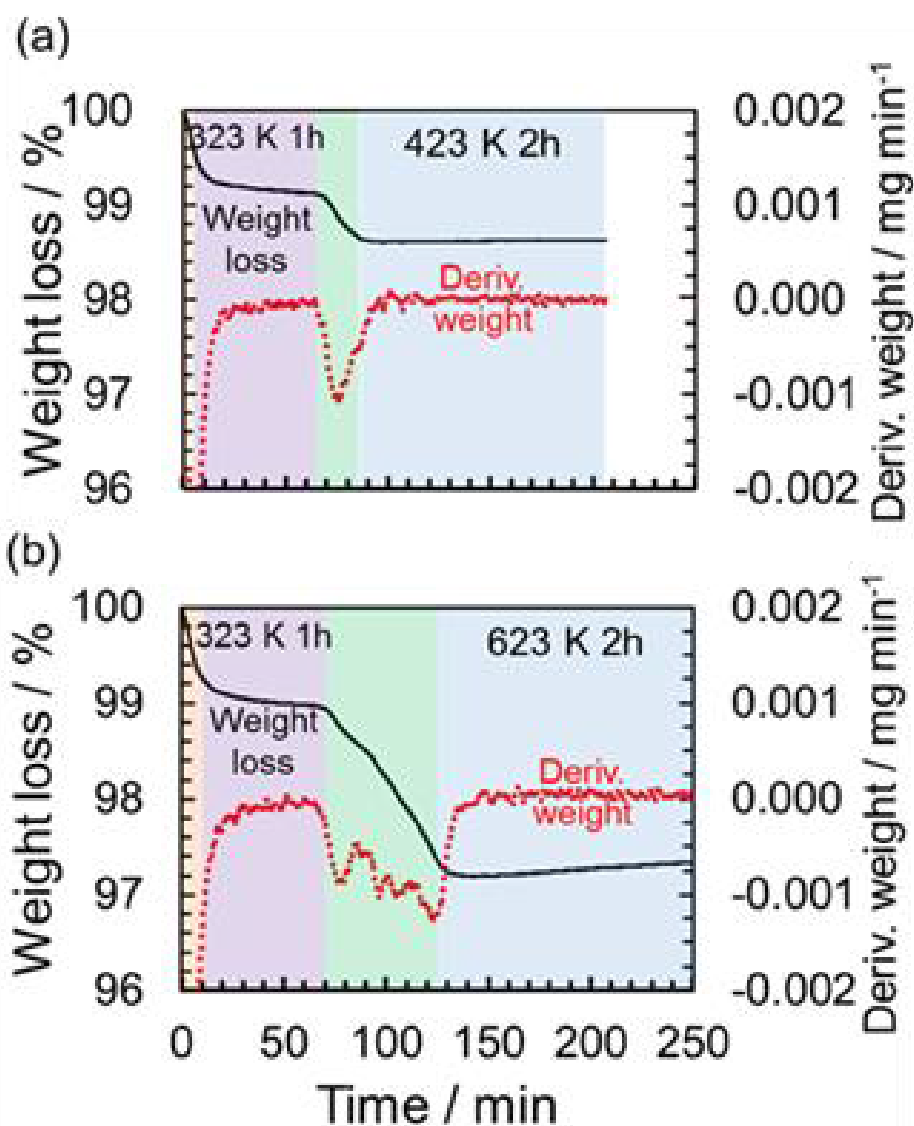


**Figure 4-4.** Thermogravimetric analyses and profile of change of mass respect of time of nanodiamonds heated at (a) 423 and (b) 623 K for 2 h in nitrogen gas (150 mL min<sup>-1</sup>). Weight loss (—) and derivative of weight loss (···). The sections shaded in colors indicate different regions of the heating profile 298-323 K (yellow), 323 K for 1 h (purple), 323 K- target temperature (green), isothermal treatment at the target temperature (blue). The heating rate during ramping was 5.0 K min<sup>-1</sup>.

The FTIR study on nanodiamonds heated ex-situ at 423 K at room temperature and relative humidity of 20% supports the presence of strongly adsorbed water, as seen in **Figure 4-5**. Although we measured the FTIR spectrum in air, the possible adsorption amount of water during the measurements is less than 6% (from the water adsorption isotherm). The FTIR spectrum shows explicitly the IR bands of water at 3320 and 1630  $\text{cm}^{-1}$ .<sup>9,10,26,27</sup> According to Jiang *et al.*, the strongest signal at 3370  $\text{cm}^{-1}$  with a shoulder at 3320  $\text{cm}^{-1}$  denotes the presence of water in the sample.<sup>10</sup> Similarly, adsorbed water provides a strong absorption band at 1630  $\text{cm}^{-1}$  due to the bending mode of the OH group of water molecules. The signals from 2250 to 2400  $\text{cm}^{-1}$  could be an artifact of  $\text{CO}_2$ , while those from 2250 to 2000  $\text{cm}^{-1}$  could indicate either the strong intrinsic absorption signal from the diamond ATR (resulting in a lower S/N ratio in this range) or CO during the measurement. The possible adsorption of CO or  $\text{CO}_2$  on nanodiamonds is negligible under the measurement conditions during the FTIR measurement (ambient conditions). Evidence of low degree of functionalization is given by very slight signals observed at 1710, 1255 and 1100  $\text{cm}^{-1}$ . Those signals correspond to oscillations of the stretching vibration mode of C-O in carbonyl and carboxyl groups, the presence of C-O from ester or epoxy groups, and the C-O stretching vibration mode in carbonyl groups, respectively.<sup>10,26-28</sup> The slight signals at 1310 and 1255  $\text{cm}^{-1}$  indicate nitrogen content in nanodiamonds, while the band 2854-2932  $\text{cm}^{-1}$  indicates different CH groups in nanodiamonds.<sup>28</sup> The present FTIR spectrum strongly suggests that water remains trapped within the nanodiamond aggregates even after the thermal treatment at 423 K for 2 h forming intermolecular hydrogen bonding resulted of the interaction of adsorbed water molecules with the neighbor's ones.

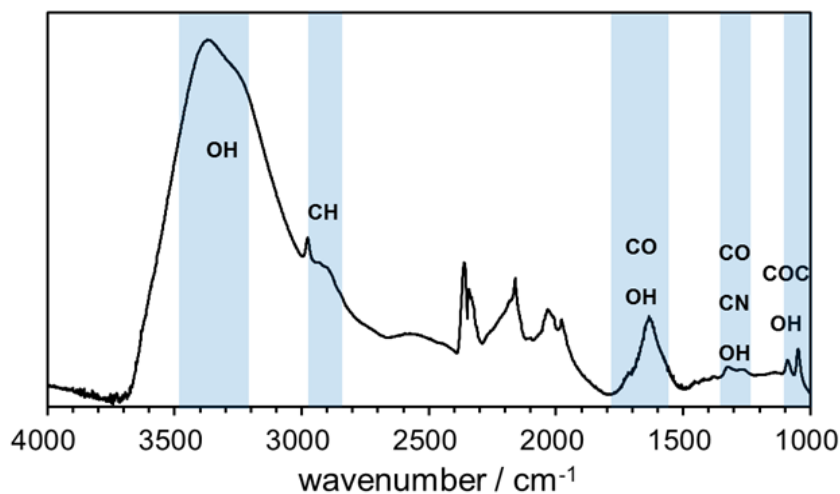


**Figure 4-5.** FTIR spectrum of nanodiamonds heated ex-situ at 423 K for 2 h in *vacuo*. The spectrum was taken at a relative humidity of 20%.

Wide range XPS showed that the major constituent of nanodiamonds was carbon and that the contents of oxygen (O1s) and nitrogen (N1s) were 2.8–4.8% and 0.8–1.0%, respectively. The oxygen detected indicates the presence of surface functional groups, which stems from the purification treatments such as oxidation with acids and bead-milling. This amount of oxygen does not change significantly after the thermal treatments applied in this study. Nitrogen comes from the precursors and the oxygen mainly located at the surface stems from the post-purification treatments; most of the commercial nanodiamonds contain a small fraction of nitrogen of 1–4%.<sup>19,20</sup> The C1s XPS spectra of nanodiamond samples before and after the thermal treatment in *vacuo* together with the deconvoluted spectra are shown in **Figure 4-6**. The higher the heating temperature, the slightly lower the oxygen content.

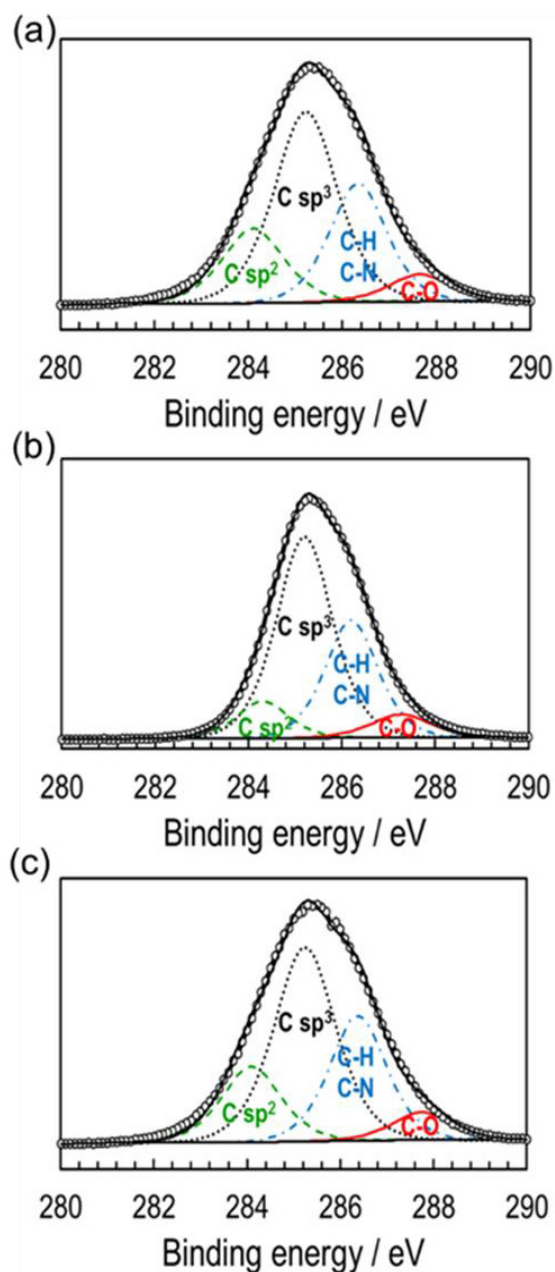


**Figure 4-6.** High-resolution C1s XPS spectra of nanodiamonds (a) non-heated and heated at (b) 423 K and (c) 623 K for 2 h in *vacuo*. Open circles indicate experimental data and straight lines indicates fitted data on deconvolution.

**Table 4-1** shows that the constituents of carbon in at.% of the nanodiamond samples are  $sp^3$ -hybridized carbon of 48%, carbon bonded to hydrogen (and nitrogen) of 26–28%,

sp<sup>2</sup>-hybridized carbon of 18% and 6–7% of carbon bonded to oxygen. The heating at 623 K does not change the content. However, we exposed the sample heated at 623 K to air before the XPS measurement. Nevertheless, we can say that the nanodiamond samples have a low amount of oxygen groups covalently bonded to carbon in nanodiamonds. The oxygen/carbon atomic ratio of nanodiamonds without heat treatment is lower than the reported value,<sup>29</sup> indicating the presence of a slight amount of surface functional groups.

**Table 4-1.** Constituents of C1s (at.%) from XPS analysis of nanodiamonds before and after thermal treatment at different temperatures in *vacuo*.

C1s components	non-treated ND		423 K; 2 h		623 K; 2 h	
	Position	%	Position	%	Position	%
C sp <sup>2</sup>	284.1	18.4	284.1	18.2	284.1	17.9
C sp <sup>3</sup>	285.2	48.0	285.3	46.6	285.2	47.5
C-H, C-N	286.3	26.9	286.4	28.2	286.4	28.1
C-O	287.7	6.7	287.8	6.9	287.8	6.5

Fitting accuracy: > 95%, G-L (60-40), FWHM 1.5 + 0.1 eV

sp<sup>2</sup>/sp<sup>3</sup> ratio: 0.38, 0.39 and 0.38 for non-treated, treated at 423 and 623 K, respectively.

### 4.3.2 Pore structure change of nanodiamond aggregates on heating

**Figure 4-7** shows the nitrogen adsorption isotherms at 77 K of thermally treated nanodiamonds. All adsorption isotherms exhibit the typical Type IV according to the IUPAC classification;<sup>30</sup> considerably large adsorption below  $P/P_0 = 10^{-2}$  from adsorption in micropores, a gradual increase in adsorption above  $P/P_0 = 10^{-2}$  due to both adsorption in large micropores and mesopores and a subsequently pronounced hysteresis loop around  $P/P_0 = 0.5-0.8$  due to typical capillary condensation in mesopores.<sup>31</sup> From **Figure 4-7a** and **Figure 4-7b**, one can observe a notorious increment in the saturated nitrogen

adsorption amount as the heating temperature increases from 423 K to 623 K. **Figure 4-7c** reveals pore size distributions in the range of 1–6 nm together with slight contribution due to ultramicropores. The pore size distribution has a predominant peak at around 4.5 nm. The heating at a higher temperature increases the porosity. Here, the observed increase suggests the pore blocking by strongly bound water molecules of the nanodiamond samples, which will be discussed later in porosity change on pre-adsorption. **Table 4-2** shows the pore structure parameters of nanodiamonds heated at different temperatures by nitrogen adsorption at 77 K. The adsorption amount increases with the heating temperature.

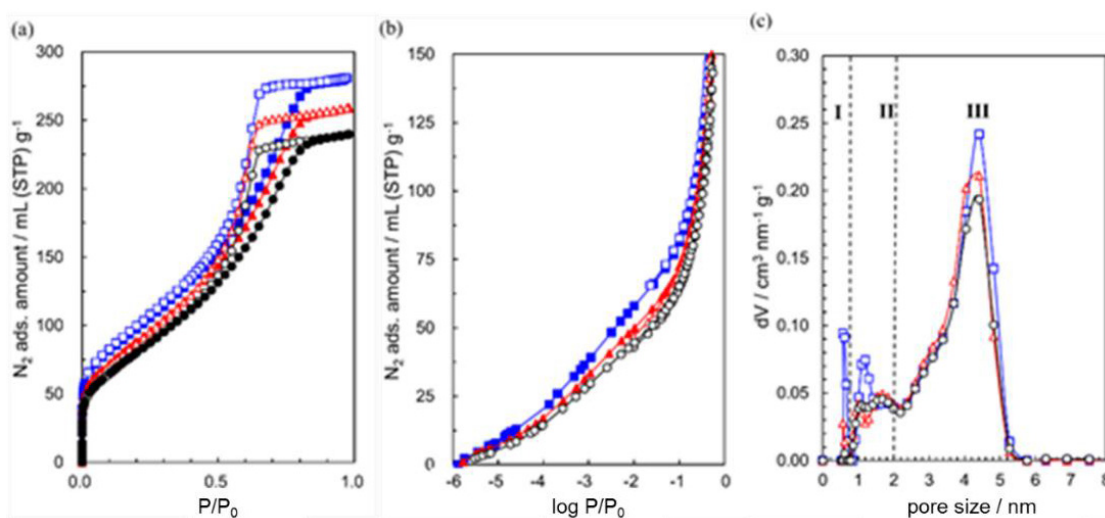


**Figure 4-7.** Nitrogen adsorption isotherms at 77 K in (a) linear scale and (b) logarithmic scale of  $P/P_0$ ; (c) QS-DFT derived-pore size distribution of nanodiamonds thermally treated at 423 K ( $\circ$ ), 523 K ( $\Delta$ ) and 623 K ( $\square$ ) for 2h in *vacuo*. Solid and open symbols indicate adsorption and desorption branches, respectively in Fig. (a) and (b). I, II and III in Fig. (c) correspond to the regions of ultramicropores, supermicropores ( $0.7 \text{ nm} < \text{pore width} < 2 \text{ nm}$ ) and mesopores, respectively.

The values of surface area calculated by  $S_{\text{BET}}$  are about 25% higher than the obtained by  $S_{\text{SPE}}$  of the  $\alpha_s$ -plots. BET method overestimates the surface area since the phenomenon of pore filling and capillary condensation is not adequately represented in the BET equation. The corresponding  $\alpha_s$ -plots are shown in **Figure 4-8**, and the calculated surface areas in **Table 4-3**. We see a gradual increase of total pore volume up to 20% from 423 to 623 K of the heating temperature; the micropore volume increases by 1.8 times.

**Table 4-2.** Pore structure parameters from nitrogen adsorption isotherms at 77 K of nanodiamonds heated at different temperatures.

Heating temperature K	Total pore volume at $P/P_0 = 0.97$ $\text{cm}^3 \text{g}^{-1}$	$S_{\text{BET}}$ $\text{m}^2 \text{g}^{-1}$	$S_{\text{SPE}}$ $\text{m}^2 \text{g}^{-1}$	Micropore volume (DFT) ( $< 2 \text{ nm}$ ) $\text{cm}^3 \text{g}^{-1}$	Mesopore volume (DFT) ( $2-6 \text{ nm}$ ) $\text{cm}^3 \text{g}^{-1}$
423	$0.36 \pm 0.02$	$295 \pm 7$	$235 \pm 5$	$0.04 \pm 0.02$	$0.30 \pm 0.02$
523	$0.39 \pm 0.03$	$317 \pm 20$	$246 \pm 32$	$0.04 \pm 0.02$	$0.33 \pm 0.02$
623	$0.43 \pm 0.02$	$349 \pm 14$	$292 \pm 29$	$0.07 \pm 0.03$	$0.34 \pm 0.02$

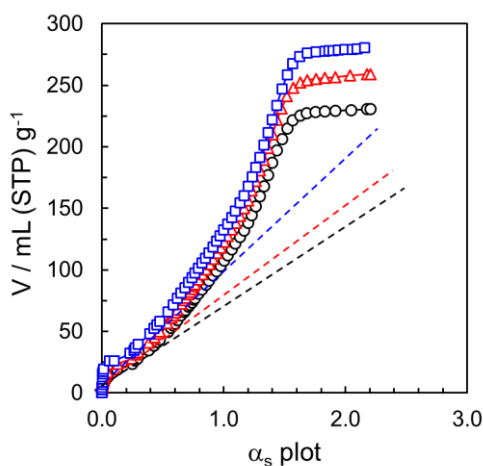


**Figure 4-8.**  $\alpha_s$ -plots of nitrogen adsorption isotherms at 77 K for nanodiamonds thermally treated at 423 ( $\circ$ ), 523 ( $\Delta$ ) and 623 K ( $\square$ ) for 2 h in *vacuo*.

**Table 4-3.** Surface areas calculated from the  $\alpha_s$ -plots of nitrogen adsorption isotherms at 77 K for nanodiamonds thermally treated at 423, 523 and 623 K for 2 h in *vacuo*.

Heating temperature	S <sub>SPE</sub>	Internal area	External area
K	m <sup>2</sup> g <sup>-1</sup>	m <sup>2</sup> g <sup>-1</sup>	m <sup>2</sup> g <sup>-1</sup>
423	231	212	19
523	268	247	22
623	312	285	27

Argon adsorption isotherms at 87 K in **Figure 4-9** show that the increase of the argon adsorption amount with an elevation of the heating temperature is not remarkable compared with nitrogen adsorption.

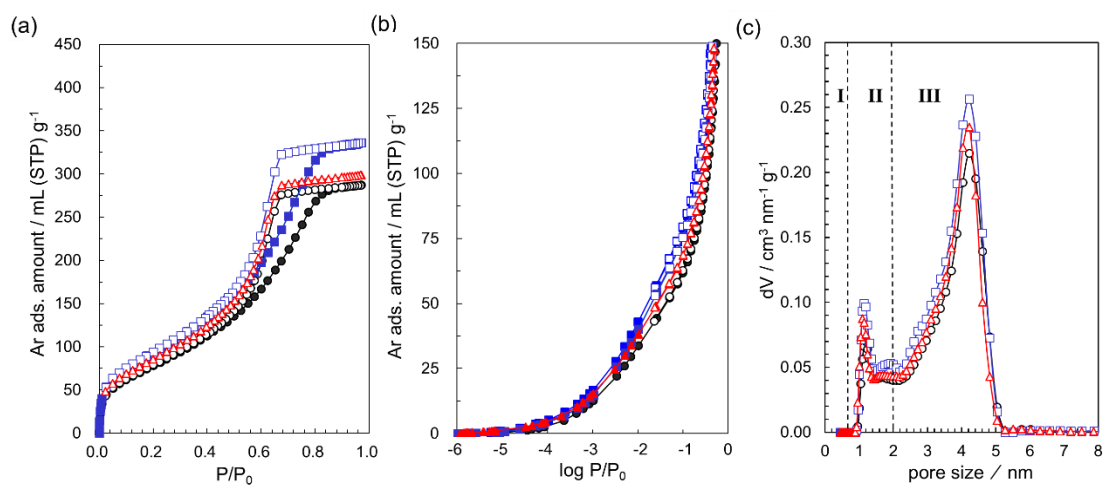


**Figure 4-9.** Argon adsorption isotherms at 87 K in (a) linear scale and (b) logarithmic scale of  $P/P_0$ ; (c) QS-DFT derived-pore size distribution of nanodiamonds thermally treated at 423 K ( $\circ$ ), 523 K ( $\Delta$ ) and 623 K ( $\square$ ) for 2 h in *vacuo*. Solid and open symbols indicate adsorption and desorption branches, respectively in Fig. (a) and (b). I, II and III in Fig. (c) correspond to the regions of ultramicro pores, supermicro pores ( $0.7 \text{ nm} < \text{pore width} < 2 \text{ nm}$ ) and mesopores, respectively.

**Table 4-4** shows the change in pore structure parameters of nanodiamonds with heating temperature from argon adsorption. The corresponding  $\alpha_s$ -plots are shown in **Figure 4-10**, and the calculated surface areas in **Table 4-5**. The heating at 523 K does not increase markedly the porosity, whereas the heating at 623 K gives a large increment of the total porosity by 20%.

**Table 4-4.** Pore structure parameters from argon adsorption isotherms at 87 K of nanodiamonds heated at different temperatures.

Heating temperature K	Total pore volume at $P/P_0 = 0.97$ $\text{cm}^3 \text{g}^{-1}$	$S_{\text{BET}}$ $\text{m}^2 \text{g}^{-1}$	$S_{\text{SPE}}$ $\text{m}^2 \text{g}^{-1}$	Micropore volume (DFT) ( $< 2 \text{ nm}$ ) $\text{cm}^3 \text{g}^{-1}$	Mesopore volume (DFT) ( $2\text{--}6 \text{ nm}$ ) $\text{cm}^3 \text{g}^{-1}$
423	$0.37 \pm 0.02$	$265 \pm 10$	$197 \pm 3$	$0.05 \pm 0.02$	$0.32 \pm 0.02$
523	$0.38 \pm 0.02$	$283 \pm 10$	$218 \pm 3$	$0.05 \pm 0.02$	$0.32 \pm 0.02$
623	$0.43 \pm 0.02$	$318 \pm 12$	$245 \pm 10$	$0.06 \pm 0.02$	$0.37 \pm 0.02$

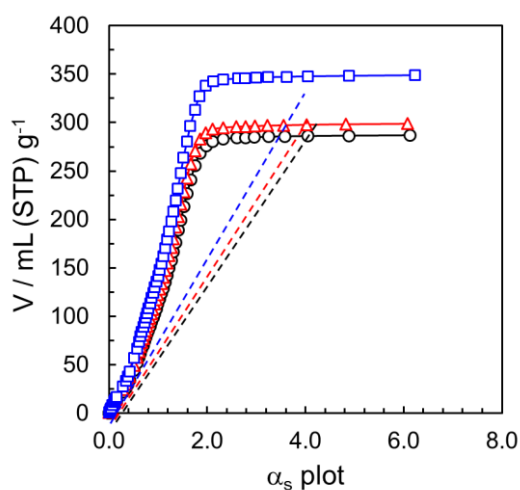


**Figure 4-10.**  $\alpha_s$ -plots of argon adsorption isotherms at 87 K for nanodiamonds thermally treated at 423 K ( $\circ$ ), 523 K ( $\Delta$ ) and 623 K ( $\square$ ) for 2 h in *vacuo*.

**Table 4-5.** Surface areas calculated from the  $\alpha_s$ -plots of argon adsorption isotherms at 87 K for nanodiamonds thermally treated at 423, 523 and 623 K for 2 h in *vacuo*.

Heating temperature K	S <sub>SPE</sub> m <sup>2</sup> g <sup>-1</sup>	Internal area m <sup>2</sup> g <sup>-1</sup>	External area m <sup>2</sup> g <sup>-1</sup>
423	195	193	2
523	218	215	3
623	252	248	3

External surface area refers to the surface of the bulk sample outside the pores, while internal surface area accounts for the surface of all pore walls. **Table 4-3** and **Table 4-5** show that about 90% of the total surface area of nanodiamonds aggregates corresponds to the internal surface area. Therefore, most of the surface area of nanodiamonds derives from the interparticle pores; micropores and small mesopores, rather than from the surface of the bulk sample outside the pores.

A comparison plot of the adsorption isotherms of nanodiamonds heated at 523 and 623 K against that of the nanodiamonds heated at 423 K in **Figure 4-11** gives important information on the pore-blocking effect due to very small microporosity. An upward deviation of the comparison plot indicates the presence of the pores having stronger adsorption sites in the nanodiamonds heated at 523 K or 623 K. The upward deviations below and above 50 mg g<sup>-1</sup> of nitrogen adsorption of nanodiamonds heated at 623 K in **Figure 4-11a** derive from adsorption in micropores and mesopores of larger capacity than in the sample heated at 423 K, respectively, agreeing with the pore size distribution of **Figure 4-7c**. The comparison plot of nanodiamonds heated at 523 K exhibits slight upward deviations similar to those heated at 623 K. Hence, the heating at 623 K can

remove more efficiently the pore blocking effects than the heating at 523 K. **Figure 4-11b** shows linear comparison plots for argon adsorption isotherms, which indicates the small pore-blocking effect even in the nanodiamonds heated at 423 K. Argon adsorption can evaluate more accurately the microporosity of nanodiamonds heated at 423 K than nitrogen adsorption. Accordingly, nanodiamonds heated at 423 K have pore mouth structures where nitrogen is not accessible, but argon is. The FTIR supports the presence of water in nanodiamond aggregates after the heating at 423 K, as shown in **Figure 4-5**.

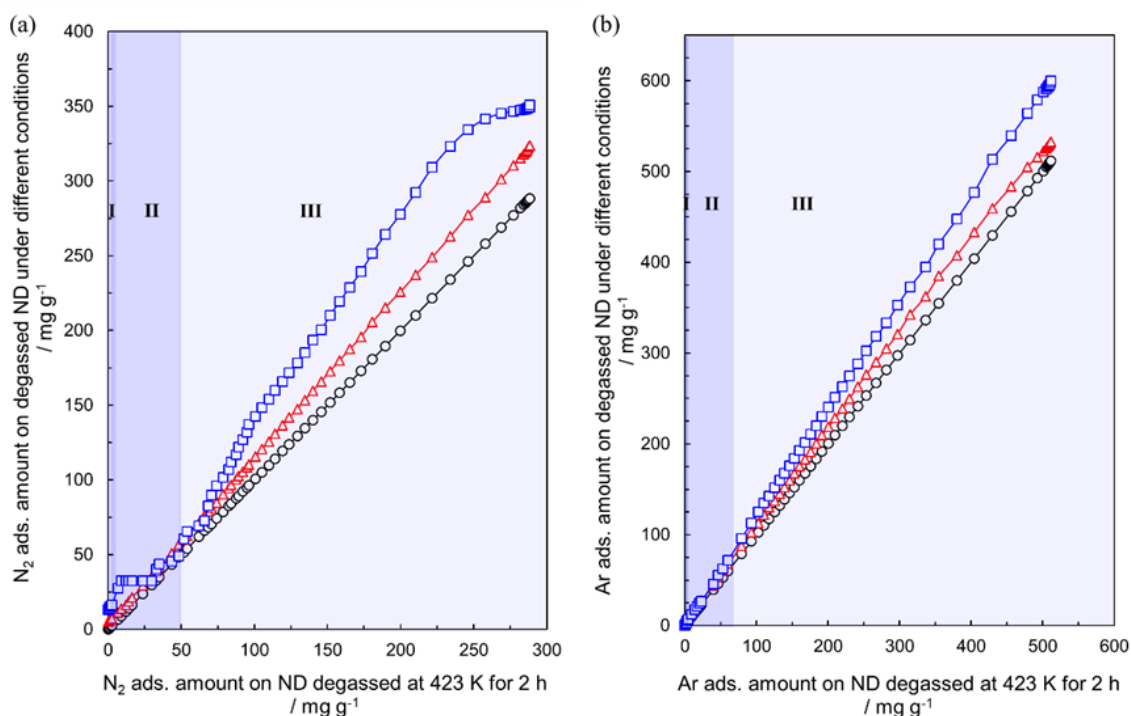


**Figure 4-11.** Comparison plots of (a) nitrogen adsorption isotherms at 77 K and (b) argon adsorption isotherms at 87 K of nanodiamonds thermally treated in *vacuo* at different temperatures: 423 K (○), 523 K (Δ) and 623 K (□) for 2 h in *vacuo*. I: ultramicro-pore range;  $P/P_0: \leq 10^{-2}$ , II: supermicro-pore range;  $P/P_0: \leq 0.05$ , III: mesopore range;  $P/P_0: \geq 0.05$ .

Water molecules strongly adsorbed in the micropores induce an explicit pore-blocking effect; the micropores link with mesopores and thereby the pore blocking free-nanodiamonds heated at 623 K provides larger microporosity and mesoporosity. The pore mouth structures of nanodiamonds heated at 523 K are not sufficiently removed compared with those in nanodiamonds heated at 623 K.

#### **4.3.3 Relationship between water adsorption property and hydrophilic pore mouth structure**

The molecular size of a water molecule is the smallest of the three probe molecules nitrogen, argon and water; their kinetic diameters are 0.36, 0.34 and 0.28 nm, respectively.<sup>12,13,32</sup> Water molecules are preferentially adsorbed on the hydrophilic sites through hydrogen bonding and water adsorption at 298 K has the great advantage of avoiding the pore blocking effect. Accordingly, comparison of water adsorption with adsorption of nitrogen and argon should give essential information on quite narrow porosity such as ultramicroporosity.<sup>33</sup> The water adsorption isotherms of nanodiamonds heated at different temperatures are shown in **Figure 4-12**. The adsorption isotherms of these nanodiamonds are similar to those of hydrophobic nanoporous carbons,<sup>34-37</sup> exhibiting a predominant adsorption hysteresis. The saturated adsorption amount increases with the elevation of the heating temperature (**Figure 4-12a**). The water adsorption isotherm of nanodiamonds has a non-negligible low-pressure adsorption hysteresis below  $P/P_0 = 0.4$ , being different from that of hydrophobic nanoporous carbons (**Figure 4-12b**). The adsorption differences between the adsorption and desorption branches below  $P/P_0 = 0.4$  for nanodiamonds samples heated at 423 K, 523 K, and 623 K are 0.1, 0.4 and 4.0%, respectively. These differences should be associated with

ultramicropores in which even water molecules cannot smoothly access.

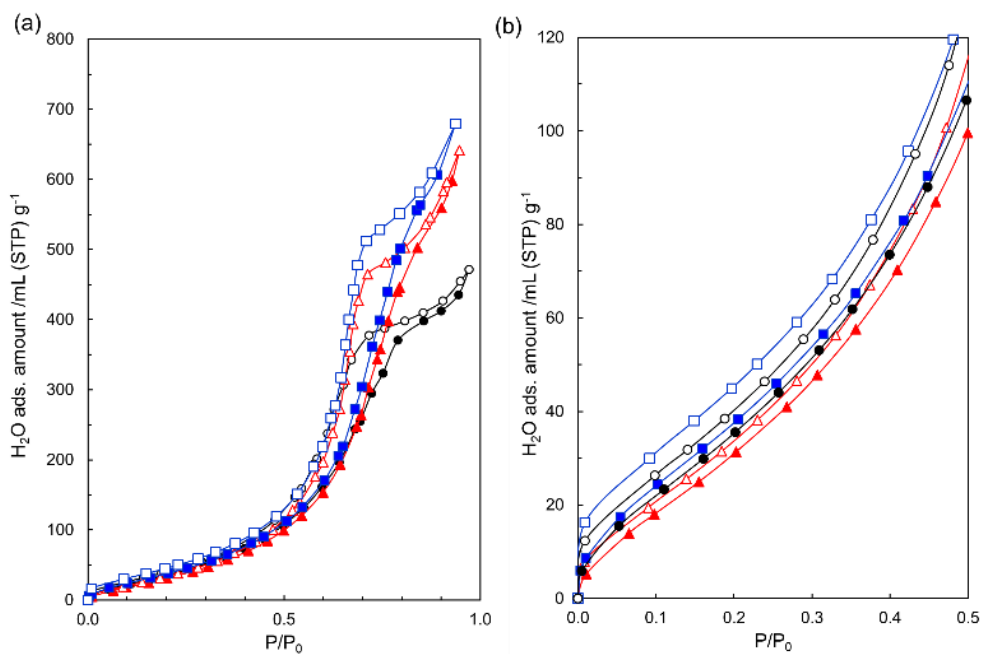


**Figure 4-12.** Water adsorption isotherms at 298 K of nanodiamonds heated at 423 K (○) 523 (△) and 623 K (□) for 2h in *vacuo* in (a) the whole  $P/P_0$  range and (b) the lower  $P/P_0$  range. Solid and open symbols indicate adsorption and desorption branches, respectively.

If we assume that the adsorbed phase in pores is liquid following the Gurvich rule,<sup>30,38</sup> we can compare the filling ratio of different probe molecules. As the steep increase of water adsorption above  $P/P_0 = 0.9$  stems from adsorption on the large mesopores that are covered with water molecules in ultramicropores on the mesopore walls, the plausible saturated water adsorption amount must be determined by the extrapolation of the isotherms in the range of  $P/P_0 = 0.7$ – $0.9$ . The corresponding adsorption isotherms are given in **Figure 4-13**. Thus, we determined the total pore volumes in liquid volume at 298 K for water, assuming the adsorbed water density as  $1 \text{ g cm}^{-3}$ .

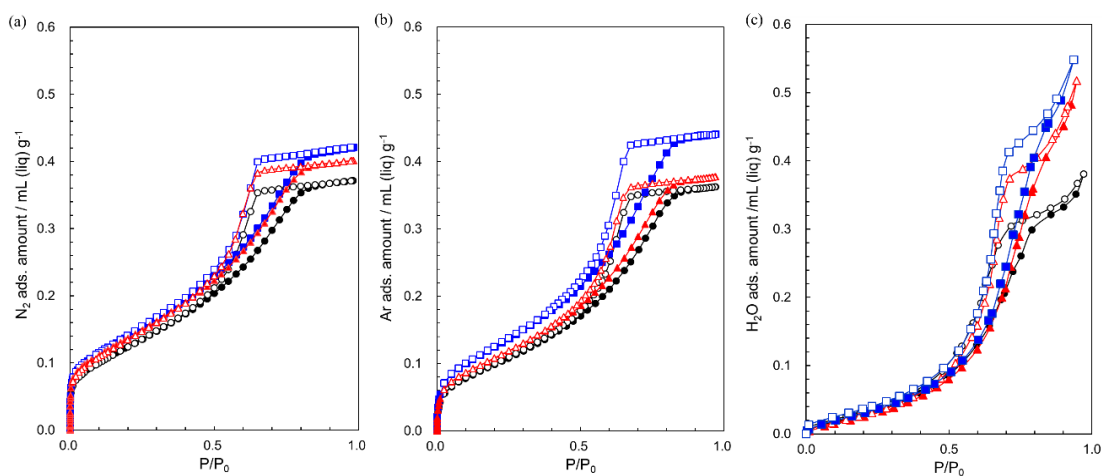


**Figure 4-13.** (a) Nitrogen (b) argon and (c) water adsorption isotherms at 77 K, 87 K and 298 K, respectively for the nanodiamonds thermally treated at 423 K ( $\circ$ ) 523 ( $\Delta$ ) and 623 K ( $\square$ ) for 2 h *in vacuo*. Here the adsorption amount is expressed by liquid volume. Solid and open symbols indicate adsorption and desorption branches, respectively.

**Table 4-6** compares the adsorption capacity of nanodiamonds heated at different temperatures in terms of liquid volume for water, nitrogen and argon. The water uptake is similar to the nitrogen or argon uptake in volume units for the sample heated at 423 K, indicating that heating at 423 K can desorb only weakly adsorbed water and not enough to remove the pore-blocking effect by strongly bound water molecules to the ultramicropores. These ultramicropores still blocked for further adsorption of even small molecules such as water. The adsorbed amount of water under the assumption of liquid state for nanodiamonds heated at 523 and 623 K is larger than the adsorption amounts of nitrogen and argon by about 15% ( $0.06 \text{ mL g}^{-1}$ ) and 24% ( $0.1 \text{ mL g}^{-1}$ ), respectively. Such values of adsorption volumes of water are calculated from the average total pore volumes at  $P/P_0 = 0.97$  for water, nitrogen and argon presented in **Table 4-6**, considering the standard deviation. These porosities of  $0.06 \text{ mL g}^{-1}$  and  $0.1 \text{ mL g}^{-1}$  for nanodiamonds

heated at 523 or 623 K, respectively should originate from small ultramicropores where only water molecules can be strongly adsorbed. Those sites should donate the high hygroscopic nature to the detonation nanodiamonds, which we previously reported.<sup>7</sup>

**Table 4-6.** Total pore volumes (at  $P/P_0 = 0.97$ ) for water, nitrogen and argon of nanodiamonds treated at different temperatures.

Heating temperature K	Water mL (liq.) g <sup>-1</sup>	Nitrogen mL (liq.) g <sup>-1</sup>	Argon mL (liq.) g <sup>-1</sup>
423	0.37 ± 0.03	0.36 ± 0.02	0.37 ± 0.02
523	0.44 ± 0.04	0.39 ± 0.03	0.38 ± 0.02
623	0.54 ± 0.02	0.43 ± 0.02	0.43 ± 0.02

The above results with the comparative analysis using adsorption of nitrogen at 77 K, argon at 87 K, and water at 298 K on nanodiamonds treated at different temperatures clearly evidence the hierarchical pore structure consisting of mesopores, supermicropores (0.7 nm < pore width < 2 nm) and ultramicropores (pore width < 0.7 nm). Here, we determined the pore structure accurately according to the IUPAC recommendation<sup>30</sup> with high-resolution  $\alpha_s$ -plots analysis and the QS-DFT method with the referable information from electron microscopic observation, thermal gravimetry, and X-ray photoelectron microscopy; the structural understanding of the ultramicropores and their role in the water vapor adsorption are firstly evidenced through this study. Preceding literature suggested the relationship between water adsorption and mesopores,<sup>39</sup> and the key role of surface functional groups, that is well-known in water adsorption on various carbon materials.<sup>40,41</sup> In hydrogenated nanodiamonds, the electron accumulation at the hydrogenated nanodiamond-water interface was evidenced to be the reason for hydrophilic nature.<sup>42,43</sup> As to our nanodiamonds are not hydrogenated, the electron accumulation effect must not

be the predominant factor. The present study newly elucidate the essential role of the ultramicropores between the surface graphene and core-diamond in addition to the surface functional group, which our preceding research could not show.<sup>7</sup> **Figure 4-14** shows a graphic representation of the differences in the water, argon and nitrogen adsorption on nanodiamonds. Here, it is clearly seen how water molecules could penetrate the interstices in nanodiamond aggregates giving rise to higher water adsorption.

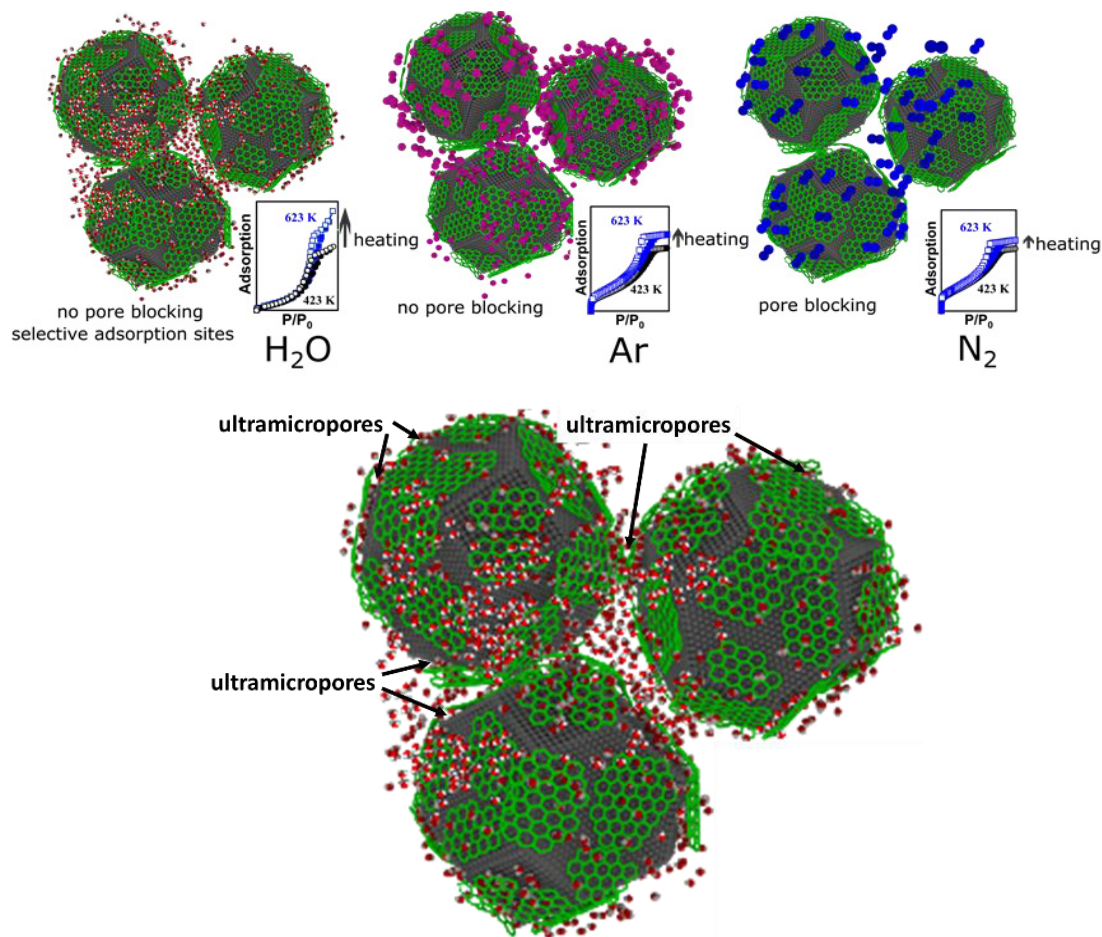


**Figure 4-14.** Adsorptive-dependent pore blocking in nanodiamonds removed by heating in *vacuo* giving rise to higher adsorption of water (above). Nanodiamond aggregate indicating ultramicropores; sites where the adsorption of water molecules is favored (below).

Since other forms of carbon can adsorb water as well, it is important to show a brief comparison. Carbon black is a widely studied material for adsorption, which is different from nanodiamonds. There are nonporous and porous carbon blacks. The pore structure of carbon blacks changes depending on the graphitization. In order to compare the water adsorption between nanodiamonds and carbon black, we must choose a highly graphitized carbon black. Graphitized carbon black cannot adsorb water at least in the low relative pressure range.<sup>44</sup> The structure of nanodiamonds  $sp^3$ -hybridized carbon covered by irregular patches of graphene-like carbon is completely different from that of carbon black with some degree of order in graphite-like crystals. Nanodiamonds present ordered structure (clear lattice structure as observed in the TEM image) and have unique ultramicropore interstices in addition to mesopores. The water adsorption starts even from low relative pressure, being indicative of the marked water affinity of nanodiamonds.

#### **4.4 Conclusions**

This study combined nitrogen, argon and water adsorption for characterization of the pore structure of nanodiamond aggregates and provides valuable information as follows. First, nanodiamond aggregates have pore mouth structure that avoids the smooth access of nitrogen molecules but not of argon and water. Second, thermal treatment at 623 K favored the increment of ultramicroporosity and large microporosity by the removal of the pore blocking by strongly adsorbed water, which induces the hydrophilic nature of nanodiamonds aggregates. Third, the high hygroscopic behavior of nanodiamonds is attributed to water molecules adsorbed in ultramicropores, where only water molecules are accessible. The hydrophilicity due to these strongly bound water molecules in ultramicropores of the nanodiamonds can be used to design a new type of porous carbons

exhibiting hydrophobic to hydrophilic property transformation.

## 4.5 Acknowledgments

Grant-in-Aid- for Scientific Research (B) (17H03039) and OPERA project from JST.

## 4.6 References

- (1) Barnard, A. S.; Sternberg, M. Crystallinity and Surface Electrostatics of Diamond Nanocrystals. *J. Mater. Chem.* **2007**, *17* (45), 4811–4819.
- (2) Barnard, A. S. Self-Assembly in Nanodiamond Agglutinates. *J. Mater. Chem.* **2008**, *18* (34), 4038–4041.
- (3) Ōsawa, E.; Ho, D.; Huang, H.; Korobov, M. V.; Rozhkova, N. N. Consequences of Strong and Diverse Electrostatic Potential Fields on the Surface of Detonation Nanodiamond Particles. *Diam. Relat. Mater.* **2009**, *18* (5–8), 904–909.
- (4) Chang, S. L. Y.; Dwyer, C.; Ōsawa, E.; Barnard, A. S. Size-Dependent Surface Reconstruction in Detonation Nanodiamonds. *Nanoscale Horizons* **2018**, *3* (2), 213–217.
- (5) Ozawa, M.; Inaguma, M.; Takahashi, M.; Kataoka, F.; Krüger, A.; Ōsawa, E. Preparation and Behavior of Brownish, Clear Nanodiamond Colloids. *Adv. Mater.* **2007**, *19* (9), 1201–1206.
- (6) Korobov, M. V.; Avramenko, N. V.; Bogachev, A. G.; Rozhkova, N. N.; Ōsawa, E. Nanophase of Water in Nano-Diamond Gel. *J. Phys. Chem. C* **2007**, *111* (20), 7330–7334.
- (7) Pina-Salazar, E.-Z.; Urita, K.; Hayashi, T.; Futamura, R.; Vallejos-Burgos, F.; Włoch, J.; Kowalczyk, P.; Wiśniewski, M.; Sakai, T.; Moriguchi, I.; Terzyk, A. P.;

- Osawa, E.; Kaneko, K. Water Adsorption Property of Hierarchically Nanoporous Detonation Nanodiamonds. *Langmuir* **2017**, *33* (42), 11180–11188.
- (8) Petit, T.; Yuzawa, H.; Nagasaka, M.; Yamanoi, R.; Ōsawa, E.; Kosugi, N.; Aziz, E. F. Probing Interfacial Water on Nanodiamonds in Colloidal Dispersion. *J. Phys. Chem. Lett.* **2015**, *6* (15), 2909–2912.
- (9) Ji, S.; Jiang, T.; Xu, K.; Li, S. FTIR Study of the Adsorption of Water on Ultradispersed Diamond Powder Surface. *Appl. Surf. Sci.* **1998**, *133* (4), 231–238.
- (10) Jiang, T.; Xu, K. FTIR Study of Ultradispersed Diamond Powder Synthesized by Explosive Detonation. *Carbon*. **1995**, *33* (12), 1663–1671.
- (11) Wang, S.; Morelos-Gómez, A.; Lei, Z.; Terrones, M.; Takeuchi, K.; Sugimoto, W.; Endo, M.; Kaneko, K. Correlation in Structure and Properties of Highly-porous Graphene Monoliths Studied with a Thermal Treatment Method. *Carbon*. **2016**, *96*, 174–183.
- (12) Thommes, M.; Morell, J.; Cychosz, K. A.; Fröba, M. Combining Nitrogen, Argon, and Water Adsorption for Advanced Characterization of Ordered Mesoporous Carbons (CMKs) and Periodic Mesoporous Organosilicas (PMOs). *Langmuir* **2013**, *29* (48), 14893–14902.
- (13) Helmich, M.; Luckas, M.; Pasel, C.; Bathen, D. Characterization of Microporous Activated Carbons Using Molecular Probe Method. *Carbon* **2014**, *74*, 22–31.
- (14) Setoyama, N.; Suzuki, T.; Kaneko, K. Simulation Study on the Relationship between a High-Resolution  $\alpha_s$ -Plot and the Pore Size Distribution for Activated Carbon. *Carbon* **1998**, *36* (10), 1459–1467.
- (15) Neimark, A. V.; Lin, Y.; Ravikovitch, P. I.; Thommes, M. Quenched Solid Density Functional Theory and Pore Size Analysis of Micro-Mesoporous Carbons. *Carbon*

- 2009, 47 (7), 1617–1628.
- (16) Zeiger, M.; Jäckel, N.; Aslan, M.; Weingarh, D.; Presser, V. Understanding Structure and Porosity of Nanodiamond-Derived Carbon Onions. *Carbon* **2015**, 84, 584–598.
- (17) Xie, F. Y.; Xie, W. G.; Gong, L.; Zhang, W. H.; Chen, S. H.; Zhang, Q. Z.; Chen, J. Surface Characterization on Graphitization of Nanodiamond Powder Annealed in Nitrogen Ambient. *Surf. Interface Anal.* **2010**, 42 (9), 1514–1518.
- (18) Sotoma, S.; Akagi, K.; Hosokawa, S.; Igarashi, R.; Tochio, H.; Harada, Y.; Shirakawa, M. Comprehensive and Quantitative Analysis for Controlling the Physical/chemical States and Particle Properties of Nanodiamonds for Biological Applications. *RSC Adv.* **2015**, 5 (18), 13818–13827.
- (19) Post, G.; Dolmatov, V. Y.; Marchukov, V. A.; Sushchev, V. G.; Veretennikova, M. V.; Sal'ko, A. E. Industrial Synthesis of Ultradisperse Detonation Diamonds and Some Fields of Their Use. *Russ. J. Appl. Chem.* **2002**, 75 (5), 755–760.
- (20) Dolmatov, V. Y. Detonation-Synthesis Nanodiamonds: Synthesis, Structure, Properties and Applications. *Russ. Chem. Rev.* **2007**, 76 (4), 339–360.
- (21) Zou, Q.; Wang, M. Z.; Li, Y. G. Analysis of the Nanodiamond Particle Fabricated by Detonation. *J. Exp. Nanosci.* **2010**, 5 (4), 319–328.
- (22) Volkov, D. S.; Proskurnin, M. A.; Korobov, M. V. Elemental Analysis of Nanodiamonds by Inductively-Coupled Plasma Atomic Emission Spectroscopy. *Carbon* **2014**, 74, 1–13.
- (23) Nunn, N.; Torelli, M.; McGuire, G.; Shenderova, O. Nanodiamond: A High Impact Nanomaterial. *Curr. Opin. Solid State Mater. Sci.* **2017**, 21 (1), 1–9.
- (24) Szymański, G. S.; Karpiński, Z.; Biniak, S.; Świątkowski, A. The Effect of the

- Gradual Thermal Decomposition of Surface Oxygen Species on the Chemical and Catalytic Properties of Oxidized Activated Carbon. *Carbon* **2002**, *40* (14), 2627–2639.
- (25) A. Koscheev. Gas Desorption from Detonation Nanodiamonds during Temperature-Programmed Pyrolysis. In *Carbon Nanomaterials for Gas Adsorption*; Terranova, M. L., Orlanducci, S., Rossi, M., Eds.; Singapore, 2012; pp 219–252.
- (26) Shenderova, O.; Panich, A. M.; Moseenkov, S.; Hens, S. C.; Kuznetsov, V.; Vieth, H. M. Hydroxylated Detonation Nanodiamond: FTIR, XPS, and NMR Studies. *J. Phys. Chem. C* **2011**, *115* (39), 19005–19011.
- (27) Dolmatov, V. Y.; Kulakova, I. I.; Myllymäki, V.; Vehanen, A.; Panova, A. N.; Voznyakovskii, A. A. IR Spectra of Detonation Nanodiamonds Modified during the Synthesis. *J. Superhard Mater.* **2014**, *36* (5), 344–357.
- (28) Kovtyukhova, N. I.; Mallouk, T. E.; Pan, L.; Dickey, E. C. Individual Single-Walled Nanotubes and Hydrogels Made by Oxidative Exfoliation of Carbon Nanotube Ropes. *J. Am. Chem. Soc.* **2003**, *125* (32), 9761–9769.
- (29) Baidakova, M.; Vul', A. New Prospects and Frontiers of Nanodiamond Clusters. *J. Phys. D. Appl. Phys.* **2007**, *40* (20), 6300–6311.
- (30) Thommes, M.; Kaneko, K.; Neimark, A. V.; Olivier, J. P.; Rodriguez-Reinoso, F.; Rouquerol, J.; Sing, K. S. W. Physisorption of Gases, with Special Reference to the Evaluation of Surface Area and Pore Size Distribution (IUPAC Technical Report). *Pure Appl. Chem.* **2015**, *87* (9–10), 1051–1069.
- (31) Katsumi, K. Determination of Pore Size and Pore Size Distribution. 1. Adsorbents and Catalysts. *J. Memb. Sci.* **1994**, *96* (1–2), 59–89.

- (32) Wang, S.; Minami, D.; Kaneko, K. Comparative Pore Structure Analysis of Highly Porous Graphene Monoliths Treated at Different Temperatures with Adsorption of N<sub>2</sub> at 77.4 K and of Ar at 87.3 K and 77.4 K. *Microporous Mesoporous Mater.* **2015**, *209*, 72–78.
- (33) Lodewyckx, P. The Effect of Water Uptake in Ultramicropores on the Adsorption of Water Vapour in Activated Carbon. *Carbon* **2010**, *48* (9), 2549–2553.
- (34) Miyawaki, J.; Kanda, T.; Kaneko, K. Hysteresis-Associated Pressure-Shift-Induced Water Adsorption in Carbon Micropores. *Langmuir* **2001**, *17* (3), 664–669.
- (35) Mowla, D.; Do, D. D.; Kaneko, K. Adsorption of Water Vapor on Activated Carbon: A Brief Overview. In *Chemistry and Physics of Carbon*; Radovic, L., Ed.; Dekker: New York, 2003; pp 229–262.
- (36) Pina-Salazar, E. Z.; Kaneko, K. Adsorption of Water Vapor on Mesoporosity-Controlled Single Wall Carbon Nanohorn. *Colloids Interface Sci. Commun.* **2015**, *5*, 8–11.
- (37) Ono, Y.; Futamura, R.; Hattori, Y.; Utsumi, S.; Sakai, T.; Kaneko, K. Isotope Effect on Water Adsorption on Hydrophobic Carbons of Different Nanoporosities. *Carbon* **2017**, *119*, 251–256.
- (38) Rouquerol, J.; Rouquerol, F.; Lley, P.; Maurin, G.; Sing, K. S. W. *Adsorption by Powders and Porous Solids: Principles, Methodology and Applications*, 2nd ed.; Academic Press, 2014.
- (39) Korobov, M. V.; Batuk, M. M.; Avramenko, N. V.; Ivanova, N. I.; Rozhkova, N. N.; Osawa, E. Aggregate Structure Of “single-Nano Buckydiamond” in Gel and Dried Powder by Differential Scanning Calorimetry and Nitrogen Adsorption.

- Diam. Relat. Mater.* **2010**, *19* (5), 665–671.
- (40) Denisov, S. A.; Sokolina, G. A.; Bogatyreva, G. P.; Grankina, T. Y.; Krasil'nikova, O. K.; Plotnikova, E. V; Spitsyn, B. V. Adsorption and Electrical Properties of Nanodiamond Powders in the Presence of Water Vapor. *Prot. Met. Phys. Chem. Surfaces* **2013**, *49* (3), 286–291.
- (41) Petit, T. Interactions with Solvent. In *Nanodiamonds*; Arnault, J.-C., Ed.; Elsevier: Amsterdam, 2017; pp 301–321.
- (42) Petit, T.; Girard, H. A.; Trouvé, A.; Batonneau-Gener, I.; Bergonzo, P.; Arnault, J. C. Surface Transfer Doping Can Mediate Both Colloidal Stability and Self-Assembly of Nanodiamonds. *Nanoscale* **2013**, *5* (19), 8958–8962.
- (43) Petit, T.; Puskar, L.; Dolenko, T.; Choudhury, S.; Ritter, E.; Burikov, S.; Laptinskiy, K.; Brzustowski, Q.; Schade, U.; Yuzawa, H.; Nagasaka, M.; Kosugi, N.; Kurzyp, M.; Venerosy, A.; Girard, H.; Arnault, J. C.; Osawa, E.; Nunn, N.; Shenderova, O.; Aziz, E. F. Unusual Water Hydrogen Bond Network around Hydrogenated Nanodiamonds. *J. Phys. Chem. C* **2017**, *121* (9), 5185–5194.
- (44) Naono, H.; Shimoda, M.; Morita, N.; Hakuman, M.; Nakai, K.; Kondo, S. Interaction of Water Molecules with Nongraphitized and Graphitized Carbon Black Surfaces. *Langmuir* **1997**, *13* (5), 1297–1302.



## Chapter 5

### 5. Anomalous water adsorption behavior of prolonged heated nanodiamonds

**Abstract.** Nanodiamond aggregates have attracted attention as hygroscopic materials. They contain water in the aggregated structure that could be removed by long-time thermal treatments. Removal of water from nanodiamonds must leave a higher amount of available pores for further adsorption of target molecules. Hard-hydrogel of detonation nanodiamonds was thermally treated at 423 K for 2, 10 and 52 h, followed by humidity-controlled exposure (RH = 10, 50 and 96%) in order to determine the mechanism of water pore filling, and the optimum range of humidity for their best sensitivity and water adsorption performance. Long-term heated nanodiamond aggregates agglomerate further decreasing the small porosity available for nitrogen adsorption due to the loss of structural water molecules. However, they have a flexible structure that can be expandable by the adsorption of water molecules.

## 5.1 Introduction

Control of humidity levels is important to assure human comfort and proper state of some equipment, goods, food, and so on. A hygroscopic material can be applied as a humidity controller because it can quickly absorb water. As mentioned before, aggregates of nanodiamonds have the ability of hydration when exposed to humid air and retain moisture.<sup>1,2</sup> Some studies relate this property to the hydrogen bonding due to the electron accumulation at the nanodiamond-water interface in hydrogenated nanodiamonds.<sup>3</sup> Recently, we described the relationship between pore structure of nanodiamonds aggregates and water vapor adsorption. The higher the outgassing of nanodiamonds, the greater ability to adsorb water.<sup>4</sup> Hydrogels of nanodiamond aggregates have a structure of sp<sup>3</sup>-hybridized carbon covered by partially oxidized sp<sup>2</sup>-hybridized carbon, and surrounded by a hydration shell, hierarchical porosity; micropores and mesopores; and high specific area; about 300 m<sup>2</sup> g<sup>-1</sup> when heating at 623 K for 2 h in *vacuo*.<sup>2</sup> Ji *et al.* reported a strong adsorption of water molecules even at a relative humidity (RH) lower than 35%. Water contained in nanodiamonds could be completely removed by long-time thermal treatments; 423 K for 15 h under high *vacuo*<sup>5</sup> or at 473 K under 15 hPa for 10 h for the determination of water contents in single-nano buckydiamond gels;<sup>6</sup> more pores are available for further adsorption of target molecules when water is removed from the samples. Besides, some materials show different performance on the adsorption of humidity depending on the relative humidity of the environment. For example, clays increase the water content when increasing RH, having greater adsorbed amount above 50% RH explained by capillary adsorption in the pore network, while the adsorption at lower RH is mainly due to adsorption on the external surface.<sup>7</sup> Adsorption of water by graphene oxide films show dependence to RH; at low RH, water molecules are primarily

physisorbed onto the available active sites (strong adsorption by double hydrogen bonding to hydrophilic groups or vacancies) of the graphene oxide surface yielding the first-layer of physisorbed water.<sup>8</sup> Adsorption of water on a nanodiamond film was explained by the classical model for adsorption of water on carbons involving only the presence of oxygen-containing surface groups.<sup>9</sup> However, our previous research also linked it to the presence of hydrophilic sites due to the presence of small micropores.<sup>2</sup> Nanodiamonds are suitable for water-diamond related applications due to the potential as hygroscopic materials. Therefore, the need for fundamental studies of water considering the accessibility of adsorption sites, and the interaction strength of the water-nanodiamond surface under a broad range of conditions of RH. In the present study, we report the adsorbed water content on nanodiamonds as a function of RH on different degrees of outgassed nanodiamonds at a mild temperature in order to derive the mechanism of pore filling of water and the optimum range of humidity for their best sensitivity, and water adsorption performance.

## **5.2 Experimental section**

### **5.2.1 Sample preparation**

Nanodiamonds in the form of a hard hydrogel (Nano-Carbon Research Institute, Ltd., Japan) were outgassed at 393 K for 2 h in a *vacuum* oven. Afterward, the sample was separated into several portions to apply different thermal treatments, followed by humidity-controlled tests (see **Figure 5-1**).

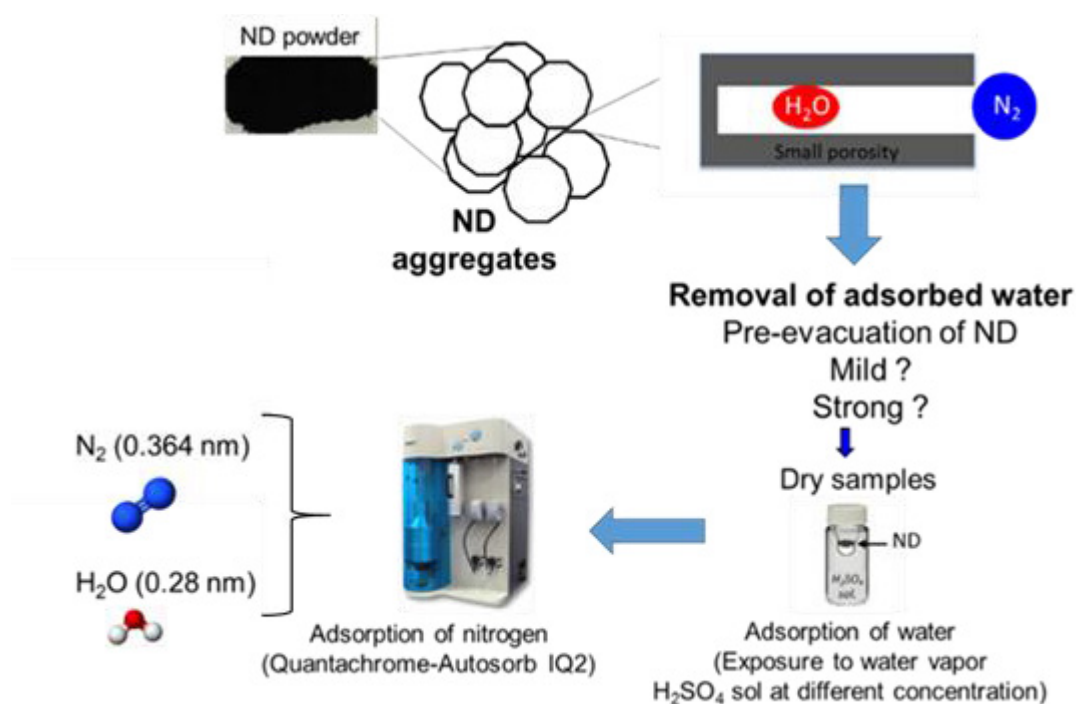


**Figure 5-1.** Experimental set-up for pre-adsorption of water on nanodiamonds.

### 5.2.2 Characterization of nanodiamonds

Thermogravimetric analysis from room temperature to 1000 K of nanodiamonds before and after heating at 423 K for 2 h and 52 h in an Ar atmosphere ( $100 \text{ mL min}^{-1}$ ) was performed by using a Thermal Analysis system STA 7200, Hitachi. XPS analysis was carried out to examine the surface chemistry of nanodiamonds before and after the thermal treatments in *vacuo* by using an AXIS-ULTRA, Kratos equipment with an Al K $\alpha$  X-ray 12 kV source. Heated samples were maintained in *vacuo* without exposure to air prior to the thermogravimetric and XPS analyses. The obtained results were calibrated at  $285 \pm 0.2 \text{ eV}$  corresponding to the  $\text{sp}^3$  carbon of nanodiamond. X-ray diffraction pattern (XRD) of nanodiamonds was measured at room temperature using the X-ray diffractometer (SmartLab X-ray, Rigaku Co.) with a Cu K $\alpha$  (40 kV and 30 mA) source.

### **5.2.3 Porosity change of nanodiamonds on pre-adsorption of water**

Water absorptivity was determined by a controlled humidity test for nanodiamonds outgassed at 423 K in *vacuo* for 2 h and 52 h to remove contained water. Specifically, 25 mg of nanodiamond powder; previously outgassed; was placed inside a glass bottle containing sulfuric acid solutions at a specific concentration to produce controlled RH of 10, 50 or 96%. The bottles at different RH were placed into a water bath at 298 K.<sup>10</sup> After that, the bottles were closed perfectly to allow the exposure of nanodiamonds only to water vapor produced by the H<sub>2</sub>SO<sub>4</sub> solution; without direct wetting by the liquid solution; for one week at room conditions. Afterward, the pore structure of nanodiamonds was evaluated by nitrogen adsorption isotherms at 77 K. The samples of nanodiamonds after outgassing at 423 K for either 2 h or 52 h, and after equilibration of water adsorption were measured in order to evaluate the porosity change on pre-adsorption of water vapor by means of a volumetric apparatus (Quantachrome-Autosorb IQ2). Pore size distributions were determined by Quenched Solid Density Functional Theory (QS-DFT) assuming a slit shape pore geometry model.

### **5.2.4 Water adsorption**

Water adsorption isotherms at 298 K of nanodiamonds outgassed at 423 K for 2 h and 52 h were performed on a VSTAR equipment (Quantachrome).

## **5.3 Results and discussion**

### **5.3.1 Structure and chemistry change of nanodiamond aggregates on heating**

**Figure 5-2** shows the change of mass of nanodiamonds before and after heating at 423 K for 2 h and 52 h and the corresponding change of weight with respect to time. Both plots

clearly show a massive weight loss for non-thermally treated nanodiamonds at a temperature lower than 750 K, which is higher than the weight loss observed for nanodiamonds heated at 423 K. This weight loss is associated with the removal of water contained in non-thermally treated nanodiamonds. The hydrogel of nanodiamonds contains water that could be removed by heating at 473 K for 10 h.<sup>6</sup> Bulk water is desorbed from nanodiamonds at a temperature below 373 K, while surface bonded water is desorbed from 373 K up to 573 K.<sup>11</sup>

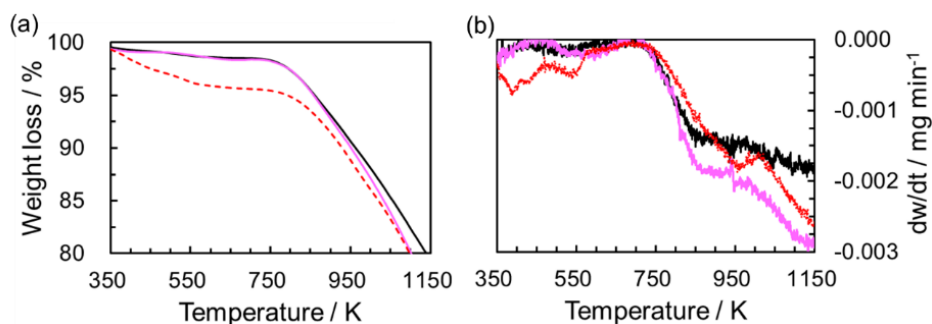


**Figure 5-2.** (a) Thermogravimetric analysis and (b) profile of change of mass respect of time of non-thermally treated nanodiamonds (red line -) and heated nanodiamonds at 423 K for 2 h (dark line -) and 52 h (pink line -) in an inert atmosphere (Ar 100 mL min<sup>-1</sup>).

**Figure 5-3** shows at.% contents of carbon (C1s), oxygen (O1s) and nitrogen (N1s) in the nanodiamonds before thermal treatments and after the shortest and longest time of treatment. As received nanodiamonds are composed of 96.5 at.%, 2.5 at.% and 1.0 at.% of C1s, O1s, and N1s, respectively. Exposure to long-time thermal treatment (52 h at 423 K and 623 K) caused a scarce chemical change, compared with non-heated nanodiamonds. Nanodiamonds samples were maintained in *vacuo* after heating, then, the difference of weight loss observed between non-heated and heated nanodiamonds must be mainly

interpreted as water molecules contained in the nanodiamonds samples that were removed upon heating, as shown in **Figure 5-2**.

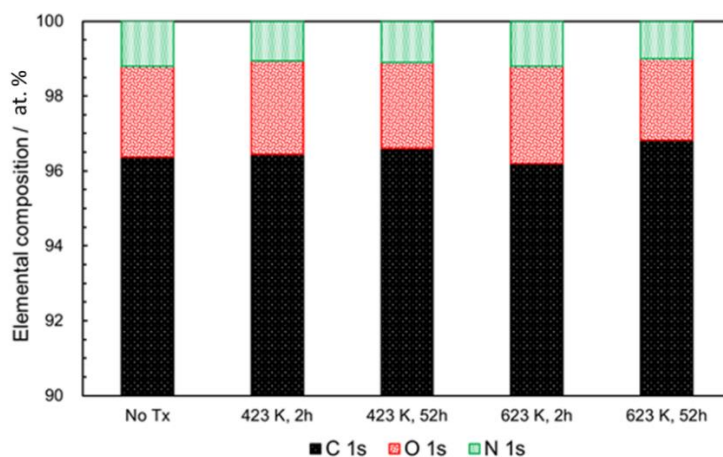


**Figure 5-3.** Atomic contents (at.%) of C 1s, O 1s, and N 1s in non-heated and heated nanodiamonds evaluated by XPS.

**Figure 5-4** shows the results of X-ray analyses of nanodiamonds heated and exposed to different RH. This profile shows signals at  $43.8^\circ$ ,  $75.4^\circ$ , and  $91.5^\circ$  that correspond to the three different facets of the crystallites [111], [220], and [311], respectively.<sup>2,12</sup> The dotted line in **Figure 5-4** points the position of the most prominent facet of nanodiamonds. There is no evident change in the scattering angle of the [111] facet of none of the analyzed samples. The signal about  $23^\circ$  is an experimental artifact resulted from the signal of the glass support used for the measurement (which depends on the sample amount of nanodiamonds used for the measurement) and does not represent a characteristic signal of nanodiamonds. Ordered systems like graphene oxide show a shift of the characteristic graphitic carbon peak to lower scattering angle due to the increment of graphene interlayer spacing when water molecules are intercalated. The higher the humidity the

higher the shifting due to the swelling in the structure.<sup>13</sup> However, we could not observe such feature in the nanodiamonds samples after exposure to RH probably due to the lack of an ordered structure in the nanodiamond aggregates system, even when adsorption of water occurs.

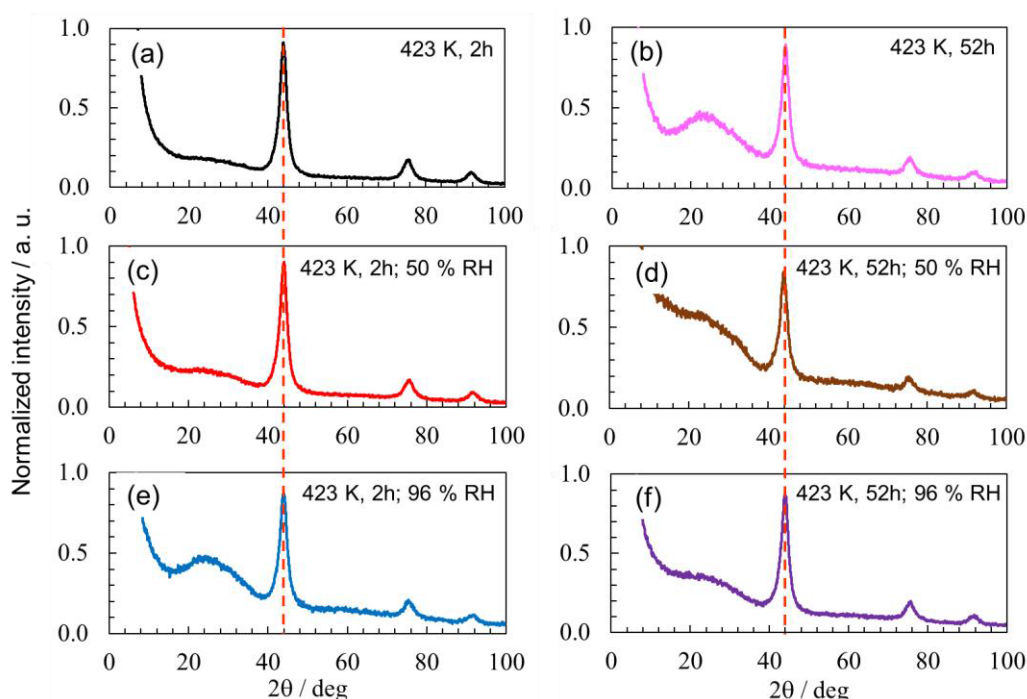


**Figure 5-4.** X-ray profiles of nanodiamonds heated at 423 K for 2 h or 52 h in *vacuo* before and after exposure to 50% RH and 96% RH.

### 5.3.2 Effect of heating time on the pore structure of nanodiamond aggregates

Nitrogen adsorption confers information on pore structure change of thermally treated nanodiamond aggregates. Our previous works demonstrated that nanodiamond aggregates had a few micropores with predominant mesopores of 4.5 nm in average size yielding unblocked ultramicropores after being outgassed at 423 K for 2 h due to the removal of strongly adsorbed water.<sup>2,4</sup> Consequently, nanodiamonds outgassed for a

longer time should present higher pore availability. **Figure 5-5a** shows the nitrogen adsorption isotherms at 77 K of thermally treated nanodiamonds at 423 K for 2 h and 52 h, and the corresponding logarithmic isotherms are presented in **Figure 5-5b**. These typical Type IV adsorption isotherms<sup>14</sup> show considerable adsorption below  $P/P_0 = 10^{-2}$  from adsorption in small micropores, a gradual increase in adsorption above  $P/P_0 = 10^{-2}$  from adsorption in large micropores and mesopores, and a subsequently pronounced hysteresis loop from  $P/P_0 = 0.5$ – $0.8$  due to capillary condensation in mesopores. The average pore size is 4.5 nm in diameter, as seen in **Figure 5-5d**.<sup>15</sup> Surprisingly, one can observe a notorious decrement in the maximum nitrogen adsorption amount as the evacuation time increases from 2 h to 52 h, with a decrease of porosity in all range of pore dimensions ( $< 6$  nm). Heating for 2 h removes water contained in nanodiamonds. Slight compaction of micropore pore occurs when more water is removed; visualized by lower adsorption of nitrogen; as the heating time increases to 10 h. Adsorption of nitrogen is even lower when the heating time is longer (52 h) due to the agglomeration of nanodiamonds, leaving inaccessible pores for adsorption of nitrogen molecules. This decrease of porosity by long-time thermal treatment originates from an aging effect of the aggregated structure of nanodiamonds; the open structure resulted by the removal of blocking molecules is not stable, due to the loss of water structural molecules, transforming the closing structure on long-time aging. Removal of the water solvate shells produces incoherent interfacial Coulombic aggregates resulting in harder gels.<sup>6,16,17</sup> **Figure 5-5c** shows linear water adsorption isotherms at 298 K. It is clearly visualized different frames of the adsorption hysteresis loop of nanodiamond samples, suggesting that water molecules are adsorbed by a different mechanism. Here, water is adsorbed and desorbed easier on nanodiamonds heated at 423 K for 2 h than on that heated for 52 h

where water molecules penetrate to small pores and adsorb strongly but do not desorb easily. Water is greatly adsorbed in nanodiamonds heated at 423 K for 52 h; nanodiamond aggregates previously compacted by outgassing are swollen by the adsorption of water separating the nanodiamond particles.

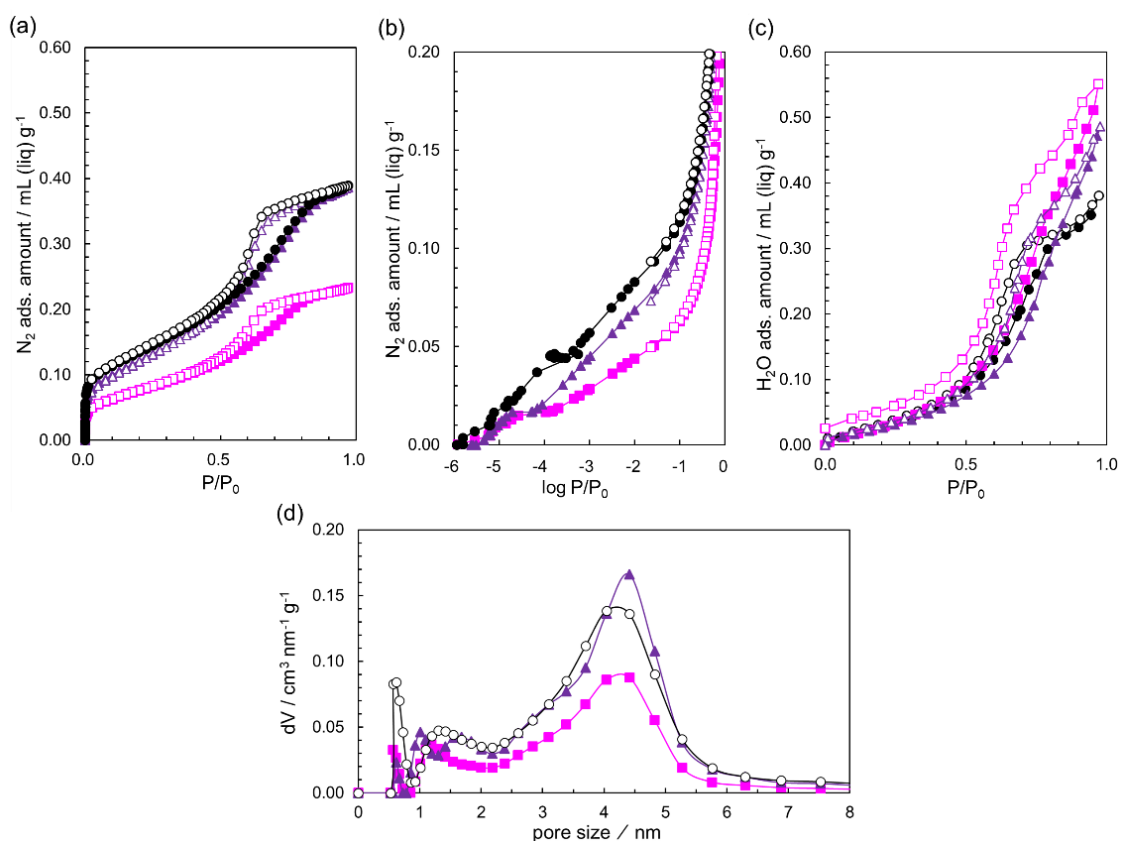


**Figure 5-5.** Adsorption isotherms of nitrogen at 77 K in (a) linear scale and (b) logarithmic scale. (c) Adsorption isotherm of water at 298 K. (d) QS-DFT derived pore size distribution (from nitrogen adsorption) of nanodiamonds thermally treated in *vacuo* at 423 K for 2 h (○), 10 h (△) and 52 h (□). In (a), (b) and (c) solid and open symbols indicate adsorption and desorption branches, respectively.

Argon adsorption at 87 K in **Figure 5-6** does not show a significant difference between the heating at 423 h for 2 h, 10 h, and 52 h.

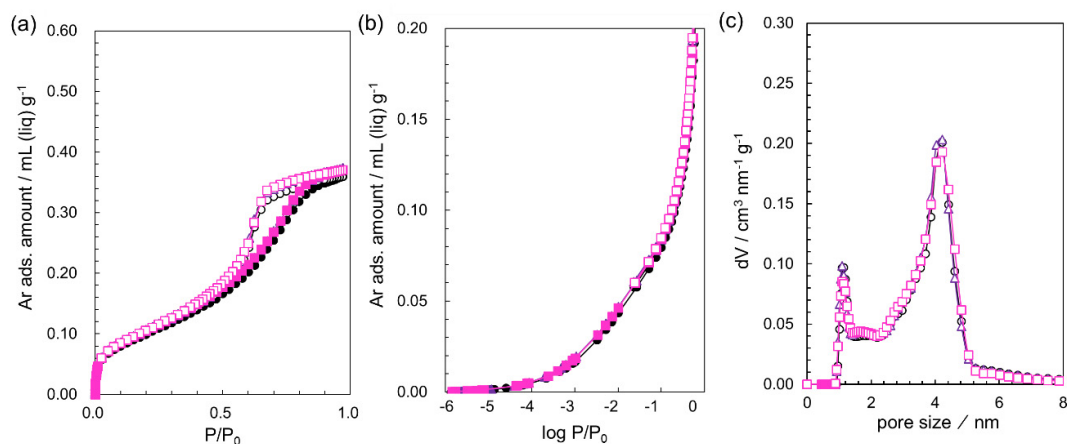


**Figure 5-6.** Adsorption isotherms of argon at 77 K in (a) linear scale and (b) logarithmic scale. (c) QS-DFT derived pore size distribution of nanodiamonds thermally treated in *vacuo* at 423 K for 2 h (○), 10 h (△) and 52 h (□). In (a) and (b) solid and open symbols indicate adsorption and desorption branches, respectively.

Nitrogen and water adsorption isotherms of nanodiamonds heated at 623 K at 2 h, 10 h, and 52 h (see **Figure 5-7**) result in a similar tendency that the treatments at 423 K. Nitrogen uptake decreased progressively with the heating time due to the removal of water molecules adsorbed on the nanodiamonds. However, there are special features in the water adsorption isotherm of nanodiamonds heated at 423 K for 52 h but not at 623 K for the same time; a hysteresis loop that keeps open even at low relative pressure and the rise of water adsorption from lower relative pressure. Besides, XPS results of nanodiamonds heated at 623 K for 2 h and 52 h show a slightly higher decrease in the oxygen content of nanodiamonds when heating for a long time due to the higher heating

temperature, an also compared to heating at 423 K, as shown in **Figure 5-7**. However, this difference still must be considered non-significant due to its low degree. Consequently, a more detailed analysis of nanodiamonds heated at 423 K is necessary due to the exclusive anomalous water adsorption behavior. As water adsorption behavior of heated nanodiamonds is quite different from adsorption of nitrogen, we need key information on water adsorption, which can be obtained from nitrogen adsorption isotherms on nanodiamonds with water adsorbed at a different pressure.

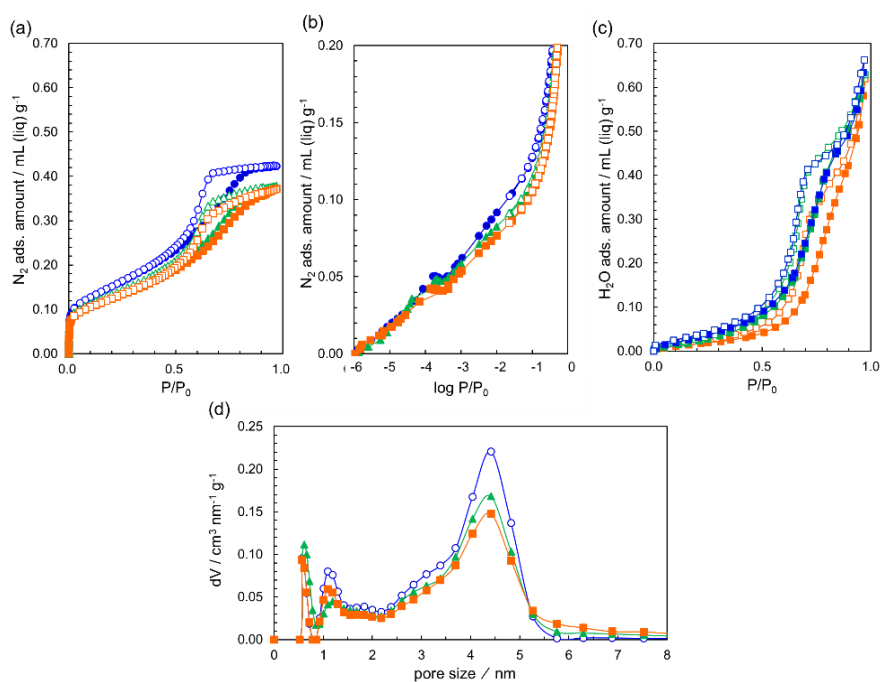


**Figure 5-7.** Adsorption isotherms of nitrogen at 77 K in (a) linear scale and (b) logarithmic scale. (c) Adsorption isotherm of water at 298 K. (d) QS-DFT derived pore size distribution (from nitrogen adsorption) of nanodiamonds thermally treated in *vacuo* at 623 K for 2h ( $\circ$ ), 10 h ( $\Delta$ ) and 52 h ( $\square$ ). In (a), (b) and (c) solid and open symbols indicate adsorption and desorption branches, respectively.

**Figure 5-8** shows nitrogen adsorption isotherms at 77 K of nanodiamonds after exposure to different % RH. **Table 5-1** shows the porosity analysis derived from nitrogen adsorption isotherms of samples outgassed at 423 K for 2 and 52 h followed by exposure to different RH, as presented in **Figure 5-8**. The total pore volume accessible for nitrogen adsorption decreases as the RH increases from 10 to 96%. This tendency is followed for the micropore and mesopore volume as well. Results from the controlled humidity test shown in **Figure 5-8** and **Table 5-1** confirm the high hygroscopic property of nanodiamond aggregates, aside from allowing the finer porosity analysis discussed earlier.

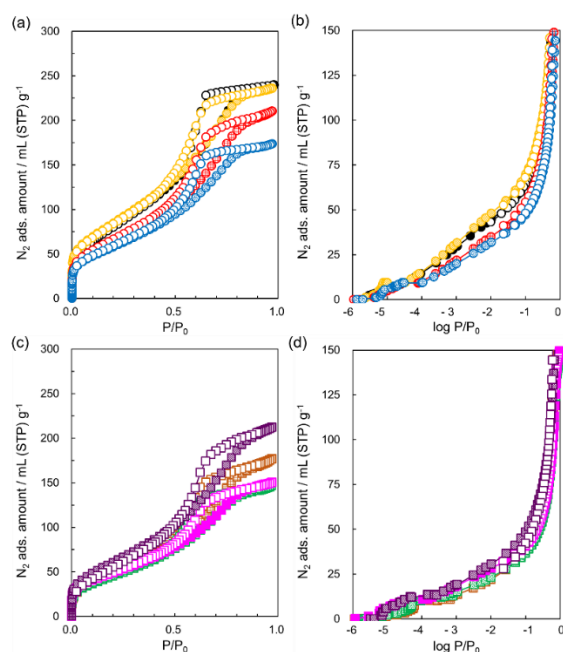


**Figure 5-8.** Nitrogen adsorption isotherms at 77 K of nanodiamonds after exposure to different % RH. Nanodiamonds (a, b) heated at 423 K for 2 h in *vacuo* ( $\circ$ ), exposed to 10% RH ( $\odot$ ), 50% RH ( $\ominus$ ) and 96% RH ( $\circ$ ) and (c, d) heated at 423 K for 52 h in *vacuo* ( $\square$ ), exposed to 10% RH ( $\square$ ), 50% RH ( $\square$ ) and 96% RH ( $\square$ ). Plots in (a) and (c) show linear scale, and (b) and (d) logarithmic scale. Solid and open symbols indicate adsorption and desorption branches, respectively.

**Table 5-1.** Porosity of nanodiamonds exposed to different levels of % RH after thermal treatment in *vacuo* at 423 K for 2 h and 52 h.

Temperature, time	Relative humidity (RH)	Total pore volume at $P/P_0 = 0.97$	Micropore volume (DFT) ( $< 2$ nm)	Mesopore volume (DFT) (2-6 nm)
K, h	%	$\text{cm}^3 \text{g}^{-1}$	$\text{cm}^3 \text{g}^{-1}$	$\text{cm}^3 \text{g}^{-1}$
423, 2	0	0.37	0.06	0.31
	10	0.36	0.06	0.30
	50	0.32	0.04	0.27
	96	0.27	0.04	0.22
423, 52	0	0.23	0.03	0.19
	10	0.35	0.02	0.32
	50	0.28	0.03	0.24
	96	0.23	0.03	0.19

**Figure 5-9** shows the profiles of water adsorptivity of nanodiamonds exposed to different levels of humidity after heating at 423 K for 2 h and 52 h. Those plots are obtained by subtracting the pore size distributions from nitrogen adsorption isotherms of samples exposed to humidity after heating to the corresponding heated samples prior to humidity exposure, used as a reference. Therefore, we can differentiate the volume of pores firstly occupied by water and the remained for nitrogen adsorption. Heating at 423 K for 2 h in *vacuo* evacuated a low amount of micropores and mesopores, while heating at 423 K for 52 h unblocked even pores of small dimensions ( $< 0.7$  nm); ultramicropores are accessible for water adsorption.<sup>18</sup> Mesopores mainly adsorb water at 10% RH when nanodiamonds are mildly heated in *vacuo*. Micropores are filled more remarkably as RH increases to 50%. Adsorption of water is greater at higher RH than at lower RH, especially

for nanodiamonds heated at 423 K for 2 h. Straight exposure to high RH (96%) of nanodiamonds heated at 423 K for 52 h results in lower total water adsorption. Nevertheless, the adsorbed water molecules have a greater affinity for ultramicropores compared to a shorter heating time at the same temperature.

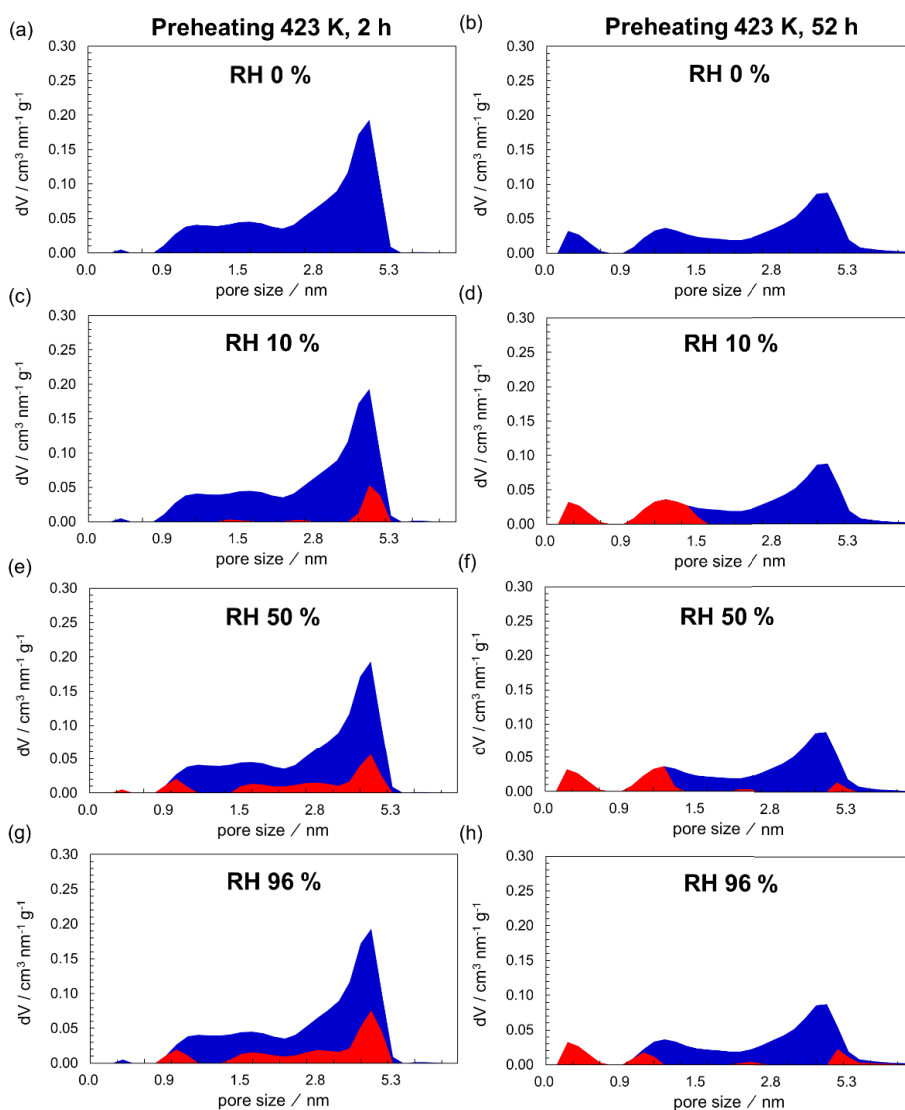


**Figure 5-9.** Profiles of water adsorptivity of nanodiamonds exposed to different levels of humidity after heating at 423 K for 2 h (a, c, e, g) and 52 h (b, d, f, h). Colors ● and ● indicate water and nitrogen adsorbed, respectively.

Heating nanodiamonds in *vacuo* for a short time at mild temperature promotes adsorption of water in micropores and mesopores. Higher volume of mesopores of 2 – 6 nm is filled as the humidity increases from 10 to 96%. However, heating nanodiamonds at the same temperature (423 K) but for a longer time (52 h compared to 2 h) promotes the adsorption of water from ultramicropores, which were unblocked of contained water molecules due to the prolonged heating. A more detailed analysis of the sites for adsorption of water is presented in **Figure 5-10**. The higher percentage of water adsorption amount comes from mesopores, which holds more volume of adsorbed water, and adsorption on ultramicropores is marked at longer heating of nanodiamonds.

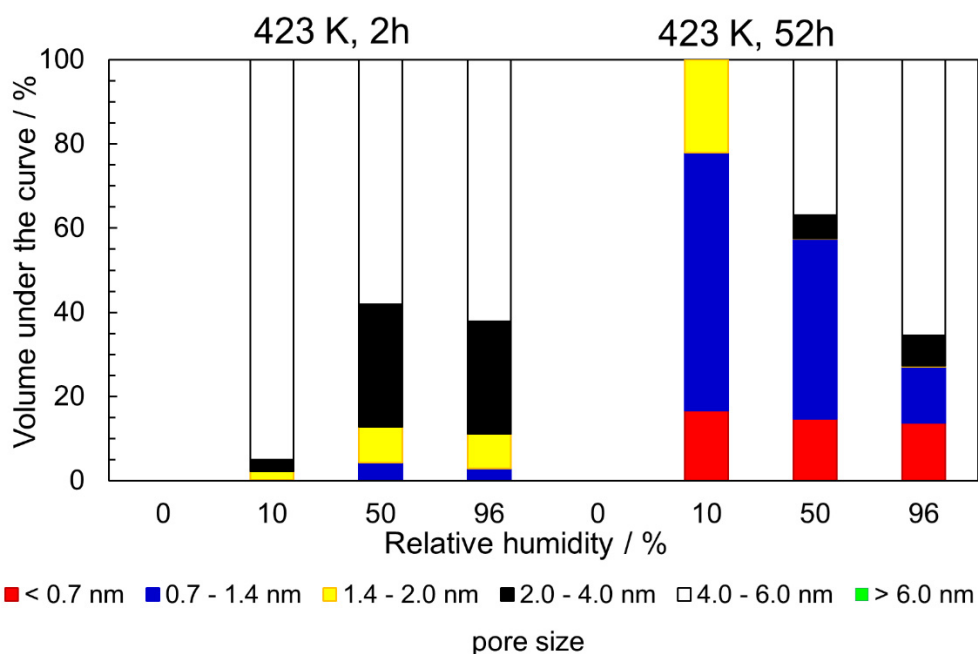


**Figure 5-10.** Normalized distributions of adsorbed water on nanodiamond pores of different dimensions evaluated from the absorptivity test at a controlled humidity of nanodiamonds after heating at 423 K for (a) 2 h, and (b) 52 h with further exposure to 10%, 50% and 96% RH.

A long-time treatment at mild temperature (423 K for 52 h) enhances the adsorption of water from ultramicropores at low relative humidity (10% RH) with consequent adsorption on supermicropores and micropores. As the relative humidity increases, water molecules start to adsorb on small mesopores and finally larger mesopores hold adsorbed water molecules. Water molecules are strongly adsorbed on ultramicropores that play the role of hydrophilic sites, and subsequent adsorption of water molecules on nanodiamonds reaches the equilibrium to give the total water adsorption amount.

## 5.4 Conclusions

Water is adsorbed on hydrophilic sites of nanodiamonds. Long exposure to thermal treatment results in the agglomeration of nanodiamond particles leaving lesser pores accessible for nitrogen uptake. However, water molecules can re-open the nanodiamond aggregate yielding significant water adsorption. Therefore, one can assume that prolonged heated nanodiamonds present a flexible structure that can be expandable by the adsorption of water molecules. Mild heating in *vacuo* cannot unblock the ultramicropores in the nanodiamond assembly. As a result, the filling of pores starts from supermicropores and continues on to mesopores as RH increases yielding higher water adsorption at higher relative humidity. On the contrary, long term-heated nanodiamond exposed to low RH provides significant water adsorption from ultramicropores, which still are accessible for adsorption of water molecules even after the conglomeration of nanodiamond particles due to the prior water removal by excessive heating time. As humidity increases, mesopores becomes important for adsorption of water.

## 5.5 Acknowledgments

The work was partially supported by Grant-in-Aid- for Scientific Research (B) (17H03039) and the Center of Innovation Program, “Global Aqua Innovation Center for Improving Living Standard and Water Sustainability” of the Japan Science and Technology Agency, JST.

## 5.6 References

- (1) Jiang, T.; Xu, K. FTIR Study of Ultradispersed Diamond Powder Synthesized by Explosive Detonation. *Carbon* **1995**, *33* (12), 1663–1671.
- (2) Pina-Salazar, E.-Z.; Urita, K.; Hayashi, T.; Futamura, R.; Vallejos-Burgos, F.; Włoch, J.; Kowalczyk, P.; Wiśniewski, M.; Sakai, T.; Moriguchi, I.; Terzyk, A. P.; Osawa, E.; Kaneko, K. Water Adsorption Property of Hierarchically Nanoporous Detonation Nanodiamonds. *Langmuir* **2017**, *33* (42), 11180–11188.
- (3) Petit, T.; Girard, H. A.; Trouvé, A.; Batonneau-Gener, I.; Bergonzo, P.; Arnault, J. C. Surface Transfer Doping Can Mediate Both Colloidal Stability and Self-Assembly of Nanodiamonds. *Nanoscale* **2013**, *5* (19), 8958–8962.
- (4) Piña-Salazar, E.-Z.; Kukobat, R.; Futamura, R.; Hayashi, T.; Sakai, T.; Ōsawa, E.; Kaneko, K. Water-Selective Adsorption Sites on Detonation Nanodiamonds. *Carbon* **2018**, *139*, 853–860.
- (5) Ji, S.; Jiang, T.; Xu, K.; Li, S. FTIR Study of the Adsorption of Water on Ultradispersed Diamond Powder Surface. *Appl. Surf. Sci.* **1998**, *133* (4), 231–238.
- (6) Osawa, E. Chemistry of Single-Nano Diamond Particles. In *Chemistry of Nanocarbons*; Akasaka, T., Wudl, F., Nagase, S., Eds.; John Wiley & Sons, Ltd.: United Kingdom, 2010; pp 413–432.

- (7) Hatch, C. D.; Wiese, J. S.; Crane, C. C.; Harris, K. J.; Kloss, H. G.; Baltrusaitis, J. Water Adsorption on Clay Minerals as a Function of Relative Humidity: Application of BET and Freundlich Adsorption Models. *Langmuir* **2012**, *28* (3), 1790–1803.
- (8) Bi, H.; Yin, K.; Xie, X.; Ji, J.; Wan, S.; Sun, L.; Terrones, M.; Dresselhaus, M. S. Ultrahigh Humidity Sensitivity of Graphene Oxide. *Sci. Rep.* **2013**, *3* (5 V), 1–7.
- (9) Yao, Y.; Chen, X.; Ma, W.; Ling, W. Quartz Crystal Microbalance Humidity Sensors Based on Nanodiamond Sensing Films. *IEEE Trans. Nanotechnol.* **2014**, *13* (2), 386–393.
- (10) Wilson, R. E. Humidity Control by Means of Sulfuric Acid Solutions, with Critical Compilation of Vapor Pressure Data. *J. Ind. Eng. Chem.* **1921**, *13* (4), 326–331.
- (11) Stehlik, S.; Glatzel, T.; Pichot, V.; Pawlak, R.; Meyer, E.; Spitzer, D.; Rezek, B. Water Interaction with Hydrogenated and Oxidized Detonation Nanodiamonds - Microscopic and Spectroscopic Analyses. *Diam. Relat. Mater.* **2016**, *63*, 97–102.
- (12) Shenderova, O. A.; Vlasov, I. I.; Turner, S.; Van Tendeloo, G.; Orlinskii, S. B.; Shiryayev, A. A.; Khomich, A. A.; Sulyanov, S. N.; Jelezko, F.; Wrachtrup, J. Nitrogen Control in Nanodiamond Produced by Detonation Shock-Wave-Assisted Synthesis. *J. Phys. Chem. C* **2011**, *115* (29), 14014–14024.
- (13) Abraham, J.; Vasu, K. S.; Williams, C. D.; Gopinadhan, K.; Su, Y.; Cherian, C. T.; Dix, J.; Prestat, E.; Haigh, S. J.; Grigorieva, I. V.; Carbone, P.; Geim, A. K.; Nair, R. R. Tunable Sieving of Ions Using Graphene Oxide Membranes. *Nat. Nanotechnol.* **2017**, *12* (6), 546–550.
- (14) Thommes, M.; Kaneko, K.; Neimark, A. V.; Olivier, J. P.; Rodriguez-Reinoso, F.; Rouquerol, J.; Sing, K. S. W. Physisorption of Gases, with Special Reference to

- the Evaluation of Surface Area and Pore Size Distribution (IUPAC Technical Report). *Pure Appl. Chem.* **2015**, *87* (9–10), 1051–1069.
- (15) Katsumi, K. Determination of Pore Size and Pore Size Distribution. 1. Adsorbents and Catalysts. *J. Memb. Sci.* **1994**, *96* (1–2), 59–89.
- (16) Ozawa, M.; Inaguma, M.; Takahashi, M.; Kataoka, F.; Krüger, A.; Ōsawa, E. Preparation and Behavior of Brownish, Clear Nanodiamond Colloids. *Adv. Mater.* **2007**, *19* (9), 1201–1206.
- (17) Ōsawa, E.; Ho, D.; Huang, H.; Korobov, M. V.; Rozhkova, N. N. Consequences of Strong and Diverse Electrostatic Potential Fields on the Surface of Detonation Nanodiamond Particles. *Diam. Relat. Mater.* **2009**, *18* (5–8), 904–909.
- (18) Pina-Salazar, E. Z.; Kaneko, K. Adsorption of Water Vapor on Mesoporosity-Controlled Single Wall Carbon Nanohorn. *Colloids Interface Sci. Commun.* **2015**, *5*, 8–11.

## Chapter 6

### 6. Unusual hygroscopic nature of nanodiamonds in comparison with well-known porous materials<sup>1</sup>

**Abstract.** Nanodiamond aggregates have interparticle pores of 4.5 nm on average, exhibiting porous nature involved in their water storage. This work studies the hygroscopic nature of porous nanodiamond aggregates by water absorption based on liquid water droplets. Nanodiamond aggregates show hydrophobicity from the water vapor adsorption. Surprisingly, porous nanodiamond aggregates quickly absorb water droplets at the bulk scale. The volume of absorbed liquid water is comparable to that of the water-absorbing clay Montmorillonite and higher than those of zeolites ZSM-5 and molecular sieve 5A. This hygroscopic nature of nanodiamonds is ascribed to the micro- and mesoporous structure of their aggregates and the special core-shell structure of each nanodiamond particle (wrapped by graphene-like carbon). The absorption rate of liquid water in the porous nanodiamonds is influenced by the surface wettability, while the hygroscopic capacity depends mainly on the hierarchical porosity.

---

<sup>1</sup> Adapted from Piña-Salazar, E. Z. *et al.* (2019). Unusual hygroscopic nature of nanodiamonds in comparison with well-known porous materials. *J. Colloid Interface Sci.* 549, 133–139.

Copyright © 2019, with permission from Elsevier.

## 6.1 Introduction

The world has increasing demands for advanced materials in water sensing from the viewpoints of water resources and medical applications. In particular, porous nanodiamonds can exhibit high electrical and thermal conductivity and are promising as high-performance water sensors due to the changes in the electrical conductivity of nanodiamonds with pre-adsorbed water when applying a thermal treatment.<sup>1</sup> Consequently, we need to clarify the origin and extent of the hygroscopic nature of nanodiamonds. A hygroscopic material has the ability to absorb water from a humid environment. Some porous materials capture liquid water in their structures depending on their hydrophilic nature, texture and hierarchical particle structure. Nanodiamonds are polyhedral particles of  $sp^3$ -hybridized carbon, wrapped by  $sp^2$ -hybridized carbon of different nature such as graphene-like, graphitic and amorphous carbon.<sup>2-6</sup> Aggregation of nanodiamond particles gives rise to pores in the order of mesopores and micropores.<sup>7-9</sup> Interaction and reactivity of nanodiamonds with water plays a significant role in the manufacture or design of new devices such as stable electrodes or biological sensors, water-absorbent materials or in their applications in fields such as biomedicine.<sup>10,11</sup> Water wettability of nanocrystalline diamond films on Si substrate in terms of the air-water contact angle (WCA) at ambient conditions is  $73 \pm 3^\circ$ , being close to the contact angles  $76 \pm 5^\circ$  and  $71 \pm 3^\circ$  of the 111 and 110 faces of diamond, respectively; while CVD nanodiamonds have a larger contact angle of  $93 \pm 2^\circ$ .<sup>12</sup> Notwithstanding the relevance of determining the wettability of nanodiamonds, their powder sample induces difficulty in the contact angle measurement due to porosity and surface roughness, which influence the wettability.<sup>13</sup> As the wettability is a key factor for the hygroscopic nature of solid materials, we need to obtain a comparative measure of the wettability of powdered

nanodiamond samples. Hydrophilic porous materials such as silica gel, zeolites, and clays have the ability to absorb water.<sup>14-16</sup> Some hydrophobic porous carbon aerogels and non-oxidized graphitic materials adsorb water vapor under a high relative pressure region ( $P/P_0 = 0.5-0.8$ ) and retain water in their micropores and small mesopores,<sup>17-19</sup> through the formation of water clusters.<sup>20</sup> Water sorption is influenced by the hydrophilic character and by the capacity and type of porosity, while the hydrophilicity of the pore walls determines wettability through the formation of hydrogen bonds between water molecules and the pore surface.<sup>18</sup> Water sorption is influenced by the hydrophilic character and by the capacity and type of porosity, while the hydrophilicity of the pore walls determines wettability through the formation of hydrogen bonds between water molecules and the pore surface.<sup>19</sup> Recently, we reported the hygroscopic phenomenon of nanodiamonds where a nanodiamond pellet quickly absorbs a water droplet, even though the water vapor adsorption isotherm of the nanodiamonds indicates a considerable hydrophobicity. That is, the water adsorption isotherm of nanodiamonds has an initial uptake below  $P/P_0 = 0.1$ , being different from the typical hydrophobic carbon.<sup>3</sup> The presence of narrow sites for adsorption in a micropore/mesopore ratio of 0.15 triggers predominant adsorption of water vapor, inducing the transformation from microscopic hydrophobicity of the surfaces involved to the hygroscopic nature of bulk nanodiamond aggregates.<sup>21</sup> This chapter presents a semi-quantitative evaluation of the hygroscopic nature of nanodiamond pellets by the relative measure in terms of the wettability for water and the amount of water absorbed in comparison with well-known porous materials and aims understanding their efficiency as hygroscopic materials and describing the porosity role (evaluated by nitrogen adsorption) on the absorption of liquid water. Absorption

refers to the intrusion of water droplets in the nanodiamond aggregates while adsorption is used for the physical attachment of nitrogen and water vapor on the surfaces.

## 6.2 Experimental section

### 6.2.1 Materials

Detonation nanodiamonds in the form of a hard hydrogel (average particle size  $3.0 \pm 0.5$  nm, density  $2.2 \times 10^{19}$  particles  $\text{g}^{-1}$ ) were obtained from the Nano-Carbon Research Institute, Ltd., Japan. Montmorillonite ( $\text{SiO}_2/\text{Al}_2\text{O}_3$  powder, pH 3-4) was purchased from Sigma-Aldrich. Mordenite ( $\text{SiO}_2/\text{Al}_2\text{O}_3$  220 mol mol<sup>-1</sup>,  $\text{Na}_2\text{O}$  0.05% wt. and LOI 6.3% wt.) and zeolite socony mobil-5 (ZSM-5; average particle size of 4.2  $\mu\text{m}$ ,  $\text{SiO}_2/\text{Al}_2\text{O}_3$  2120 mol mol<sup>-1</sup>,  $\text{Na}_2\text{O}$  0.01% wt. LOI 2.1% wt.) were obtained from TOSOH Corporation, Japan. The pelletized molecular sieve 5A (MS-5A; rod diameter of 1.6 mm, composition abt. 80% of zeolite and abt. 20% of clay binder ( $\text{Ca}_{4.5}[(\text{AlO}_2)_{12}(\text{SiO}_2)_{12}]\cdot n\text{H}_2\text{O}$ )) was obtained from Nacalai Tesque, USA. Silica gel powder was produced by grinding silica beads (type A, sphere diameter of 4–6 mm,  $\text{SiO}_2 > 99.8\%$ ) from Tokai Chemical Industry Co. Japan. Activated Carbon Fibers (ACF-A10) of hydrophobic nature obtained from Ad'all Co. Japan were used as a reference. All materials were ground with mortar to facilitate further pelletizing. Grinding treatment was performed only enough for sieving the materials by series of sieves with progressively smaller pores in the range of 500  $\mu\text{m}$  to 75  $\mu\text{m}$  for the reference solids of non-powder nature as as-received; MS-5A, silica gel, and ACF-A10. Afterward, pellets of 0.5 cm of diameter and densities between 1.0 to 1.6  $\text{g cm}^{-3}$  were produced by mechanical pressure. The optimum conditions of producing and outgassing the pellets are specified in **Table 6-1**.

**Table 6-1.** Optimum conditions for outgassing the powder materials before nitrogen (77 K) or water (298 K) adsorption, pelletizing conditions and apparent densities of the pellets.

<b>Material</b>	<b>Outgassing conditions Temperature (K); time (h)</b>	<b>Pelletizing conditions Mechanical pressure (MPa); time (min)</b>	<b>Pellet density g cm<sup>-3</sup></b>
Nanodiamond	423 K; 2 h	2 MPa; 10 min	1.3
Montmorillonite	423 K; 12 h	4 MPa; 10 min	1.3
Mordenite	573 K; 12 h	4 MPa; 10 min	1.0
ZSM-5	523 K; 3 h	4 MPa; 10 min	1.1
MS-5A	573 K; 12 h	4 MPa; 10 min	1.2
Silica gel	423 K; 12 h	4 MPa; 10 min	1.1
ACF-A10	393 K; 2 h	14 MPa; 30 min	1.0

### 6.2.2 Characterization

The morphology of pelletized nanodiamonds, Montmorillonite, mordenite, ZSM-5, MS-5A, and silica gel was examined by means of a field-emission scanning electron microscope (FE-SEM; JEOL, JSM-7000F). The pore structure was determined volumetrically by nitrogen adsorption at 77 K using the apparatus Autosorb iQ (Quantachrome), after heating at 423 K and  $10^{-4}$  Pa for 3 h applying the BET method. Pore size distributions were obtained after applying the Density Functional Theory (DFT) to the nitrogen adsorption isotherms using the software provided by Quantachrome. The pore size distribution was obtained by the solution of the General Adsorption Isotherm. Such isotherm correlates the experimental isotherms to a collection of theoretical adsorption isotherms representing the adsorption in pores of different sizes (width) of a given pore shape at a given temperature) for the particular adsorbate-adsorbent pairs

(nitrogen-carbon, nitrogen-silica, etc.).<sup>22</sup> The affinity of the materials for water was evaluated by measurements of water adsorption isotherms and contact angles. Water adsorption isotherms at 298 K were determined with a volumetric equipment (Quantachrome-Vstar) after outgassing the samples at the same conditions used when outgassing for nitrogen adsorption isotherms (**Table 6-1**). In addition, the specific surface areas calculated from water (298 K) and from nitrogen (77 K) adsorption isotherms were compared.

### **6.2.3 Wettability for water and semi-quantitative evaluation of water absorption**

Wettability of pelletized samples was measured by water contact angle measurements with a contact angle meter (Drop Master 701/DM 501) applying the half-angle method. The hygroscopic property was evaluated by measuring the amount and the rate of absorption of liquid water within dry pelletized samples. In the present study, we focus on the comparative evaluation of water absorption capacity and rate of nanodiamonds using the pelletized reference samples having similar density and total pore volume. Therefore, the range of pellet density of the reference materials was adjusted between 1.0 and 1.3 g cm<sup>-3</sup>, as the pellet density of nanodiamonds is 1.3 g cm<sup>-3</sup>. The pelletized samples were outgassed at 423 K for 3 h in *vacuo*; only the pelletized ACF-A10 was outgassed at 393 K for 2 h in order to preserve the chemical structure. The pre-evacuation condition of 393 K for 3 h is sufficient for removing adsorbed water and other gases from micropores on ACF, avoiding activation of the pore surface by removal of surface functional groups ( $O/C < 0.05$ ) on pre-evacuation at a higher temperature.<sup>23</sup> After outgassing, each pellet was placed on a PET grid (mesh size 200 μm) where a water

droplet of 6.5  $\mu\text{L}$  of deionized water (at  $7.0 < \text{pH} < 7.5$ ) was dropped. The pellet was weighed after the absorption of the water droplet. The droplets were successively dropped until the weight stopped increasing, which was considered as the saturation point. All experiments were carried out at ambient conditions ( $297 \pm 2 \text{ K}$  and  $\text{RH} = 27 \pm 5\%$ ). Changes in the weight of the pelletized samples and in the size of the water droplets with time were measured by an electronic balance and by analyzing the droplet images using the contact angle measuring equipment, respectively. In addition, we measured the pH of water and contact angle of nanodiamonds over the duration of the given measurement, to corroborate the effect of the atmospheric conditions.

## **6.3 Results and discussion**

### **6.3.1 Scanning electron microscopic images of pelletized materials**

**Figure 6-1** shows the SEM images of pelletized nanodiamonds, Montmorillonite, mordenite, ZSM-5, MS-5A, and silica gel samples. Nanodiamonds do not give clear images due to the aggregated structure of nanoparticles of 4 nm (average diameter) compared with other samples;<sup>3</sup> the enlarged image of nanodiamonds in the inset shows that nanodiamond particles form non-uniform aggregates of 20 nm of size. Other pelletized materials have randomly oriented structures in the order of  $0.1 \sim 1.0 \mu\text{m}$ , resulting in voids larger than those in the pelletized nanodiamonds.

### **6.3.2 Porosity of pelletized porous materials**

The preceding studies on nanodiamonds show that wettability and hygroscopic nature are associated with microporosity and mesoporosity.<sup>3,16,17,19</sup> The effects of pelletizing

nanodiamond powder at different pressures on the porosity were examined using nitrogen adsorption isotherms, as shown in **Figure 6-2** and **Table 6-2**.

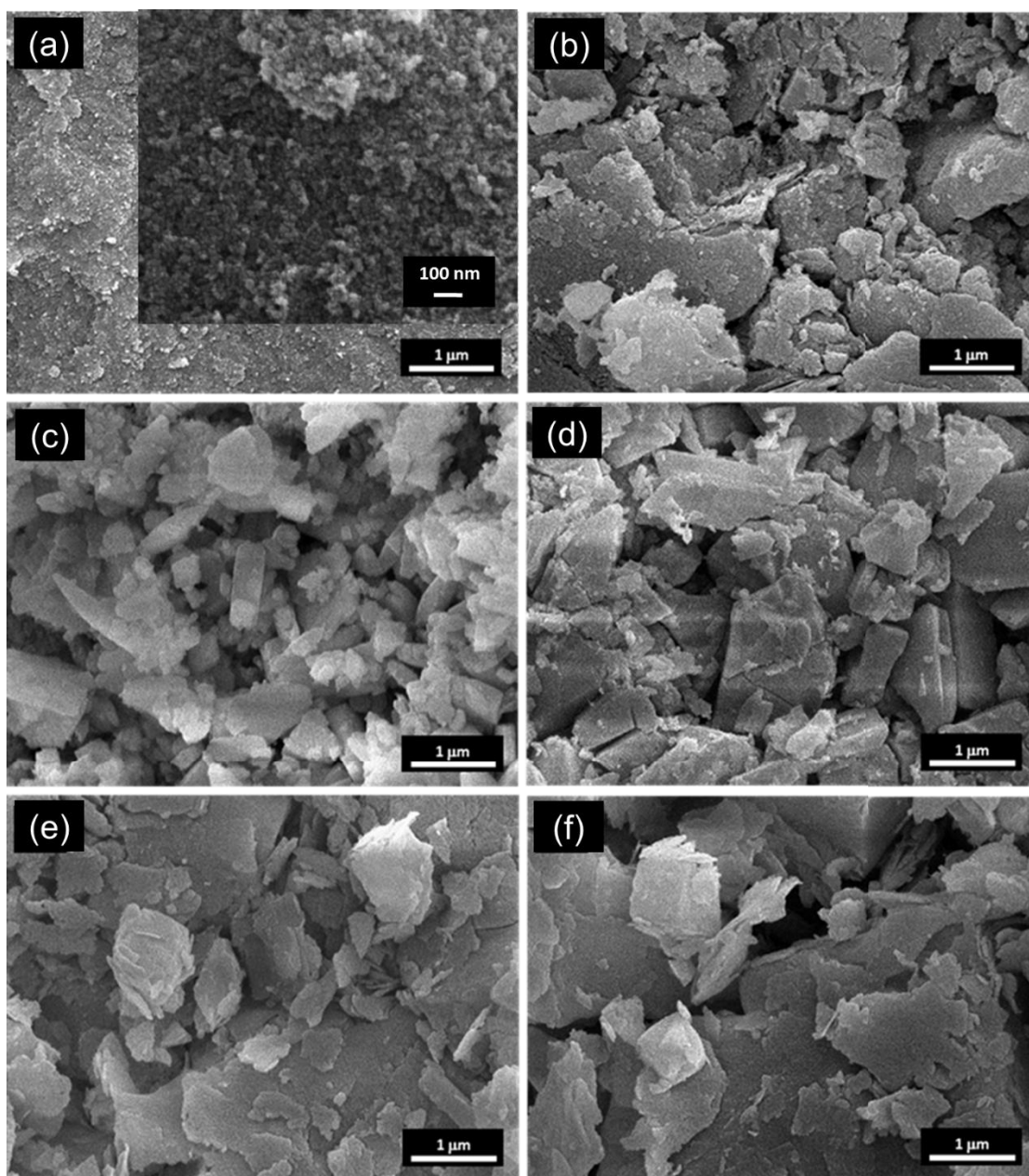


**Figure 6-1.** SEM images of pelletized (a) nanodiamonds, (b) Montmorillonite (c) mordenite, (d) ZSM-5, (e) MS-5A and (f) silica gel.

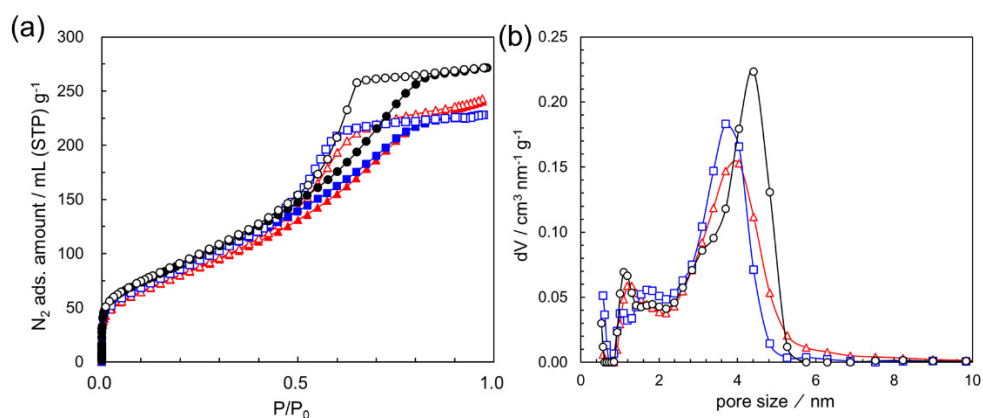


**Figure 6-2.** (a) Nitrogen adsorption isotherms of nanodiamonds at 77 K and (b) pore size distributions by QS-DFT model. As-received nanodiamonds (powder aggregates) ( $\bullet$ ), a pellet with a density of  $1.3 \text{ g cm}^{-3}$  ( $\blacktriangle$ ) and  $1.6 \text{ g cm}^{-3}$  ( $\blacksquare$ ). In (a) close and open symbols denote adsorption and desorption branches, respectively.

**Table 6-2.** Pore structure parameters from nitrogen adsorption isotherms (77 K) of nanodiamonds before and after pelletizing (outgassed at 423 K for 2 h).

Material	Pellet density $\text{g cm}^{-3}$	Total pore volume at $P/P_0 = 0.97$	$S_{\text{BET}}$	Micropore volume <sub>DFT</sub> ( $< 2 \text{ nm}$ )	Mesopore volume <sub>DFT</sub> ( $2\text{-}6 \text{ nm}$ )	Mesopore volume <sub>DFT</sub> ( $> 6 \text{ nm}$ )
		$\text{cm}^3 \text{ g}^{-1}$	$\text{m}^2 \text{ g}^{-1}$	$\text{cm}^3 \text{ g}^{-1}$	$\text{cm}^3 \text{ g}^{-1}$	$\text{cm}^3 \text{ g}^{-1}$
powder	-	$0.40 \pm 0.01$	$318 \pm 7$	$0.05 \pm 0.00$	$0.35 \pm 0.01$	$0.00 \pm 0.00$
pellet	1.3	$0.38 \pm 0.00$	$280 \pm 12$	$0.05 \pm 0.00$	$0.30 \pm 0.02$	$0.01 \pm 0.00$
pellet	1.6	$0.36 \pm 0.00$	$300 \pm 2$	$0.05 \pm 0.01$	$0.29 \pm 0.01$	$0.00 \pm 0.00$

Duplicate measurements were performed.  $S_{\text{BET}}$  areas were calculated considering data fitting following the Rouquerol rules. Cross-sectional area of nitrogen =  $0.162 \text{ nm}^2$  (standard value).

The observed nitrogen adsorption isotherms in **Figure 6-2** are of IUAPC Type IV with an adsorption hysteresis from  $P/P_0 = 0.5\text{--}0.8$ ; indicative of capillary condensation in mesopores.<sup>24</sup> Surface areas  $S_{\text{BET}}$  determined by the BET method for nitrogen are 320,

280, and 300 m<sup>2</sup> g<sup>-1</sup>, for the powdered sample, low density pelletized (1.3 g cm<sup>-3</sup>) and high-density (1.6 g cm<sup>-3</sup>) pelletized samples, respectively. A slight decrease in the adsorption hysteresis of the isotherm after pelletizing is observed, which comes from the reduction of the mesopore volume. The pore size distribution evaluated by the QS-DFT method assuming the slit-pore model<sup>25,26</sup> shows that pelletizing reduces mesopore volume and pore size. The pore volume of mesopores (pore width ≤ 5 nm) decreases by about 10%, while micropores are slightly modified. Thus, pelletizing changes the mesopore and micropore structures of nanodiamond aggregates. **Figure 6-3** shows the nitrogen adsorption isotherms and pore size distributions of representative pelletized porous samples for clarity. The rest of the materials are shown in **Figure 6-4**.

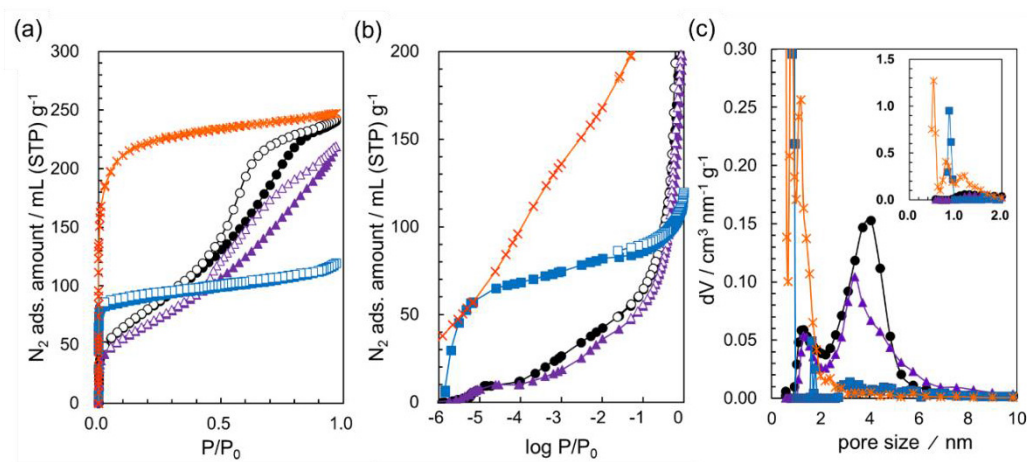


**Figure 6-3.** Nitrogen adsorption isotherms of representative pelletized porous materials in (a) linear scale and (b) logarithmic scale of the relative pressure at 77 K; (c) pore size distributions of nanodiamonds ( $\circ$ ), Montmorillonite ( $\triangle$ ), MS-5A ( $\square$ ) and ACF-A10 ( $\ast$ ). In (a) and (b) solid and open symbols denote adsorption and desorption branches, respectively. The pore size distributions of nanodiamonds, Montmorillonite, and ACF-A10 are obtained by the QS-DFT, while the NLDFT method for cylindrical pores was applied to MS-5A. The inset in (c) shows a closer view of the pore size  $\leq 2$  nm.

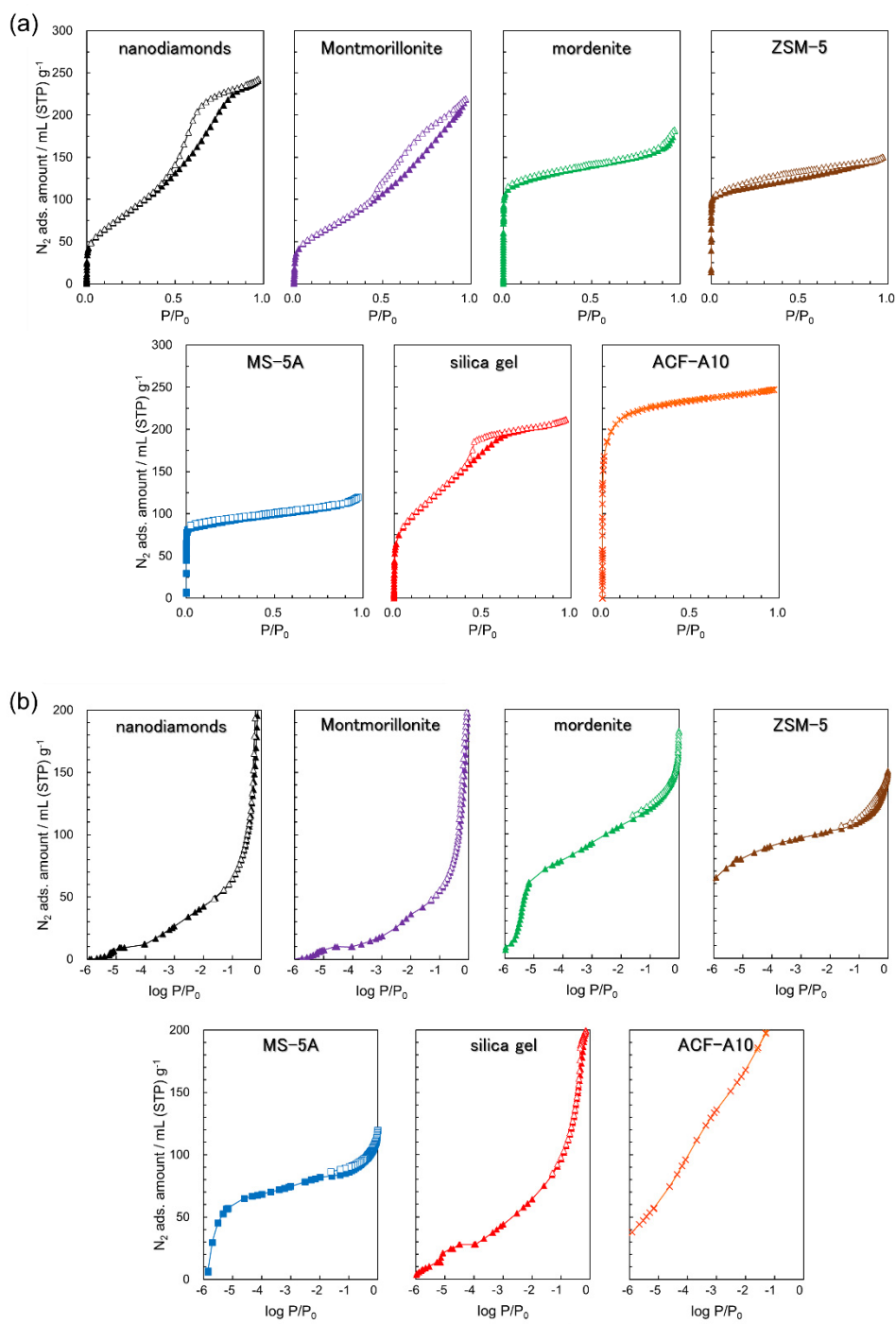


**Figure 6-4.** Nitrogen adsorption isotherms at 77 K of pelletized porous materials in (a) linear scale and (b) logarithmic scale of the relative pressure. In (a) and (b) solid and open symbols denote adsorption and desorption branches, respectively.

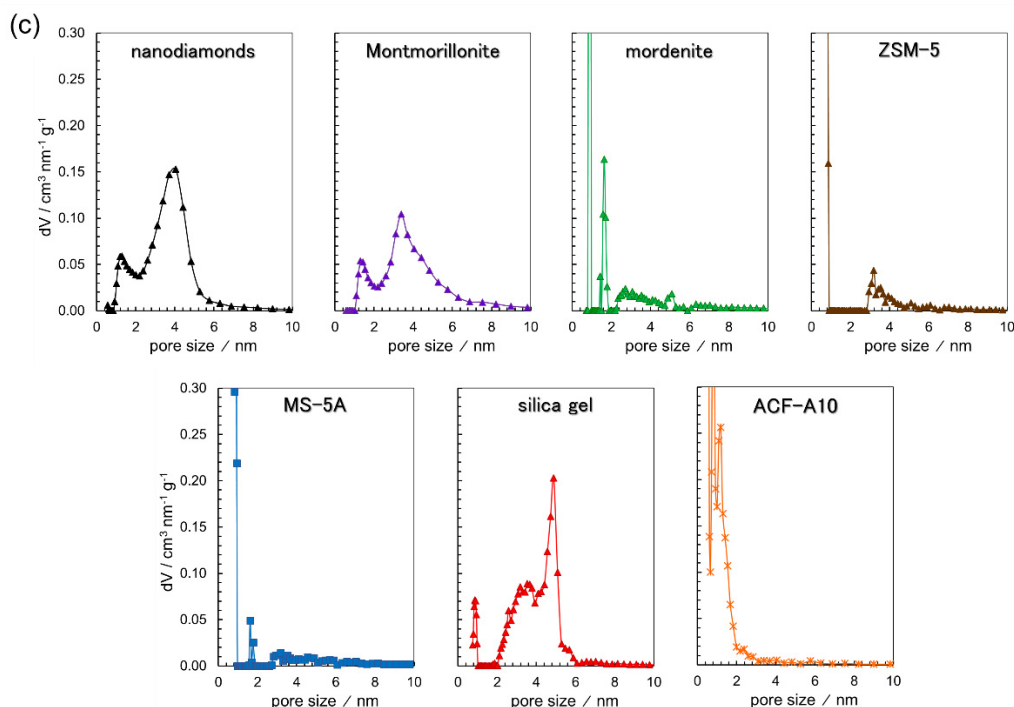


**Figure 6-4. (Continuation).** Nitrogen adsorption isotherms at 77 K of pelletized porous materials. (c) Pore size distributions of pelletized porous materials. The pore size distributions of nanodiamonds, Montmorillonite, and ACF-A10 are obtained by the QS-DFT, while NLDFT method for cylindrical pores was applied to mordenite, ZSM-5, MS-5A and silica gel.

The pore structure parameters and the surface areas of all the materials compared in this study are shown in **Table 6-3** and **Table 6-4a**, respectively. The total pore volume of the reference materials distribute from 0.2 to 0.4 cm<sup>3</sup> g<sup>-1</sup> because the intrinsic porosity and particle shape of the reference solids are different among each other, and thereby pore volume cannot be controlled. Nevertheless, the pellet density of the compared materials is  $1.2 \pm 0.2$  g cm<sup>-3</sup>, which is similar to the pellet density of nanodiamonds (1.3 g cm<sup>-3</sup>). The ACF has the maximum adsorption amount of nitrogen of all samples and nanodiamonds exhibit the second-largest adsorption amount. Nanodiamonds,

Montmorillonite, and silica gel have both micropores and mesopores according to the isotherm shape and hysteresis. The rest of the materials show IUPAC Type I isotherm, indicative of microporous materials,<sup>24,27</sup> as shown in **Figure 6-3** and **Figure 6-4**.

**Table 6-3.** Pore structure of pelletized materials by nitrogen adsorption isotherms (77 K).

Material	Total pore volume <sup>(a)</sup> P/P <sub>0</sub> =0.97 cm <sup>3</sup> g <sup>-1</sup>	Micropore volume <sup>(b)</sup> DFT (< 2 nm) cm <sup>3</sup> g <sup>-1</sup>	Volume of small mesopores <sup>(b)</sup> DFT (2-5 nm) cm <sup>3</sup> g <sup>-1</sup>	Volume of large mesopores <sup>(b)</sup> DFT (> 5 nm) cm <sup>3</sup> g <sup>-1</sup>	Ratio Micropore /small mesopore
Nanodiamonds	0.38 ± 0.00	0.05 ± 0.00	0.30 ± 0.02	0.00 ± 0.00	0.17
Montmorillonite	0.32 ± 0.02	0.04 ± 0.01	0.18 ± 0.01	0.09 ± 0.00	0.22
Mordenite	0.30 ± 0.02	0.15 ± 0.03	0.08 ± 0.04	0.08 ± 0.01	1.88
ZSM-5	0.21 ± 0.03	0.08 ± 0.02	0.10 ± 0.01	0.03 ± 0.01	0.80
MS-5A	0.21 ± 0.03	0.11 ± 0.04	0.11 ± 0.00	0.00 ± 0.00	1.00
silica gel	0.33 ± 0.02	0.01 ± 0.01	0.24 ± 0.05	0.05 ± 0.04	0.04
ACF A10	0.42 ± 0.05	0.30 ± 0.01	0.11 ± 0.08	0.01 ± 0.01	2.73

Duplicate measurements were performed.

<sup>(a)</sup> Total pore volume was obtained by the extrapolation of the desorption branch to P/P<sub>0</sub> = 0.97.

<sup>(b)</sup> Micropore and mesopore volumes were obtained as the area under the pore size distribution curve by DFT method using the IUPAC classification (micropores: pore width < 2nm, mesopores: 2 nm < pore width < 50 nm). We divided mesopores into small mesopores (pore width < 5 nm) and large mesopores (pore width > 5 nm). Here, 5 nm is the maximum limit of the mesopore size distribution of nanodiamonds.

**Table 6-3** shows that the total pellet pore volumes of the three zeolites are smaller than 0.30 cm<sup>3</sup> g<sup>-1</sup>, with a ratio micropores to small mesopores volume of 0.8 (ZSM-5), 1.0 (MS-5A) and 1.9 (mordenite). On the contrary, larger pore volumes are obtained for nanodiamonds, Montmorillonite, and silica gel, which have mesopores. The pore volume

ratio (micropores to small mesopores) of these mesoporous materials are at most 0.22 for Montmorillonite.

**Table 6-4a.** Surface areas of powdered and pelletized samples from adsorption isotherms of nitrogen at 77 K and water at 298 K.

Material	$S_{\text{BET}}^{(a)}(\text{N}_2)$	$S_{\text{BET}}^{(a)}(\text{N}_2)$	$S_{\text{BET}}^{(a)}(\text{H}_2\text{O})$	$S_{\text{BET}}^{(a)}(\text{H}_2\text{O})$
	(powder)	(pellet)	(powder)	(pellet)
	$\text{m}^2 \text{g}^{-1}$	$\text{m}^2 \text{g}^{-1}$	$\text{m}^2 \text{g}^{-1}$	$\text{m}^2 \text{g}^{-1}$
Nanodiamond	318 <sup>(b)</sup>	281 <sup>(b)</sup>	219 <sup>(d)</sup>	185 <sup>(d)</sup>
Montmorillonite	249 <sup>(b)</sup>	234 <sup>(b)</sup>	293 <sup>(e)</sup>	245 <sup>(e)</sup>
Mordenite	562 <sup>(b)</sup>	477 <sup>(b)</sup>	193 <sup>(d)</sup>	101 <sup>(d)</sup>
ZSM-5	564 <sup>(b)</sup>	430 <sup>(b)</sup>	67 <sup>(d)</sup>	61 <sup>(d)</sup>
MS-5A	615 <sup>(b)</sup>	343 <sup>(b)</sup>	234 <sup>(d)</sup>	202 <sup>(d)</sup>
Silica gel	483 <sup>(c)</sup>	334 <sup>(c)</sup>	321 <sup>(e)</sup>	227 <sup>(e)</sup>
ACF-A10	1050 <sup>(b)</sup>	797 <sup>(b)</sup>	-	-

<sup>(a)</sup>  $S_{\text{BET}}$  calculated considering data fitting following the Rouquerol rules.

<sup>(b)</sup> Cross sectional area of nitrogen = 0.162 nm<sup>2</sup> (standard value).

<sup>(c)</sup> Cross sectional area of nitrogen = 0.135 nm<sup>2</sup> for silica and other polar surfaces.

<sup>(d)</sup> Cross sectional area of water = 0.108 nm<sup>2</sup>.

<sup>(e)</sup> Cross sectional area of water = 0.148 nm<sup>2</sup>.

Samples outgassed before adsorption measurements at the conditions specified in **Table 6-1** in *vacuo* at 1 mPa and 0.1 Pa for nitrogen and water, respectively.

The nitrogen adsorption isotherms of all the compared materials before pelletizing are shown in **Figure 6-5**. **Figure 6-6** shows the comparison of nitrogen adsorption isotherms (77 K) of the materials in a semi-logarithmic scale before and after pelletizing. According to the isotherms, pelletizing of powdered samples decreases the total adsorbed amount of nitrogen due to blocking and/or collapsing pores. The pelletizing reduces the maximum nitrogen adsorption amounts by 20-30% for MS-5A and ZSM-5, about 15% for silica gel

and less than 10% for ACF, Montmorillonite, mordenite, and nanodiamonds. Such reduced porosities mainly arise from the decrease of pores of small dimensions in MS-5A, ZSM-5, and mordenite, and from both micropores and mesopores for the cases of nanodiamonds and Montmorillonite.

**Table 6-4b.** Total pore volumes of powdered and pelletized samples from adsorption isotherms of nitrogen at 77 K and water at 298 K.

Material	Total pore volume	Total pore volume	Total pore volume	Total pore volume
	at $P/P_0 = 0.97$ (N <sub>2</sub> ) (powder) cm <sup>3</sup> g <sup>-1</sup>	at $P/P_0 = 0.97$ (N <sub>2</sub> ) (pellet) cm <sup>3</sup> g <sup>-1</sup>	at $P/P_0 = 0.97$ (H <sub>2</sub> O) (powder) cm <sup>3</sup> g <sup>-1</sup>	at $P/P_0 = 0.97$ (H <sub>2</sub> O) (pellet) cm <sup>3</sup> g <sup>-1</sup>
Nanodiamond	0.42	0.38	<b>0.49</b>	0.35
Montmorillonite	0.36	0.34	<b>0.52</b>	<b>0.44</b>
Mordenite	0.29	0.28	<b>0.33</b>	0.15
ZSM-5	0.29	0.22	0.16	0.17
MS-5A	0.26	0.18	<b>0.42</b>	<b>0.27</b>
Silica gel	0.40	0.33	<b>0.40</b>	<b>0.37</b>
ACF-A10	0.53	0.38	0.50	0.37

Total pore volume was obtained by the extrapolation of the desorption branch to  $P/P_0 = 0.97$ .

Outgassing before adsorption measurements at the conditions specified in **Table 6-1** in *vacuo* at 1 mPa and 0.1 Pa for nitrogen and water, respectively.

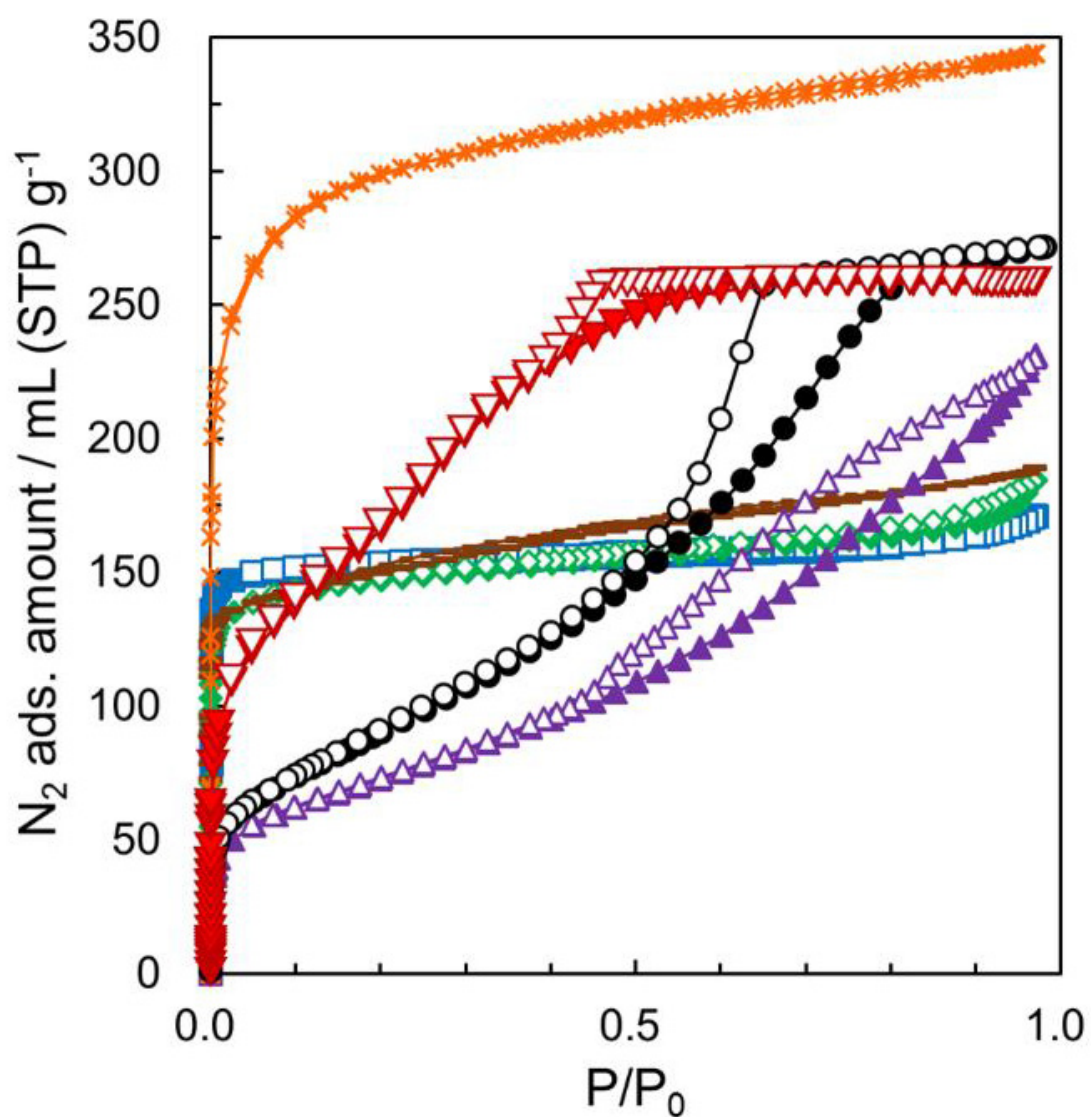


**Figure 6-5.** Nitrogen adsorption isotherms at 77 K of powdered samples of nanodiamonds ( $\circ$ ), Montmorillonite ( $\triangle$ ), mordenite ( $\diamond$ ), MS-5A ( $\square$ ), ZSM-5 ( $-$ ), ACF-A10 ( $*$ ) and silica gel ( $\nabla$ ). Solid and open symbols denote adsorption and desorption branches, respectively.

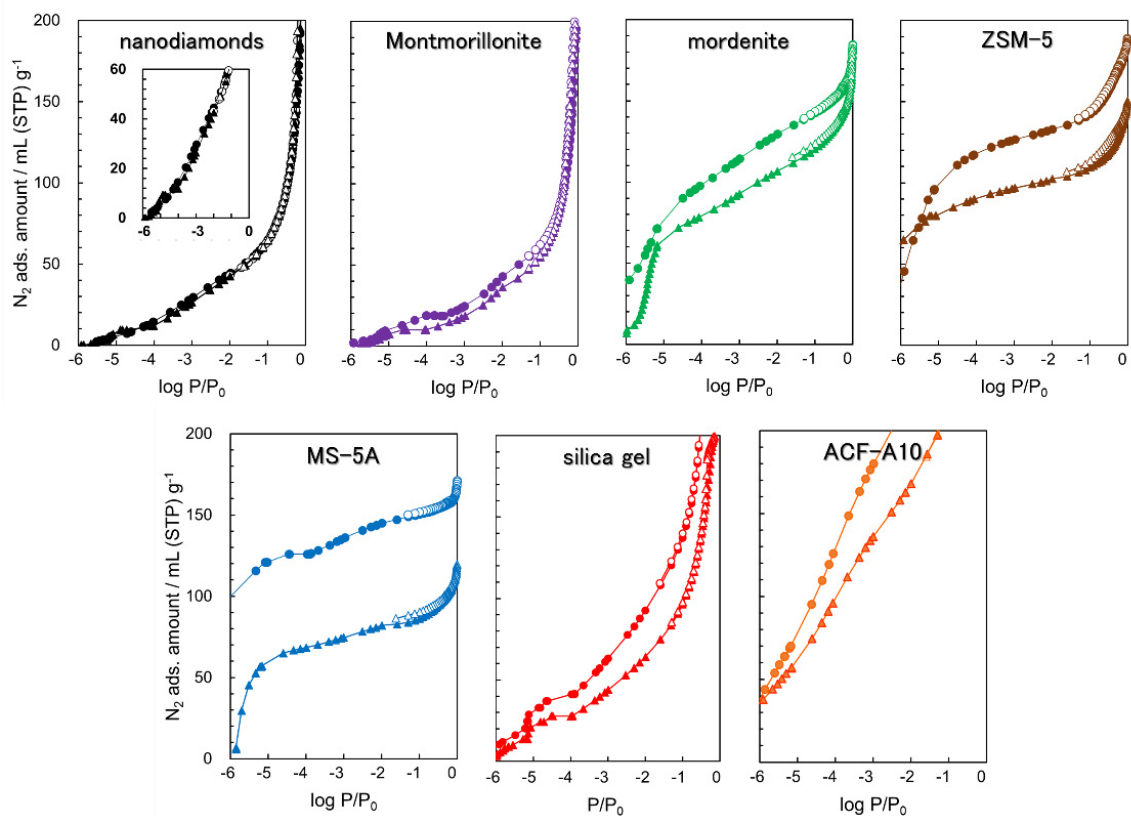


**Figure 6-6.** Nitrogen adsorption isotherms at 77 K of powdered ( $\circ$ ) and pelletized ( $\Delta$ ) samples in logarithmic scale of the relative pressure. Solid and open symbols denote adsorption and desorption branches, respectively.

### 6.3.3 Water absorption ability and wettability for water

**Figure 6-7a** and **Figure 6-7b** include only four water adsorption isotherms to show the representative adsorption isotherms of porous materials at 298 K in a nominal and normalized scale, respectively. The rest of the adsorption isotherms are shown in **Figure 6-8**. The descending order of the saturated water adsorption amount is ACF, Montmorillonite, silica gel, nanodiamonds, mordenite, MS-5A and ZSM-5. The adsorption isotherms of the samples except for MS-5A exhibit a gradual increase in adsorption with the  $P/P_0$  and adsorption hysteresis, indicating that these solids are not

necessarily hydrophilic in the low  $P/P_0$  region. The increase in adsorption on silica gel is similar to nanodiamonds at  $P/P_0 < 0.05$ . At  $P/P_0 = 0.2$  water adsorption is lower on ZSM-5 and similar in mordenite compared to that on nanodiamonds. Only the water adsorption isotherm of MS-5A is unique, showing Type I shape; water vapor is fully adsorbed in the micropores of MS-5A even in the low  $P/P_0$  region. These three zeolites (ZSM-5, mordenite and MS-5A) have micropore volumes larger than nanodiamonds (**Table 6-3**). Nanodiamonds and Montmorillonite show a similar increase in adsorption with  $P/P_0$ . The adsorbed water amount on ACF in the low  $P/P_0$  is the lowest of all the samples, even though ACF has the largest saturated adsorption amount.<sup>28</sup> In case of porous carbons, the water adsorption isotherm of porous carbon of smaller pore width rises from a lower  $P/P_0$  region, indicating that the pore size is key to the apparent affinity of carbon porosity to water.<sup>17,29</sup>

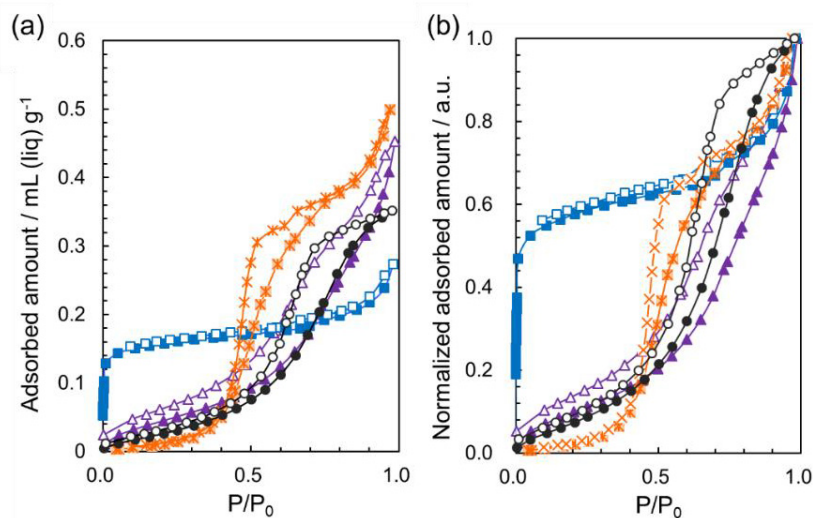


**Figure 6-7.** Water adsorption isotherms of representative pelletized porous materials (298 K) in (a) linear scale and (b) normalized scale of nanodiamonds (○), Montmorillonite (△), MS-5A (□) and ACF-A10 (\*). Solid and open symbols denote adsorption and desorption branches, respectively.

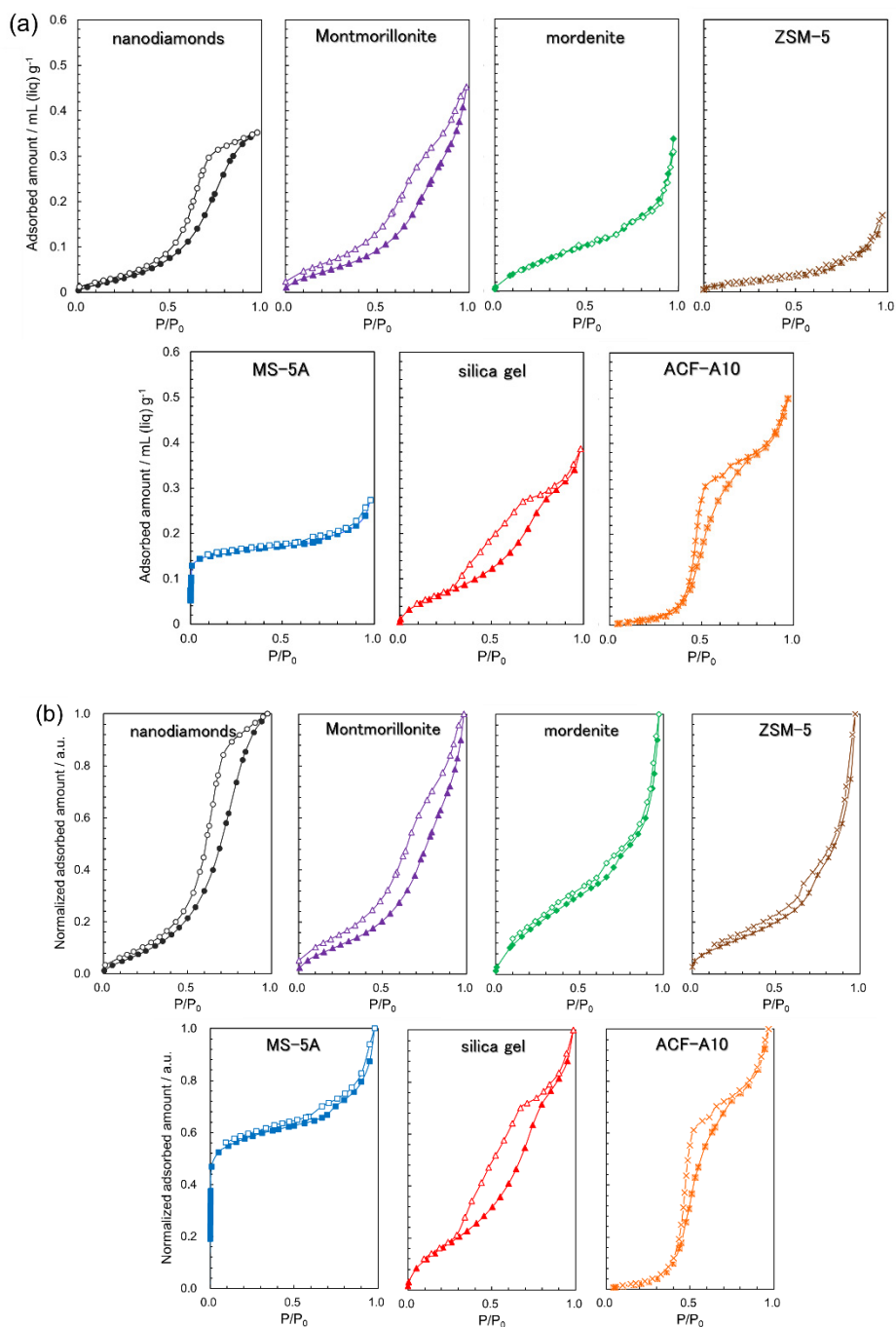


**Figure 6-8.** Water adsorption isotherms (298 K) in (a) linear scale and (b) normalized scale of nanodiamonds ( $\circ$ ), Montmorillonite ( $\triangle$ ), mordenite ( $\diamond$ ), ZSM-5 ( $\times$ ), MS-5A ( $\square$ ), silica gel ( $\triangle$ ) and ACF-A10 ( $\times$ ). Solid and open symbols denote adsorption and desorption branches, respectively.

The water adsorption isotherms at 298 K were interpreted to yield a specific surface area, which was compared to that obtained from the nitrogen adsorption isotherms at 77 K, as shown in **Table 6-4a**. Those water adsorption isotherms of powdered and pelletized samples are shown in **Figure 6-9**. Surface areas from water (BET\_H<sub>2</sub>O) are smaller than those areas obtained from nitrogen (BET\_N<sub>2</sub>) because the BET\_H<sub>2</sub>O model is sensitive to the hydrophilic-hydrophobic character of the samples when determining the adsorption of the first monolayer of water molecules. Instead, the comparison of total pore volumes by nitrogen and water in **Table 6-4b** shows that all the materials adsorb higher total volume of water than nitrogen at  $P/P_0 = 0.97$ , except ACF-A10 and ZSM-5 indicating less hydrophilicity.

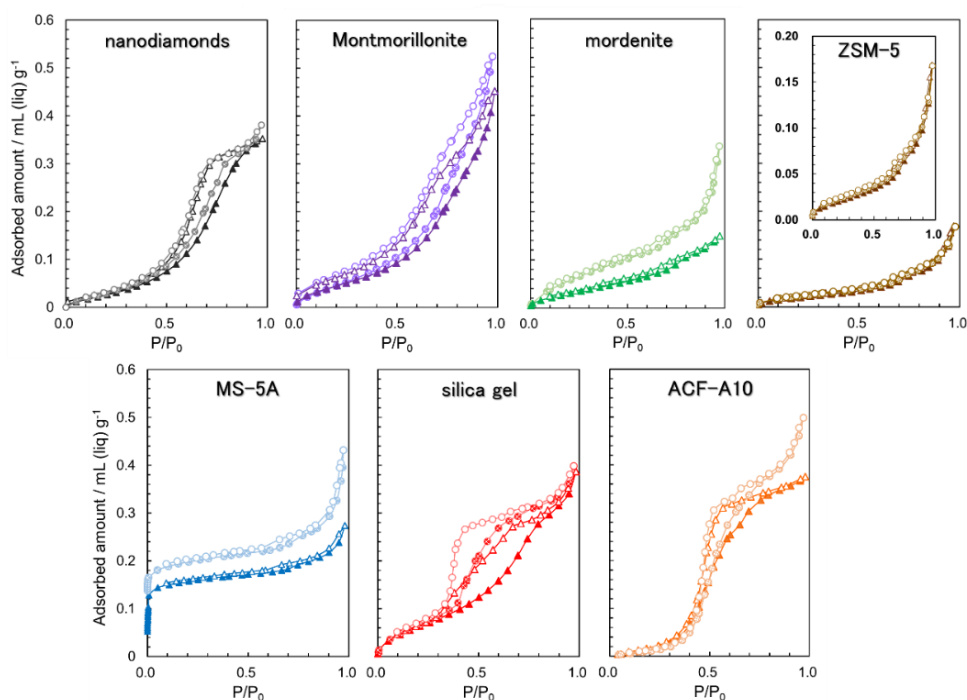


**Figure 6-9.** Water adsorption isotherms at 298 K of powdered ( $\circ$ ) and pelletized ( $\Delta$ ) samples. Solid and open symbols denote adsorption and desorption branches, respectively.

According to the literature, water contact angles of hydrophilic porous materials are unmeasurable with sufficient reliability due to their markedly high absorption rate of water droplets and we cannot refer to literature values of the contact angle.<sup>13</sup> Therefore, we measured the water contact angles for the pelletized samples hydrated in advance under the same conditions, as shown in **Figure 6-10**. Hence, these water contact angle values indicate the wettability of the materials saturated with water vapor at ambient conditions ( $T = 297\text{ K}$  and  $\text{RH} = 33\%$ ). Silica gel gives the smallest contact angle:  $25 \pm 4^\circ$ , i.e. the highest wettability, followed by nanodiamonds ( $28 \pm 3^\circ$ ), Montmorillonite ( $34 \pm 1^\circ$ ), mordenite ( $33 \pm 1^\circ$ ), ZSM-5 ( $34 \pm 3^\circ$ ), MS-5A ( $45 \pm 3^\circ$ ). ACF and graphite have large water contact angles of  $76 \pm 2^\circ$  and  $77 \pm 1^\circ$ , respectively, indicating typical hydrophobicity. The literature reports water contact angles of about  $76 \pm 5^\circ$  and  $71 \pm 3^\circ$  for diamonds and  $93 \pm 2^\circ$  for CVD nanodiamonds,<sup>30,31</sup> showing rather hydrophobic nature. Zeolites such as ZSM and mordenite, clays as Montmorillonite and silica gel are among the three main groups of water sorbents,<sup>16</sup> while ACF is well known to be hydrophobic.<sup>28</sup>

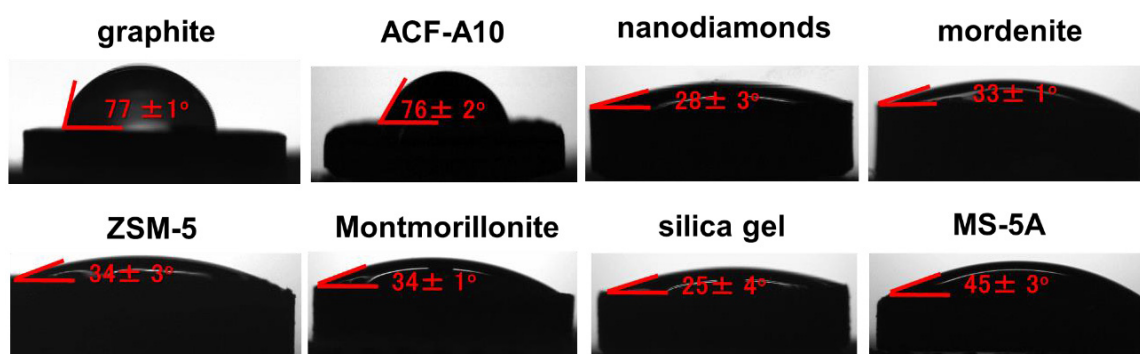


**Figure 6-10.** Water contact angles on graphite, ACF-A10, nanodiamonds, mordenite, ZSM-5, Montmorillonite, silica gel and MS-5A.

We measured the water contact angle of a bulk-scale diamond crystal by the sessile drop method, leading to a value of  $74.5 \pm 3^\circ$  (**Figure 6-11**). The experimentally obtained value ( $74.5 \pm 3^\circ$ ) agrees with the literature value of  $76 \pm 5^\circ$  and  $71 \pm 3^\circ$  for the 111 and 110 faces of the diamond, respectively, confirming the hydrophobic nature of the single crystal surface of the diamond.

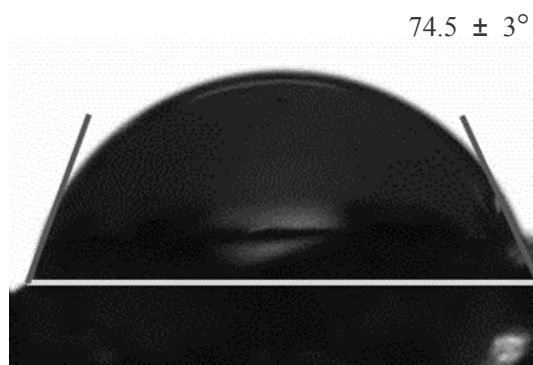


**Figure 6-11.** The water contact angle of a bulk diamond.

According to **Figure 6-10**, the measured water contact angle of nanodiamonds is about  $28 \pm 3^\circ$  ( $T = 298$  K and  $RH = 28\%$ ), indicating rather hydrophilic nature. This is due to the pre-saturation treatment of the nanodiamonds. Besides, measurement of the water contact angle of the pelletized samples at different relative humidities during the contact angle measurement indicates no significant influence of the relative humidity used in this study on the water contact angle, as shown in **Figure 6-12**.

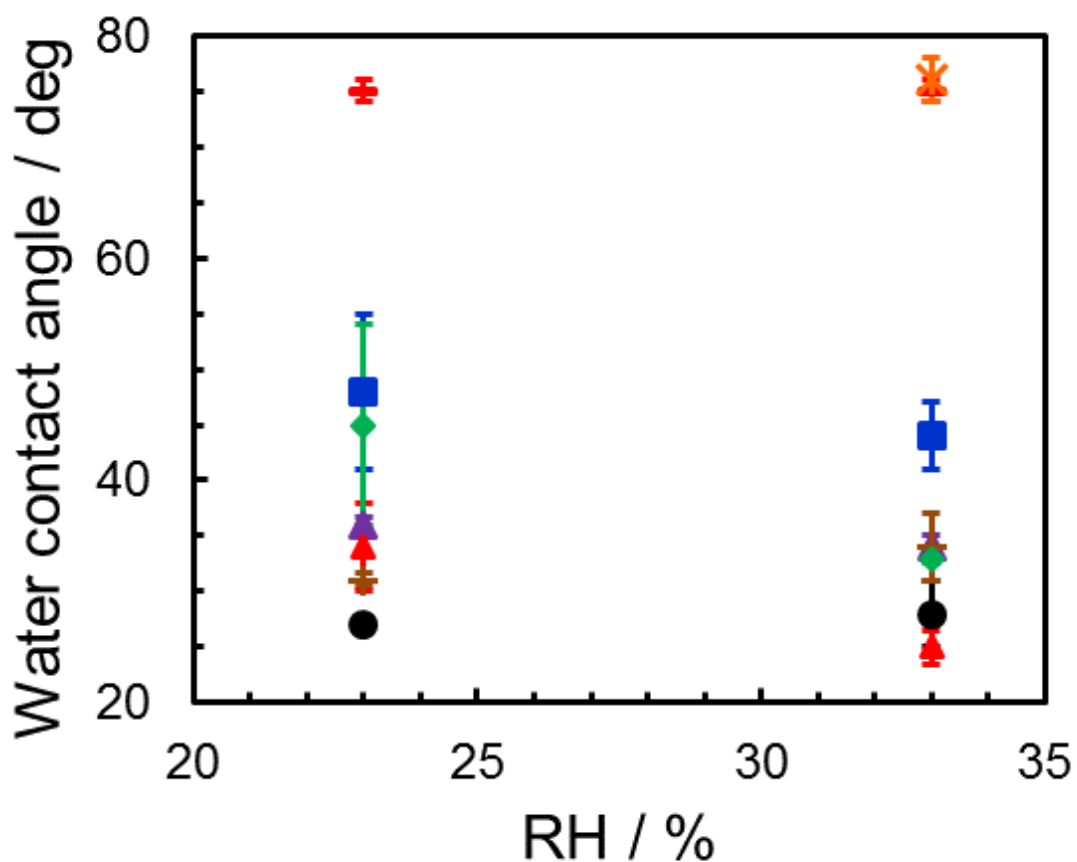


**Figure 6-12.** Water contact angle of pelletized samples of nanodiamonds (●), Montmorillonite (▲), MS-5A (■), ACF (A10) (×), mordenite (◆), ZSM-5 (✱), silica gel (▲) and graphite (-) at 297 K under different relative humidity (RH = 23% and RH = 33%).

We measured the pH of the water and the contact angle of nanodiamonds with the time of measurement, to corroborate the effect of the atmospheric conditions. The effect due to CO<sub>2</sub> in the volume of water exposed to atmospheric conditions is not evident in the pH or in the water contact angle, as the pH varies only by 0.4 units of pH and the water contact angle by 4°, as shown in **Figure 6-13**.

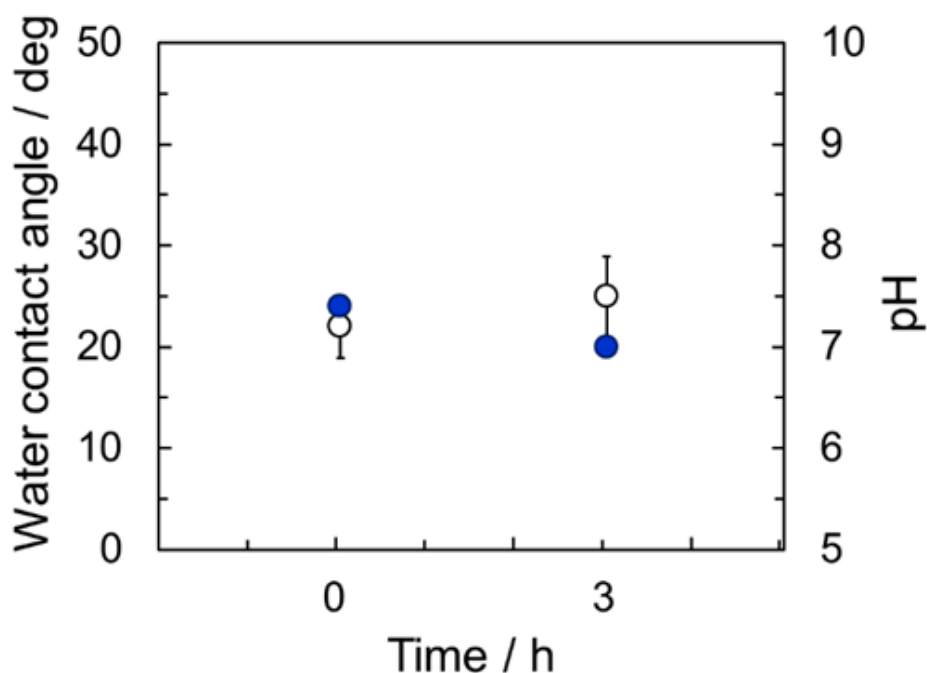


**Figure 6-13.** Water contact angle on nanodiamonds (○) and pH of deionized water (●) *versus* time under atmospheric conditions (297 K and RH = 33%).

The evaluation of grinding treatment indicates that the more the grinding, the smaller the particle size of the non-powder samples (MS-5A, silica gel, and ACF-A10); the solid sample having a smaller size is ground for a longer time. The other sample solids were compared before grinding and after grinding. The water contact angles of nanodiamonds slightly increase from  $14 \pm 1^\circ$  to  $28 \pm 3^\circ$  with grinding; suggesting that the effect of the grinding depends on the bonding structure of the porous solid. The contact angle of MS-5A does not change, as shown in **Figure 6-14**, because MS-5A is hydrophilic due to the ionic structure. Small particles of nanodiamonds and silica gels show a slightly larger contact angle, suggesting that the surface roughness is an important factor.

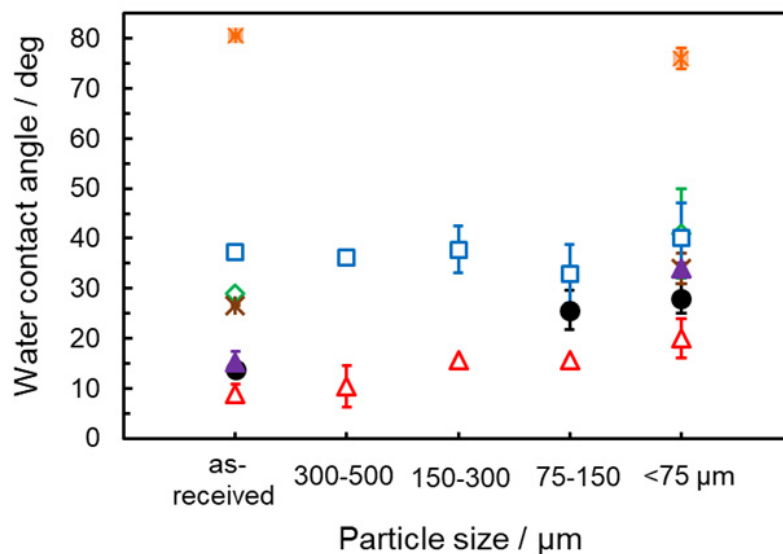


**Figure 6-14.** Effect of particle size of ground samples on the water contact angle of pelletized samples of nanodiamonds (●), Montmorillonite (▲), MS-5A (□), ACF (A10) (×), mordenite (◇), ZSM-5 (✱) and silica gel (△). Here, the average size of the ground particles was determined using stacked sieves of different sizes from 500  $\mu\text{m}$  to 75  $\mu\text{m}$ ; the longer the grinding time the smaller the particle size.

The preceding study using TEM and EELS methods showed that each nanodiamond particle is coated with graphene-like carbon films.<sup>2</sup> The graphene-wrapped nanodiamond particles are associated with each other providing micropores and small mesopores yielding hygroscopic nature. Here, we measured the absorption rate and absorption amount of water by nanodiamonds in comparison with reference materials. **Figure 6-15a** shows the water absorption capacity of the pelletized materials after normalizing with the apparent pellet density. The highest absorption amount for water is obtained by ACF followed by mordenite (1.0 and 0.6  $\text{mL}_{(\text{liq.})} \text{H}_2\text{O g}^{-1}$ , respectively). The nanodiamond pellet absorbs water droplets up to a volume of 0.54  $\text{mL}_{(\text{liq.})} \text{H}_2\text{O g}^{-1}$  (filling ~80% void

space), which is comparable to  $0.53 \text{ mL}_{(\text{liq.})} \text{ H}_2\text{O g}^{-1}$  for the mesoporous Montmorillonite (filling  $\sim 37\%$  void space), and at least 15% larger than those of the microporous ZSM-5 and MS-5A. Here, the void space of each pellet is evaluated considering the pellet and bulk densities of each material and the percentage of filling as the maximum absorbed water amount expressed as liquid volume of water per the volume of void space.

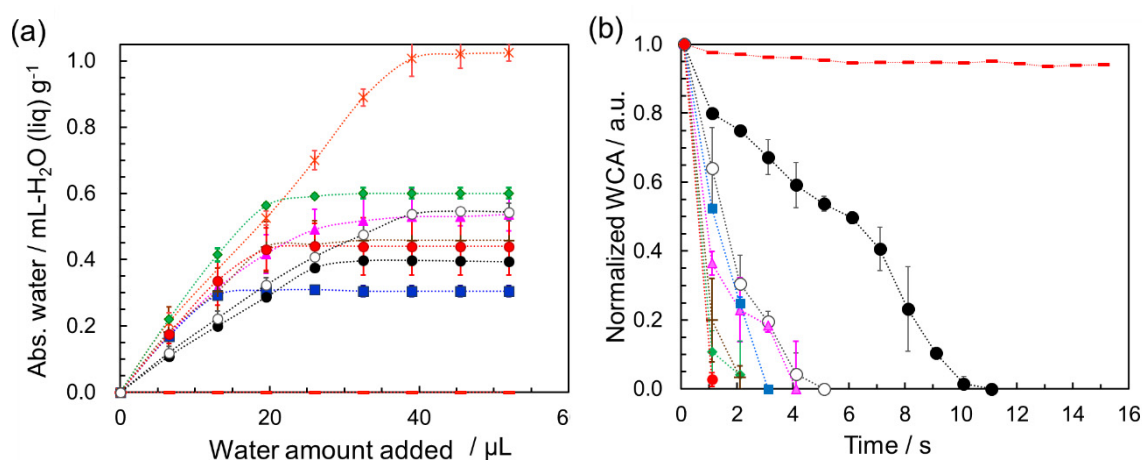


**Figure 6-15.** (a) Absorption of water droplets and (b) kinetics of first water droplet absorption on pelletized porous materials evaluated by water contact angle (WCA); graphite (-), high-density nanodiamonds (●) and low-density nanodiamonds (○), Montmorillonite (▲), MS-5A (■), ACF (A10) (\*), mordenite (◆), ZSM-5 (+), and silica gel (●). In (a) absorption of water was normalized by pellet densities (refer to **Table 6-1** to consult the pellet density values).

The analysis of the water adsorption isotherm of nanodiamonds in **Figure 6-8** indicates that water molecules adsorb in ultramicropores up to  $0.01 \text{ cm}^3 \text{ g}^{-1}$  ( $P/P_0 < 0.03$ ). Therefore, subsequent adsorption of water in mesopores up to  $0.35 \text{ cm}^3 \text{ g}^{-1}$  occurs. The reason is that the strongly adsorbed water molecules in ultramicropores distributed on the

mesopore walls can donate hydrophilicity to induce additional filling of mesopores with liquid-like water up to 0.54 mL (liq.) H<sub>2</sub>O g<sup>-1</sup>. Subsequently, the macropores are filled with water. The density of strongly adsorbed water in the ultramicropores accounts for 1 x 10<sup>-5</sup> mL (liq.)-H<sub>2</sub>O nm<sup>-2</sup>-ND, considering that the total ultramicropores (ultramicropore volume = 1 x 10<sup>-4</sup> cm<sup>3</sup> g<sup>-1</sup>) are distributed on the mesopore walls. **Figure 6-15b** shows the absorption kinetics of water after dropping the first droplet on the pelletized sample. The absorption rate on nanodiamonds is among the lowest of the compared porous materials, only higher than those of ACF and graphite, which reflects low hydrophilic nature.<sup>12</sup> The change of WCA of ACF with time was not measured due to serious deformation of the pellet surface. However, experimental observation showed a longer time to absorb the water droplet on ACF than on nanodiamonds. Nevertheless, the low-density nanodiamond pellet has a relatively high absorption rate, i.e. half of those of Montmorillonite and MS-5A. This is noteworthy because a lower density nanodiamond pellet should give an absorption rate higher than those rates of Montmorillonite, MS-5A, and other hydrophilic materials, although production of the low-density nanodiamond pellet is quite difficult due to ultrafine nanoscale particles. Consequently, we can say that the nanodiamonds have a clear hygroscopic nature, competing with representative hydrophilic porous materials.

**Figure 6-16a** shows that the time required for the first water droplet to be absorbed by the pellet after touching its surface involves a dependency on the apparent water contact angle. Silica gel, mordenite, ZSM-5, and MS-5A show the fastest rate of droplet absorption, followed by nanodiamonds pellet of low-density. The plot in **Figure 6-16b** shows that the maximum water absorption capacity correlates to the ratio of

micropores/mesopores (not larger than 5 nm width).

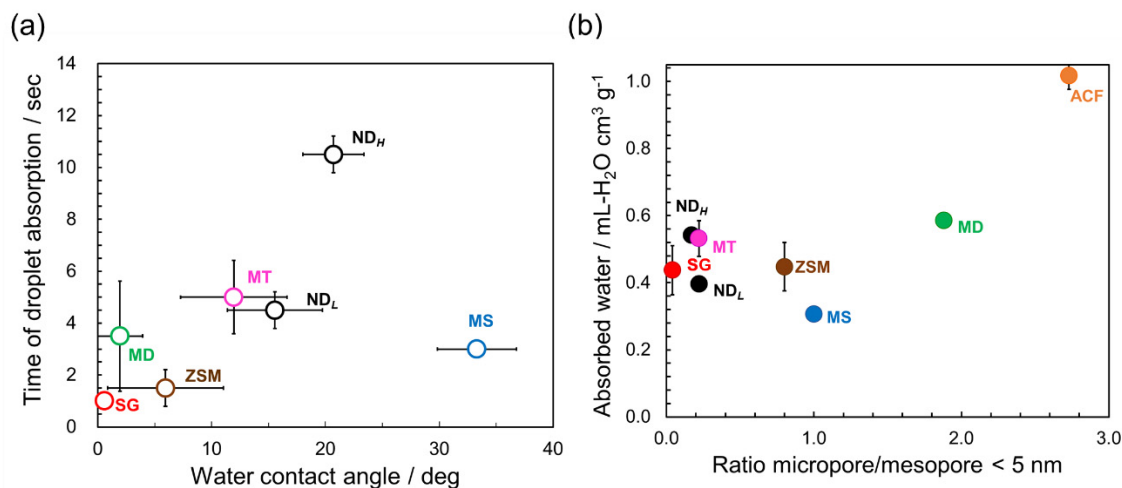


**Figure 6-16.** (a) Relationship between the completion time of first water droplet absorption and apparent water contact angle. (b) Relationship between total absorbed liquid water and the volume ratio micropore/mesopore ( $\leq 5$  nm) of pelletized samples of nanodiamonds (ND<sub>H</sub> and ND<sub>L</sub>, high and low density, respectively), Montmorillonite (MT), mordenite (MD), ZSM-5 (ZSM), molecular sieve 5A (MS), silica gel (SG) and activated carbon fiber A-10 (ACF). In (a) apparent contact angle refers to the contact angle of the first droplet in contact with the pellet surface at 100 ms. Here, ACF is not included, because the apparent water contact angle was not measured due to the serious deformation of the pellet surface.

The adsorption of water on graphitic pore and nanodiamonds is still challenging. There is a correlation between the maximum amount of water adsorbed and the total pore volume of micropores and small mesopores (not larger than 5 nm width) for carbon nanohorns, which are a type of hydrophobic carbons.<sup>19</sup> Carbon nanotubes show a hydrophobic surface depending on their orientation; higher hydrophobicity when they are

vertically arranged. This surface wettability can be modified by oxidation. In such a case, water percolates in the nanotube mat depending on the pores resulted from the nanotubes arrangement.<sup>32</sup> Graphitic materials have a hydrophobic surface, not adsorbing water up to relative humidity above 90%. However, they take up water even at a relative humidity as low as 50% when they possess micropores and small mesopores as part of their structure, irrespective of the presence of hydrophilic heteroatoms, explained by adsorption of water clusters.<sup>18,20</sup> In the case of nanodiamonds, the presence of micropores and small mesopores in the nanodiamond assembly is a key factor that confers special hygroscopic nature, due to a higher interaction potential from the curvature of such small cavities, and localized oxygen-containing functionalities on those pores and in the mesopore walls that attract water molecules to fill these pores.<sup>19-21</sup> Here, the pellet microstructure; that promotes water adsorption; influences the macroscopic absorption process, showing the importance of adsorbed water molecules on the hydrophilic sites for further adsorption and total absorption of water. Still, other factors such as the interconnected structure of pores, the surface roughness of the pellet and inhomogeneity of packing density need to be considered for sufficient understanding of the water-wettability and hygroscopic nature of porous materials like nanodiamond aggregates. Nevertheless, we have shown that 5.5% ( $0.03 \text{ cm}^3 \text{ g}^{-1}$  of  $0.54 \text{ cm}^3 \text{ g}^{-1}$ ) of the water is adsorbed in micropores, and the mesopores and larger pores are associated to give the total liquid water absorption capacity, as explained before. As a result, high wettability explained by a low water contact angle is desirable, but not indispensable, when the maximum absorption capacity is the most important characteristic to choose a hygroscopic material. **Figure 6-17** depicts the comparison of the maximum liquid water

absorbed by representative materials and their chemical structures: nanodiamonds, clay (Montmorillonite), zeolites (mordenite and molecular sieve 5A) and silica gel.

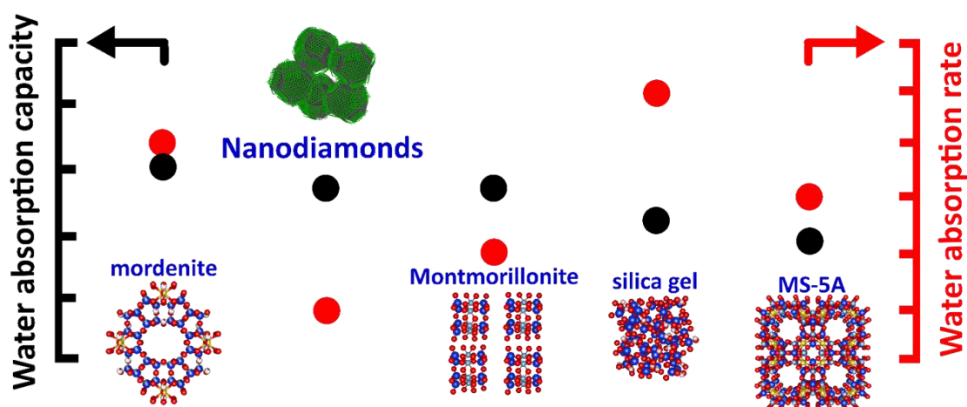


**Figure 6-17.** Maximum liquid water absorbed by representative materials: nanodiamonds, clay (Montmorillonite), zeolites (mordenite and molecular sieve 5A) and silica gel.

## 6.4 Conclusions

Nanodiamonds are hydrophobic porous materials, as revealed by water adsorption isotherms. Interestingly, nanodiamond pellets exhibit an intensive hygroscopic nature under ambient conditions in spite of the hydrophobicity at the molecular level. The measured water contact angle of nanodiamond pellets is in the order of 20-30° under ambient conditions, indicating hydrophilicity. Water wettability is a key factor in the hygroscopic nature of hydrophilic materials, such as silica gel, zeolites, and clays, which exhibit high water uptake. Previous studies discussed the hygroscopic nature of nanodiamonds only from the water wettability. The present work correlates the hygroscopic nature of nanodiamonds with their unique porosity and the water molecules pre-adsorbed in ultramicropores to induce the small contact angle with liquid water.

Furthermore, the hygroscopic nature of nanodiamonds is semi-quantitatively evaluated by the comparison of total absorption amount and absorption rate of liquid water of well-known hygroscopic porous materials such as zeolites and Montmorillonite. The total capacity of absorbed liquid water by nanodiamond pellets is larger than those capacities of zeolites ZSM-5 and MS-5A and comparable to that of Montmorillonite. On the other hand, the absorption rate of nanodiamond pellets of low-density ( $1.3 \text{ g cm}^{-3}$ ) is half of those of Montmorillonite and zeolite MS-5A. Thus, we can understand the hygroscopic nature of nanodiamonds using two comparative parameters; the total absorption amount of liquid water and the absorption rate for liquid water, which are essentially valuable for structural designing and unique application of nanodiamonds in future.

## 6.5 Acknowledgments

The work was partially supported by the Grant-in-Aid- for Scientific Research (B) (17H03039) and the OPERA project from JST.

## 6.6 References

- (1) Piña-Salazar, E.-Z.; Sagisaka, K.; Hattori, Y.; Sakai, T.; Futamura, R.; Ōsawa, E.; Kaneko, K. Electrical conductivity changes of water-adsorbed nanodiamonds with thermal treatment. *Chem. Phys. Lett. X.* **2019**, *2*, 100018. doi:10.1016/j.cpletx.2019.100018.
- (2) Ozawa, M.; Inaguma, M.; Takahashi, M.; Kataoka, F.; Krüger, A.; Ōsawa, E. Preparation and Behavior of Brownish, Clear Nanodiamond Colloids. *Adv. Mater.* **2007**, *19* (9), 1201–1206.
- (3) Pina-Salazar, E.-Z.; Urita, K.; Hayashi, T.; Futamura, R.; Vallejos-Burgos, F.;

- Włoch, J.; Kowalczyk, P.; Wiśniewski, M.; Sakai, T.; Moriguchi, I.; Terzyk, A. P.; Osawa, E.; Kaneko, K. Water Adsorption Property of Hierarchically Nanoporous Detonation Nanodiamonds. *Langmuir* **2017**, *33* (42), 11180–11188.
- (4) Petit, T.; Arnault, J. C.; Girard, H. A.; Sennour, M.; Bergonzo, P. Early Stages of Surface Graphitization on Nanodiamond Probed by X-Ray Photoelectron Spectroscopy. *Phys. Rev. B - Condens. Matter Mater. Phys.* **2011**, *84* (23), 233407.
- (5) Krueger, A.; Lang, D. Functionality Is Key: Recent Progress in the Surface Modification of Nanodiamond. *Adv. Funct. Mater.* **2012**, *22* (5), 890–906.
- (6) Carlisle, J. A.; Auciello, O. Ultrananocrystalline Diamond. *Interface-Electrochemical Soc.* **2003**, *12* (1), 28–32.
- (7) Korobov, M. V.; Batuk, M. M.; Avramenko, N. V.; Ivanova, N. I.; Rozhkova, N. N.; Osawa, E. Aggregate Structure of “Single-Nano Buckydiamond” in Gel and Dried Powder by Differential Scanning Calorimetry and Nitrogen Adsorption. *Diam. Relat. Mater.* **2010**, *19* (5), 665–671.
- (8) Kondo, T.; Kobayashi, M.; Saito, T.; Kadota, Y.; Kameshima, T.; Aikawa, T.; Kawai, T.; Yuasa, M. Micrometer-Sized Mesoporous Diamond Spherical Particles. *Diam. Relat. Mater.* **2014**, *43*, 72–79.
- (9) Korobov, M. V.; Batuk, M. M.; Avramenko, N. V.; Ivanova, N. I.; Rozhkova, N. N.; Osawa, E. Do Primary Particles of Detonation Nanodiamond Form a Secondary Structure? *Fullerenes Nanotub. Carbon Nanostructures* **2011**, *19* (1–2), 58–62.
- (10) Shenderova, O. A.; McGuire, G. E. Science and Engineering of Nanodiamond Particle Surfaces for Biological Applications (Review). *Biointerphases* **2015**, *10* (3), 030802.

- (11) Krueger, A. Diamond Nanoparticles: Jewels for Chemistry and Physics. *Adv. Mater.* **2008**, *20* (12), 2445–2449.
- (12) Ostrovskaya, L.; Perevertailo, V.; Ralchenko, V.; Dementjev, A.; Loginova, O. Wettability and Surface Energy of Oxidized and Hydrogen Plasma-Treated Diamond Films. *Diam. Relat. Mater.* **2002**, *11* (3), 845–850.
- (13) Alghunaim, A.; Kirdponpattara, S.; Newby, B. M. Z. Techniques for Determining Contact Angle and Wettability of Powders. *Powder Technol.* **2016**, *287*, 201–215.
- (14) Uddin, F. Clays, Nanoclays, and Montmorillonite Minerals. *Metall. Mater. Trans. A Phys. Metall. Mater. Sci.* **2008**, *39* (12), 2804–2814.
- (15) Yang, S.; Navrotsky, A. Energetics of Formation and Hydration of Ion-Exchanged Zeolite Y. *Microporous Mesoporous Mater.* **2000**, *37* (1–2), 175–186.
- (16) Ng, E. P.; Mintova, S. Nanoporous Materials with Enhanced Hydrophilicity and High Water Sorption Capacity. *Microporous Mesoporous Mater.* **2008**, *114*, 1–26.
- (17) Hanzawa, Y.; Kaneko, K. Lack of a Predominant Adsorption of Water Vapor on Carbon Mesopores. *Langmuir* **1997**, *13* (22), 5802–5804.
- (18) Kaneko, K. Graphitic Nanopores: Water Capture in Carbon Cuboids. *Nat. Chem.* **2015**, *7* (3), 194–196.
- (19) Pina-Salazar, E. Z.; Kaneko, K. Adsorption of Water Vapor on Mesoporosity-Controlled Single Wall Carbon Nanohorn. *Colloids Interface Sci. Commun.* **2015**, *5*, 8–11.
- (20) Ohba, T.; Kanoh, H.; Kaneko, K. Affinity Transformation from Hydrophilicity to Hydrophobicity of Water Molecules on the Basis of Adsorption of Water in Graphitic Nanopores. *J. Am. Chem. Soc.* **2004**, *126* (5), 1560–1562.
- (21) Piña-Salazar, E.-Z.; Kukobat, R.; Futamura, R.; Hayashi, T.; Sakai, T.; Ōsawa, E.;

- Kaneko, K. Water-Selective Adsorption Sites on Detonation Nanodiamonds. *Carbon* **2018**, *139*, 853–860.
- (22) Ravikovitch, P. I.; Neimark, A. V. Density Functional Theory Model of Adsorption Deformation. *Langmuir* **2006**, *22* (26), 10864–10868.
- (23) Ono, Y.; Futamura, R.; Hattori, Y.; Sakai, T.; Kaneko, K. Adsorption-desorption mediated separation of low concentrated D<sub>2</sub>O from water with hydrophobic activated carbon fiber. *J. Colloid Interface Sci.* **2017**, *508*, 14–17. doi:10.1016/j.jcis.2017.08.016.
- (24) Katsumi, K. Determination of Pore Size and Pore Size Distribution. 1. Adsorbents and Catalysts. *J. Memb. Sci.* **1994**, *96* (1–2), 59–89.
- (25) Neimark, A. V.; Lin, Y.; Ravikovitch, P. I.; Thommes, M. Quenched Solid Density Functional Theory and Pore Size Analysis of Micro-Mesoporous Carbons. *Carbon* **2009**, *47* (7), 1617–1628.
- (26) Zeiger, M.; Jäckel, N.; Aslan, M.; Weingarth, D.; Presser, V. Understanding Structure and Porosity of Nanodiamond-Derived Carbon Onions. *Carbon* **2015**, *84*, 584–598.
- (27) Thommes, M.; Kaneko, K.; Neimark, A. V.; Olivier, J. P.; Rodriguez-Reinoso, F.; Rouquerol, J.; Sing, K. S. W. Physisorption of Gases, with Special Reference to the Evaluation of Surface Area and Pore Size Distribution (IUPAC Technical Report). *Pure Appl. Chem.* **2015**, *87* (9–10), 1051–1069.
- (28) Miyawaki, J.; Kanda, T.; Kaneko, K. Hysteresis-Associated Pressure-Shift-Induced Water Adsorption in Carbon Micropores. *Langmuir* **2001**, *17* (3), 664–669.
- (29) Thommes, M.; Morell, J.; Cychosz, K. A.; Fröba, M. Combining Nitrogen, Argon,

- and Water Adsorption for Advanced Characterization of Ordered Mesoporous Carbons (CMKs) and Periodic Mesoporous Organosilicas (PMOs). *Langmuir* **2013**, *29* (48), 14893–14902.
- (30) Hansen, J. O.; Copperthwaite, R. G.; Derry, T. E.; Pratt, J. M. A Tensiometric Study of Diamond (111) and (110) Faces. *J. Colloid Interface Sci.* **1989**, *130* (2), 347–358.
- (31) Ostrovskaya, L.; Perevertailo, V.; Ralchenko, V.; Saveliev, A.; Zhuravlev, V. Wettability of Nanocrystalline Diamond Films. *Diam. Relat. Mater.* **2007**, *16* (12), 2109–2113.
- (32) Pavese, M.; Musso, S.; Bianco, S.; Giorcelli, M.; Pugno, N. An analysis of carbon nanotube structure wettability before and after oxidation treatment. *J. Phys. Condens. Matter.* **2008**, *20*,. doi:10.1088/0953-8984/20/47/474206.



## Chapter 7

### 7. Electrical conductivity changes of water-adsorbed nanodiamonds with thermal treatment<sup>1</sup>

**Abstract.** Detonation nanodiamonds hard-hydrogels are aggregates of polyhedral particles of  $sp^3$ -hybridized-carbon coated by atomically thin  $sp^2$ -hybridized carbon. Electronic properties of diamond are sensitive to water in the surrounding environment. The effect of adsorbed water on the electrical conductivity of detonation nanodiamonds was studied by exposure to humid air after thermal treatment in *vacuo*. The electrical conductivity increases with heating and decreases during the isothermal treatment at 393 K due to the release of strongly adsorbed water and gradually increases on exposing to humid air, indicating adsorption of water molecules on micropores and mesopores in the nanodiamond aggregates.

**Keywords:** nanodiamonds, electrical conductivity, outgassing, water, graphene-like carbon.

---

<sup>1</sup> Adapted from Piña-Salazar, E. Z. *et al.* (2019). Electrical conductivity changes of water-adsorbed nanodiamonds with thermal treatment. *Chem. Phys. Lett. X*, 2, 100018.

Copyright © 2019, with permission from Elsevier.

## 7.1 Introduction

Detonation nanodiamonds have a relatively high surface area, excellent mechanical properties and considerably high electrical conductivity being suitable for the development of supercapacitors and electronic devices.<sup>1</sup> Nanodiamonds are polyhedral particles (3–5 nm in diameter) of  $sp^3$ -hybridized carbon coated with graphene-like films. They have aggregate structures of micropores and mesopores where water and other molecules are adsorbed.<sup>2</sup>

Non-oxidized carbon surfaces are basically hydrophobic, although nanoporous carbons can adsorb sufficiently water vapor.<sup>3–5</sup> Nanodiamond aggregates are almost hydrated under exposure to atmospheric air.<sup>6–10</sup> The hydrated water can be released by outgassing. This water consists of strongly and weakly bound water molecules in micropores and mesopores.<sup>2</sup> In particular, water molecules adsorbed in ultramicropores cannot be easily desorbed under mild evacuation conditions.<sup>4,11</sup> Hence, water bound on the detonation nanodiamond aggregates must be studied with an adsorbed water-sensitive method. The electrical conductivity of detonation nanodiamonds is in the order of  $10^{-11}$   $\text{Ohm}^{-1} \text{cm}^{-1}$ ,<sup>12</sup> depending on the presence of defects, impurities or dopants. Electronic properties of carbon materials are sensitive to adsorption of water and oxygen from the surrounding environment.<sup>13</sup> Therefore, their sensor applications have been studied.<sup>14–16</sup> Changes in the electrical conductivity of nanodiamonds with the presence of water were reported.<sup>17</sup> The present chapter discusses the relationship between the electrical conductivity change and adsorbed water on different sites of the nanodiamonds.

## **7.2 Experimental section**

### **7.2.1 Electrical conductivity measurement**

The electrical conductivity of nanodiamonds was measured with a two-probe electrical resistance system for powdered and pelletized samples of nanodiamonds by using a compressor device coupled to a *vacuum* chamber to evaluate quantitatively the electrical conductivity with water adsorption. The ground nanodiamonds (Hard hydrogel; Nano-Carbon Research Institute, Ltd., Japan) were placed in the chamber in *vacuo* at 303 K for 30 min. After that, a gradual compression with the pressure from 0.1 to 1.0 MPa was applied to produce the pelletized nanodiamonds; the electrical resistance was measured with the compression at intervals of 0.1 MPa up to 1.0 MPa. The sample was thermally treated as follows: heated up gradually to 393 K, isothermally heated at 393 K for 4.5 h and then cooled down to 303 K. Two cycles of heating up and cooling down of the nanodiamond pellets were performed. Afterward, we measured the electrical conductivity of the nanodiamond pellets on exposure to humid air. The electrical conductivity of the nanodiamond pellet was determined using the cross-sectional area (diameter = 0.5 cm) and the thickness of the nanodiamond pellet.

### **7.2.2 Characterization**

The nitrogen adsorption isotherms of nanodiamonds were measured at 77 K with a volumetric apparatus (Quantachrome-Autosorb IQ2). The adsorption isotherms were analyzed by the Brunauer–Emmett–Teller (BET) and subtracting pore effect (SPE) methods to obtain the pore structures. Water adsorption isotherms at 298 K were measured in a volumetric apparatus VSTAR-Quantachrome. Surface chemistry of nanodiamonds was studied by X-ray photoelectron spectra (XPS) analysis by using a monochromatized

Al K $\alpha$  X-ray 12 kV source with an AXIS-ULTRA, Kratos equipment. The XPS spectra for as-received nanodiamonds and nanodiamonds treated at 393 K in 10<sup>-1</sup> Pa for 4.5 h were taken. Calibration of the C1s signal was at 285  $\pm$  0.2 eV corresponding to nanodiamond carbon. C1s was deconvoluted into four peaks using sp<sup>2</sup>-hybridized carbon at 284.1 eV, sp<sup>3</sup>-hybridized carbon at 285.2 eV, C-H bonds and C-N at 286.3 eV and C-O bonds at 287.7 eV. Isothermal thermogravimetric analysis of nanodiamonds at 393 K was conducted under argon (300 mL min<sup>-1</sup>) with a heating rate of 5.0 K min<sup>-1</sup> using a Thermal Analysis System (STA7200, Hitachi) in order to determine the sample weight loss during heating. Hall mobility was measured up to 20 h of outgassing at room temperature by using a DC/AC Hall measurement system 8400 (Lake shore cryotronics).

## 7.3 Results and discussion

### 7.3.1 Effect of thermal outgassing on the morphology and surface chemistry of nanodiamonds

Morphological and chemical structures of the nanodiamonds by use of SEM, TEM, XRD, and EELS were reported previously.<sup>2,11</sup> The effect of thermal outgassing on the surface chemistry of nanodiamonds is shown in **Figure 7-1**. As we need to determine the amount of desorbed water on heating in *vacuo*, we isothermally heated nanodiamonds at 393 K for 4.5 h (being the same conditions for the electrical resistivity experiment). There is a slight weight loss after heating 4.5 h at 393 K, as shown in **Figure 7-1a**. This plot indicates two-step desorption of weakly adsorbed water and of strongly adsorbed water.<sup>11,18</sup> **Figure 7-1b** and **Table 7-1** show XPS results of nanodiamonds before and after heating in *vacuo* at 393 K for 4.5 h; nanodiamonds are mainly composed of sp<sup>3</sup>-hybridized carbon with the presence of sp<sup>2</sup>-hybridized carbon, and hydrogen and nitrogen

bonded to carbon. Traces of substitutional nitrogen are incorporated in the nanodiamond lattices, while oxygen (10 at.%) is bonded to carbon on the surface. There is negligible surface chemistry change after outgassing at 393 K for 4.5 h. Therefore, the weight loss after heating corresponds to water desorbed on nanodiamonds, as explained above.

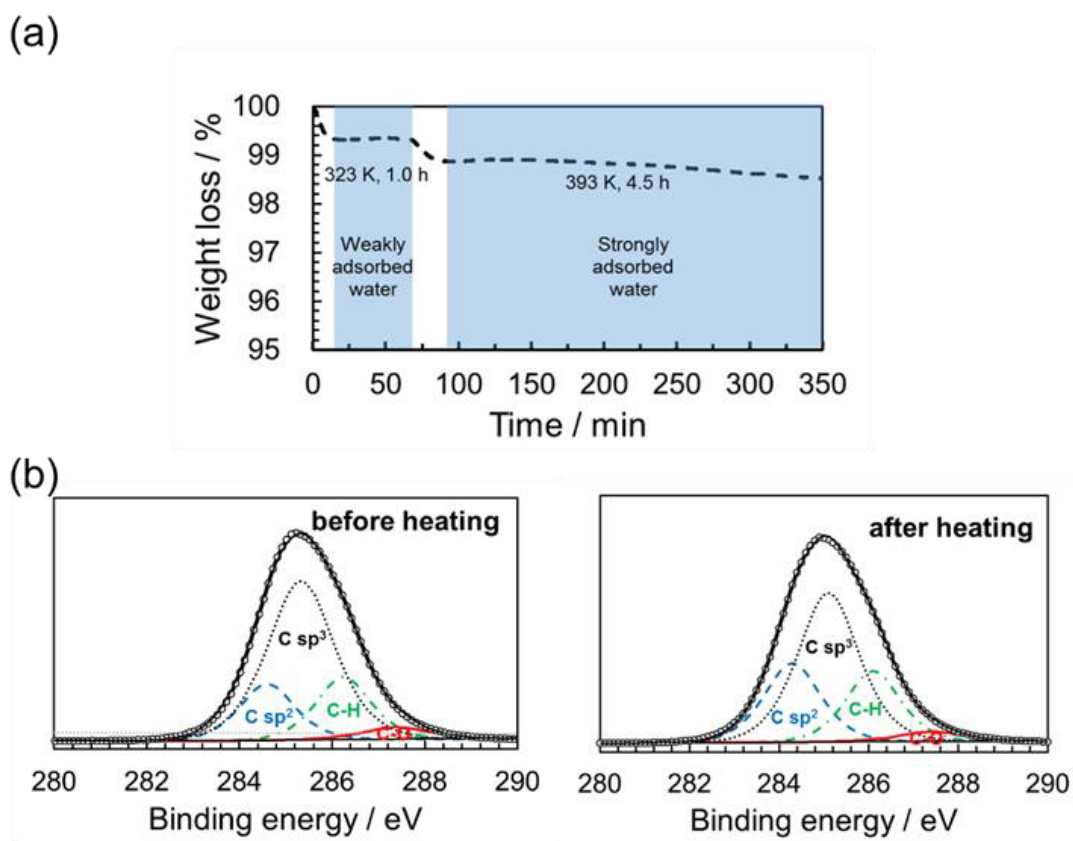


**Figure 7-1.** (a) Isothermal gravimetric analysis of nanodiamonds heated at 393 K for 4.5 h in argon, and (b) high-resolution C1s XPS spectra of nanodiamonds before and after heating at 393 K for 4.5 h. Open circles indicate experimental data and straight lines indicates fitted data on deconvolution.

**Table 7-1.** Constituents of C1s (at.%) from XPS analysis of nanodiamonds before and after thermal treatment in *vacuo*.

C1s components	non-heated ND			ND heated at 393 K for 4.5 h		
	Position	FWHM	% Area	Position	FWHM	% Area
C sp <sup>2</sup>	284.5	1.45	23.4	284.3	1.45	24.7
C sp <sup>3</sup>	285.3	1.65	54.2	285.1	1.65	52.5
C-H, C-N	286.2	1.40	19.1	286.1	1.40	19.3
C-O	287.4	1.70	3.3	287.4	1.70	3.5

Fitting accuracy: >95%, G-L (60-40), FWHM 1.55 + 0.15 eV

### 7.3.2 Effect of heating and compression on the porosity of nanodiamonds

Effects of heating and compression on the porosity of nanodiamonds were evaluated by nitrogen adsorption isotherms at 77 K, as shown in **Figure 7-2** and **Table 7-2**.

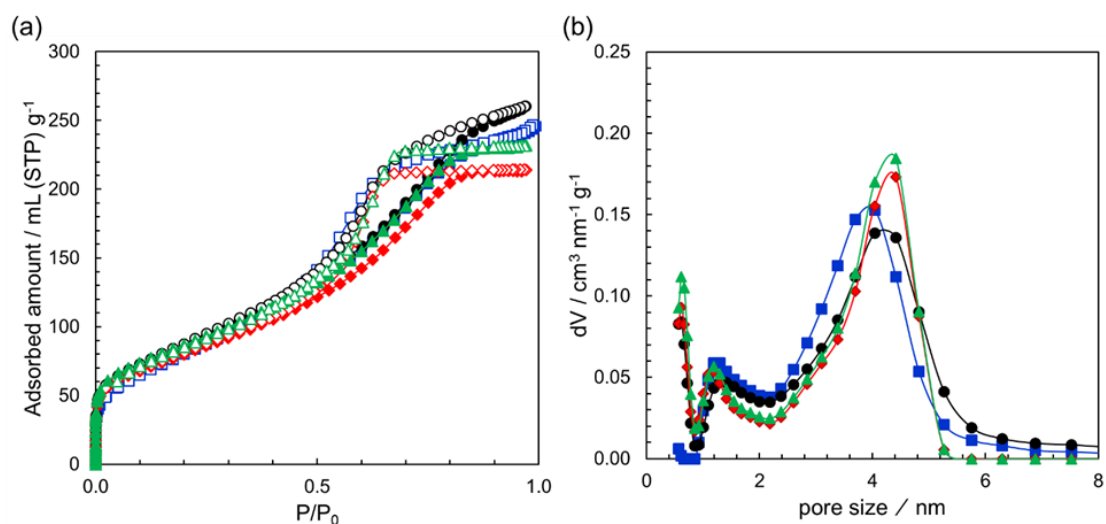


**Figure 7-2.** (a) Nitrogen adsorption isotherms at 77 K and (b) QS-DFT derived-pore size distribution of nanodiamonds without treatment ( $\diamond$ ), heated at 393 K for 4.5 h in *vacuo* before grinding ( $\Delta$ ), after grinding ( $\circ$ ) and as a pellet ( $\square$ ). In (a) solid and open symbols indicate adsorption and desorption branches, respectively.

The adsorption isotherms in **Figure 7-2a** are typical IUPAC Type IV having a sharp uptake due to adsorption in small micropores up to  $P/P_0 = 10^{-2}$  and gradual adsorption in larger micropores and mesopores up to  $P/P_0 = 0.8$ . The average pore volume and surface area (SPE/BET) of  $0.33 \text{ cm}^3 \text{ g}^{-1}$  and  $250/280 \text{ m}^2 \text{ g}^{-1}$ , respectively. A noticeable hysteresis loop is observed in the  $P/P_0$  range of 0.5–0.8, stemming from capillary condensation in mesopores.<sup>2,19</sup>

**Table 7-2.** Pore parameters from nitrogen adsorption isotherms at 77 K of nanodiamonds before and after outgassing.

Sample	Total pore volume $P/P_0 = 0.97$ $\text{cm}^3 \text{ g}^{-1}$	Micropore volume DFT (< 2 nm) $\text{cm}^3 \text{ g}^{-1}$	Mesopore volume DFT (2-6 nm) $\text{cm}^3 \text{ g}^{-1}$	Surface area SPE/BET $\text{m}^2 \text{ g}^{-1}$	Internal surface area SPE $\text{m}^2 \text{ g}^{-1}$	External surface area SPE $\text{m}^2 \text{ g}^{-1}$
ND	0.33	0.06	0.26	250/280	247	3
ND-h	0.36	0.06	0.27	270/310	265	5
ND-h-gs	0.40	0.06	0.33	235/320	215	20
ND-h-ps	0.38	0.05	0.31	175/260	161	14

ND: nanodiamonds, ND-h: heated ND, ND-h-gs: heated ground nanodiamonds, ND-h-ps: heated nanodiamond pellet. Heating treatment at 393 K for 4.5 in *vacuo*.

**Figure 7-3** shows the corresponding  $\alpha_s$ -plots of nanodiamonds used to determine external and internal surface areas by SPE method, which is effective for pore analysis of porous carbons without overestimation of the surface area.<sup>20,21</sup> The internal surface area accounts for the pores in the nanodiamond aggregates. This area is predominant over the external one in all cases. Therefore, the ratio of external to internal surface area is less

than 0.1 indicating that most of the total surface area of nanodiamonds aggregates derives from the interparticle pores. The average pore width is 4.5 nm, as shown in **Figure 7-2b**. Heat-treatment in *vacuo* and the compression treatment increase slightly mesopore volume. Thus, the pore structure of nanodiamonds has stability against heat-treatment in *vacuo* and compression.

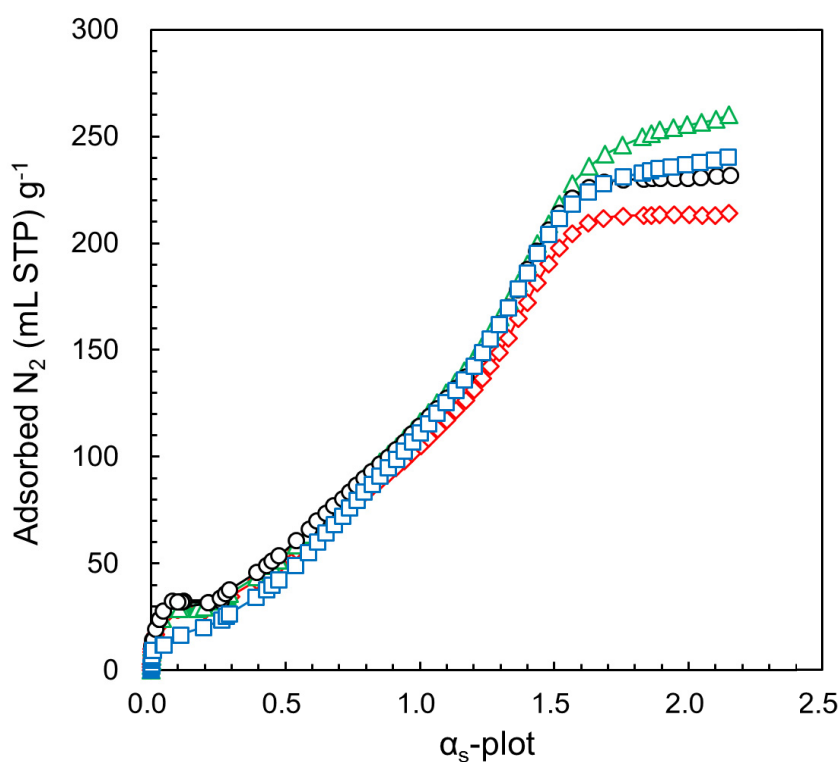


**Figure 7-3.**  $\alpha_s$ -plots of nanodiamonds without treatment ( $\diamond$ ) and outgassed at 393 K for 4.5 h in *vacuo* before grinding ( $\Delta$ ), after grinding ( $\circ$ ) and as a pellet ( $\square$ ).

**Figure 7-4a** and **Figure 7-4b** show the nitrogen adsorption isotherms at 77 K expressed as liquid volume for nanodiamonds before and after heating at 393 K for 4.5 h in *vacuo*. Water adsorption isotherms at 298 K in **Figure 7-4c** show that the outgassed nanodiamonds give a larger adsorption amount in the low relative pressure.

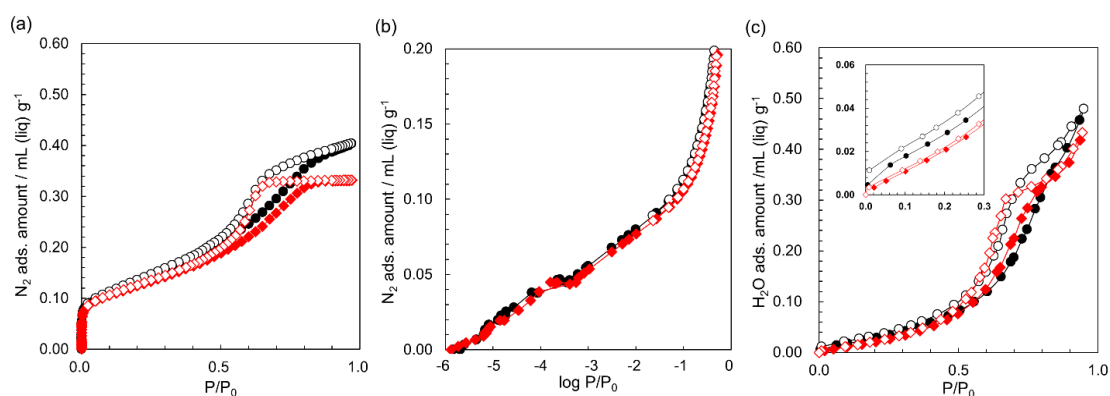


**Figure 7-4.** Nitrogen adsorption isotherms at 77 K in (a) lineal scale and (b) logarithmic scale. (c) Water adsorption isotherms at 298 K and a closer look at  $P/P_0 < 0.3$ , of nanodiamonds before treatment ( $\diamond$ ) and after outgassing at 393 K for 4.5 h ( $\circ$ ). Solid and open symbols indicate adsorption and desorption branches, respectively.

### 7.3.3 Effect of compression on the electrical conductivity on nanodiamonds

Effect of compression on the electrical conductivity of nanodiamonds was measured at 303 K under atmospheric conditions and in *vacuo*. The initial electrical conductivities were  $2.5 \times 10^{-5}$  and  $2.5 \times 10^{-7}$   $\text{Ohm}^{-1} \text{cm}^{-1}$  under atmospheric conditions and in *vacuo*, respectively, as shown in **Figure 7-5**. The stepwise compression from atmospheric pressure to 1.0 MPa was applied to nanodiamond powder in *vacuo*. The compression increased the electrical conductivities up to  $4.0 \times 10^{-2}$  and  $4.0 \times 10^{-7}$   $\text{Ohm}^{-1} \text{cm}^{-1}$  in atmospheric conditions and in *vacuo*, respectively. Similarly, the compression increased the sample density by 20% (from  $1.05 \text{ g-ND cm}^{-3}$  to  $1.3 \text{ g-ND cm}^{-3}$ ). The compression effect on electrical conductivity is more evident under atmospheric conditions due to more water adsorbed than in *vacuo*.

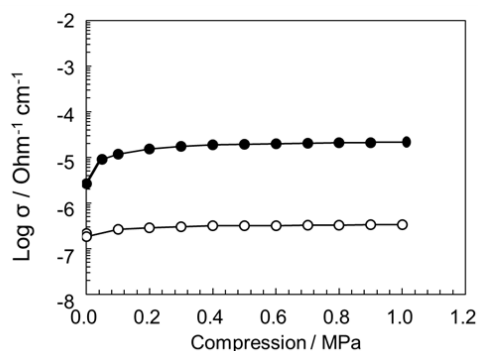


**Figure 7-5.** Effect of compressing pressure on the electrical conductivity of nanodiamonds under atmospheric conditions (●) and in *vacuo* (○).

### 7.3.4 Effect of water adsorption on the electrical conductivity of nanodiamonds

Effect of water adsorption on the electrical conductivity of nanodiamonds is shown in **Figure 7-6**. The electrical conductivity of nanodiamonds depends on the temperature and exposure to humid air. First, the electrical conductivity of the nanodiamond pellet ( $3.4 \times 10^{-7} \text{ Ohm}^{-1} \text{ cm}^{-1}$ ) increases by 17% ( $2.0 \times 10^{-6} \text{ Ohm}^{-1} \text{ cm}^{-1}$ ) on heating from 303 K to 393 K. This value decreases by 35 times ( $2.0 \times 10^{-6} \text{ Ohm}^{-1} \text{ cm}^{-1}$  to  $5.6 \times 10^{-8} \text{ Ohm}^{-1} \text{ cm}^{-1}$ ) after heating at 393 K for 4.5 h and finally reaches  $4.0 \times 10^{-9} \text{ Ohm}^{-1} \text{ cm}^{-1}$  on cooling down to 303 K. A second heating cycle slightly increases electrical conductivity by 15%. The final electrical conductivity of nanodiamonds at 303 K is  $4.0 \times 10^{-9} \text{ Ohm}^{-1} \text{ cm}^{-1}$ . There is a clear hysteresis in the first cycle of electrical conductivity through the thermal treatment but not in the second one. The higher electrical conductivity observed during the first cycle indicates that water adsorbed on the nanodiamond aggregates enhances electrical conductivity, while the dry nanodiamonds in the second cycle have a lower electrical conductivity. Further cooling or heating of the outgassed sample exhibits no significant change. The temperature dependence of the electrical conductivity over the

range of 303 to 393 K gives the activation energy for conduction of 0.3 eV. The activation energy ( $E_a = 0.2$  eV) does not significantly change on heating at 393 K for 4.5 h in *vacuo* in the successive cycle. Effect of exposure to humid air on the electrical conductivity of outgassed nanodiamonds provides important information on the influence of adsorbed water. The blue line in **Figure 7-6a** shows the enhancement of the electrical conductivity on exposing to humid air. The time changes in electrical conductivity are shown in **Figure 7-6b**.

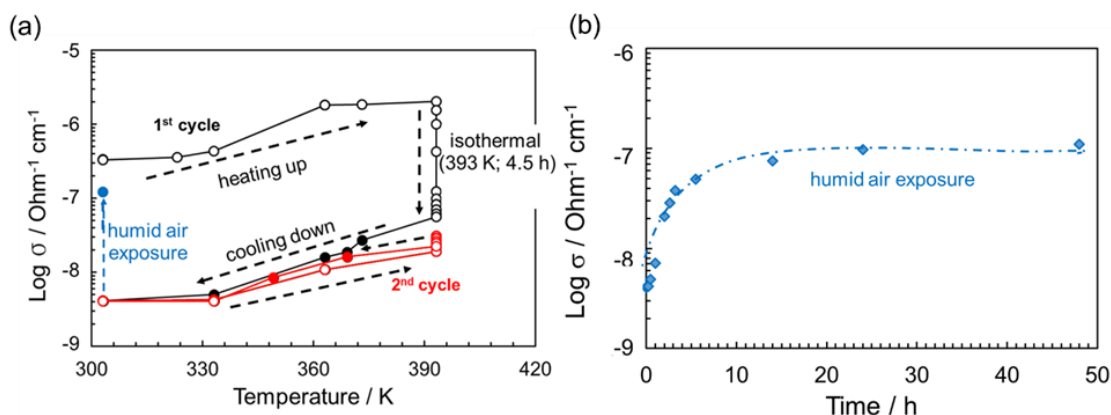


**Figure 7-6.** (a) Electrical conductivity ( $\sigma$ ) change of nanodiamonds with heating treatment in *vacuo* and upon exposure to humid air, and (b) change of electrical conductivity of nanodiamonds with the time after the exposure to humid air.

**Figure 7-7** shows that electrical conductivity of nanodiamonds is not significantly enhanced during the first 15 min after exposure to humid air. The considerable increment of electrical conductivity is observed after several hours, reaching a plateau. The higher electrical conductivity is obtained on exposure to 75% RH for 10–14 h, giving  $1.0 \times 10^{-7}$   $\text{Ohm}^{-1} \text{cm}^{-1}$  (nearly 30 times higher than in the dry state). There is no agreement between

the electrical conductivities of the nanodiamonds pellet before outgassing and after the exposure to humid air. This phenomenon should be associated with the packing structure difference between water-adsorbed and dry nanodiamonds. The drier nanodiamond pellet shows lower porosity, as seen in **Figure 7-2b**.

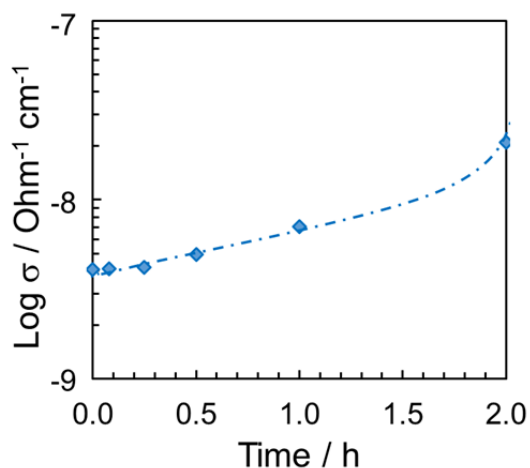


**Figure 7-7.** Time course of electrical conductivity ( $\sigma$ ) of nanodiamonds on the exposure to humid air during the first hours.

The outgassing time dependence of electrical conductivity, Hall mobility, and carrier concentration are shown in **Figure 7-8**. The longer the outgassing time, the slightly the lower the concentration of carriers. Carrier mobility refers in general to both electron and hole mobility. Therefore, the total carrier concentration refers to the sum of electrons (p-type) and holes (n-type) carrier in the system. The measured carrier mobility is expressed as "Hall mobility" since it was measured using the Hall effect. Hall effect; discovered by Edwin Hall in 1879; refers to the production of a difference of voltage (Hall voltage) across an electrical conductor, transverse to an electric current in the conductor and to an applied magnetic field perpendicular to the current. Our results suggest that the longer the

outgassing time, the slightly the lower the concentration of carriers, due to the loss of hydronium ions ( $\text{H}_3\text{O}^+$ ) that act as n-type charge carriers.

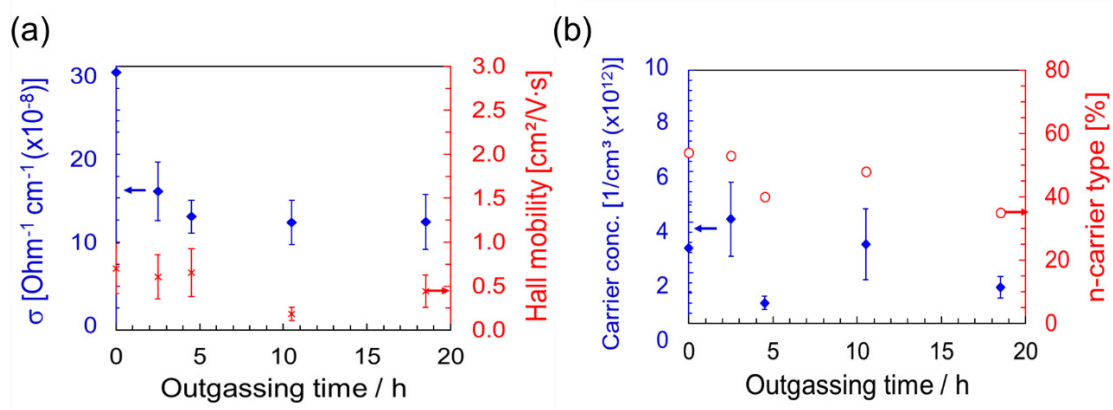


**Figure 7-8.** (a) Electrical conductivity “ $\sigma$ ”, Hall mobility and (b) carrier concentration dependence of outgassing time.

The previous studies on the electrical conductivity of nanodiamond powders and carbon nanotube mats show the increase of the electrical conductivity in the presence of water vapor.<sup>17,22</sup> In this study, we attempt to clarify the electrical conductivity changes from adsorption of water vapor in the micropores and mesopores of the nanodiamond aggregates.

The electrical conductivity changes with the treatments using an adsorption model of water molecules in pores of the nanodiamonds are depicted in **Figure 7-9**. Compressing nanodiamonds slightly reduces pores in the nanodiamond aggregates, yielding a slight increase in electrical conductivity. The heat treatment in *vacuo* removes adsorbed water molecules from the nanodiamond aggregates, dropping the electrical conductivity in two orders of magnitude. Exposure of nanodiamonds to the humid air recovers gradually the

electrical conductivity. The mechanism of the electrical conductivity changes of nanodiamond aggregates under humid air is as follows: initially, water molecules adsorb as a monolayer on the micropores of the nanodiamond aggregates; which act as selective sites for adsorption of water molecules. Multilayer physical adsorption of water molecules and additional pore filling occur with the increase of the humidity. Adsorbed water molecules are ionized producing hydronium ions ( $\text{H}_3\text{O}^+$ ) as charge carriers in a similar way to bulk liquid water.<sup>23</sup> Multilayer adsorbed water induces proton hopping conduction between adjacent water molecules with charge transport taking place via the conductivity generated by the Grotthuss chain reaction  $\text{H}_2\text{O} + \text{H}_3\text{O}^+ \rightarrow \text{H}_3\text{O}^+ + \text{H}_2\text{O}$ .<sup>24</sup> Additionally, we propose a scheme of the changes of the electrical conductivity of nanodiamonds as an electric circuit indicating that conductance is a function of water molecules adsorbed in micropores and mesopores, as shown in **Figure 7-10**.

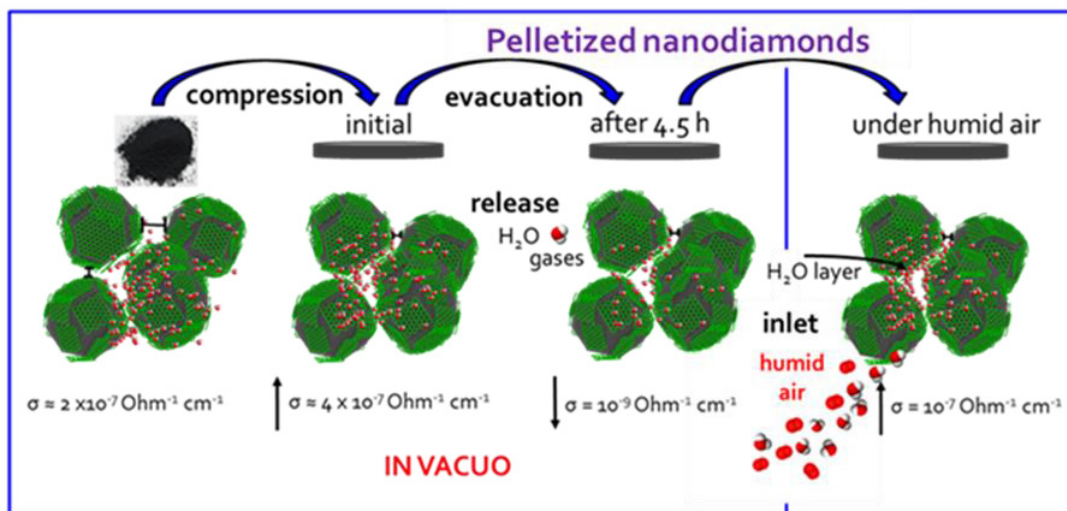
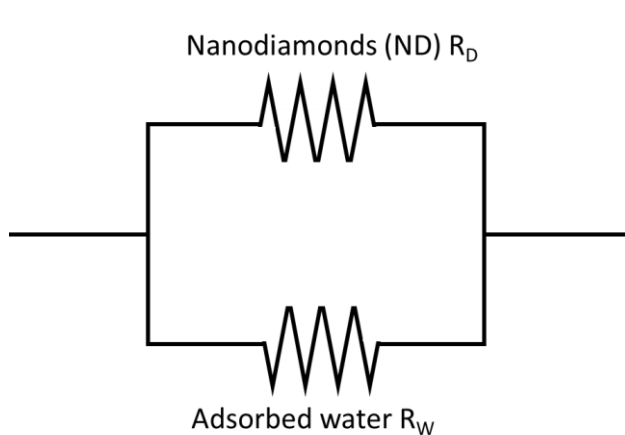


**Figure 7-9.** Mechanism of changes in the electrical conductivity of nanodiamonds pellet upon evacuation (393 K for 4.5 h in *vacuo*) and exposure to humid air.



$$\frac{1}{R} = \frac{1}{R_D} + \frac{1}{R_W}$$

$$\frac{1}{R} = \frac{R_D + R_W}{R_D R_W} = G$$

$$G = \frac{1 + \frac{R_W}{R_D} \approx 0}{R_W} = \frac{1}{R_W}$$

where

$G$  = conductance

$R_D$  = nanodiamond resistance

$R_W$  = water resistance

Here  $G$  is a function of water molecules adsorbed in micropores and mesopores.

**Figure 7-10.** Dependence of electrical conductivity of nanodiamonds as a function of adsorbed water, schematized by a parallel electrical equivalent circuit model of water adsorbed on the nanodiamond pellet.

## 7.4 Conclusions

We elucidated the presence of weakly and strongly adsorbed water on nanodiamond aggregates with the electrical conductivity measurement by changing of heat-treatment and evacuation conditions. Water molecules adsorbed in mesopores of nanodiamond aggregates are easily desorbed by heating in *vacuo* at 393 K. Desorption of loosely adsorbed water in mesopores induces the decrease of electrical conductivity, whereas the exposure to humid air causes adsorption in mesopores, causing the rapid increase of electrical conductivity. On the other hand, it takes a long time for water molecules to be

adsorbed strongly in the interstitial ultramicropores of nanodiamond aggregates, leading to the observed delayed increase of the electrical conductivity on exposure to humidity.

## 7.5 Acknowledgments

The work was partially supported by the Grant-in-Aid- for Scientific Research (B) (17H03039) and the OPERA project from JST.

## 7.6 References

- (1) Kovalenko, I.; Bucknall, D. G.; Yushin, G. Detonation Nanodiamond and Onion-like-Carbon-Embedded Polyaniline for Supercapacitors. *Adv. Funct. Mater.* **2010**, *20* (22), 3979–3986.
- (2) Pina-Salazar, E.-Z.; Urita, K.; Hayashi, T.; Futamura, R.; Vallejos-Burgos, F.; Włoch, J.; Kowalczyk, P.; Wiśniewski, M.; Sakai, T.; Moriguchi, I.; Terzyk, A. P.; Osawa, E.; Kaneko, K. Water Adsorption Property of Hierarchically Nanoporous Detonation Nanodiamonds. *Langmuir* **2017**, *33* (42), 11180–11188.
- (3) Fowkes, F. M.; Harkins, W. D. The State of Monolayers Adsorbed at the Interface Solid-Aqueous Solution. *J. Am. Chem. Soc.* **1940**, *62* (12), 3377–3386.
- (4) Pina-Salazar, E. Z.; Kaneko, K. Adsorption of Water Vapor on Mesoporosity-Controlled Single Wall Carbon Nanohorn. *Colloids Interface Sci. Commun.* **2015**, *5*, 8–11.
- (5) Kaneko, K. Graphitic Nanopores: Water Capture in Carbon Cuboids. *Nat. Chem.* **2015**, *7* (3), 194–196.
- (6) Ji, S.; Jiang, T.; Xu, K.; Li, S. FTIR Study of the Adsorption of Water on Ultradispersed Diamond Powder Surface. *Appl. Surf. Sci.* **1998**, *133* (4), 231–238.

- (7) Korobov, M. V.; Avramenko, N. V.; Bogachev, A. G.; Rozhkova, N. N.; Ōsawa, E. Nanophase of Water in Nano-Diamond Gel. *J. Phys. Chem. C* **2007**, *111* (20), 7330–7334.
- (8) Korobov, M. V.; Batuk, M. M.; Avramenko, N. V.; Ivanova, N. I.; Rozhkova, N. N.; Osawa, E. Aggregate Structure of “Single-Nano Buckydiamond” in Gel and Dried Powder by Differential Scanning Calorimetry and Nitrogen Adsorption. *Diam. Relat. Mater.* **2010**, *19* (5), 665–671.
- (9) Batsanov, S. S.; Batsanov, A. S. Effect of Diamond on Structure and Properties of Confined Water. *Chem. Phys. Lett.* **2016**, *651*, 8–12.
- (10) Petit, T.; Puskar, L.; Dolenko, T.; Choudhury, S.; Ritter, E.; Burikov, S.; Laptinskiy, K.; Brzustowski, Q.; Schade, U.; Yuzawa, H.; Nagasaka, M.; Kosugi, N.; Kurzyp, M.; Venerosy, A.; Girard, H.; Arnault, J. C.; Osawa, E.; Nunn, N.; Shenderova, O.; Aziz, E. F. Unusual Water Hydrogen Bond Network around Hydrogenated Nanodiamonds. *J. Phys. Chem. C* **2017**, *121* (9), 5185–5194.
- (11) Piña-Salazar, E.-Z.; Kukobat, R.; Futamura, R.; Hayashi, T.; Sakai, T.; Ōsawa, E.; Kaneko, K. Water-Selective Adsorption Sites on Detonation Nanodiamonds. *Carbon* **2018**, *139*, 853–860.
- (12) Belobrov, P. I.; Bursill, L. A.; Maslakov, K. I.; Dementjev, A. P. Electron Spectroscopy of Nanodiamond Surface States. *Appl. Surf. Sci.* **2003**, *215*, 169–177.
- (13) Chakrapani, V.; Angus, J. C.; Anderson, A. B.; Wolter, S. D.; Stoner, B. R.; Sumanasekera, G. U. Charge Transfer Equilibria Between Diamond and an Aqueous Oxygen Electrochemical Redox Couple. *Science (80-. )*. **2007**, *318* (5855), 1424–1430.
- (14) Collins, P. G. Extreme Oxygen Sensitivity of Electronic Properties of Carbon

- Nanotubes. *Science* (80-. ). **2009**, *1801* (2000), 1801–1805.
- (15) Kong, J.; Franklin, N. R.; Zhou, C.; Chapline, M. G.; Peng, S.; Cho, K.; Dai, H. Nanotube Molecular Wires as Sensors. *Science* (80-. ). **2000**, *287*, 622–625.
- (16) Rebollo-Plata, B.; Munoz-Sandoval, E.; Lopez-Urias, F.; Hernandez-Cortina, E. L.; Terrones, H.; Terrones, M. Efficient Vapor Sensors Using Foils of Dispersed Nitrogen-Doped and Pure Carbon Multiwalled Nanotubes. *J. Nanosci. Nanotechnol.* **2010**, *10* (6), 3965–3972.
- (17) Denisov, S. A.; Sokolina, G. A.; Bogatyreva, G. P.; Grankina, T. Y.; Krasil'nikova, O. K.; Plotnikova, E. V.; Spitsyn, B. V. Adsorption and Electrical Properties of Nanodiamond Powders in the Presence of Water Vapor. *Prot. Met. Phys. Chem. Surfaces* **2013**, *49* (3), 286–291.
- (18) Szymański, G. S.; Karpiński, Z.; Biniak, S.; Świątkowski, A. The Effect of the Gradual Thermal Decomposition of Surface Oxygen Species on the Chemical and Catalytic Properties of Oxidized Activated Carbon. *Carbon* **2002**, *40* (14), 2627–2639.
- (19) Thommes, M.; Kaneko, K.; Neimark, A. V.; Olivier, J. P.; Rodriguez-Reinoso, F.; Rouquerol, J.; Sing, K. S. W. Physisorption of Gases, with Special Reference to the Evaluation of Surface Area and Pore Size Distribution (IUPAC Technical Report). *Pure Appl. Chem.* **2015**, *87* (9–10), 1051–1069.
- (20) Kaneko, K.; Ishii, C.; Ruike, M.; Kuwabara, H. Origin of Superhigh Surface Area and Microcrystalline Graphitic Structures of Activated Carbons. *Carbon* **1992**, *30* (7), 1075–1088.
- (21) Setoyama, N.; Suzuki, T.; Kaneko, K. Simulation Study on the Relationship between a High-Resolution  $\alpha_s$ -Plot and the Pore Size Distribution for Activated

Carbon. *Carbon* **1998**, *36* (10), 1459–1467.

- (22) Zahab, A.; Spina, L.; Poncharal, P.; Marliere, C. Water-Vapor Effect on the Electrical Conductivity of a Single-Walled Carbon Nanotube Mat. *Phys. Rev. B* **2000**, *62* (15), 10000–10003.
- (23) Bi, H.; Yin, K.; Xie, X.; Ji, J.; Wan, S.; Sun, L.; Terrones, M.; Dresselhaus, M. S. Ultrahigh Humidity Sensitivity of Graphene Oxide. *Sci. Rep.* **2013**, *3* (5 V), 1–7.
- (24) Gao, W.; Singh, N.; Song, L.; Liu, Z.; Reddy, A. L. M.; Ci, L.; Vajtai, R.; Zhang, Q.; Wei, B.; Ajayan, P. M. Direct Laser Writing of Micro-Supercapacitors on Hydrated Graphite Oxide Films. *Nat. Nanotechnol.* **2011**, *6* (8), 496–500.



## Chapter 8

### 8. Adsorption of water vapor on mesoporosity-controlled single-wall carbon nanohorn<sup>1</sup>

**Abstract.** The adsorption mechanism of water vapor in hydrophobic carbon mesopores is not clearly understood. Single-wall carbon nanohorns (SWCNH) having different tube diameters in the range of 2 to 6 nm were oxidized at a lower temperature than the widely used temperature of 823 K. Oxidation at 633 K can selectively open thinner tubes of SWCNH and then the oxidation at different times can control the mesoporosity. The porosity of the oxidized SWCNH was evaluated from the nitrogen adsorption isotherms at 77 K. The pore volume ratio of micropores to mesopores was in the range of 0.50 to 0.90. The linear relationship between water adsorption amount and the pore volume of micropores and small mesopores (< 5 nm) was observed, showing that water molecules are adsorbed even in small mesopores by the cluster-mediated filling mechanism as well as in micropores.

---

<sup>1</sup> Adapted from Pina-Salazar, E. Z. *et al.* (2015). Adsorption of water vapor on mesoporosity-controlled single wall carbon nanohorn. *Colloids Interface Sci. Commun.*, 5, 8-11.

Copyright © 2015, with permission from Elsevier.

## 8.1 Introduction

Carbon surfaces are basically hydrophobic, although the contact angle of graphite surfaces for liquid water is still controversial.<sup>1,2</sup> Water vapor is not adsorbed on crystalline carbon blacks below  $P/P_0 = 0.9$ .<sup>3</sup> On the other hand, water molecules are adsorbed on activated carbon without oxidation treatment even below  $P/P_0 = 0.9$ .<sup>4,5</sup> For example, the adsorption isotherm of pitch-based activated carbon fibers (ACFs) on which surface functional groups are the least of various ACFs rises steeply above  $P/P_0 = 0.5$ , depending on the pore width; the larger the pore width, the larger the rising  $P/P_0$ .<sup>6</sup> Furthermore, the adsorption amount is often larger than 1 g-water per g-carbon. This rising pressure is not described by the Kelvin equation and therefore the adsorption of water vapor on activated carbons is not described by the conventional capillary condensation mechanism.<sup>7</sup> Ohba *et al.* (2004) have shown that cluster formation of water molecules is indispensable to induce the predominant water adsorption on activated carbon above  $P/P_0 = 0.5$ ; they indicated that the size of the water clusters should match with pore width.<sup>8</sup> Hanzawa and Kaneko (1997) explicitly showed that water molecules were not adsorbed in mesopores of 28 nm in width, but in micropores of 0.7 nm in width in case of activated carbon aerogel.<sup>7</sup> However, still we do not understand adsorption of water in small carbon mesopores whose width is less than 10 nm, although Thommes *et al.* (2013) started to study water vapor adsorption on ordered mesoporous carbon.<sup>9</sup> Single-wall carbon nanohorn (SWCNH) are one of the single-wall carbon nanotubulites, being better characterized porous carbons than activated carbon.<sup>10</sup> Transmission electron microscopic (TEM) observations showed that a SWCNH particle had a tube and a tip structure, where the tube diameter was in the range of 2 to 6 nm.<sup>10</sup> Raman spectroscopy and electrical conductivity studies elucidated that the single carbon wall of SWCNH was less-crystalline, being

different from that of single-wall carbon nanotubes. Utsumi *et al.* (2005) reported that simple oxidation using oxygen gives nanoscale windows on the single graphene wall; the oxidation at 823 K provides the high surface area of  $1420 \text{ m}^2 \text{ g}^{-1}$  due to the formation of nanoscale windows (nanowindows) on the graphene wall.<sup>10</sup> Consequently, SWCNH having nanowindows, are an optimum model of porous carbons for the study on the relationship between water adsorption and small mesoporosity, whose width is less than 6 nm. This article reports water vapor adsorption isotherms of SWCNH of different mesoporosity obtained by oxidation at temperatures lower than 823 K.

## **8.2 Experimental section**

### **8.2.1 Opening of SWCNH**

SWCNH was purchased from NEC (purity > 85%), and it was used without further purification. The main impurity is graphite. Thermal gravimetric (TG) analysis of SWCNH was carried out under flow of a He (80%)-O<sub>2</sub> (20%) mixed gas with a flow rate of  $10 \text{ K min}^{-1}$ . Evolved gases during the TG measurement were analyzed by mass spectrometry (TG-DTA-PIMS, Rigaku Co.). We oxidized SWCNHs at temperatures lower than 823 K which gave the highest porosity in the preceding study. SWCNHs were oxidized in the temperature range of 573 to 633 K under the He-O<sub>2</sub> mixed gas ( $100 \text{ mL min}^{-1}$ ) for different periods of “zero” to 12 h. Here “zero” means that oxidation stopped just after reaching the target temperature. Since oxidation at 823 K should produce nanoscale windows whose size is widely distributed, oxidation temperatures as low as 633 K in reference to TG results were used (**Figure 8-1**).

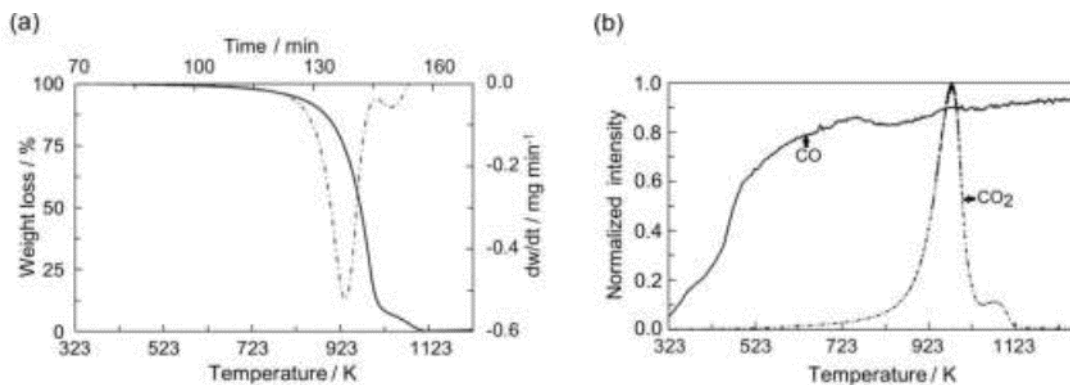


**Figure 8-1.** (a) TG analysis of SWCNH under He-O<sub>2</sub> (80/20%); weight loss (—) and derivative of TG curve (...), (b) Evolved gases on the course of TG measurement of SWCNH; CO (m/z = 28) and CO<sub>2</sub> (m/z = 44).

### 8.2.2 Characterization of SWCNH samples and water adsorption

The nanoporosity of SWCNH samples oxidized at different conditions was determined by nitrogen adsorption at 77 K using a volumetric apparatus (Quantachrome-Autosorb IQ2). The nitrogen adsorption isotherms were analyzed by the Subtracting Pore Effect (SPE) method using the  $\alpha_s$ -plot<sup>11</sup> and the Quenched Solid Density Functional Theory (QS-DFT)<sup>12</sup> to provide the pore structure parameters and pore size distributions. Infrared spectra of the SWCNH before and after oxidation treatment in the range of 1000 to 4000 cm<sup>-1</sup> were obtained with the KBr method on an FT-IR spectrometer (Nicole 6700 FT-IR). Temperature-programmed desorption (TPD) profiles of the SWCNH before and after the oxidation treatment were measured in the temperature range of 373 to 1273 K under He flow of 300 mL min<sup>-1</sup> at a heating rate of 10 K min<sup>-1</sup> using the apparatus TG-DTA-PIMS (Rigaku Co.). Prior to this measurement, samples were degassed for 2 h in *vacuo* at 393 K. The water vapor adsorption isotherms of SWCNH were measured at 298

K with a volumetric equipment using Quantachrome-Hydrosorb after pretreating at 423 K and 2 mPa for 2 h.

## 8.3 Results and discussion

### 8.3.1 Nanoporosity and surface chemistry

**Figure 8-2a** shows the nitrogen adsorption isotherms of SWCNH oxidized at different conditions. The nitrogen adsorption isotherm of closed SWCNH (before oxidation) is of typical IUPAC Type II, indicating a minor contribution of micropores and mesopores. Oxidation of SWCNH at 633 K varies the shape of the adsorption isotherm and increases remarkably the adsorption amount. These adsorption isotherms have the nature of Type I and Type II, indicating the marked increase of microporosity and mesoporosity coming from small mesopores. Consequently, nanowindows are produced in the graphene walls of SWCNH by the oxidation treatments.<sup>13</sup> Also, a slight low-pressure adsorption hysteresis is observed; the narrow hysteresis loop does not close up to the vertical axis, in particular, for oxidized SWCNH samples except for SWCNH oxidized at 633 K for 12 h.

This hysteresis should come from the restricted diffusion of the nitrogen molecules at the nanowindows, suggesting that the size of the nanowindows is smaller than the bimolecular size of the nitrogen molecule (0.7 nm).<sup>14</sup> The oxidation at 633 K for 12 h, increases the nanowindows size. The adsorption behavior in the  $P/P_0$  range of  $10^{-6}$  to  $10^{-3}$  (**Figure 8-2b**) suggests an intensive growth of micropores by the oxidation for a longer time.

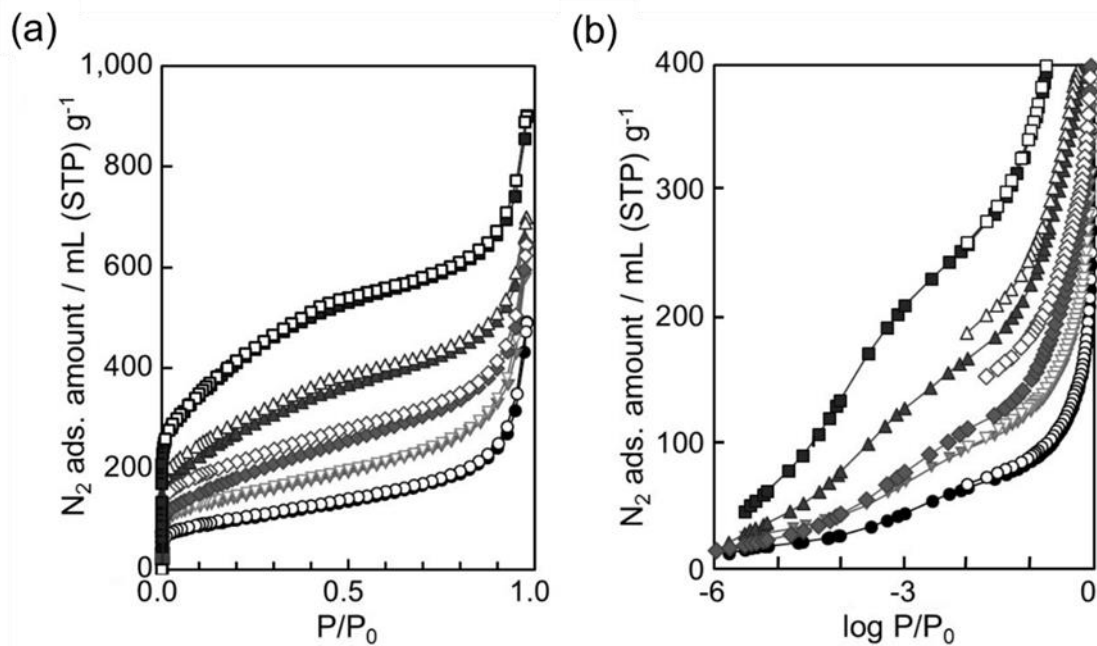


**Figure 8-2.** Nitrogen adsorption isotherms of SWCNH samples at 77 K. Pristine SWCNH (●) SWCNH oxidized at 573 K for 2 h (▼), 633 K for 0 h (◆); for 4 h (▲) and for 12h (■).  $P/P_0$  is expressed in (a) the linear scale and (b) logarithmic scale. Closed and opened symbols indicate adsorption and desorption branches, respectively.

**Figure 8-3a** shows the high-resolution  $\alpha_s$ -plots of the nitrogen adsorption isotherms. The high-resolution  $\alpha_s$ -plots have an upward deviation of filling swing below  $\alpha_s = 0.5$ . The filling swing, as well as the condensation swing ( $\alpha_s > 0.5$ ) of SWCNH oxidized at 633 K for 12 h, is the most predominant. Analyzing these  $\alpha_s$ -plots provides the average pore parameters of SWCNH samples, as shown in **Table 8-1**.

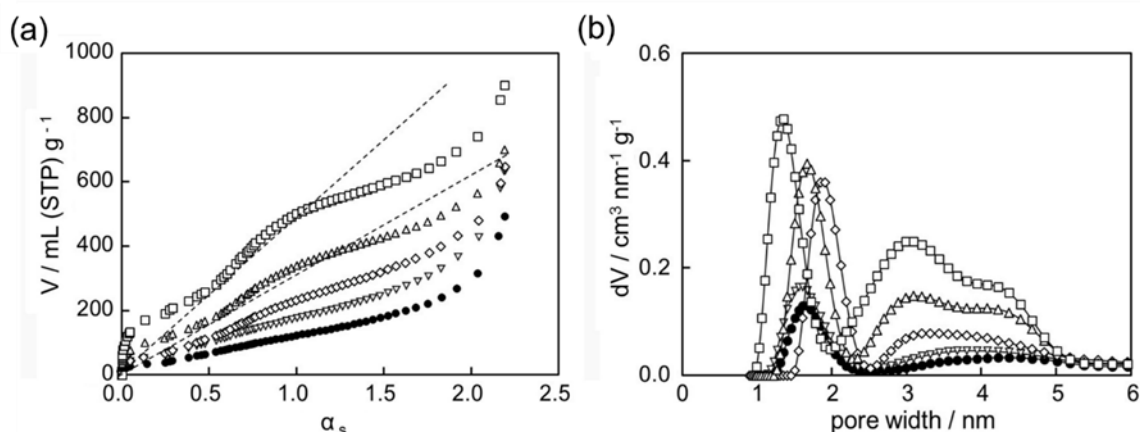


**Figure 8-3.** (a)  $\alpha_s$ -plots of the nitrogen adsorption isotherms at 77 K and (b) pore size distributions of SWCNH samples by QS-DFT for cylindrical pores. Pristine SWCNH (●) and SWCNH oxidized at 573 K for 2 h (▽), 633 K for 0 h (◇), 4 h (△) and 12 h (□).

**Table 8-1.** Pore parameters of pristine SWCNH and SWCNH oxidized at different conditions from nitrogen adsorption isotherms.

Oxidation conditions	Surface area <sup>a</sup>	Micropore volume (QS-DFT)	Micropore volume (DR) <sup>b</sup>	Total pore volume P/P <sub>0</sub> = 1	Microp./mesop. volume ratio <sup>c</sup>
	m <sup>2</sup> g <sup>-1</sup>	cm <sup>3</sup> g <sup>-1</sup>	cm <sup>3</sup> g <sup>-1</sup>	cm <sup>3</sup> g <sup>-1</sup>	
pristine	445	0.065	0.170	0.940	0.90
573 K for 2 h	490	0.092	0.200	1.170	0.90
633 K for 0 h	600	0.120	0.240	1.160	0.60
633 K for 4 h	870	0.190	0.330	1.200	0.60
633 K for 12 h	1380	0.240	0.480	1.520	0.50

<sup>a</sup> The surface area is determined by the subtracting pore effect (SPE) method.

<sup>b</sup> This value is determined from the Dubinin-Radushkevich (DR) plot for the P/P<sub>0</sub> range of 10<sup>-4</sup> to 10<sup>-2</sup>.

<sup>c</sup> The ratio of micropore volume against mesopore volume of mesopores smaller than 5 nm, which is determined from the pore size distribution with QS-DFT method.

Almost all oxidations other than oxidation at 573 K for 2 h increase significantly the surface area and the micropore volume. In particular, oxidation at 633 K for 12 h gives the largest surface area and pore volume, being close to the published results ( $1420 \text{ m}^2 \text{ g}^{-1}$ ) of SWCNH oxidized at 823 K. The nitrogen adsorption isotherms were analyzed by the QS-DFT method using the cylindrical pore model to obtain the pore size distributions, as shown in **Figure 8-3b**. Non-oxidized SWCNH has micropores with slight mesopores whose width is smaller than 5 nm. The pore volume ratio of micropores to mesopores was determined from the pore size distribution, as listed in **Table 8-1**. The open SWCNH obtained by milder oxidation has a larger pore volume of micropores to mesopores, indicating that the milder oxidation produces nanowindows in SWCNHs of smaller diameter. It is well known that oxidation begins at the pentagons in the cap of carbon nanotube families.<sup>15,16</sup> Hence, oxidation starts at the pentagons in the tip of SWCNH whose tube diameter is smaller. The microporosity/mesoporosity ratio is in the range of 0.50 to 0.90. These SWCNH samples are appropriate for the study on the effect of small mesopores on observable water adsorption.

As water adsorption is sensitively affected by surface functional groups due to its ability to form hydrogen bonds,<sup>5</sup> the surface functional groups were determined by FT-IR spectroscopy, as shown in **Figure 8-4**. Characteristic vibration modes at 1100, 1380, 1600, 2920 and  $3400 \text{ cm}^{-1}$ , were assigned to the stretching vibration modes of C-O groups, C-OH groups, C=C of the benzene ring, C-H of methylene group and O-H group, respectively.<sup>17,18</sup> The oxidation of SWCNH at 633 K for 12 h increases the peak intensities of the C-OH and the C-O. On the contrary, the peak intensity of the C=C mode does not change significantly.

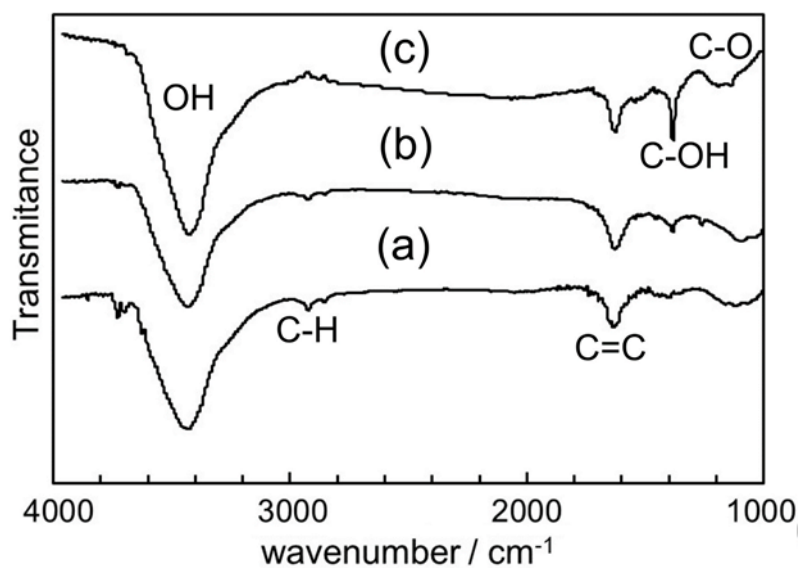


**Figure 8-4.** FT-IR spectra of (a) pristine SWCNH, (b) SWCNH oxidized at 573 K for 2 h, and (c) at 633 K for 12 h.

We can refer to the established assignment of the evolved CO and CO<sub>2</sub> to different kinds of surface functional groups.<sup>19-21</sup> The observed TPD profile of SWCNH oxidized at 633 K for 12 h shows two stronger evolution peaks of CO<sub>2</sub> centered at 649 K and 760 K than the non-oxidized SWCNH, as shown in **Figure 8-5**. Specifically, the areas under the curve of the evolution of CO<sub>2</sub> from 573 to 698 K (highest signal at 649 K), and from 698 to 823 K (highest signal at 760 K) are larger by about 2 times for the oxidized SWCNH than the non-oxidized SWCNH (**Figure 8-5**). Evolution of CO<sub>2</sub> from the samples must indicate the presence of carboxyl, carboxyl anhydrous and lactone groups on the SWCNH structure, which decompose as CO<sub>2</sub>.<sup>21</sup> It is worth pointing out that the density of surface functional groups of the oxidized SWCNH is nearly half of that of the pristine SWCNH, as it will be explained later. Therefore, these functionalities should be

located mainly as active sites on the edges of the nanowindows created by the oxidation, as Bekyarova *et al.* suggested.<sup>20</sup>

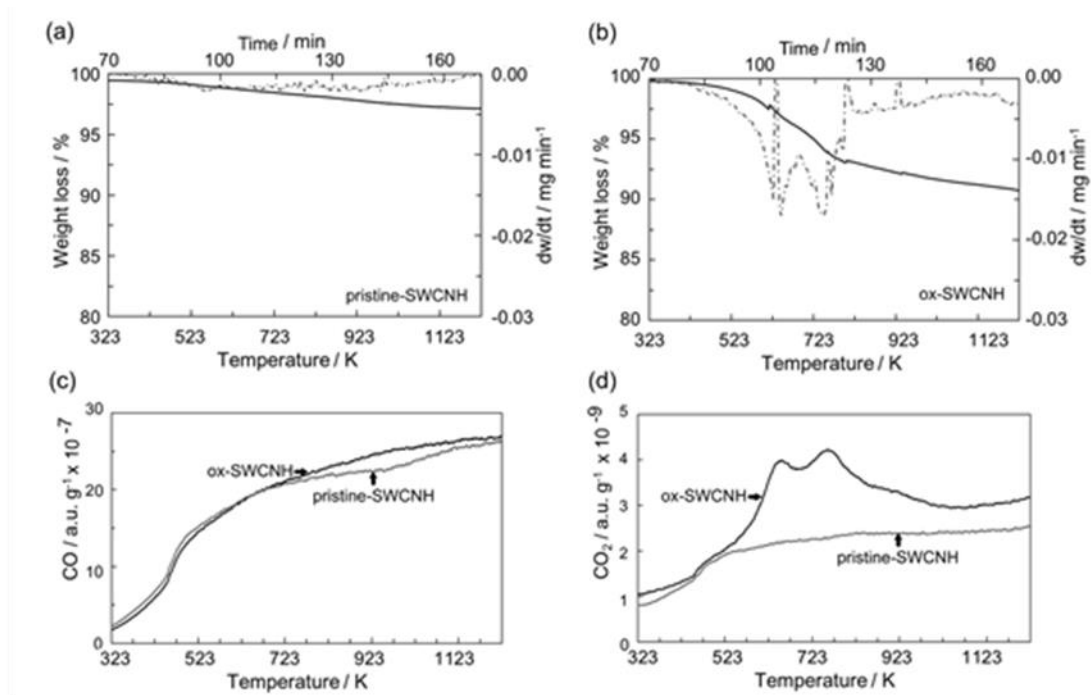


**Figure 8-5.** TG analysis of (a) SWCNH and (b) SWCNH oxidized at 633 K for 12 h under He (300 mL min<sup>-1</sup>); weight loss (—) and derivative of TG curve (...). (c) CO ( $m/z = 28$ ) profiles and (d) CO<sub>2</sub> ( $m/z = 44$ ) profiles of evolved gases in the course of TG measurement of SWCNH and SWCNH oxidized at 633 K for 12 h measured by TPD.

### 8.3.2 Water adsorption

**Figure 8-6a** shows water adsorption isotherms of SWCNH samples at 298 K. Adsorption below  $P/P_0 = 0.3$  for all SWCNH samples is negligibly small, indicating that these samples are hydrophobic, even though the surface functional groups, are detected by the FT-IR and TPD examinations (**Figure 8-4** and **Figure 8-5**, respectively).

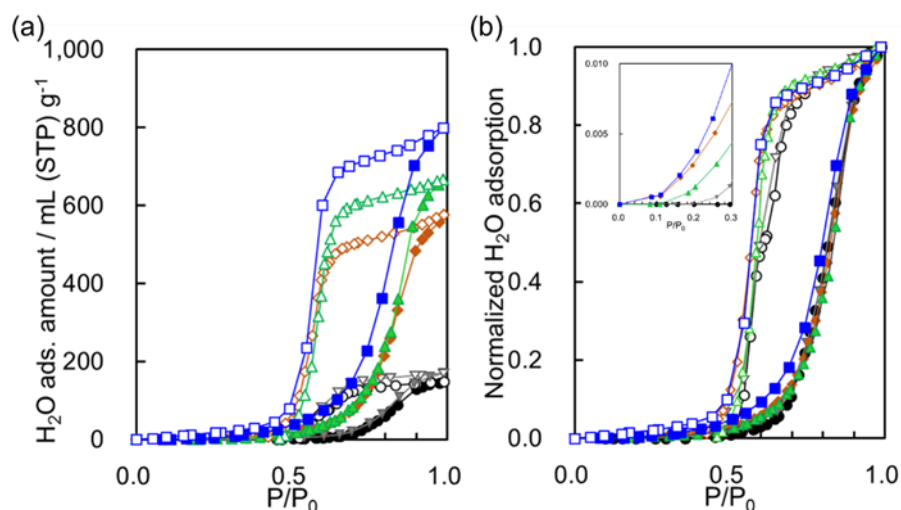


**Figure 8-6.** Water adsorption isotherms of SWCNH samples at 298 K; pristine (●) and oxidized at 573 K for 2 h (▼), 633 K for 0 h (◆); 4 h (▲) and 12 h (■). Here, the water adsorption amount of **Figure 8-6b** is normalized using the saturated adsorption amount. Closed and opened symbols indicate adsorption and desorption branches, respectively.

The predominant water adsorption starts above  $P/P_0 = 0.6$  for all samples, accompanying with an explicit adsorption hysteresis. The water adsorption isotherms are similar to those of hydrophobic ACFs, which have only micropores whose width is smaller than 1.5 nm. The rising  $P/P_0$  of the adsorption branch of the adsorption isotherm of ACFs depends on the pore width; the larger the pore width, the larger the rising  $P/P_0$ .<sup>6</sup> The hysteresis loop of water adsorption isotherms of ACFs also depends on the pore width.<sup>22</sup> On the other hand, the basic frame of the adsorption hysteresis loop of the SWCNH samples is almost similar to each other, as shown in **Figure 8-6b**, suggesting that water molecules are adsorbed with a similar mechanism. However, the rising  $P/P_0$  value of SWCNH oxidized is slightly larger than that of the pristine SWCNH. In particular, the rising  $P/P_0$  of the SWCNH oxidized at 633 K for 12 h is the smallest among the samples regardless of only a small difference. This should be associated with slight

adsorption below  $P/P_0 = 0.4$ . The inset in **Figure 8-6b** shows the adsorption branches of the normalized water adsorption isotherms below  $P/P_0 = 0.3$ . The larger slope of the adsorption isotherm in this range indicates the presence of more surface functional groups,<sup>4</sup> as seen in **Figure 8-7a**.

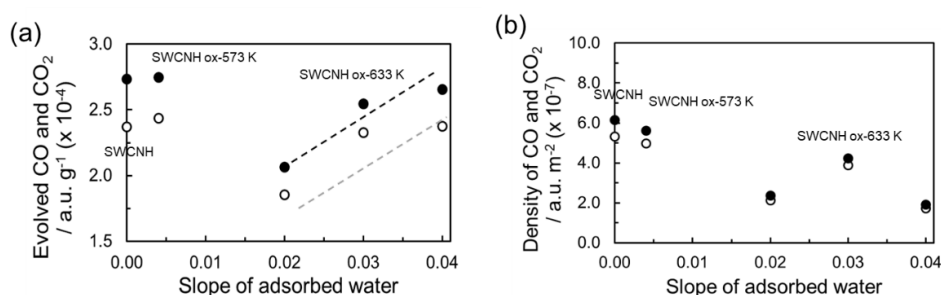


**Figure 8-7.** (a) Evolved gases CO ( $m/z = 28$ ) and CO<sub>2</sub> ( $m/z = 44$ ) and (b) density of CO and CO<sub>2</sub> in the course of TG measurement of SWCNH before and after oxidation in relation to the slope of the normalized water adsorption isotherm in low relative pressure range ( $P/P_0 < 0.3$ ). The sum of CO and CO<sub>2</sub> evolved at 573-698 K (○) and 698-823 K (●) is obtained as the sum of area under the curve (AUC) of each evolved gas in the desired range of temperature.  $AUC = (\text{Temperature 2} - \text{Temperature 1}) * \text{intensity of evolved gas}$  in  $\text{a.u.g}^{-1}$ . The density of CO and CO<sub>2</sub> =  $AUC$  in  $\text{a.u.g}^{-1} / \text{surface area in m}^2 \text{g}^{-1}$ .

**Figure 8-7a** shows the evolved gases CO ( $m/z = 28$ ) and CO<sub>2</sub> ( $m/z = 44$ ) and **Figure 8-7b** shows the density of CO and CO<sub>2</sub> in the course of TG measurement of SWCNH before and after oxidation in relation to the slope of the normalized water adsorption isotherm in low relative pressure range ( $P/P_0 < 0.3$ ). Correspondingly, the SWCNH sample oxidized at 633 K for a longer period has the largest slope. Hence, the presence of more surface functional groups promotes the cluster filling of water molecules at a

smaller rising  $P/P_0$ . Nevertheless, this promotion of the cluster filling by the surface functional groups is too limited to influence the adsorption mechanism.

Pristine SWCNH contains amorphous carbon product of laser abrasion process, defective carbon (5 or 7 membered rings) situated in the cone caps and bending sites, tubular graphene carbon, and thin graphitic carbon composed by small graphene sheets.<sup>10</sup> Evolution of CO and CO<sub>2</sub> under inert atmosphere from pristine SWCNH derives from the removal of amorphous carbon. Nanowindows are not donated at very mild oxidation (573 K). However, interstitial pores are unblocked by the removal of part of amorphous carbon. The slight unblocking of interstitial pores explains the higher slope of water adsorption; water is adsorbed in those interstitial pores. There is not noticeable oxygen donation, which is confirmed by the FTIR analysis. Therefore, the amount of CO and CO<sub>2</sub> evolved during the TPD analysis remains practically similar to that of pristine SWCNH. At oxidation at 633 K, besides the removal of more amorphous carbon, there is nanowindows generation at the reactive defective sites (mainly 5 membered rings and neighboring carbons). The longer the oxidation time, the more nanowindows donation, deriving in the higher rising of water adsorption (indicated by the higher slope of water adsorption). Nanowindows donation requires the removal of defective carbon or combustion of tubular graphene by oxidation and the passivation with H or O atoms of the carbon bonds at the edges. The oxygen content increases with oxidation. However, there is only scarce donation of oxygen-containing functionalities to oxidized SWCNH since the oxidation temperature is low, confirmed by the FTIR analysis of SWCNH oxidized at 633 K for 12 h. The removal of amorphous carbon and defective carbon, besides the low content of

oxygen functionalities after the oxidation explains the low evolution of CO and CO<sub>2</sub> during the TPD analysis.

FTIR spectrum (**Figure 8-4**) shows that the presence of oxygen-containing functional groups in oxidized SWCNH for a longer time is higher than that of the pristine SWCNH. The amount of CO + CO<sub>2</sub> released from the oxidized SWCNH for longer time (633 K for 12 h) seems to be similar to that of the pristine one. However, the density of functional groups on the sample is nearly half of that of the pristine SWCNH, as the surface area of the sample was increased by the oxidation, as shown in **Figure 8-7b**. The density of functional groups on the sample is obtained by dividing the absolute amount of evolved CO and CO<sub>2</sub> in a.u. g<sup>-1</sup> (TPD in **Figure 8-5**) by the decomposition of the surface functional groups by the sample surface area in m<sup>2</sup> g<sup>-1</sup> (**Table 8-1**). Therefore, we concluded that the functional groups should be located on the edges of the nanowindows donated by oxidation.

The cluster-mediated filling mechanism is applied to water adsorption on typical microporous carbons. We need to examine the applicability of cluster-mediated filling mechanism to adsorption of water on carbon mesopores using SWCNH samples having different mesoporosity. We find a linear correlation between the maximum amount of water adsorbed and the total pore volume of micropores and mesopores not larger than 5 nm, as shown in **Figure 8-8**. The linear relation supports that water adsorption even in small mesopores occurs in the same way as in micropores. Water molecules are not adsorbed in micropores by capillary condensation,<sup>7</sup> but by the cluster-mediated filling mechanism. We must study the adsorption process using small-angle X-ray scattering in

order to obtain the information on the structure change of adsorbed water in small carbon mesopores with  $P/P_0$  in the future.

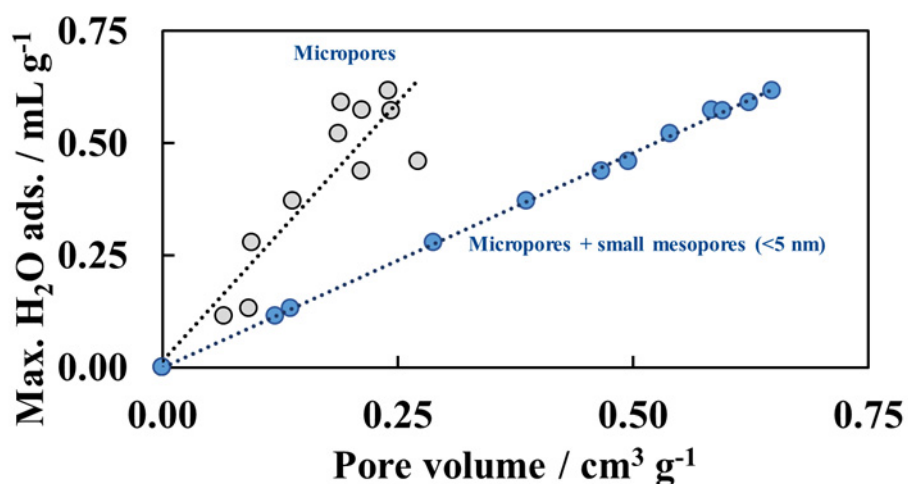


**Figure 8-8.** Relation between water adsorbed and pore volume of the SWCNH samples.

**Figure 8-9** shows the different sites for water adsorption on SWCNH prior to and after oxidation under mild and severe conditions. Pristine SWCNH's do not possess abundant sites for adsorption of water molecules. Thinner SWCNH are more prone to be oxidized than wider ones, when a mild oxidation treatment for a short time is applied, creating controlled nanowindows in the SWCNH tips. Those sites are more selective for the adsorption of water. On the contrary, severe oxidation targets all the SWCNH creating larger nanowindows that work as water-adsorption selective sites.

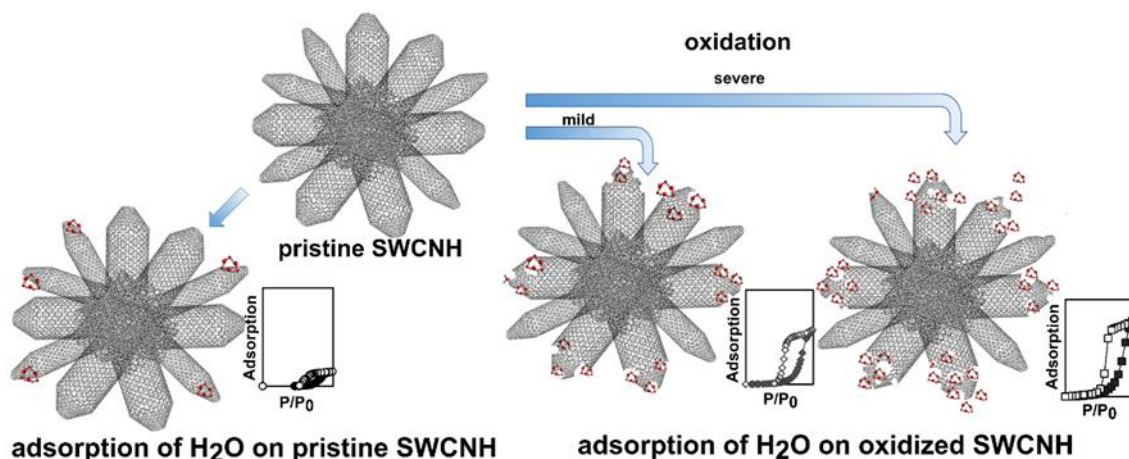


**Figure 8-9.** Diagram of water adsorption on pristine SWCNH and oxidized SWCNH under mild and severe conditions.

## 8.4 Conclusions

Mild oxidation for a shorter time opens only the thinner tubes. The mild oxidation at different time controls the mesoporosity. SWCNH that possess mesoporosity present a water adsorption isotherm close to that of microporous carbon. The amount of water adsorbed has a linear relation with the mesopore volume. Water molecules are adsorbed in carbon mesopores (< 5 nm) by cluster mechanism. The present contribution to water adsorption on SWCNH gives key information to understand the hygroscopic nature of nanodiamonds.

## 8.5 Acknowledgments

The authors are thankful to the Grant-in-Aid for Scientific Research (A) (24,241,038) and partial support by the Center of Innovation Program from Japan Science and Technology Agency, JST.

## 8.6 References

- (1) Fowkes, F. M.; Harkins, W. D. The state of monolayers adsorbed at the interface solid aqueous solution. *J. Am. Chem. Soc.* **1940**, *62*, 3377–3386.
- (2) Shrader, M. E. Ultrahigh-vacuum techniques in the measurement of contact angles. LEED study of the effect of structure on the wettability of graphite. *J. Phys. Chem.* **1980**, *84*, 2774–2779.
- (3) Asai, M.; Ohba, T.; Iwanaga, T.; Kanoh, H.; Endo, M.; Campos-Delgado, J.; Terrones, M.; Nakai, K.; Kaneko, K. Marked adsorption irreversibility of graphitic nanoribbons for CO<sub>2</sub> and H<sub>2</sub>O. *J. Am. Chem. Soc.* **2011**, *133*, 14,880–14,883.
- (4) Salame, I. I.; Bandoz, T. J. Experimental study of water adsorption on activated carbons. *Langmuir* **1999**, *15*, 587–593.
- (5) Kaneko, K. Water capture in carbon cuboids, *Nat. Chem.* **2015**, *7*, 194–196.
- (6) Miyawaki, J.; Kanda, T.; Kaneko, K. Hysteresis-associated pressure-shift-induced water adsorption in carbon micropores. *Langmuir* **2001**, *17*, 664–669.
- (7) Hanzawa, Y.; Kaneko, K. Lack of a predominant adsorption of water vapor on carbon mesopores. *Langmuir* **1997**, *13*, 5802–5804.
- (8) Ohba, T.; Kanoh, H.; Kaneko, K. Affinity transformation from hydrophilicity to hydrophobicity of water molecules on the basis of adsorption of water in graphitic nanopores. *J. Am. Chem. Soc.* **2004**, *126*, 1560–1562.
- (9) Thommes, M.; Morell, J.; Cychosz, K. A.; Froba, M. Combining nitrogen, argon, and water adsorption for advanced characterization of ordered mesoporous carbons (CMKs) and periodic mesoporous organosilicas (PMOs). *Langmuir* **2013**, *29*, 14 893–14902.

- (10) Utsumi, S.; Miyawaki, J.; Tanaka, H.; Hattori, Y.; Itoi, T.; Ichikuni, N.; Kanoh, H.; Yudasaka, M.; Iijima, S.; Kaneko, K. Opening mechanism of internal nanoporosity of single-wall carbon nanohorn. *J. Phys. Chem. B* **2005**, 109(30), 14319-14324.
- (11) Kaneko, K.; Ishii, C.; Kanoh, H.; Hanzawa, Y.; Setoyama, N.; Suzuki, T. Characterization of porous carbons with high-resolution  $\alpha_s$ -analysis and low temperature magnetic susceptibility. *Adv. Colloid Interface Sci.* **1998**, 76, 295-320.
- (12) Neimark, A. V.; Lin, Y.; Ravikovitch, P. I.; Thommes, M. Quenched solid density functional theory and pore size analysis of micro-mesoporous carbons. *Carbon* **2009**, 47, 1617–1628.
- (13) Murata, K.; Kaneko, K.; Steele, W. A.; Kokai, F.; Takahashi, K.; Kasuya, D.; Yudasaka, M.; Iijima, S. Porosity evaluation of intrinsic intraparticle nanopores of single wall carbon nanohorns. *Nano Lett.* **2001**, 1, 197–199.
- (14) Thommes, M. Physical adsorption characterization of nanoporous materials. *Chem. Ing. Tech.* **2010**, 8, 1059–1073.
- (15) Harris, P. J. F. Filled and heterogenous nanotubes, Carbon nanotube science, synthesis, properties and applications. Cambridge University Press, Cambridge **2009**, pp. 247–274.
- (16) Fujimori, T.; Urita, K.; Tománek, D.; Ohba, T.; Moriguchi, I.; Endo, M. Kaneko, K. Selective probe of the morphology and local vibrations at carbon nanoasperities. *J. Chem. Phys.* **2012**, 136, 064, 505, 1–5.
- (17) Kovtyukhova, N. I.; Mallouk, T. E.; Pan, L.; Dickey, E. C. Individual single-walled nanotubes and hydrogels made by oxidative exfoliation of carbon nanotube ropes. *J. Am. Chem. Soc.* **2003**, 125, 9761–9769.

- (18) Ellison, M. D.; Gasda, P. J. Functionalization of single-walled carbon nanotubes with 1,4-benzenediamine using a diazonium reaction. *J. Phys. Chem. C* **2008**, 112, 738–740.
- (19) Chand Bansal, R.; Donnet, J. -B.; Stoeckli, F. Active carbon. Marcel Dekker Inc., New York, **1988**.
- (20) Bekyarova, E.; Hanzawa, Y.; Kaneko, K.; Silvestre-Albero, J.; Sepulveda-Escribano, A.; Rodriguez-Reinoso, F.; Kasuya, D.; Yudasaka, M.; Iijima, S. Cluster-mediated filling of water vapor in intratube and interstitial nanospaces of single-wall carbon nanohorns. *Chem. Phys. Lett.* **2002**, 366, 463–468.
- (21) Szymanski, G. S.; Karpinski, Z.; Biniak, S.; Swiatkowski, A. The effect of the gradual thermal decomposition of surface oxygen species on the chemical and catalytic properties of oxidized activated carbon. *Carbon* **2002**, 40, 2627–2639.
- (22) Nakamura, M.; Ohba, T.; Branton, P.; Kanoh, H.; Kaneko, K. Equilibration-time and pore-width dependent hysteresis of water adsorption isotherm on hydrophobic microporous carbons, *Carbon* **2010**, 48, 305–312.



## Chapter 9

### 9. Atomistic model-aided Small Angle X-ray Scattering method for evaluation of the individual particle size of aggregated detonation nanodiamonds<sup>1</sup>

**Abstract.** The detonation nanodiamonds form colloidal aggregates with polydisperse core-shell nanodiamond crystallites. The knowledge of the size distribution of detonation nanodiamonds is crucial for various applications of these carbon gems. We present a simple polydisperse model for the evaluation of the size distribution of detonation nanodiamond crystallites from small-angle X-ray scattering. Detonation nanodiamonds are modeled as a collection of spherical diamond-like particles, where all correlations are included through the structure factor of hard-spheres with an optimized volume fraction of 0.13. Atomistic modeling of ~5 nm nanodiamonds, high-resolution transmission microscopy observations, and wide-angle X-ray scattering experiment support a simplified treatment of core-shell detonation nanodiamonds by spherical diamond-like particles. Reconstruction of the size distribution function from the atomistic model-aided small-angle X-ray scattering shows that detonation nanodiamonds are a polydisperse colloidal system with a lognormal size distribution, an average radius of 1.88 nm, and standard deviation of  $\pm 0.87$  nm, being smaller than the average from high-resolution transmission electron microscopy.

---

## 9.1 Introduction

Since the discovery of nanodiamond particles in detonation soot (DNs),<sup>1-3</sup> a wide range of potential applications of DNs in drug delivery, gene therapy, bio-imaging, tissue engineering, photonic, spintronic and nanocomposites have been proposed.<sup>4-6</sup> A major weakness of the currently produced DNs is their size distribution (typical sizes between 4 and 8 nm) and complex structure of a tightly bound irregular aggregate.<sup>7-9</sup> The control of the purity, surface chemistry, and polydispersity of DNs is crucial for the realization of their potential applications. Therefore, we must develop reliable methods for the characterization of DN polydispersity over the volume of the sample, which is not directly measurable in an experiment.

High-resolution transmission microscopy (HR-TEM),<sup>10</sup> dynamic light scattering (DLS),<sup>11</sup> atomic force microscopy (AFM) and the wide-angle X-ray scattering (WAXS)<sup>12</sup> has been routinely used for determination of the size distribution of DN crystallites. HR-TEM technique provides direct images of nanometer-size DN, which allowed determination of particle size distribution.<sup>10</sup> The disadvantage of HR-TEM analysis is an estimation of DN size from 2D images, elaborate sample preparation procedure, and poor statistics due to averaging over a finite number of images. In particular, it is quite difficult to evaluate precisely the individual particle size of the mutually aggregated DN without overestimation. The hydrodynamic radius of DN dispersed in water solutions can be extracted from DLS data using the Stokes-Einstein (SE) equation.<sup>13</sup> However, we must point out that the SE hydrodynamic radius of DN aggregates diffusing in water solutions corresponds to the effective size of spherical-like aggregates not to individual nanodiamond.<sup>13</sup> In addition, the size of DN can be influenced by the water solvation

shell bonded to the nanodiamond surface due to slower diffusion of nanodiamonds with adsorbed water molecules.<sup>14</sup> The mean size of nanodiamond crystallites can be estimated from [111] and [220] diamond-type reflections measured from WAXS after the instrumental broadening correction.<sup>10</sup> While the X-ray scattering pattern determined on the wide-angle (i.e. high-Q) region is very useful method for the study of DNs at the atomistic scale, it does not contain information about the polydispersity of DNs on the mesoscopic scale. Recently, Stehlik *et al.*<sup>11</sup> have pointed out that AFM measurements provide a more accurate estimate of DNs size distribution compared to DLS and WAXS. In AFM, the sizes of DNs are determined from a maximum height of a particle. Because the AFM cannot distinguish between a single particle and cluster/agglomerate of particles,<sup>15</sup> the application of this method is limited to DNs samples with a large fraction of a single crystallite. Unfortunately, as pointed out by Krüger *et al.*<sup>9</sup> de-aggregation of DNs is a very challenging task due to strong bonding between individual nanodiamonds and their fast aggregations.

Small-angle X-ray scattering (SAXS) is a powerful method for the structural characterization of polydisperse disordered colloidal systems (e.g. nanoparticles, mixed alloys, colloids, and others).<sup>16,17</sup> Compared to other methods, SAXS provides more statistically reliable estimates of particle size distributions because the scattering intensity is averaged over the irradiated sample volume. However, we must underline that the polydispersity and aggregation of individual nanodiamond crystallites cause difficulty in the analysis of the particle distribution by SAXS, because, contrary to monodisperse NDs, the measured intensity is no longer related to the scattering from a single nanodiamond crystallite. Instead, each individual nanodiamond crystalline present in the investigated

sample adds to the scattering pattern, resulting in an averaged intensity. Furthermore, the short-range correlations between individual nanodiamonds tightly packed in irregular aggregates will contribute to the measured scattering intensity.<sup>16</sup>

In this study, we present the polydisperse model for determination of the size distribution function of DNs from a single SAXS experiment. First, we generated a spectrum of the atomistic structural models of ~5 nm DNs to better understand the structure of the individual DNs at the atomistic scale. From these models, HR-TEM images, and WAXS scattering data, we extracted the prior knowledge about the shape, radial carbon density profile of individual DNs in aggregates. Second, we formulated a polydisperse SAXS model and the optimization method for the selection of the unknown volume fraction of DNs in irregular aggregates. With the optimized volume fraction of DNs, we computed the size distribution function of DNs and its moments by fitting the proposed polydisperse model to the scattering intensity measured by SAXS. Finally, we compared and critically discussed the size distributions of DNs obtained from HR-TEM images and the SAXS implemented with a novel polydisperse model.

## **9.2 Theory and modeling**

### **9.2.1 Atomistic structural model of DNs**

To calculate the scattering intensity produced by polydisperse samples of DNs on the small-angle scattering range (i.e. low-Q), prior knowledge about the approximate shape and carbon atom density profile in an individual DNs is needed. For this purpose, we construct a series of 15 atomistic structural models of ~5 nm DNs using temperature-quench Monte Carlo simulations.

Our methodology consists of three steps.<sup>10</sup> In the first step, we generated a ~5 nm carbon sphere by cutting a perfect diamond supercell using spherical coordinates. Each sphere consists of ~8400 carbon atoms. In the second step, we used the Monte Carlo (MC) quench simulations in NVT ensemble to relax and minimize the energy of the atomistic structural models of DNs.<sup>18</sup> A three-body environmental-dependent interatomic potential (EDIP) was used for computing carbon-carbon interactions.<sup>19</sup> As previously, the temperature decreases linearly from 3000 K down to 30 K, with a step of 10 K.<sup>10</sup> For each temperature, 1000 MC displacement steps were performed using the Metropolis algorithm.<sup>10,20</sup> The displacement of carbon atoms was adjusted every 1000 MC steps to maintain the acceptance ratio of 0.4. In the final step, the energy of a quenched ~5 nm nanodiamond crystallites was minimized in the general utility lattice program (GULP) implemented with EDIP potential using a constant volume optimization with conjugate gradients.<sup>21</sup> From the atomistic structural models of DNs, we computed the theoretical intensity and structure factor in the wide-angle scattering range using the Debye model,<sup>22-25</sup> as given by eqs. 1 and 2,

$$I(q) = S(q)/f^2 \quad \text{eq. 1}$$

$$S(q) = 1 + \frac{1}{N} \left[ \sum_{i,j=1}^N \frac{\sin(qr_{ij})}{qr_{ij}} \right]_{i \neq j} \quad \text{eq. 2}$$

where N is the total number of carbon atoms in the atomistic structural model of DNs,  $r_{i,j}$  is the interatomic distance between i-th and j-th carbon atoms,  $q = 4\sin \theta / \lambda$  is the

modulus of the scattering vector, where  $2\theta$  is the scattering angle,  $\lambda$  is the wavelength of the incident X-ray beam, and  $f$  is the atomic scattering factor of a carbon atom.<sup>24</sup> To validate atomistic structural models of ~5 nm DNs, we compared the position and shape of the scattering peaks against experimental WAXS measurements and the reflection lines corresponding to diamond and graphite crystals.<sup>10</sup>

HR-TEM images provide only qualitative information about the 2D shape of DNs. In contrast, deformation of the nanodiamond crystalline shape from the sphere can be computed from the atomistic structural model of DNs via the concept of the “asphericity”,<sup>26</sup>

$$A = \frac{1}{2} \left\langle \frac{(\lambda_1 - \lambda_2)^2 + (\lambda_2 - \lambda_3)^2 + (\lambda_3 - \lambda_1)^2}{(\lambda_1 + \lambda_2 + \lambda_3)^2} \right\rangle \quad \text{eq. 3}$$

where  $\langle \dots \rangle$  denotes the average over an ensemble of DNs crystallites generated from temperature-quench Monte Carlo method, and  $\lambda_1, \lambda_2, \lambda_3$  are the three eigenvalues of the tensor of the radius of gyration, defined by,<sup>26</sup>

$$T_{\alpha,\beta} = \frac{1}{2N^2} \sum_{j=1}^N (r_{i\alpha} - r_{j\alpha}) (r_{i\beta} - r_{j\beta}) \quad \text{eq. 4}$$

Here  $N$  is the total number of carbon atoms in the atomistic structural model of DNs,  $\alpha, \beta = 1, 2, 3$  denote the three Cartesian components and  $r_{i\alpha}$  is the  $\alpha$  component of the position of the  $i$ -th carbon atom in the atomistic structural model of DNs. The asphericity  $A$  takes a value between 0 (sphere) and 1 (rod).<sup>26</sup>

The carbon density profile in DNs is not directly measurable in an experiment. From the atomistic structural model of ~5 nm DNs, we computed the radial carbon density profile by counting the number of carbon atoms in a certain volume bins registering these numbers in suitable histograms.<sup>27</sup>

### 9.2.2 Polydispersity of DNs: Small-Angle X-ray Scattering

We treated DNs as tightly bound irregular aggregates consisting of spherical diamond-like particles of different sizes. We assume that the size of those particles varies slowly with the position in the aggregate so that every particle is surrounded by particles of the same size (so-called the local monodisperse approximation).<sup>28-30</sup> Upon these restrictions, the scattering intensity in the small-angle region is calculated as the incoherent sum of the scattering intensities of monodisperse subsystems weighted with the size distribution function,  $N(R)$ ,<sup>28</sup>

$$I(q) = \Delta\rho^2 \int_0^\infty \Phi(q, R)^2 S(q, R; \eta) N(R) dR \quad \text{eq. 5}$$

where  $\Delta\rho$  is the excess scattering-length density,  $q$  is the modulus of the scattering vector, and  $\eta$  is the volume fraction of DNs.

The form factor,  $\Phi(q, R)^2$ , for a monodisperse spherical diamond-like particle with uniform scattering length density can be computed from,<sup>28-30</sup>

$$\Phi(q, R) = 3V_0 [\sin(qR) - qR\cos(qR)] / (qR)^3 \quad \text{eq. 6}$$

where  $V_0 = (\frac{4}{3})\pi R^3$  denotes the volume of the sphere

The structure factor,  $S(q, R; \eta)$ , describing all correlations between DNs in aggregates is approximated by the structure factor of the monodisperse hard-spheres,<sup>31,32</sup>

$$S(q, R; \eta) = [1 - C(q, R; \eta)]^{-1} \quad \text{eq. 7}$$

Here,  $(q, R; \eta)$  is the Fourier transform of the interparticle correlation function given by eq. 8,<sup>31,32</sup>

$$C(q, R; \eta) = -\frac{24\eta}{x^6} \{ \alpha x^3 (\sin x - x \cos x) + \beta x^2 [2x \sin x - (x^2 - 2) \cos x - 2] + \gamma [(4x^3 - 24x) \sin x - (x^4 - 12x^2 + 24) \cos x + 24] \} \quad \text{eq. 8}$$

where  $x = 2qR$ ,  $\alpha = \frac{(1 + 2\eta)^2}{(1 - \eta)^4}$ ,  $\beta = \frac{-6\eta(1 + \eta/2)^2}{(1 - \eta)^4}$   
and  $\gamma = \frac{\eta(1 + 2\eta)^2}{[2(1 - \eta)^4]}$

Note that the volume fraction of hard-spheres,  $\eta$ , in eqs. 7 and 8 are unknown and it is difficult to measure directly from the experiment. Thus, we propose to optimize the value of  $\eta$  using the method of perceptual criteria.<sup>33</sup> Following to Svergun,<sup>33</sup> the reconstructed size distribution function,  $N(R)$ , should be smooth and positive definite over the entire range of DNs sizes. Therefore, in the first step, we inverted eq. 5 for selected values of  $\eta$  in eq. 7 using an in-house implementation of the second-order

Tikhonov's regularization method.<sup>34</sup> As previously, the heuristic L-curve criterion was used for selection of the optimal value of the regularization parameter.<sup>34,35</sup> In the second step, for each solution,  $N(R;\eta)$ , we defined and computed the oscillations,  $\gamma_o$ , (e.g. OSCILL) and positivity,  $\gamma_p$  (e.g. POSITV) criteria from the following expressions, respectively,<sup>33</sup>

$$\gamma_o(\eta) = \frac{\|N'(R;\eta)\|}{\|N(R;\eta)\|} \quad \text{eq. 9}$$

$$\gamma_p(\eta) = \frac{\|N^+(R;\eta)\|}{\|N(R;\eta)\|} \quad \text{eq. 10}$$

where  $\|f\| = \left[ \int_{x_{\min}}^{x_{\max}} f^2(x) dx \right]^{1/2}$  is the norm of an arbitrary function  $f(x)$  in real space,  $f'(x) = df(x)/dx$  denotes derivative of the function, and  $f^+(x) = f(x)$  if  $f(x) > 0$ , otherwise  $f^+(x) = 0$ .<sup>33</sup> Note that for non-negative function, POSITV = 1, and for a smooth monomodal function OSCILL is close to 1.<sup>33</sup> Therefore, the optimized volume fraction of hard-spheres in eq. 7 corresponds to the minimum of  $\gamma_o$  and the maximum of  $\gamma_p$ .

We would like to stress that the optimization of  $\eta$  based on perceptual criteria is not a unique approach, as pointed out by Svergun.<sup>33</sup> However, detailed analysis of the optimisation results clearly showed that the unphysical;  $N(R)$  functions are rejected with perceptual criteria. In particular, we found that all  $N(R)$  computed from eq. 5 and volume fractions of hard-spheres  $\eta > \sim 0.2$  in eq. 7 have spurious oscillations that cannot be justified on the basis of physical intuition. Moreover, from the experimental HR-TEM,

we concluded that the optimized value of  $\eta = 0.13$  is physically sound. The fractal-like structures of DNs aggregates indicate non-regular and inhomogeneous packing of spherical nanodiamond crystallites.

For the optimized volume fraction of 0.13, we computed the average radius of DNs and their dispersion from the moments of the size distribution function,  $N(R)$ ,<sup>28,29</sup>

$$\langle R \rangle = \frac{\overline{R^1}}{\overline{R^0}} \quad \text{eq. 11}$$

$$\sigma(r)^2 = \int_0^\infty (R - \langle R \rangle)^2 N(R) dR / \overline{R^0} \quad \text{eq. 12}$$

$$\overline{R^k} = \int_0^\infty R^k N(R) dR \quad \text{eq. 13}$$

Finally, we compared the characteristics of the size distribution of DNs computed from a single SAXS intensity curve and the series of HR-TEM images.<sup>10</sup>

### 9.3 Results and discussion

Let us first compare the HR-TEM images of DNs with the representative atomistic structural models of  $\sim 5$  nm DNs simulated from Monte Carlo quench simulations implemented with the three-body EDIP potential. HR-TEM images (**Figure 9-1a**) and the atomistic snapshots (**Figure 9-1b**) show that DNs are spherical-like particles with a core-shell structure. Indeed, the asphericity of  $\sim 0.00012$  computed from atomistic structural models of DNs is quite small (**Table 9-1**), but its non-zero value indicates some deviations

of DNs shapes from a perfect sphere, which is also visible on HR-TEM images (**Figure 9-1a**). Due to high surface to volume fractions, the reconstructed  $sp^2$  graphitic carbon shells enclose the  $sp^3$  nanodiamond cores. Interestingly, patchy-like shells with  $sp^2$ -hybridized carbon atoms rather than a defect-free single graphene shell enclose the  $sp^3$  nanodiamond cores in theoretical DNs. It is worth noting that the toy-model of nanodiamond shell proposed by Mochalin *et al.*<sup>36</sup> consists of  $sp^2$  graphitic patches and chains. The average binding energy between carbon atoms in simulated DNs of -7.126 eV/atom is slightly higher than the binding energy between two carbon atoms in graphite and diamond crystal, e.g. -7.3768 and -7.3464 eV/atom, respectively (**Table 9-1**). The surface reconstruction of nanodiamond crystallites explains the low value of the binding energy per carbon atom and their spherical shapes (**Table 9-1**). In other words, the stability of DNs cannot be achieved without surface reconstruction, as shown in the HR-TEM image (**Figure 9-1a**) and the reconstructed atomistic models of DNs (**Figure 9-1b**). An average radial carbon density profile of ~5 nm DNs shows a non-monotonic decrease in carbon density close to the surface due to the patchy-like structure of  $sp^2$  graphitic shells (**Figure 9-1c**). The thickness of the interfacial region obtained from the fitting of hyperbolic-tangent function<sup>18</sup> is ~0.7 nm (**Figure 9-1c**), indicating the disordered structure of the  $sp^2$  graphitic shells.

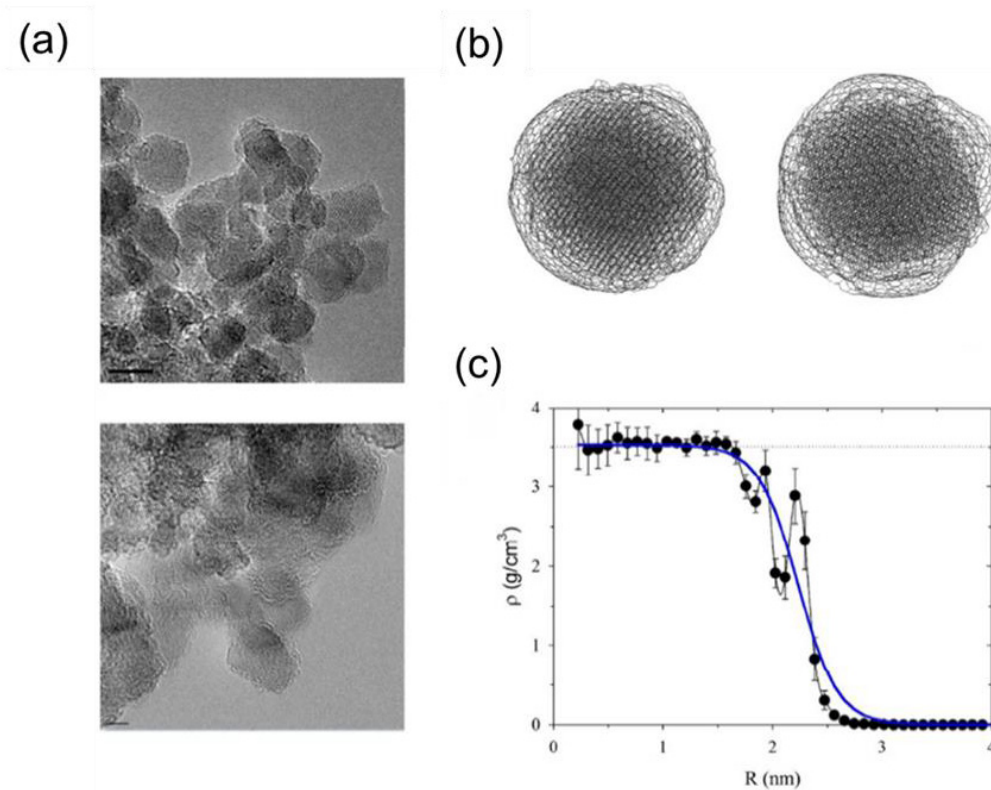


**Figure 9-1.** (a) HR-TEM images of irregular aggregates of DNs. (b) Representative atomistic structural models and (c) the average radial carbon density profile computed from the atomistic structural models of  $\sim 5$  nm DNs. Interfacial density profile fitted by hyperbolic tangent function (solid blue line) and density of cubic diamond crystal (horizontal dotted line) is displayed on (c).

**Table 9-1.** Structural and energetic parameters of DNs estimated from atomistic structural models, HR-TEM observations, and SAXS using the proposed polydisperse model.

Asphericity <sup>[a]</sup>	$E_{\text{avg}}^{\text{[b]}}$ eV / atom	$R_{\text{avg}}^{\text{[c]}}$ nm	$R_{\text{avg}}^{\text{[d]}}$ nm	$R_{\text{avg}}^{\text{[e]}}$ nm
$0.00012 \pm 7.4e^{-5}$	$-7.126 \pm 0.004$	$1.88 \pm 0.87$	$1.81 \pm 0.92$	$2.25 \pm 0.35$

[a] Asphericity and [b] the average binding energy between carbon atoms in atomistic structural models of  $\sim 5$  nm DNs, an average radius of DNs computed from [c] SAXS size distribution and [d] lognormal distribution fitted to the reconstructed SAXS size distribution, [e] an average size of DNs extracted from the HR-TEM images.<sup>10</sup>

**Figure 9-2** compares the WAXS scattering intensity measured on DNs with the theoretical one computed from the atomistic structural models of ~5 nm DNs using Debye model. We noticed that the theoretical and experimental diffraction patterns are very similar, including positions and dispersions of peaks. Both theoretical and experimental scattering intensities contain the most prominent [111] and [220] diamond-type reflections. The [100] graphitic type reflection is convoluted with [111] diamond-type reflection. The absence of the general  $[hkl]$  diffraction peaks indicates the lack of graphitic -ABAB- stacking structures in  $sp^2$  shells, which is fully consistent with our previous study.<sup>10</sup>

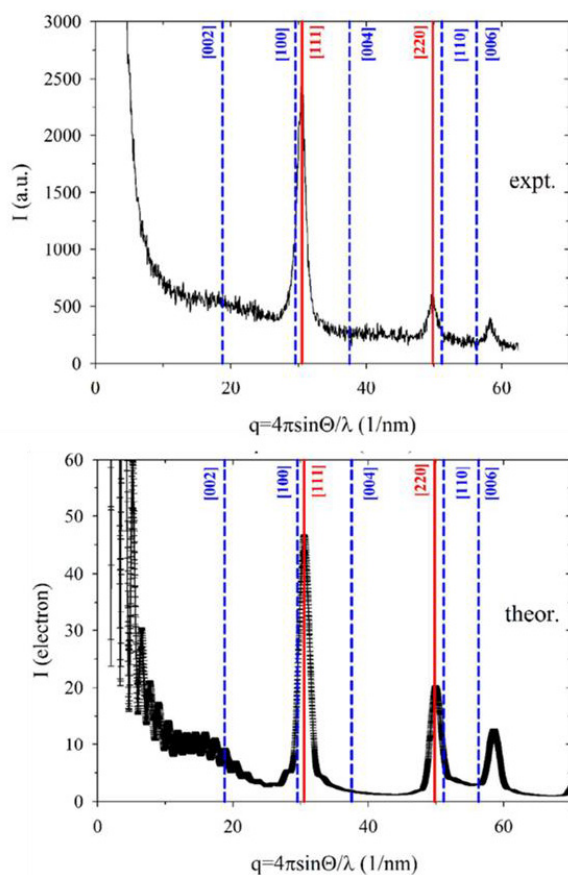


**Figure 9-2.** Comparison of the experimental (expt.) WAXS with the atomistic model-derived one (theor.).

From HR-TEM images, wide-angle X-ray scattering experiments, and atomistic modeling of individual  $\sim 5$  nm nanodiamond crystallites we concluded that the irregular aggregates of DNs can be approximated as tightly bound aggregates of spherical diamond-like particles on the mesoscopic level. The optimized value of the volume fraction of hard-spheres of 0.13 in eq.7 provides a reasonable approximation to the structure factor of DNs due to the fractal-like structure of their aggregates. **Figure 9-3** presents the comparison between the size distribution of nanodiamond crystallites evaluated from HR-TEM images and polydisperse SAXS model. A smooth linear shape of the SAXS intensity in log-log coordinates is a signature of the polydispersity of DNs. Indeed, a single smooth peak characterizes the size distribution of DNs evaluated from SAXS. By far the most significant difference between size distribution functions determined from HR-TEM images and SAXS data is the shape and dispersion (**Figure 9-3**). The lognormal size distribution of DNs with an average radius of 1.88 nm and a standard deviation of  $\pm 0.87$  nm is obtained from the fitting of SAXS data with a polydisperse model. More symmetric size distribution of DNs with an average radius of  $\sim 2.25$  nm and a standard deviation of  $\pm 0.35$  nm is extracted from HR-TEM images.<sup>10</sup> The smaller variance extracted from HR-TEM images is theoretically justified. The radius of the dominant fraction of nanodiamond crystallites determined by SAXS of  $\sim 2.0$  nm (**Figure 9-3** and **Figure 9-4**), is slightly lower than the published radii of DNs of 2.2-2.5 nm.<sup>9,10</sup> The fitting of the reconstructed size distribution function with a parametric log-normal distribution model and plotting of SAXS results in lin-log coordinates confirmed that the sizes of DNs are log-normally distributed (**Figure 9-3** and **Figure 9-4**). The individual particle size of DNs determined by the present atomistic model aided SAXS

method has no overestimation that cannot be removed by the HR-TEM method due to the strong bindings between the particles.

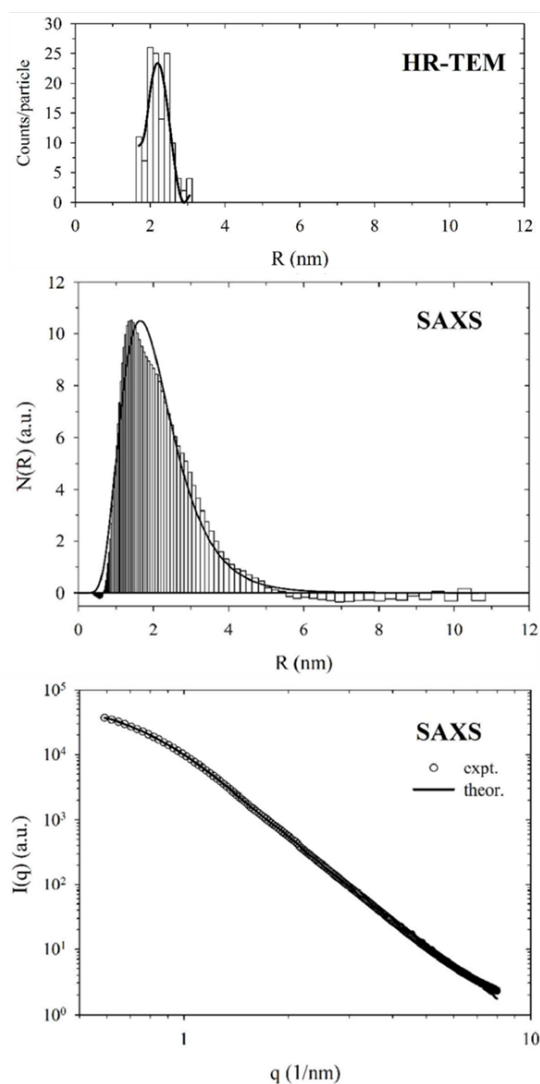


**Figure 9-3.** The size distribution of DN crystallites evaluated from HR-TEM images and reconstructed from the SAXS intensity (vertical bars: model-free reconstruction with an optimized volume fraction of 0.13, solid line: lognormal fit to the reconstructed size distribution with a correlation coefficient of 0.98). Bottom panels show the fitting of the SAXS intensity by the polydisperse model with an optimized volume fraction of hard-spheres in eq.7 of 0.13.

To the best of our knowledge, the detailed mechanism of the nucleation and growth of detonation nanodiamond crystallites is still a debated topic. The lognormal size distribution of DNs is obtained from the solution of the Smoluchowski's coagulation equation using Monte Carlo simulations.<sup>37</sup> The Smoluchowski coagulation model is an idealistic treatment of a closed system with an initially large population of small DNs coagulates. The collision and coagulation of nanodiamond control the process. Over time, the mean particle size increases, and the system gradually runs out from small DNs.<sup>37</sup> The random growth duration model of Kiss *et al.* (1999)<sup>38</sup> explains log-normal particle size distributions from first principles in a physically realistic way, without coagulation. Small nucleus particles enter into the active zone and travel through it via diffusion and drift. The growth occurs in active zone only, where it is controlled by the relative diffusion and drift transport. The nucleation and growth of nanodiamonds during detonation of explosives are out-of-equilibrium processes, thus, we postulate that the random growth duration model is the most probable mechanism that explains the log-normal size distribution of DNs reconstructed from the SAXS data. The coarse-grained modeling of interactions between individual DNs is crucial for the understanding of their aggregations and clustering on the mesoscopic level. The present precise size evaluation with atomistic model-aided SAXS enables to derive the above essential insight.

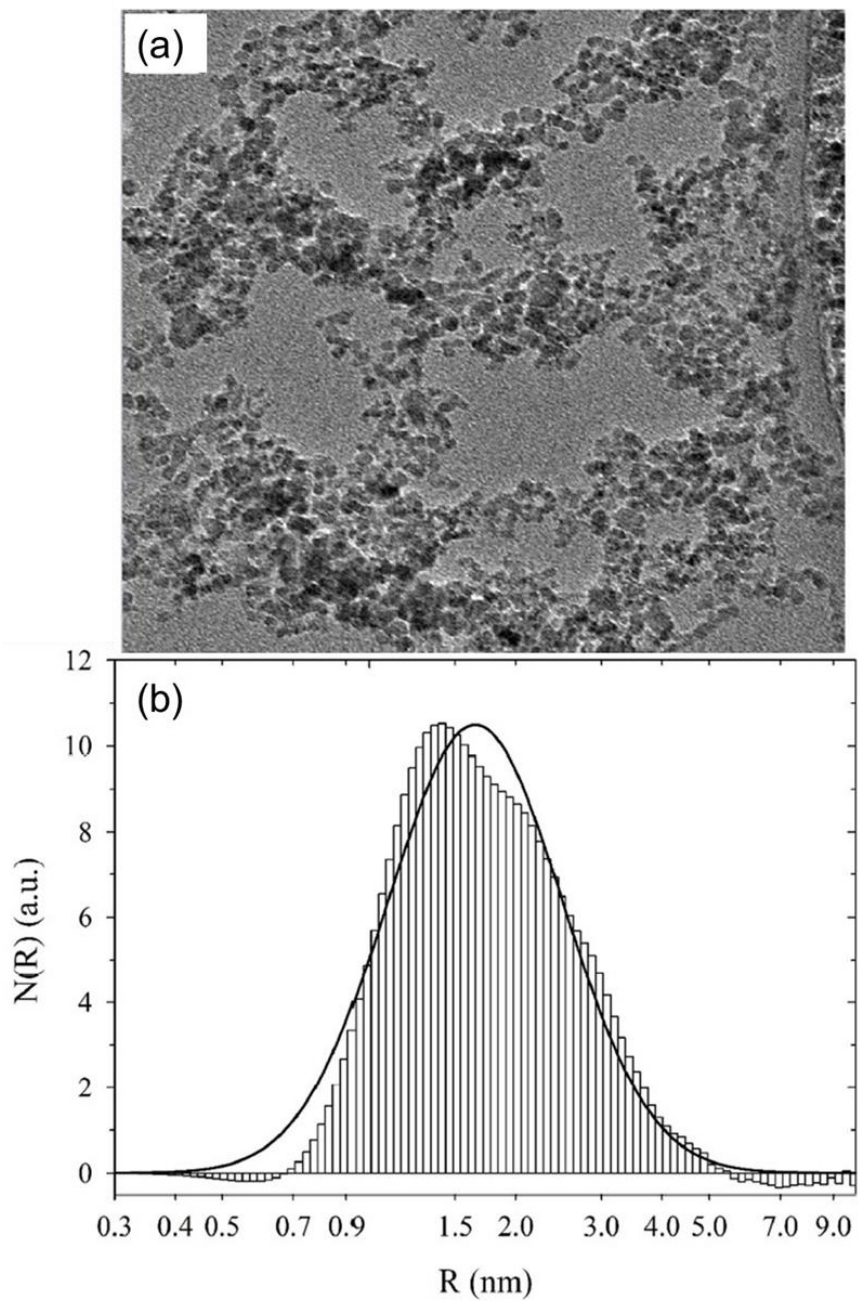


**Figure 9-4.** (a) HR-TEM image of DN fractal-like aggregates on the mesoscopic scale (b) lin-log plot of the SAXS size distribution functions (see **Figure. 9-3**). Note the Gaussian shape of SAXS size distribution functions in lin-log coordinates.

## 9.4 Conclusions

We present a simple polydisperse model for determination of the size distribution function of DNs crystallites from the small-angle X-ray scattering. From the atomistic structural models of  $\sim 5$  nm DNs simulated using Monte Carlo quenched method, we found that nanodiamonds have a core-shell structure. The  $sp^3$  nanodiamond cores are enclosed with patchy-like graphitic  $sp^2$  carbon shells. The thickness of the interfacial region obtained from the fitting of hyperbolic-tangent function to simulated data is  $\sim 0.7$  nm. This indicates that  $sp^2$  graphitic shells have a disordered structure. The asphericity of  $\sim 0.00012$  computed from atomistic structural models of DNs is quite small, indicating a small deviation of DNs shapes from a perfect sphere, which is consistent with HR-TEM observations. On the mesoscopic level, DNs are modeled as an assembly of spherical diamond-like particles with a distribution of particle sizes. The structure factor of the hard-spheres model with an optimized fraction of 0.13 is used to include the correlations between individual DNs in aggregates. The simplified model of DNs polydispersity fitted the experimental SAXS data very well. It is discovered that DNs are polydisperse and their sizes are log-normally distributed. The average radius of DNs of 1.88 and 2.25 nm computed from SAXS and HR-TEM images is comparable. However, the fraction of NDs crystallites with a larger radius of  $\sim 3$  nm is only visible on SAXS, which can be explained by the poor statistic of HR-TEM image analysis. Our modeling and investigations reveal a log-normal size distribution of DNs crystallites. The random growth duration model rather than Smoluchowski's coagulation model was postulated as a probable mechanism of NDs nucleation and growth.

## 9.5 Acknowledgments

The work was partially supported by Grant-in-Aid for Scientific Research (B) (17H03039) and the JST OPERA project.

## 9.6 References

- (1) Danilenko, V. V. On the history of the discovery of nanodiamond synthesis. *Phys. Solid State* **2004**, 46, 595-599.
- (2) Greiner, N. R.; Phillips, D. S.; Johnson, J. D.; Volk, F. Diamonds in detonation soot. *Nature* **1988**, 333, 440-442.
- (3) Shenderova, O. A.; Zhirnov, V. V.; Brenner, D. W. Carbon nanostructures. *Crit. Rev. Solid. State. Mater. Sci.* **2002**, 27, 227-356.
- (4) Krueger, A. Diamond nanoparticles: jewels for chemistry and physics. *Adv. Mater.* **2008**, 20, 2445-2449.
- (5) Roy, U.; Drozd, V.; Durygin, A.; Rodriguez, J.; Barber, P.; Atluri, V.; Liu, X.; Voss, T. G.; Saxena, S.; Nair, M. Characterization of nanodiamond-based anti-HIV drug delivery to the brain. *Sci. Rep.* **2018**, 8, 1603.
- (6) Vul', A. Ya., Shenderova, O. A. (Eds.) Detonation Nanodiamonds. Science and Applications. Pan Stanford Publishing Pte. Ltd.: Singapore, **2014**.
- (7) Osawa, E. Recent progress and perspectives in single-digit nanodiamond. *Diamond Relat. Mater.* **2007**, 16, 2018-2022.
- (8) Tomchuk, O. V.; Volkov, D. S.; Bulavin, L. A.; Rogachev, A. V.; Proskurnin, M. A.; Korobov, M. V.; Avdeev, M. V.; Structural characteristics of aqueous dispersions of detonation nanodiamond and their aggregate fractions as revealed by small-angle neutron scattering. *J. Phys. Chem. C* **2015**, 119, 794-802.

- (9) Kruger, A.; Kataoka, F.; Ozawa, M.; Fujino, T.; Suzuki, Y.; Aleksenskii, A. E.; Vul, A. Y.; Osawa, E. Unusually tight aggregation in detonation nanodiamond: identification and disintegration. *Carbon* **2005**, 43, 1722-1730.
- (10) Pina-Salazar, E. Z.; Urita, K.; Hayashi, T.; Futamura, R.; Vallejos-Burgos, F.; Włoch, J.; Kowalczyk, P.; Wiśniewski, M.; Sakai, T.; Moriguchi, I.; Terzyk, A. T.; Osawa, E.; Kaneko, K. Water adsorption property of hierarchically nanoporous detonation nanodiamonds. *Langmuir* **2017**, 33, 11180-11188.
- (11) Stehlik, S.; Varga, M.; Ledinsky, L.; Jirasek, V.; Artemenko, A.; Kozak, H.; Ondic, L.; Skakalova, S.; Argentero, G.; Pennycook, T.; Meyer, J. C.; Fejfar, A.; Kromka, A.; Rezek, B. Size and Purity Control of HPHT Nanodiamonds down to 1 nm. *J. Phys. Chem. C* **2015**, 119, 27708-27720.
- (12) Ozerin, A. N.; Kurkin, T. S.; Ozerina, L. A.; Dolmatov, V. Yu. X-ray diffraction study of the structure of detonation nanodiamonds. *Crystal. Rep.* **2008**, 53, 60-67.
- (13) Williams, O. A.; Hees, J.; Dieker, Ch.; Jager, W.; Kirste, L.; Nebel, Ch. E. Size dependent reactivity of diamond nanoparticles. *ACS Nano* **2010**, 4, 4824-4830.
- (14) Dhindsa, G. K.; Bhowmik, D.; Goswami, M.; O'Neill, H.; Mamontov, E.; Sumpter, B. G.; Hong, L.; Ganesh, P.; Chu, X-Q Enhanced dynamics of hydrated tRNA on nanodiamond surfaces: a combined neutron scattering and MD simulation study. *J. Phys. Chem. B* **2016**, 120, 10059-10068.
- (15) Qahtani, H. S. Al; Higuchi, R.; Sasaki, T.; Alvino, J. F.; Metha, G. F.; Golovko, V. B.; Adnan, R.; Andersson, G. G.; Nakayama, T.; Grouping and aggregation of ligand protected Au<sub>9</sub> clusters on TiO<sub>2</sub> nanosheets. *RSC Adv.* **2016**, 6, 110765-110774.

- (16) Petersen, J. S.; Analysis of small-angle scattering data from colloids and polymer solutions: modelling and least-squares fitting. *Adv. Coll. Int. Sci.* **1997**, 70, 171-210.
- (17) Andersen, E. S.; Dong, M.,; Nielsen, M. M.; Jahn, K.; Subramani, R.; Mamdouh, W.; Golas, M. M.; Sander, B.; Stark, H.; Oliveira, C. L. P.; Pedersen, J. S.; Birkedal, V.; Besenbacher, F.; Gothelf, K. V.; Kjems, J. Self-assembly of a nanoscale DNA box with a controllable lid. *Nature* **2009**, 459, 73-76.
- (18) Allen, M. P.; Tildesley, D. J. Computer simulation of liquids. Clarendon Press: Oxford, **1987**.
- (19) Marks, N. A. Generalizing the environment-dependent interaction potential for carbon. *Phys. Rev. B* **2000**, 63, 35401-1-7.
- (20) Kowalczyk, P.; Terzyk, A. P.; Gauden, P. A.; Furmaniak, S. Kaneko, K. Toward in silico modelling of palladium-hydrogen-carbon nanohorn nanocomposites. *Phys. Chem. Chem. Phys.* **2014**, 16, 11763-11769.
- (21) Gale, J. D. GULP: A computer program for the symmetry-adapted simulation of solids. *J. Chem. Soc. Faraday Trans.* **1997**, 93, 629-637.
- (22) Biscoe, J.; Warren, B. E. An X - Ray study of carbon black. *J. Appl. Phys.* **1942**, 13, 364-372.
- (23) Jurkiewicz, K.; Hawełek, Ł.; Balin, K.; Szade, J.; Braghiroli, F. L.; Fierro, V.; Celzard, A.; Burian, A. Conversion of natural tannin to hydrothermal and graphene-like carbons studied by wide-angle X-ray scattering. *J. Phys. Chem. A* **2015**, 119, 8692-8701.
- (24) Hubbell, J. H.; Veigele, Wm. J.; Briggs, E. A.; Brown, R. T. ; Cromer, D. T.; Howerton, R. J. Atomic form factors, incoherent scattering functions, and photon scattering cross sections. *J. Phys. Chem. Ref. Data* **1975**, 4, 471-538.

- (25) Gelisio, L.; Scardi, P. 100 years of Debye's scattering equation. *Acta Cryst.* **2016**, *A72*, 608-620.
- (26) Hsiao, P.-T. Chain morphology, swelling exponent, persistence length, like-charge attraction, and charge distribution around a chain in polyelectrolyte solutions: effects of salt concentration and ion size studied by Molecular Dynamics simulations. *Macromolecules* **2006**, *29*, 7125-7137.
- (27) Kowalczyk, P.; Gauden, P. A.; Terzyk, A. P. Cryogenic separation of hydrogen isotopes in single-walled carbon and boron-nitride nanotubes: insight into the mechanism of equilibrium quantum sieving in quasi-one-dimensional pores. *J. Phys. Chem. B* **2008**, *112*, 10137-10141.
- (28) Pedersen, J. S. Determination of size distributions from small-angle scattering data for systems with effective hard-sphere interactions. *J. Appl. Cryst.* **1994**, *24*, 595-608.
- (29) Pedersen, J. S.; Posselt, D.; Mortensen, M. Analytical treatment of the resolution function for small-Angle scattering. *J. Appl. Cryst.* **1990**, *23*, 321-333.
- (30) Svergun, D. I.; Mathematical methods in small-angle scattering data analysis. *J. Appl. Cryst.* **1991**, *24*, 485-492.
- (31) Kinning, D. J.; Thomas, E. L. Hard-sphere interactions between spherical domains in diblock copolymers. *Macromolecules* **1984**, *17*, 1712-1718.
- (32) Ashcroft, N. W.; Lekner, J. Structure and resistivity of liquid metals. *J. Phys. Rev.* **1966**, *145*, 83-90.
- (33) Svergun, D. I. Determination of the regularization parameter in indirect-transform methods using perceptual criteria. *J. Appl. Cryst.* **1992**, *25*, 495-503.

- (34) Kowalczyk, P.; Gauden, P. A.; Terzyk, A. P.; Neimark, A. V. Screening of carbonaceous nanoporous materials for capture of nerve agents. *Phys. Chem. Chem. Phys.* **2013**, 15, 291-298.
- (35) Hansen, P. H. Rank-deficient and discrete ill-posed problems. SIAM: Philadelphia, **1992**.
- (36) Mochalin, V. N.; Shenderova, O.; Ho, D.; Gogotsi, Y. The properties and applications of nanodiamonds. *Nature Nanotech.* **2012**, 7, 11-23.
- (37) Fenglei, H.; Yi, T.; Shourong, Y. Synthesis mechanism and technology of ultrafine diamond from detonation. *Phys. Solid State* **2004**, 46, 601-604.
- (38) Kiss, L. B.; Soderlund, J.; Niklasson, G. A.; Granqvist, C. G. The real origin of lognormal size distributions of nanoparticles in vapor growth processes. *Nanostructured Materials* **1999**, 12, 327-332.



## Chapter 10

### 10. General conclusions and perspectives

This research focused on a deeper understanding of the hygroscopic property of nanodiamonds; an interfacial property deeply involved in the processes where water-nanodiamond interaction is present. Several aspects related to the hygroscopic property of nanodiamonds were targeted through the development of this research.

First, previous nanodiamonds-water related studies were presented in order to have a general overview of the state of art. Origin, structure, and chemistry of nanodiamond is the basic knowledge to explain the hygroscopic ability of nanodiamonds. Association of 3-5 nm nanodiamonds; forming nanodiamonds aggregates of 50-500 nm; leave inter-particle pores. These aggregates contain structural water, and possess ability to hydrate.

Second, current research has not deeply considered the inter-particle pores in the hygroscopic ability of nanodiamonds. Therefore, a short review of the fundamentals of adsorption was presented in order to understand the implications of considering the textural properties of nanodiamonds aggregates in the explanation of their hygroscopic property. Water, nitrogen, and argon adsorption isotherms gave information on the textural properties of nanodiamond aggregates.

Third, experimental and modeling studies were performed to propose a mechanism of the hygroscopic ability and water adsorption property of hierarchically nanoporous

detonation nanodiamonds. The hygroscopic nature of nanodiamonds is associated with the surface functionalities situated on the graphitic shell, and with the ultramicropores among nanodiamond particles in the aggregates and on the mesopore walls.

Fourth, availability of water-selective adsorption sites on detonation nanodiamonds depends on heating (in the range of 423 K – 623 K); the higher the heating in *vacuo*, the higher amount of water-selective adsorption sites, which are responsible for the hygroscopic behavior.

Fifth, prolonged heated nanodiamonds shows an anomalous water adsorption behavior. Heating at 423 K for 52 h changes the aggregate structure of nanodiamonds by removing structural water molecules that stabilized the aggregate structure, resulting in tighter aggregation of nanodiamond particles. Further adsorption of water molecules can re-open the aggregate structure.

Sixth, structural water contained in nanodiamond aggregates, or subsequently loosely or strongly adsorbed water (due to their hygroscopic ability) enhances their intrinsic property of electrical conductivity.

Seventh, wettability and hygroscopic property of nanodiamonds were compared to other commercially available hydrophilic or hydrophobic porous materials. Nanodiamond aggregates, at bulk scale, quickly absorb water droplets. The water absorption capacity of nanodiamonds is comparable to that of the clay Montmorillonite and higher than those of the zeolites ZSM-5 and molecular sieve 5A. Such comparisons

were addressed by contact angle measurements and absorption of liquid water droplets.

Eighth, the contribution to water adsorption on SWCNH addressed, where are shown selective sites for water adsorption gives the key to understand the hygroscopic behavior of nanodiamonds.

Ninth, simulation studies based on experimental data on SAXS helped to determine the nanodiamond structure and dimensions more accurately, which is essential to understand the hygroscopic nature of nanodiamonds.

Finally, considering that a projection from the United Nations Environment Program indicates that severe water shortages will affect 4 billion people by 2050, nanodiamond hygroscopic ability; whose approach remind mimicking mechanisms in nature; must be exploited in future for designing nanodiamond-based materials for water sustainability.

*“Look deep into nature and then you will understand everything better.”*

*Albert Einstein*



# Chapter 11

## 11. Scientific products

### 11.1 Publications

- 11.1.1 E. Z. Pina-Salazar, K. Kaneko. (2015) Adsorption of water vapor on mesoporosity-controlled single-wall carbon nanohorn. *Colloids Interface Sci. Commun.*, 5, 8–11.
- 11.1.2 E. Z. Pina-Salazar, K. Urita, T. Hayashi, R. Futamura, F. Vallejos-Burgos, J. Włoch, P. Kowalczyk, M. Wiśniewski, T. Sakai, I. Moriguchi, A. P. Terzyk, E. Ōsawa, K. Kaneko. (2017) Water adsorption property of hierarchically nanoporous detonation nanodiamonds. *Langmuir*, 33(42), 11180-11188.
- 11.1.3 E. Z. Piña-Salazar, R. Kukobat, R. Futamura, T. Hayashi, T. Sakai, E. Ōsawa, K. Kaneko. (2018) Water-selective adsorption sites on detonation nanodiamonds. *Carbon*, 139, 853-860.
- 11.1.4 E. Z. Piña-Salazar, K. Sagisaka, Y. Hattori, T. Sakai, R. Futamura, E. Ōsawa, K. Kaneko. (2019) Electrical conductivity changes of water-adsorbed nanodiamonds with thermal treatment. *Chem. Phys. Lett. X*, 2, 100018.
- 11.1.5 E. Z. Piña-Salazar, T. Sakai, E. Ōsawa, R. Futamura, K. Kaneko. (2019) Unusual hygroscopic nature of nanodiamonds in comparison with well-known porous materials. *J. Colloid. Interface Sci.* 549, 133–139.

## 11.2 Seminars and conferences

- 11.1.1 Oral presentation: E. Z. Piña-Salazar, T. Sakai, K. Kaneko. Comparative study on hygroscopic properties of nanodiamonds. 97<sup>th</sup> Annual Meeting of The Chemical Society of Japan, Keio University, Yokohama, Japan, March 16<sup>th</sup> to 19<sup>th</sup>, **2017**.
- 11.1.2 Poster presentation: E. Z. Piña -Salazar, K. Urita, T. Hayashi, E. Ōsawa, F. Vallejos - Burgos, R. Futamura, T. Sakai, K. Kaneko. Role of Porosity in the Hygroscopic Nature of Nanodiamonds Monoliths, 6CBNM, Shinshu University, Nagano, Japan, July **2017**.
- 11.1.3 Poster presentation: E. Z. Piña-Salazar, K. Urita, T. Hayashi, E. Ōsawa, T. Sakai, K. Kaneko. Role of Porosity in the Hygroscopic Nature of Nanodiamonds. The World Conference on Carbon 2017, Melbourne Australia, July 23<sup>rd</sup> to 27<sup>th</sup>, **2017**.
- 11.1.4 Oral presentation. E. Z. Pina-Salazar, R. Kukobat, T. Sakai, E. Ōsawa, K. Kaneko. Exact pore structural analysis of nanodiamonds of hygroscopic property. 31<sup>st</sup> Annual Meeting of The Japan Society on Adsorption, Shizuoka Japan, November 16<sup>th</sup> to 17<sup>th</sup>, **2017**.
- 11.1.5 Oral presentation: E. Z. Pina-Salazar, K. Sagisaka, T. Hayashi, T. Sakai, E. Ōsawa, K. Kaneko. Electronic transport properties of nanodiamonds with relevance to adsorbed water. 98<sup>th</sup> Annual Meeting of The Chemical Society of Japan, Nihon University, Funabashi, Japan, March 20<sup>th</sup> to 23<sup>rd</sup>, **2018**.
- 11.1.6 Oral presentation: E. Z. Piña-Salazar, R. Kukobat, K. Sagisaka, Y. Hattori, T. Sakai, E. Ōsawa, K. Kaneko. Effects of preheating on electronic transport of detonation nanodiamonds. The World Conference on Carbon 2018, Madrid, Spain, July 1<sup>st</sup> to 6<sup>th</sup>, **2018**.